## Into the stellar glare

Leveraging astrometry to directly detect and characterise substellar companions and their satellites

**Thomas Otto Winterhalder** 



München 2025

## Into the stellar glare

# Leveraging astrometry to directly detect and characterise substellar companions and their satellites

**Thomas Otto Winterhalder** 

Dissertation

der Fakultät für Physik

der Ludwig-Maximilians-Universität

München

vorgelegt von Thomas Otto Winterhalder aus Donaueschingen

München, den 6. August 2025

The work presented in this thesis was conducted by the author while employed at the European Southern Observatory in Garching, Germany, and enrolled as a doctoral student at the Ludwig Maximilian University of Munich between September 2022 and August 2025. It was jointly supervised by A. Glindemann, A. Mérand and S. Lacour.

Erstgutachter: Priv.-Doz. Dr Andreas Glindemann

Zweitgutachter: Dr Gaël Chauvin

Tag der mündlichen Prüfung: 12. September 2025

# Contents

$\mathbf{Z}_{\mathbf{l}}$	usam	nmenfassung	XV
$\mathbf{A}$	bstra	act	xvii
1	Intr	roduction	1
	1.1	Worlds imagined, worlds found	 1
	1.2	The current state of exoplanet science	 3
		1.2.1 Detection and characterisation methods	 3
		1.2.2 Demographics	 12
		1.2.3 Formation scenarios	 17
	1.3	Gaia	 23
		1.3.1 Design and functionality	23
		1.3.2 Hunting planets with Hipparcos & Gaia	24
		1.3.3 Hunting planets with Gaia DR3?	 25
	1.4	Fringe science: optical interferometry	27
		1.4.1 The yoke of the Rayleigh criterion	27
		1.4.2 Evading the diffraction limit	28
		1.4.3 Turning fringes into precision measurements	30
	1.5	VLTI and the GRAVITY instrument	34
		1.5.1 Design and functionality	34
	1.6	Thesis outline	 36
2	Fro	om blind to semi-targeted searches: HIP 99770 b	39
	2.1	Introduction	 41
	2.2	Observations and data reduction	 42
		2.2.1 Previous observations	42
		2.2.2 VLTI/GRAVITY	42
	2.3	Orbital analysis	45
	2.4	Spectral analysis	50
		2.4.1 Spectral classification	50
		2.4.2 Constraining the system age	
		2.4.3 Atmospheric forward modelling	
		2.4.4 Comparing evolutionary and atmospheric modelling	 59

<u>iv</u> CONTENTS

	2.5	Conclusions
3	Fro	m semi- to fully-targeted searches: the Gaia-GRAVITY synergy 63
	3.1	Introduction
	3.2	Observations
		3.2.1 Using Gaia as a signpost
		3.2.2 Following-up with GRAVITY
	3.3	Methods
		3.3.1 Making Gaia and GRAVITY 'talk'
		3.3.2 Orbital refinements
		3.3.3 Nailing down dynamical masses
		3.3.4 Photometric characterisation
	3.4	Discussion
		3.4.1 On the Gaia–GRAVITY synergy
		3.4.2 Orbital refinements and dynamical masses
		3.4.3 Inferring ages from evolutionary models 81
	3.5	Conclusion
4	C	
4		veying the planetary frontier: pushing Gaia-GRAVITY to the limit 85
	4.1	Motivation for the observing programme
		4.1.1 A logical next step
	4.0	4.1.2 A matter of timing
	4.2	Target selection
		4.2.1 Preliminary filtering
		4.2.2 Age filtering
		4.2.3 Position predictions
	4.3	Results of the observing programme
		4.3.1 Missing APMPM J0710-5704 (b)
		4.3.2 Unveiling LP 754-5 (b)'s true identity
	4.4	Gaia follow-up observations in context
5	Tak	ing the next step: hunting exomoons with optical interferometry 97
_	5.1	Introduction
	5.2	The planetometric signal
	J	5.2.1 Planetometric signal amplitude
		5.2.2 Simulating the signal variation in time
	5.3	Expected signals in the context of measurement uncertainties
	5.4	Modelling multi-epoch detection attempts
	9.4	5.4.1 Defining observing strategies
		5.4.1 Denning observing strategies
		5.4.2 Creating the planetometric mock epochs
		5.4.4 Estimating the detection significance
	55	Multi-epoch sensitivity curves
	5.5	With epoch sensitivity curves

Inhaltsverzeichnis	v
--------------------	---

	5.6	Conclusions	114
6	Out	look	117
	6.1	Quo vadis, HIP 99770 b?	119
	6.2	Untapped resources in Gaia DR3	119
	6.3	What Gaia DR4 will bring to the table	121
		6.3.1 Pushing for an overlap between radial velocity and direct imaging.	121
		6.3.2 Additional avenues to pursue	123
	6.4	Companion on the brink: the tale of WT 766 B	125
	6.5	What's next for exomoons?	127
7	Sun	nmary & Conclusions	129
$\mathbf{A}$	App	pendix to Chapter 2	133
		Correcting for throughput losses	133
			133
	A.3	Additional orbital fitting plots	136
	A.4	Additional spectral fitting plots	137
В	App	pendix to Chapter 3	139
	B.1	Correcting for throughput losses	139
	B.2	Inflation factors for <i>Gaia</i> uncertainties	139
	B.3	Additional tables and plots	140
$\mathbf{C}$		pendix to Chapter 4	153
	C.1	Additional plots	153
Bi	bliog	raphy	157
Li	st of	Publications	175
Ac	knov	vledgements	177

# List of Figures

1.1	Schematic of the radial velocity and transit methods	6
1.2	Schematic of the astrometric method	8
1.3	Schematic of the direct imaging method	10
1.4	Mass–semi-major axis distribution of the known exoplanet sample	13
1.5	Two visualisations of the radius gap	14
1.6 1.7	Turnover in the occurrence rate of giant exoplanets at the ice-line Schematic of the core accretion model and simulation of a gravitationally unstable disc	16 21
1.8	Gaia satellite during pre-launch sunshield deployment test	$\frac{21}{25}$
1.9	Young's double-slit experiment and interferogram	29
1.10	Schematic of a basic interferometer	31
1.11	VLT under construction and VLTI schematic	35
2.1	HIP 99770 b GRAVITY detection	43
2.2	Combining on- and off-axis GRAVITY spectra	46
2.3	HIP 99770 b orbit projected onto the plane of the sky	48
2.4	Orbital parameter posterior distributions for HIP 99770 b	49
2.5	Colour-magnitude diagram with literature BD and exoplanet populations and HIP 99770 b	52
2.6	Goodness-of-fit statistic, $G_k$ , as a function of spectral type	52 - 53
2.7	Mass-magnitude plane with model isochrones and HIP 99770 b	55
2.8	Spectral energy distribution of HIP 99770 b with different best-fit models.	57
2.9	Mass-metallicity plane with literature planet population and HIP 99770 b.	59
2.10	Comparison between atmospheric and evolutionary model inferences	61
3.1	Position probability maps as computed from the <i>Gaia</i> NSS two-body orbit catalogue	68
3.2	Orbital parameter posterior distributions for the different target systems .	73
3.3	Companion orbits projected onto the plane of the sky	74
3.4	Mass-magnitude plane with model isochrones and detected companions	75
3.5	Age, effective temperature, and radius constraints as derived from evolu-	
	tionary models	76

3.6	Colour-magnitude diagram with literature BD and exoplanet populations and detected companions	77 80
4.1	Gaia-GRAVITY planet detection region	88
4.2 4.3	GRAVITY contrast limit as a function of host-to-companion separation K-band magnitudes as a function of mass for two <i>Gaia</i> planet candidates	90
4.4	feasible for a GRAVITY follow-up	91 92
5.1 5.2	Schematic of the orbital wobble caused by different exomoons RV and planetometric signal amplitudes in the vicinity of the putative exo-	104
5.3 5.4	moon around $\beta$ Pic b	107 109 112
6.1 6.2 6.3	Position predictions for HIP 99770 b	120 122
	midpoint estimates	126
7.1 7.2	Mass—semi-major axis distribution of the known exoplanet sample with $Gaia$ —GRAVITY synergy detections and targeted sensitivity regions Artist's impression of a close-in BD companion	131 132
A.1	Normalised coupling efficiency, $\gamma$ , as a function of angular separation be-	
11.1	tween host and HIP 99770 b	133
A.2 A.3	Stellar calibration model spectra for HIP 99770 A and HD 196885 AB Orbital parameter sampling corner plot for HIP 99770 b	135 136
A.4	Atmospheric model posterior sampling corner plot for the DRIFT-PHOENIX	40=
A.5	and Sonora Diamondback models	<ul><li>137</li><li>138</li></ul>
B.1	Normalised coupling efficiency, $\gamma$ , as a function of the angular separation	
	between hosts and companions	140
B.2	Gaia NSS position angle predictions compared to GRAVITY detections	143
B.3 B.4	GRAVITY contrast spectra for the different target systems	<ul><li>144</li><li>145</li></ul>
B.5	Orbital parameter sampling corner plot for the CD-50 869 system	$145 \\ 146$
B.6	Orbital parameter sampling corner plot for the HD 17155 system	147
B.7	Orbital parameter sampling corner plot for the WT 766 system	148
B.8	Orbital parameter sampling corner plot for the G3872 system	149

	Orbital parameter sampling corner plot for the G1920 system	
B.10	Orbital parameter sampling corner plot for the StKM1-1494 system	151
C.1	u- $v$ plane coverage during the observations of LP 754-5 (b)	153
C.2	Closure phase and best-fit model of LP 754-5 (b) observations from 2nd and	
	3rd of June 2024	154
C.3	Visibility amplitude and best-fit model of LP 754-5 (b) observations from	
	2nd and 3rd of June 2024	155
C.4	Posterior sampling corner plots for observations from 2nd and 3rd of June	
	2024	156

# List of Tables

2.1	GRAVITY observation log of the target HIP 99770 b and of the swap cali-	
	brator HD 196885 AB	45
2.2	Astrometric detections of HIP 99770 b	47
2.3	Orbital parameter priors and posteriors	51
2.4	Atmospheric forward modelling posteriors	58
3.1	Astrometric epochs of the respective companions obtained with GRAVITY.	69
3.2	Semi-major axes, inflation factors and reduced chi-squared values for the detected companions	81
4.1	GRAVITY observation log of LP 754-5	93
4.2	Parameter posteriors obtained from the PMOIRED fitting routine	94
5.1	Planetometric signal amplitudes for different case examples and approximate	
	planetometric measurement precisions	105
A.1	Inferred stellar model atmosphere parameters	134
В.1	Observation log of the GRAVITY follow-up	140
B.2	Stellar magnitudes in different wavelength bands used for the spectral fits	
	performed in Sect. 3.4.3	141
В.3	Synthetic absolute magnitudes of the different companions	141
B.4	Orbital and evolutionary model parameters of the respective target systems.	142

## List of Abbreviations

AC Across-Scan

**AF** Astrometric Field

AL Along-Scan

ALMA Atacama Large Millimeter/submillimeter Array

AMBER Astronomical Multi-BEam combineR

AO Adaptive Optics
AT Auxiliary Telescope

BD Brown Dwarf
CA Core Accretion

**CCD** Charge-Coupled Devices

CHARIS Coronagraphic High Angular Resolution Imaging Spectrograph

CMD Colour Magnitude Diagram

**COM** Centre Of Mass

**DDT** Director's Discretionary Time

DI Direct ImagingDR Data Release

ELT Extremely Large Telescope
ESO European Southern Observatory
ESPRI Exoplanet Search with PRIMA

ESPRESSO Echelle SPectrograph for Rocky Exoplanet- and Stable Spectro-

scopic Observations

FoV Field of View FT Fringe Tracker

GAIA Global Astrometric Interferometer for Astrophysics

GGPP Giant Gaseous ProtoPlanet GI Gravitational Instability

**GPAO** GRAVITY Plus Adaptive Optics

GPI Gemini Planet Imager GPIES GPI Exoplanet Survey

HGCA Hipparcos-Gaia Catalogue of AccelerationsHipparcos High Precision Parallax Collecting Satellite

**HJ** Hot Jupiter

IRDIS Infra-Red Dual-beam Imager and Spectrograph

LGS Laser Guide Star

LLA Local Linear Approximation

MATISSE Multi-AperTure mid-Infrared SpectroScopic Experiment

MCMC Markow-Chain-Monte-Carlo

MID-infrared Interferometric instrument

MJD Modified Julian Date
NGS Natural Guide Star

NGTS Next Generation Transit Survey

NSS Non-Single-Star

**OPD** Optical Path Difference

PHASES Palomar High-precision Astrometric Search for Exoplanets
PIONIER Precision Integrated-Optics Near-infrared Imaging ExpeRiment

PMa Proper Motion Anomaly

PRIMA Phase-Referenced Imaging and Microarcsecond Astrometry

**PSF** Point-Spread Function

PTI Palomar Testbed Interferometer

RV Radial Velocity
SC Science Combiner

SHINE SpHere Infrared Exoplanet Survey

S/N Signal-to-Noise

SPLAT SpeX Prism Library Analysis Toolkit

**SPHERE** Spectro-Polarimetric High-contrast Exoplanet REsearch

**TESS** Transiting Exoplanet Survey Satellite

TI Thiele-Innes
UT Unit Telescope

UTC Coordinated Universal Time

VLT Very Large Telescope

VLTI Very Large Telescope Interferometry

## Zusammenfassung

Die direkte Beobachtung und Erforschung von Riesenplaneten ist eine der Schlüsselmethoden zur Erforschung der Entstehungsprozesse, Entwicklung und atmosphärischen Merkmale dieser fernen Welten. Und dennoch, das grelle Licht des Muttersterns und instrumentelle Komplikationen haben zur Folge, dass die Anwendung des Verfahrens derzeit auf massive und auf weiten Umlaufbahnen kreisenden Planeten beschränkt ist. Um Aufschluss über die Entstehungsgeschichte unseres eigenen Sonnensystems zu erhalten sowie darüber ob und wie repräsentativ es ist, müssen wir die Anzahl hinreichend gut verstandener Exoplaneten auf engen Umlaufbahnen vergrößern.

In dieser Arbeit präsentiere ich einen neuen Ansatz zur Ausweitung unserer Sensitivität zur direkten Beobachtung kleinerer planetarer Massen und engerer Umlaufbahnen. Diese Bemühungen basieren auf der Verknüpfung des astrometrischen und des direkten Entdeckungsverfahrens und ermöglichen eine sorgfältige und effiziente Charakterisierung individueller Planeten. In diesem Sinne legt diese Arbeit den Grundstein für den Aufbau einer repräsentativen Population direkt detektierter Planeten auf engen Umlaufbahnen. Die Abfolge der einzelnen Themen ist so gestaltet, dass sich ein kohärentes Narrativ bildet, das die Entwicklung unserer Fähigkeiten Nachfolgebeobachtungen gezielt durchzuführen beschreibt. Dieser zugrundeliegende rote Faden führt von mehr oder weniger blinden direkten Beobachtungen zu halb-gezielten Verfahren, die auf einer begründeten Zielauswahl von wahrscheinlichen Muttersternen beruhen, bis hin zu einer gänzlich gezielten Methodik, die imstande ist genaue Positionen planetarer Kandidaten relativ zu deren Muttersternen vorherzusagen.

Nach einer kurzen Einleitung der Themen, auf die sich diese Arbeit stützt, präsentiere ich eine neue Untersuchung von HIP 99770 b, dem ersten Exoplaneten, dessen direkte Detektion auf einer langfristigen Unregelmäßigkeit der Eigenbewegung des Muttersterns basiert. Auf der Grundlage von Daten, die mithilfe des GRAVITY Interferometers gewonnen wurden, schränke ich die Umlaufbahn des Begleiters ein, erschließe sein Alter und ermittle eine Reihe atmosphärischer Eigenschaften. Die aus diesen Untersuchungen hervorgehenden Ergebnisse verdeutlichen das Leistungsvermögen aber auch die Beschränkungen der Eigenbewegungs-Unregelmäßigkeiten Methode und werden letzten Endes dabei helfen, die Entstehungsgeschichte von HIP 99770 b zu klären.

Als nächstes demonstriere ich, wie die vom *Gaia* Weltraumteleskop gewonnenen astrometrischen Daten dazu benutzt werden können die relativen Positionen substellarer Begleiter einzelner Muttersterne vorherzusagen. Dieses neue Verfahren unterscheidet sich

von der Eigenbewegungs-Unregelmäßigkeiten Methode dadurch, dass es präzise, effiziente und gänzlich gezielte Nachfolgebeobachtungen ermöglicht. Im Anschluss an den Nachweis von acht Begleiterkandidaten zeige ich, wie es die Verknüpfung der zugrundeliegenden *Gaia* Daten mit einer einzigen GRAVITY Astrometrie Messung erlaubt, die Umlaufbahnen und Massen der ins Ziel gefassten Begleiter einzuschränken und dadurch deren tatsächliches Wesen aufzudecken: Fünf der neu entdeckten Begleiter sind nachweislich substellarer Natur.

Ich fahre damit fort, dieses Verfahren auf Begleiterkandidaten im planetaren Massebereich anzuwenden. Ich beschreibe das Verfahren zur Auswahl der Ziele und präsentiere dann die Auswertung der gewonnenen Daten und zeige dabei, dass es sich beim einzigen Zielsystem dieser Beobachtungsreihe in Wirklichkeit um einen Doppelstern handelt. Ich erörtere, wie diese Objekte mit planetenbeherbergenden Sternen verwechselt werden können und bespreche die Nicht-Detektion im Kontext anderer Studien, die die Kontamination des Gaia Datensatzes durch Fehlerkennungen untersuchen.

Indem ich auf dieselbe Methode zurückgreife, die Gaia zur Detektion von Planeten auf Umlaufbahnen um Sterne verwendet, demonstriere ich als nächstes, wie die unübertroffene astrometrische Präzision der optischen und nahinfraroten Interferometrie dazu genutzt werden kann Monde auf Umlaufbahnen um Exoplaneten zu entdecken. Durch Simulation der schwerkraftbedingten Störungen, die sie in den planetaren Umlaufbahnen erzeugen, berechne ich die ersten Exomond-Sensitivitätskurven für verschiedene interferometrische Instrumente. Bisher konnte noch keine belastbaren Detektionen dieser Objekte erzielt werden. Ihre Existenz und weite Verbreitung werden jedoch als wahrscheinlich erachtet. Die bevorstehende empirische Entdeckung von Exomonden wird unsere Theorien zur Planetenentstehung und unsere Suche nach bewohnbaren Welten beeinflussen.

Zum Schluss werfe ich noch einen Blick darauf, wohin die in dieser Arbeit entwickelten Verfahren in Zukunft führen könnten. Von der Bedeutung bevorstehender Datenveröffentlichungen und neuer Beobachtungsanlagen zur Erforschung von Exoplaneten bis hin zu den Aussichten für die Entdeckung und Erforschung von Exomonden bespreche ich eine Reihe kommender wissenschaftlicher Fragestellungen, um den in dieser Arbeit erzielten Fortschritt einzuordnen.

Insgesamt zeigt diese Arbeit auf, wie präzise Astrometrie dazu genutzt werden kann, Nachfolgebeobachtungen zu planen und Riesenplaneten zu erforschen. Sie hebt das Potential der Verknüpfung verschiedener Detektionsmethoden sowie die einzigartigen Fähigkeiten der optischen und nahinfraroten Interferometrie im Bereich der Exoplanetenforschung hervor. Alles in allem bereitet diese Arbeit den Weg zum Aufbau einer repräsentativen Population direkt detektierter Planeten, die jenen in unserem Sonnensystem ähneln und uns so dabei helfen dessen Entstehungsgeschichte zu verstehen.

### Abstract

The direct detection and characterisation of gas giant exoplanets is a key method for investigating the formation, evolution and atmospheric properties of these distant worlds. Yet, at present, the intense glare of the host stars and instrumental intricacies of the technique limit its application to massive planets orbiting their host stars on wide, far-out orbits. To shed light on the formation history of our own Solar System and assess how representative it is among other stellar systems, we need to expand the sample size of well-characterised exoplanets at short orbital separations.

In this thesis, I present a novel approach to extending our direct detection sensitivity towards lower companion masses and shorter orbital separations. This effort builds on the combination of the astrometric and direct detection methods and enables a thorough and efficient characterisation of individual planets. In this sense, the work presented in this thesis lays the groundwork for building a population-level sample of directly detected, short-separation exoplanets. The structure in which the different topics are presented is intended to convey a coherent narrative that illustrates an advance in our direct detection targeting capabilities. This underlying theme draws a line from mostly blind direct imaging studies to semi-targeted approaches based on an informed target selection of stars likely to host an exoplanet, to ultimately arrive at a fully-targeted technique that is capable of predicting the exact position of a planet candidate relative to its host.

After a brief introduction of the topics upon which this thesis rests, I present an updated study of HIP 99770 b, the first exoplanet directly detected on the basis of long-term proper motion irregularities presented by its host star. Drawing on data obtained by the GRAVITY interferometer, I constrain the orbital solution of the companion, infer its age and determine a set of atmospheric parameters. The results obtained from this thorough analysis offer valuable insights into the potential and limitations of the proper motion technique and will eventually help clarify the formation history of HIP 99770 b.

I next demonstrate how astrometric data collected by the *Gaia* space telescope can be used to reliably predict the position of substellar companions relative to their hosts. This new technique differs from the proper motion method in that it facilitates precise and efficient GRAVITY follow-up observations in a fully targeted manner. After the successful detection and confirmation of eight candidates, I show how the combination of the underlying *Gaia* data with a single GRAVITY astrometric epoch can enable tight constraints on the orbits and dynamical masses of the targeted companions and thereby reveal their true nature: five of the newly detected companions are shown to be substellar.

xviii Abstract

I continue by applying this technique to companion candidates in the planetary mass regime. After describing the target selection process, I present an analysis of the observational data we obtained for a single companion candidate and show that the target system actually corresponds to a stellar binary. I address how these objects can be mistaken for planet-hosting systems and discuss the non-detection in the context of other studies investigating the false-positive contamination of the *Gaia* data set.

Applying the same method *Gaia* employs to detect planets around stars, I next demonstrate how the unmatched astrometric precision enabled by optical and near-infrared interferometry can be exploited to detect moons around exoplanets. Simulating the gravitational perturbations they induce in planetary orbits, I compute the first exomoon sensitivity curves for different interferometric instruments. To date, no such object has been robustly detected. Yet, they are likely to exist in large numbers and – once detected – exomoons will impact current theories of planet formation and our search for habitable worlds.

Finally, I provide an outlook at what lies ahead for the techniques developed in this thesis. From the likely implications of upcoming data releases and observational facilities on exoplanet science to the prospects for exomoon detection and characterisation in the more distant future, I discuss a set of flagship science cases that serve to further contextualise the progress made in this thesis.

Overall, the work presented in this thesis demonstrates how to harness precision astrometry for informing follow-up observations and characterising gas giant exoplanets. It highlights the potential of leveraging synergies between different detection methods and the unique capabilities that optical and near-infrared interferometry can bring to exoplanet research. All things considered, it paves the way towards building a population-level sample of directly detected planets resembling those we see in our own Solar System and understanding its formation history.

## Chapter 1

## Introduction

Moreover, there is an infinite number of worlds, some like this world, others unlike it.

— *Epicurus*, Letter to Herodotus, transl. R. D. Hicks

#### 1.1 Worlds imagined, worlds found

The notion that, apart from the planets in our Solar System, there might be other worlds orbiting distant stars, further islands harbouring life out there in the cosmos has long held a deep fascination for mankind. Such ideas reach as far back as the writings of the Greek atomists Democritus and Epicurus (e.g. Long 1974), went mostly forgotten during the Middle Ages and eventually made a comeback during the Renaissance, when – in the aftermath of the Copernican revolution – the likes of Giordano Bruno, Johannes Kepler and Christiaan Huygens contemplated the possibility of life on these distant worlds (Granada 2008; van den Berg 2019). Indeed, thoughts and speculations on the subject can be found throughout documented history. It was Huygens who first proposed a method as to how it might be possible to detect such extrasolar planets, or exoplanets as we shall call them throughout this work. In his posthumously published Cosmotheoros (Huygens 1698), he conceived of the idea of imaging a planet's light directly, marking the first documented attempt at devising a method for studying extrasolar planets. On the other hand, the concept of discerning planets as they briefly occult their host stars during what is commonly referred to as a transit, a methodological cornerstone of contemporary exoplanet research, was formulated as recently as the first half of the twentieth century (Belorizky 1938).

While various claims of successful exoplanet detections were made and dismissed throughout the following decades, the first confirmed discovery of worlds beyond the Solar System was presented in the early 1990s (Wolszczan & Frail 1992). Orbiting the millisecond pulsar PSR B1257+12, two rocky companion planets revealed themselves through the timing variations they induced in the pulses of their host. It took another three years before 51 Pegasi b, the first planet around a Sun-like star, was found by monitoring its host's

1. Introduction

reflex radial motion induced by the presence of the orbiting companion (Mayor & Queloz 1995). This groundbreaking discovery – which was to earn the authors the 2019 Nobel prize – represents the starting point of modern exoplanet science.

Since then, the field has developed into one of the most prolific astrophysical disciplines, with the grand total of confirmed exoplanets currently approaching the 6000 mark (Akeson et al. 2013). In light of this fast growth, researchers are now beginning to shift their focus from the detection of ever more planets to the thorough characterisation of their atmospheres, the inference of formation and evolution processes, the sampling of the underlying planetary demographics and the possibility of finding life on these island worlds.

Besides understanding the processes that initially form and later continue to affect exoplanets throughout the different phases of their lifetimes, a prime objective of and source of motivation for pursuing exoplanet research is the possibility of drawing conclusions as to the history and future of our own Solar System. Are we living in a fairly common planetary system such as we see many of in our Galactic neighbourhood, or is its architecture rather unusual, perhaps even singular? How rare are Earth-like planets around Sun-like stars? Should we expect to find habitable worlds everywhere we look or are these islands few and far between? How do rocky exoplanets fit into the picture that is gradually emerging of highly dynamic formation processes involving giant gaseous exoplanets migrating through the protoplanetary disc? We have only just begun tackling these questions about the early phases and likely architectures of planetary systems. While the last thirty years of exoplanet science have seen the development of several different planet detection and characterisation methods, the one technique lending itself most effectively to the study of young planets is direct imaging.

This thesis intends to break new ground in the field of direct imaging by combining different methods, observational techniques, astronomical facilities and instruments, with the eventual goal of expanding the sensitivity of direct imaging studies down to lower planetary masses and smaller separations from their respective hosts. It therefore paves the way towards routinely imaging bodies resembling those found in our own Solar System, enhancing our understanding of its formation and ultimately helping us answer the question as to how we got here. Additionally, it discusses the role optical interferometry might soon play in applying various key exoplanet observation techniques to taking the next step in exoplanet research: the detection and eventual characterisation of exomoons.

#### 1.2 The current state of exoplanet science

Despite its relative youth the field of exoplanet research has come a long way since the discovery of 51 Pegasi b. Here we give a short overview of the various methods available to discover and study new planets as well as of what we have learned about their demographics and the processes that likely lead to their formation. These topics are of relevance to the underlying theme and narrative of this thesis.

#### 1.2.1 Detection and characterisation methods

The study of exoplanets comes with extreme technical challenges. In terms of mass, radius and brightness these objects are dominated by the host stars they orbit. This mismatch makes detection and characterisation efforts extraordinarily difficult. To date, several different exoplanet observation methods have been developed, the main ones of which are briefly laid out in the following.

Radial velocity method: This technique being the first one ever employed for the detection of an exoplanet around a Sun-like star (Mayor & Queloz 1995), it is only fitting to start this overview with the radial velocity (RV) method. This approach exploits the fact that in a two-body system such as a star-planet pair, instead of the lower-mass component orbiting the stationary higher-mass component, both components actually exhibit orbital motion around their mutual centre of mass<sup>1</sup>. Naturally, this barycentre will be close to the geometrical centre of the star. In the extreme case where the planet's mass is completely negligible as compared to that of its host, the barycentre will practically coincide with the centre of the star and the stellar orbital motion will be vanishingly small. In case of a non-negligible mass ratio between planet and host, however, the star's orbital reflex motion can be sufficiently fast along the line of sight to manifest as a measurable Doppler shift in its spectrum. Repeated measurements of this shift covering multiple stellar orbits can reveal a periodic modulation of the star's radial velocity as a result of being orbited by a planet. A schematic depiction of how such an "RV curve", that is its radial velocity as a function of orbital phase, is obtained is shown in the left panel of Fig. 1.1. One of key observables that can be extracted from this curve is the RV semi-amplitude,  $K_*$ , which relates to the system's properties according to

$$K_* = \frac{28.4329 \,\mathrm{m/s}}{\sqrt{1 - e^2}} \frac{M_{\rm pl} \sin(i)}{\mathrm{M}_{\rm Jup}} \left(\frac{M_* + M_{\rm pl}}{\mathrm{M}_{\odot}}\right)^{-2/3} \left(\frac{P}{1 \,\mathrm{yr}}\right)^{-1/3},\tag{1.1}$$

where e is the orbital eccentricity mutual to star and planet,  $M_{\rm pl}$  the planetary mass, i the inclination,  $M_*$  is the host star's mass and P is the mutual orbital period. Moreover,  $M_{\odot}$  and  $M_{\rm Jup}$  denote one solar and Jupiter mass, respectively, which are units that will

<sup>&</sup>lt;sup>1</sup>The motion of the barycentre is significantly more complex for systems consisting of more than two bodies. We shall here only consider the case where perturbations stemming from additional planets are negligible compared to the stellar reflex motion induced by the planet of interest.

4 1. Introduction

reappear regularly throughout this thesis. A detailed derivation of Eq. 1.1 can be found in Lovis & Fischer (2010). For reference, a single Earth-like planet orbiting a Sun-like star would induce a miniscule stellar RV semi-amplitude of approximately  $9 \,\mathrm{cm/s}$  (e.g. Fischer et al. 2016).

Since the system's barycentre moves away from the centre of the star for larger planetary masses and smaller planet-star separations, the RV method is inherently biased towards detecting close-in massive planets. The fact that systems featuring close-in planets will exhibit shorter orbital periods adds to this bias since it will be easier and less time-consuming to robustly sample the RV-curve over a full orbit (Cumming et al. 1999). Finally, the RV method is also biased towards edge-on orbit configurations, that is systems that are oriented such that to an observer on Earth the planet's orbital motion appears as a back-and-forth movement along a straight line as projected onto the plane of the sky. This is due to the fact that – as its name implies – this technique is sensitive to the radial component of the star's reflex motion only. Since the velocity component parallel to the plane of the sky does not impart a Doppler shift to the stellar spectrum, it is not measurable by means of the RV method. In a perfectly edge-on orbit where the planet's orbital inclination is exactly 90° the radial velocity component is maximised rendering it the most favourable orientation to RV studies. Vice versa, a planet in a precisely face-on orbit as projected onto the plane of the sky does not induce any radial velocity in its host resulting in a vanishing  $K_*$  as is evident from Eq. 1.1. Such face-on planets are thus not detectable by means of the RV monitoring. The technique's sensitivity to the system's orientation has another consequence: since the orbital inclination cannot be measured using only the RV method, the inferred mass from a model fit to the sampled RV curve inherently constitutes a lower limit,  $M_{\rm obs} = M_{\rm true} \sin(i)$  (e.g. Hatzes 2016). Here,  $M_{\rm obs}$  and  $M_{\rm true}$  are the observed and true planetary masses respectively and i denotes the orbital inclination. Thus, one essentially determines which planetary mass required to induce the stellar reflex motion assuming an edge-on orbit. Depending on the inclination, however, the necessary mass can be much larger. This degeneracy can only be broken by follow-up studies using other techniques that are capable of measuring i, such as the transit and astrometry methods (see below). Another limitation of the method is its susceptibility to stellar activity (Saar & Donahue 1997). Especially young stars can be very active, exhibiting flares granulation and starspots, phenomena that can mimic planetary RV signatures (e.g. Queloz et al. 2001). Such RV noise stemming from the stars' activity is commonly referred to as stellar "jitter".

Under ideal observing conditions targeting the most favourable, that is quite, stars current state-of-the-art instruments such as ESPRESSO (Echelle SPectrograph for Rocky Exoplanet- and Stable Spectroscopic Observations) at the European Southern Observatory's (ESO) Very Large Telescope (VLT) can reach an instrumental RV precision of  $10\,\mathrm{cm/s}$  (Pepe et al. 2021). Note that this value is remarkably close to the RV amplitude of  $9\,\mathrm{cm/s}$  expected for an Earth analogue around a Sun-like star mentioned above. However, the stellar jitter can easily dominate these signals making Earth twin detections challenging even for instruments such as ESPRESSO (Cegla 2019).

Transit method: As of now, judging by sheer number the most successful technique of exoplanet detection is the transit method. This approach banks on precisely monitoring the brightness of stars within a large Field-of-View (FoV) over long periods of time in order to temporally resolve any brief dimming they might exhibit. Such a decrease in the apparent brightness of a given star can be caused by an orbiting planet blocking a small fraction of the stellar flux from reaching the observer. Registered at periodic intervals these transits as they are commonly called can provide dependable planetary detections. A visualisation of how an exoplanet can move across the stellar disc and how this manifests in the detected flux is presented in the right panel of Fig. 1.1.

The first transit of an exoplanet was detected almost simultaneously by Charbonneau et al. (2000) and Henry et al. (2000). At the time, the planet, HD 209458 b, was already known from RV studies but the observation of its transit yielded a precise inclination estimate thereby breaking the mass degeneracy and for the first time enabled a direct measurement of a planetary radius outside of our Solar System. Indeed, the sizes of both the eclipsing and the eclipsed body are directly related to the fraction of stellar flux being blocked from reaching our telescopes, a quantity also known as the transit depth

$$\Delta F \propto \left(\frac{R_{\rm pl}}{R_*}\right)^2,$$
 (1.2)

where  $R_{\rm pl}$  and  $R_*$  are the planetary and stellar radius, respectively (Deeg & Alonso 2018). Thus, provided one knows the stellar radius, a measurement of  $\Delta F$  will yield an estimate of the planet's radius. Apart from the orbital inclination and companion radius, a repeated transit detection of a given planet also yields, among other things, the orbital period, P and the transit duration, T, which can be used to compute the semi-major axis, a. Moreover, in cases where the observed flux originating from the planet's dayside is non-negligible, an additional temporary drop-off in flux occurs when the planet moves behind and is occulted by the star. Such an event, referred to as a secondary transit or eclipse and first detected by Deming et al. (2005), is also included in the visualisation provided in Fig. 1.1.

While transits evidently unlock a wealth of observables that can be used to characterise a target planet, this method comes with one major drawback. Assuming the orbital orientations of exoplanetary systems are randomly distributed, only a small percentage of systems are fortuitously aligned such that they will show transits. In order to do so, the orbit of a given companion must exhibit an inclination, i, sufficiently close to the edge-on configuration so as to be encompassed by the transit opening angle,  $\vartheta$ , which – following the derivations in Barnes (2007a), Burke (2008) and Beatty & Seager (2010) – can be written as

$$\vartheta = \arcsin\left(\frac{R_*}{a} \cdot \frac{1 + e\sin(\omega)}{1 - e^2}\right). \tag{1.3}$$

Here,  $R_*$  is the host star's radius, a is the planet's semi-major axis, e is its orbital eccentricity and  $\omega$  denotes the argument of periapsis. This requirement significantly narrows down the number of planets accessible to transit studies. As can also be seen from Eq. 1.3, the method is inherently biased towards such companions on very close in orbits. These

6 1. Introduction

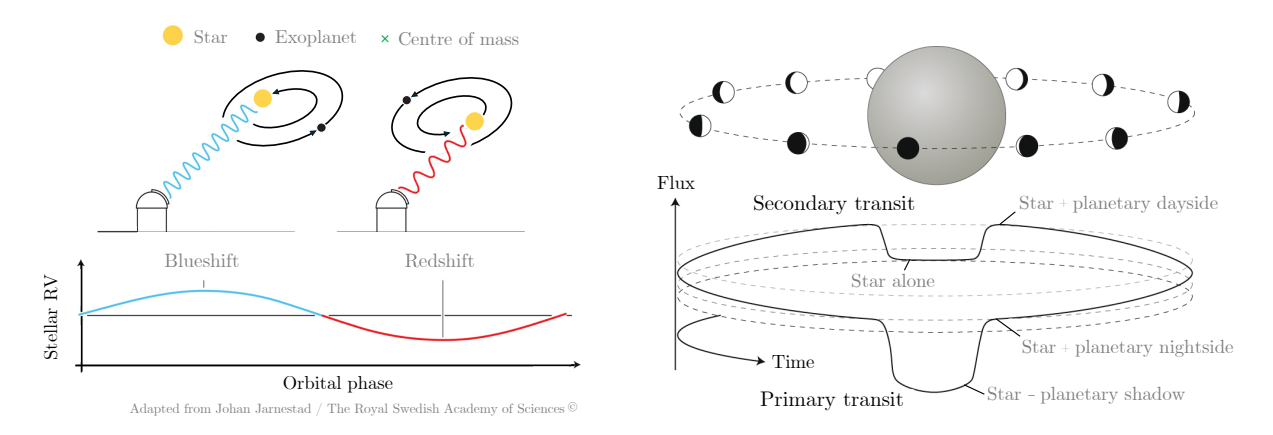


**Figure 1.1:** Illustrations of the RV and transit methods of exoplanet detection and characterisation. The *left* panel visualises how the star's radial velocity modulation over time can reveal the presence of an orbiting companion. Figure adapted from Johan Jarnestad/The Royal Swedish Academy of Sciences. The *right* panel shows how the star's flux drops temporarily as a result of the planet moving across and behind the stellar disc as seen from Earth. Figure adapted from Deming & Knutson (2020).

will exhibit a larger transit opening angle and possess a smaller orbital period resulting in more frequent transits and a higher likelihood of detection. Additionally, since the main observable of any transit study is the transit depth as defined in Eq. 1.2, the technique is more sensitive to systems featuring large planets or small stars.

At the time of writing, 75 per cent of all planets listed in the NASA exoplanet archive (Akeson et al. 2013) were marked as initially detected by means of the transit method. Among these, 63 per cent (or alternatively, 47 per cent of entire exoplanet sample) were detected by the Kepler space telescope (Borucki et al. 2010). Its observational strategy of continuously monitoring a single patch of sky throughout the several-year nominal phase of the mission, coupled with its high-precision photometric capabilities (e.g. Koch et al. 2010) have made it the most prolific exoplanet detection facility to date.

While not directly relevant to the content of this thesis, it should be noted that transit observations can also enable the study of exoplanet atmospheres via transmission spectroscopy (e.g. Birkby 2018). This powerful technique exploits the circumstance that the stellar light passing through the planetary atmosphere during the transit event carries its spectral fingerprints and can thus reveal properties such as the atmospheric composition, temperature, pressure and even climate (e.g. Snellen et al. 2010; Crossfield 2015; Kreidberg 2018). First applied by Charbonneau et al. (2002), transmission spectroscopy has developed into one of the essential techniques for studying the characteristics of individual exoplanets in minute detail.

**Astrometry:** Similar to the RV method, the astrometric exoplanet detection technique exploits the stellar reflex motion to infer the presence of a perturbing companion. Unlike the RV method, however, the key observable here is not the star's one-dimensional radial

velocity component but its precisely measured two-dimensional position on the plane of the sky. As such, astrometrically detecting a planet amounts to spatially and temporally resolving the orbit of its host around the system's barycentre. The angular amplitude of this stellar motion, a quantity also referred to as the astrometric signal, can be written as

$$A = \left(\frac{G}{4\pi^2}\right)^{1/3} \left(\frac{P}{M_* + M_{\rm pl}}\right)^{2/3} \frac{M_{\rm pl}}{d},\tag{1.4}$$

where G is the gravitational constant, P is the orbital period,  $M_*$  and  $M_{\rm pl}$  are the stellar and planetary mass, respectively, and d is the target system's distance (Quirrenbach 2010). However, the barycentric motion is not the only movement a planet-hosting star exhibits. As illustrated in Fig. 1.2, one needs to also account for proper and parallax motion, which can both be significantly more pronounced than the orbital reflex movement (Kervella et al. 2016).

A successful astrometric planet detection can unlock a large array of system parameters. Fitting a Keplerian model to an astrometric time series that ideally covers a considerable fraction or the entirety of the stellar orbit around the barycentre directly yields the orbital period, the star's semi-major axis,  $a_*$ , and the inclination, i, which can then be used to constrain the mass of the perturbing planet,  $M_{\rm pl}$ , provided the stellar mass is known (see Ranalli et al. 2018 for an example of a fitting framework).

The main biases to be aware of when attempting to detect planets astrometrically can be identified from Eq. 1.4. Since it represents an angle on the plane of the sky, the astrometric signal decreases as the distance to the prospective host star increases. For comparison, the RV and transit methods are not affected by such a distance-dependence (Sahlmann et al. 2013b). Furthermore, the signal strength increases for longer orbital periods. Thus, astrometric surveys are more sensitive to companions on far-out orbits around their hosts. This specific bias is complimentary in nature to the ones encountered for the RV and transit techniques. Lastly, the astrometric method is biased towards large mass ratios between planet and star. In other words, all other parameters being kept fixed, systems featuring more massive planets or less massive stars will exhibit stronger astrometric signals.

One of the main limitations of this technique is the seeing that ground-based telescopes are subject to. The distortions experienced by the wavefront as a result of passing through turbulent atmospheric layers manifest themselves as random two-dimensional shifts of the stellar centroid (Roddier 1981). Thus, there exists an angular resolution limit that cannot easily be overcome. Measuring the target star's relative position with respect to a close-by reference star whose light traverses the same turbulent pockets of air and thus sustains similar distortions can alleviate the challenge (e.g. see Lindegren 1980). Nevertheless, this strategy comes with its own hurdles. For instance, unknown motions and rotations of the local frame as defined by the two stars rule out any measurement of the target's proper motion (Quirrenbach 2010). Knowledge of the latter is crucial, though, since it necessarily needs to be disentangled from the orbital motion if one is to search for companion planets. Alternatively, the situation can be remedied by using a telescope equipped with an Adaptive

8 1. Introduction

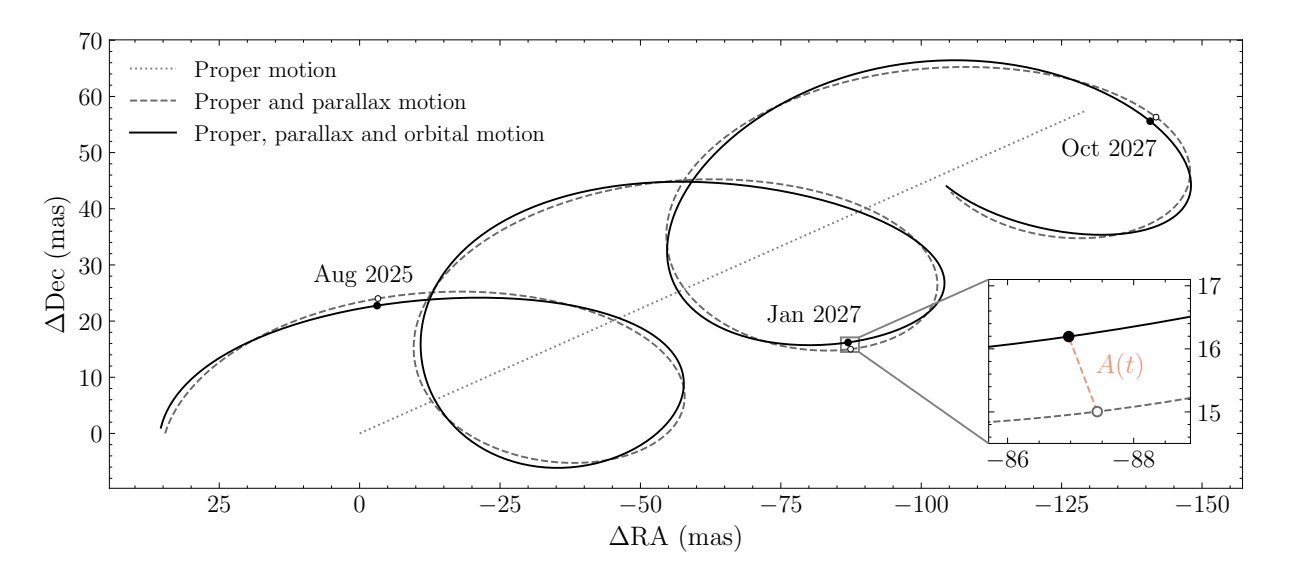


**Figure 1.2:** Schematic visualising the movement of a star as projected onto the plane of the sky. Depending on its space velocity and distance, a given star will show a linear proper and elliptical parallax motion, the combination of both tracing out a spiral trajectory. The presence of a companion imparts an additional motion component that corresponds to the star's orbital reflex motion around the system's barycentre. Accordingly, the time-dependent difference between the trajectory taking account of the orbital motion component and one composed merely of the proper and parallax motion corresponds to the momentary astrometric signal, A(t).

Optics (AO) system, which can correct for much of the atmospheric distortion experienced by the target star's wavefront (e.g. Babcock 1953; Tyson 1998; Roddier 1999).

Another aspect making the astrometric detection of exoplanets particularly challenging is the potential degeneracies between the star's orbital motion and its apparent parallax movement. Naturally, this becomes most problematic for planets exhibiting periods close to one year, in which case disentangling the two motion components can be impossible (Butkevich 2018). While this obstacle can be overcome for nearby systems or particularly eccentric orbits (El-Badry et al. 2024), overall it results in a bias against the detection of one-year-orbits by the astrometric method.

Historically, several facilities have been designed and built in part to conduct surveys searching for exoplanets by means of high-precision stellar astrometry. Examples include the Palomar High-precision Astrometric Search for Exoplanets (PHASES; Lane & Muterspaugh 2004; Muterspaugh et al. 2006) at the Palomar Testbed Interferometer (PTI; Colavita et al. 1999) and the Exoplanet Search with PRIMA (ESPRI; Launhardt et al. 2008; Sahlmann et al. 2013a). Here, PRIMA stands for Phase-Referenced Imaging and Microarcsecond Astrometry (Delplancke 2008) at the Very Large Telescope Interferometer (VLTI). Both of these projects were designed to exploit the unmatched angular resolution capabilities provided by optical and near-infrared interferometry. We shall later see how interferometric techniques can unlock an astrometric precision unattainable by

individual imaging telescopes (see Sect. 1.4). Despite these early efforts, to date, there have only been a handful of successful astrometric planet detections. While firmly in the brown dwarf (BD) mass regime, the first low-mass substellar companion discovered in this manner was DENIS-P J082303.1-491201 b (Sahlmann et al. 2013c). Despite its currently modest detection tally, the astrometric method possesses huge potential for the future – not least due to its strong complementarity with other detection methods (Sozzetti 2005). A main driver of this approaching astrometric revolution is the European Space Agency's Gaia satellite (Gaia Collaboration et al. 2016; see Sect. 1.3). While conducting its all-sky survey, the mission has collected a wealth of astrometric data predicted to enable the detection of thousands of previously unknown exoplanets (Perryman et al. 2014) once all the data are published, thereby finally establishing astrometry among the most prolific techniques of planet detection.

Direct imaging: The methods we have introduced so far have one aspect in common. They enable us to infer the presence of a planet within a given stellar system based on its indirect effects on the appearance of the host. Crucially, these techniques are not based on and make no attempt at observing the planet itself. This aspect sets the direct imaging (DI) technique to be discussed here apart from the ones outlined above. As a method of discovering new planets it encapsulates the most intuitive notion of how one is to detect an orbiting companion: as its name implies it aims at spatially separating the planet from its host star and thus capturing an image of the planet itself, a feat that represents a profound technological challenge.

There are two main reasons why DI is so demanding from a technical point of view and why it is thus still in its infancy compared to the RV and transit methods. Firstly, the contrasts that need to be overcome to image a planet next to its stellar host are astonishing. For instance, a target system composed of a Jupiter analogue orbiting a Sunlike star would exhibit a cotrast of approximately  $10^{-9}$  which corresponds to a difference of 22.5 magnitudes (Traub & Oppenheimer 2010). Since newborn planets retain some of the energy linked to their formation process as heat which – over the course of a few million years (hereafter denoted as Myr) – is gradually radiated away, by specifically targeting young stars one can maximise the expected contrast between companion and host (Baraffe et al. 2003, 2015). To illustrate, at an age of 10 Myr a 5 M<sub>Jup</sub> planet orbiting a Sun-like star is expected to exhibit a contrast of  $10^{-4}$ . For the same system at an age of 5 billion years (Gyr), this number drops to a mere  $10^{-10}$  (Bowler 2016). Thus, the choice of sufficiently young target systems is key to the successful direct detection of exoplanets. Apart from selecting the most favourable targets, the contrast limitation can also be tackled through technological means. Using an optical device called a coronagraph, which suppresses the direct stellar light, one can improve the achievable contrasts by several orders of magnitude (e.g. Guyon et al. 2006). Finally, a combination of sophisticated observation strategies and post-observation image processing procedures such as Angular Differential Imaging (Marois et al. 2006) can further enhance the contrast of an observation. Despite these optimisation stratagems, the effects of which are visualised for the HR 8799 system in Fig. 1.3, the 1. Introduction

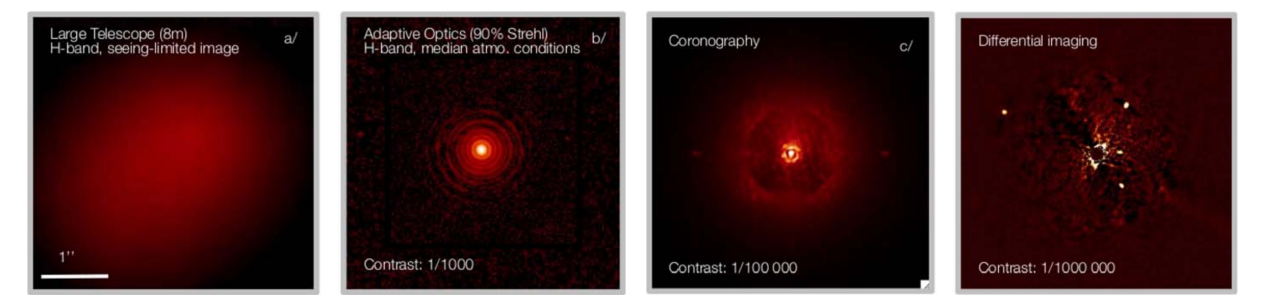


Figure 1.3: Stages of a typical direct imaging observing and data reduction procedure on the basis of the HR 8799 system. From left to right: uncorrected (seeing-limited) image of a potential host; adaptive-optics corrected (diffraction-limited) image with visible Airy pattern; image after blocking out the stellar light using a coronagraph; resulting image after applying a differential imaging technique to further improve the contrast capability. The typical contrast achievable during each step of the procedure is given at the bottom of the respective panels. Figure adapted from Chauvin (2024).

contrasts achievable today still limit the DI technique to giant planets above a few Jupiter masses. As is evident from evolutionary models of exoplanets (e.g. Baraffe et al. 2003, 2015), even when orbiting the faintest of host stars, in general, planets of lower mass lack the intrinsic luminosity required to surpass the limiting contrasts of present-day imaging instruments. That being said, recent work has demonstrated that, in favourable cases, sub-Jovian and even cold, mature planets can be imaged (Matthews et al. 2024; Lagrange et al. 2025).

The second challenge affecting DI studies is the fact that, depending on the distance to the target system, the angular separation between the star and its companion can be exceedingly small. Following Traub & Oppenheimer (2010), the maximum separation between both bodies for a given system can be computed via

$$\theta = (a/AU) \frac{(1+e)}{(d/pc)}, \tag{1.5}$$

where again a, e and d are the planetary orbit's semi-major axis, its eccentricity and the system's distance, while AU and pc denote one astronomical unit and one parsec, respectively. Accordingly, a planet on an Earth-like orbit around a star 10 pc away would appear at an angular separation of 100 milliarcseconds (hereafter denoted as mas). Such scales are unresolvable from the ground unless the atmospheric seeing is corrected for by means of AO systems (Milli et al. 2016). Yet, even if one manages to reach the angular resolution necessary to separate the target system into two distinct bodies, aberrations in the telescope optics as well as speckle noise can dominate the produced image such that a faint planet is drowned out and undetectable (e.g. Kenworthy & Haffert 2025).

Provided these procedures are executed successfully and one manages to resolve and capture the photons coming from an exoplanet, the insight thus made accessible is manifold. In case the instrument used for the observation is capable of dispersing the collected

planetary light into a spectrum, a thorough study of the body's atmosphere is possible (e.g. Currie et al. 2023a). Moreover, while a single detection already yields the projected separation between host and companion, a series of observations can enable an orbital analysis. Fitting a Keplerian orbit model to the relative astrometry epochs, that is the on-sky planetary positions with respect to the host, can yield estimates of the planet's semi-major axis, eccentricity, inclination and – perhaps most notably – its dynamical mass (e.g. Blunt et al. 2020). In contrast to the planet masses derived from their respective ages and luminosities via evolutionary models, dynamical masses only rely on the accuracy of the astrometric detections and the validity of Kepler's laws of planetary motion. Thus, they are the most dependable mass estimates available and are vital for calibrating the evolutionary models required to characterise such planets for which DI is not an option or whose periods are too large to discern any orbital motion when detected repeatedly (e.g. Brandt et al. 2021a).

Since a large host-companion separation is desirable for imaging, far-out planets on orbits that are close to face-on, that is parallel to the plane of the sky, are favoured. In this sense, the biases affecting DI studies are roughly complementary to the RV and transit methods. As mentioned above, due to the challenging contrasts involved there exists a preference for young, massive planets. For the same reasons, it is exceedingly difficult to image planets around bright stars. Lastly, by design, the use of coronagraphs entails a blocked off region around the on-axis target, which is typically chosen to be the host star (e.g. Guyon 2005). The distance from the on-axis target at which a throughput of 50% is reached for a given off-axis light source such as a planet is defined as the inner working angle (Beuzit et al. 2019). The blocked out region within this angle is generally inaccessible to DI studies, limiting the orbital separations that can be probed by this method.

The first planet ever captured using the imaging method was 2MASSWJ 1207334-393254 b (Chauvin et al. 2004). The discovery neatly demonstrates the intricacies of the DI method: as a member of the TW Hydrae Association, which – with an estimated age of 10 Myr (e.g. Bell et al. 2015) – is the youngest known stellar population within 100 pc (e.g. Luhman et al. 2023 and references therein), the planet-to-host contrast proved large enough to be observed using VLT/NACO (Rousset et al. 2003; Lenzen et al. 2003). At  $(5.5 \pm 0.5) \,\mathrm{M_{Jup}}$  (Luhman et al. 2023) it sits at the lower end of mass scale spanned by the current population of imaged planets. Depending on where one sets the threshold between planets and BDs (while conventionally taken to be delineated by the deuterium-burning mass limit (Spiegel et al. 2011), some authors argue that the companion-to-host mass ratio should also be taken into account; for an example see Currie et al. 2023b) approximately 50 planets² have been imaged since the first direct detection by Chauvin et al. (2004).

The quest to expand upon this number is well underway with several surveys complete, ongoing or currently in preparation. Notable examples are the SPHERE infrared survey for exoplanets (SHINE; Desidera et al. 2021; Langlois et al. 2021; Vigan et al. 2021) on VLT/SPHERE (Beuzit et al. 2019) and the GPI Exoplanet Survey (GPIES; Nielsen et al.

 $<sup>^2</sup>$ to be precise, at the time of writing, there are 53 entries listed in the NASA Exoplanet Archive (Akeson et al. 2013) that exhibit a mass below  $13\,\mathrm{M_{Jup}}$  when accounting for the lower uncertainty

1. Introduction

2019) using the Gemini Planet Imager (GPI; Macintosh et al. 2006) at Gemini Observatory. We will outline the findings of these surveys in detail in Section 1.2.2.

Other methods: In addition to the approaches introduced above there are several other techniques capable of detecting and characterising exoplanets. Examples include methods based on microlensing events (e.g. Gaudi 2012), transit timing and transit duration variations (e.g. Agol & Fabrycky 2018) as well as pulsar timing variations (e.g. Kramer 2018). Seeing that these techniques are not pertinent to the topics covered in this thesis, we refer the reader to the relevant literature.

The above is only a brief review of the techniques now available to detect and characterise extrasolar planets. Judging by the almost 6000 detections over the last 30 years, we can already note that the methodological diversity of approaches and their resulting complementarity allows us to sample and populate a large region of the parameter space in which exoplanets reside. This circumstance becomes apparent in Fig. 1.4 where we present the entire confirmed exoplanet population as of July 2025 as a function of the planetary mass and orbital semi-major axis. The methods by which these planets were first detected are indicated by colour. Far from being uniformly distributed throughout the displayed two-dimensional parameter space, the techniques are confined to different regions by their respective biases. For reasons touched upon in the respective paragraphs, transit detections are restricted to small semi-major axes, direct detections occupy the large separation and high mass domain, while RV detected planets largely inhabit the intermediate territory. Evidently, such complementarity is exceptionally helpful in probing as large a fraction of the existing "exoplanet zoo" as possible. Nonetheless, to achieve a meticulous characterisation of planets that dwell in any given parameter range or indeed of specific individual planets, it is also desirable to apply several methods at once. This combination of multiple techniques, applied to a broad swath of the known population, is the path to a thorough characterisation and understanding of extrasolar planets and is one of the directions the field should drift towards in the near future. In this sense, attaining widespread overlap between different methods represents a landmark achievement that will reveal new insights into the nature of planetary systems. While this process has already started, the goal of extending the domains in which we possess such methodological redundancy is one of the main drivers and a cornerstone of this thesis. By combining the astrometric and direct detection methods, we aim to increase the overlap at the intersection between the DI and RV techniques (see Chapter 3) and even facilitate bridging the wide gap between DI and transit studies in the future (see Sect. 6.4).

#### 1.2.2 Demographics

Observational exoplanet research can be subdivided into two distinct categories: a given study either investigates and seeks to thoroughly characterise individual specimens, or attempts to identify patterns in large data sets comprising many different planets. Naturally,

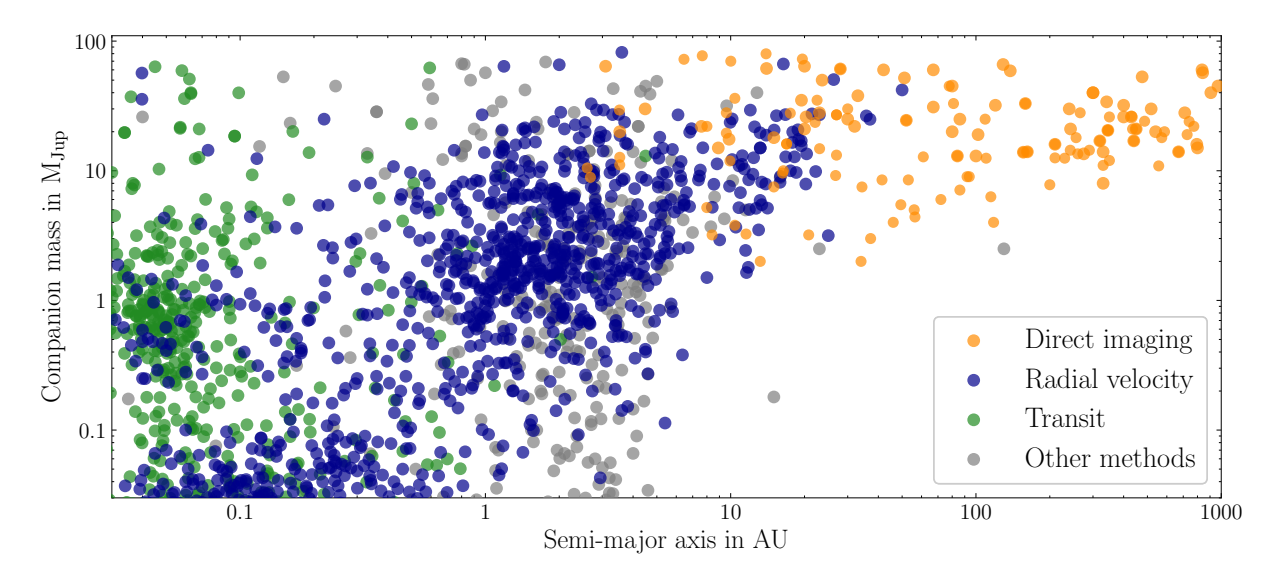


**Figure 1.4:** The known exoplanet sample (as of July 2025) in the mass–semi-major axis plane. The methods by which the individual planets have first been detected are indicated by different colours. The "Other methods" bin includes the astrometric and microlensing techniques as well as several transit timing methods.

the second approach, commonly labelled "exoplanet demographics", builds on the findings of the first. It can, however, reveal population-level trends and features and provide a handle on the degree of diversity between objects that the examination of individual exoplanets – no matter how comprehensive – is oblivious to. Here, we briefly summarise the main findings and open questions stemming from the demographics of exoplanets.

Planet classes and radius gap: As the number of known exoplanets has grown, the bulk parameter distributions that have gradually emerged serve as a new window through which the processes that govern the nature of individual exoplanets, such as their likely formation and evolution, can be studied. The radius distribution of confirmed exoplanets serves as an instructive example of this methodology. The full exoplanet population can be parsed into the following taxonomic sub-categories: rocky planets (0.5 to 1 Earth radii, hereafter denoted as R<sub>E</sub>), super-Earths (1 to 1.75 R<sub>E</sub>), sub-Neptunes (1.75 to 3.5 R<sub>E</sub>), sub-Jovians (3.5 to 6 R<sub>E</sub>), and Jovians (6 to 14.3 R<sub>E</sub>; e.g. Kopparapu et al. 2018). These radius boundaries are informed by demographic features of the exoplanet population. At the lower radius end, the rocky planets bin is constrained by the radius below which planets seem to be unable to retain their atmospheres due insufficient surface gravity (Zahnle & Catling 2017). The boundaries of the next two classes, super-Earths and sub-Neptunes, are based on the so-called "radius gap", an observed shortage of planets around 1.75 R<sub>E</sub>. First suggested to exist by Youdin (2011) and later confirmed by Fulton et al. (2017) using data collected by the Kepler space telescope, the gap is believed to be caused by stellar UV and X-ray radiation eroding the atmospheres of gaseous planets. Such intense photoevaporation – predominantly taking place when stars and planets are still young – 1. Introduction

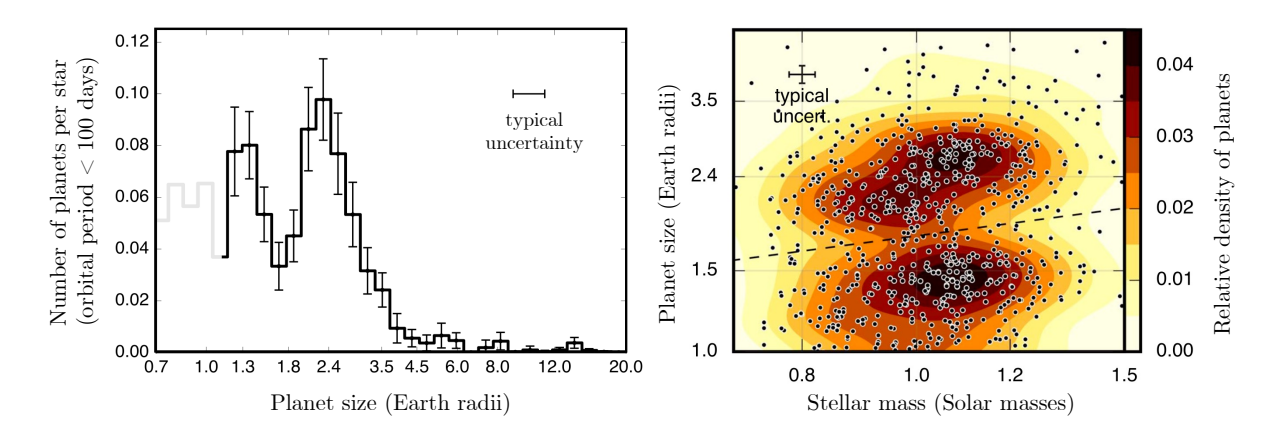


Figure 1.5: The exoplanet radius gap as detected in the Kepler population for planets orbiting their hosts in less than 100 days. *Left:* Planet distribution as a function of the planetary radius. Note that the histogram range plotted in grey was not included in the fit since it lacks completeness. Figure adapted from Fulton et al. (2017). *Right:* Relative density of exoplanets as a function of radius and host mass. The dashed line traces the position of the gap and suggests a monotonic dependence on the stellar mass. Figure adapted from Fulton & Petigura (2018).

produces a measurable dichotomy in the planetary radius distribution (e.g. Owen & Wu 2013, 2017). Figure 1.5 shows the gap manifest in the radius distribution of the Kepler planet population as well as its dependence on the host star mass. Again based on the findings reported in Fulton et al. (2017), the upper limit of the sub-Jovian bracket is based on the minor peak in the radius distribution at  $6\,R_E$  also visible in Fig. 1.5. Finally, this classification scheme is capped by the Jovian planet class which – at its upper limit – borders the BD regime (Chen & Kipping 2017). Note that every now and then new planetary sub-categories are suggested and other classification schemes exist. Some studies distinguish between terrestrial, gas giant and ice giant planets for instance (e.g. Ida & Lin 2004b).

Eccentricity distribution: Planetary radii are by no means the only characteristic that can be investigated on a population-level scale. The orbital eccentricity distribution of RV planets for instance shows a clear and well defined shape that peaks at an eccentricity of zero and decreases steeply towards larger values. As shown by Kipping (2013), it can be closely parametrised by a beta distribution of parameters  $\alpha = 0.867$  and  $\beta = 3.03$ , although more recent work based on a larger sample of RV planets suggests other parametrisations to be more accurate (Stevenson et al. 2025). The question whether the DI population of exoplanets, that is a sample detected at much larger separations from their hosts, exhibits the same eccentricity distribution is still not conclusively answered. While Bowler et al. (2020) find a distribution that is strongly peaked at  $\bar{e} = 0.13$ , Nagpal et al. (2023) have

shown these results to be mainly hyperprior-driven<sup>3</sup>. Nevertheless, the two studies agree on the fact that the BD sample shows an eccentricity distribution which is distinct from that of the DI population. Indeed, BDs appear to follow a distribution that is broadly peaked around  $\bar{e} = 0.6$  to 0.8. It should be noted though that the DI planet sample size is still limited and the inferred distributions may change as more planets on wide orbits are detected and have their eccentricities measured. We will explore what these results imply in terms of potentially different formation channels for the respective planetary and BD populations in Sect. 1.2.3.

Obliquity distribution: Another example of a feature that surfaces in demographic exoplanet studies is the shape of the obliquity distribution. The stellar obliquity is defined as the angle between the rotational axis of the host star and the normal vector of the planetary orbital plane. The fact that – outside of interferometric observations (see Sect. 1.4) – stellar discs are practically never spatially resolvable makes measuring the obliquity particularly difficult. Nevertheless, through a combination of specifically targeting transiting planets, which necessarily reside on almost edge-on orbits, and measuring different effects that are sensitive to the host's rotational inclination such as the Rossiter-McLaughlin effect (Holt 1893; Rossiter 1924; McLaughlin 1924) or rotational line broadening, one can constrain a given system's obliquity angle (Albrecht et al. 2022). Despite the challenging nature of this measurement a small sample size of successful attempts has already revealed the circumstance that cool parent stars appear to host planets exhibiting smaller obliquities than do hot ones (Winn et al. 2010). The threshold between the cold and hot stars initially fixed at 6250 K (again, Winn et al. 2010) has proved robust following an increase in sample size by a factor of three (Albrecht et al. 2022).

Occurrence rates: The prevalence of different types of planets, for instance binned according to the system introduced in the previous paragraph (see Kopparapu et al. 2018), as a function of stellar type, orbital period or other parameters can reveal additional information about the most prevalent architectures and likely evolutionary history of exoplanetary systems. In this sense, constraining these so-called occurrence rates is a sub-discipline of demographic planet studies. Since they describe and govern the make-up of the global exoplanet population, occurrence rates are of particular relevance to the quest of efficiently expanding the known exoplanet sample. In turn, these results are pertinent to the content of this thesis and warrant a brief introduction.

One of the main results facilitated by the large pool of Kepler planets was the realisation that within the sample of planets exhibiting orbital periods, P, of less than 50 days, smaller planets are significantly more common than large ones with the peak of the distribution located between 2 and  $4 R_{\rm E}$ . Furthermore, planet occurrence is particularly low in the

<sup>&</sup>lt;sup>3</sup>In this context, hyperpriors are the prior distributions used to describe a set of hyperparameters which themselves govern how the prior distributions of the actual model parameters are shaped. This concept is relevant for hierarchical Bayesian modelling, a two-tier approach to population-level analysis (see e.g. Section 2 of Hogg et al. 2010).

1. Introduction

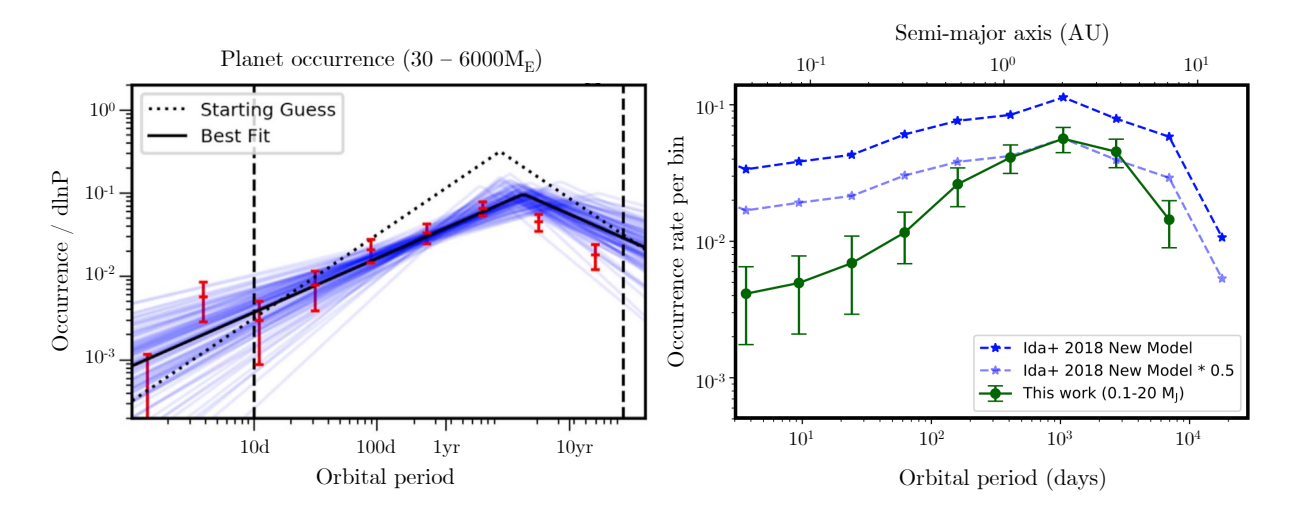


Figure 1.6: Turnover of the giant planet occurrence rate around the ice-line as extracted from Kepler and RV survey data. Left: Broken power-law fit to the Kepler-based occurrence rates per unit logarithmic period interval,  $d \ln P$ , as a function of period showing a clear peak around 2000 days. Right: Comparison of the RV-based occurrence rate as a function of period with results from the population synthesis models outlined in Ida et al. (2018). Both figures adapted from Fernandes et al. (2019).

region P < 2 days but increases steeply towards longer periods (Howard et al. 2012).

The most prominent findings concerning the architecture of systems harbouring giant planets in wide orbits on the other hand have been uncovered by the SHINE survey at VLT/SPHERE and the GPIES survey using GPI (both of which were briefly introduced in Sect. 1.2.1). As reported in Nielsen et al. (2019) and Vigan et al. (2021), both surveys agree on a strong dependence of the occurrence rate on the host star's mass. Earlier-type, that is more massive stars appear to host more giant planets accessible to direct imaging studies. Additionally, giant planets are most commonly found between 1 and 10 AU (Nielsen et al. 2019). This pile up around the so-called "ice-line", where temperatures are sufficiently cool such that volatile species are present in their solid phase (e.g. Hayashi 1981), is confirmation of theoretical predictions (see e.g. Ida & Lin 2004a and Mordasini et al. 2009a) and supported by studies approaching the regime from the lower mass and shorter separation side (Fernandes et al. 2019; Fulton et al. 2021)<sup>4</sup>. See Fig. 1.6 for a visualisation of the occurrence rate as a function of orbital period.

The results outlined above will become relevant in Chapter 3, where we will explore a novel method that aims to push the direct detection of exoplanets to smaller separations in order to tap the large reservoir of detectable giant planets expected to reside there.

<sup>&</sup>lt;sup>4</sup>Note that more recent work by Lagrange et al. (2023) calls the possibility of robustly inferring the distribution of giant planets into question given the scant sampling available at present.

Apart from the demographic patterns introduced above, there is a growing list of further population trends discernible in the ever increasing sample of confirmed exoplanets. For a comprehensive review see for instance Gaudi et al. (2021).

#### 1.2.3 Formation scenarios

The endeavour to understand the processes that give rise to planets and planetary systems has developed from a theoretical, simulation-based undertaking mainly guided by the makeup of our own Solar System to one of the most active sub-disciplines of modern astrophysics, that draws upon a rich set of observational clues. The main goal of this effort is to shed light on the period between the formation of the host star and the state in which most planetary systems present themselves to us: a main-sequence star orbited by one or more mature planets after the disc in which they have formed has fully dispersed.

The processes preceding the planet formation phase we are interested in are fairly well understood (e.g. McKee & Ostriker 2007). A dense molecular cloud undergoes gravitational collapse to form a protostar that accretes further infalling gas while the natal cloud flattens out to form a rotating circumstellar disc (e.g. Armitage 2011). While the host, now referred to as a pre-main-sequence star, undergoes further contraction and proceeds through various evolutionary stages that depend mainly on its mass (Palla & Stahler 1993) to eventually mature into a main-sequence star, it is in the surrounding disc that planets are believed to form within the few Myr of its existence (Mamajek 2009). Extended and bright, this protoplanetary disc can be resolved and observed directly, making it possible to discern features such as gaps, rings and clumps (Andrews 2020). Identifying embedded protoplanets caught in the act of accreting material from the disc represents a milestone towards clarifying a great many open questions in relation to planet formation (e.g. Haffert et al. 2019). That being said, only PDS 70 has been unequivocally confirmed as a protoplanet-hosting system (Keppler et al. 2018).

In the absence of a large sample of observable and well studied protoplanets, the current picture of planet formation builds on two model frameworks that reproduce several detectable features of fully formed planets: the core-accretion and the gravitational instability model. In the following, we will briefly introduce both of them before providing a short overview of how they are linked to demographic features in the exoplanet sample as well as which characteristic fingerprints they impart on individual planetary specimens.

Core accretion model: In general, the core accretion model (CA; Pollack et al. 1996) builds on the supposition that the early formation stages of rocky and giant planets are similar. The latter then undergo an additional runaway gas accretion phase that ultimately bestows the thick atmosphere that is characteristic for these planets.

In this picture, the formation process commences with the small fraction of dust contained in the otherwise gaseous protoplanetary disc gradually coagulating into coarser units and settling in the disc midplane as a consequence of the increased vertical friction it experiences. Following D'Angelo et al. (2010), the vertical motion of this solid disc component

can be described as

$$z \approx z_0 \left( e^{-t\Omega^2 \tau_f} - \Omega^2 \tau_f^2 e^{-t/\tau_f} \right), \tag{1.6}$$

where z(t) is a given particle's time-dependent elevation above (or below) the disc midplane,  $z_0$  is its initial elevation,  $\Omega$  is its angular velocity resulting from its orbital motion around the star and  $\tau_f$  is the friction timescale. Since the second term of Equation 1.6 vanishes quickly, the description simplifies to the first term only.

Having thus grown from micrometre to centimetre-sized solid particles, these units must next grow to kilometre-sized planetesimals. The processes that govern this particular step, required for the CA model to move forward, remain enigmatic. However, the streaming instability mechanism proposed by Youdin & Goodman (2005) can help bridge this barrier. For a review of other proposed planetesimal formation processes see Birnstiel et al. (2016). Once formed, the planetesimals tend to collide and merge, over time growing to an entity referred to as a planetary embryo (Kokubo & Ida 1998). The time scale of this accretion process is inversely proportional to the mass of the host star and proportional to the planetesimal's distance from it (D'Angelo et al. 2010). It should be noted that a sped-up version of this growth phase can be achieved if the embryo undergoes so-called pebble accretion (Lambrechts & Johansen 2012). This formation phase is concluded once an embryo's orbital environment is depleted of planetesimals.

The above described mechanisms that give birth to planetary embryos are mainly concerned with the behaviour of and interactions between the solid material in the disc. Eventually, though, the accrued embryo mass suffices to capture and bind pockets of the surrounding gas. This is the case when the escape velocity at the embryo's surface surpasses the thermal velocity of the surrounding medium. This condition is met when

$$M_{\text{Embryo}} \ge \sqrt{\frac{M_*^3}{a^3 \rho_{\text{solid}}}} \left(\frac{H}{a}\right)^3,$$
 (1.7)

where  $M_*$  is the stellar mass, a is the embryo's semi-major axis and H is the vertical scale-height associated to the gaseous component of the disc (D'Angelo et al. 2010). A tenuous atmosphere can already be retained by objects as massive as Earth's Moon (Mordasini et al. 2008). With an approximate timescale of up to 0.5 Myr, this first formation phase can be described as relatively short-lived. The subsequent phase of slow gas accretion, on the other hand, can last up to several Myr. Unless gas accretion ceases beforehand, eventually the continual build-up of the planetary atmosphere results in the embryo reaching a critical mass at which the envelope collapses. This process triggers a brief phase of runaway gas accretion that can be viewed as the final stage of the CA formation process (Perri & Cameron 1974; Mizuno 1980).

The CA model as briefly introduced above and schematically visualised in the left panel of Fig. 1.7, is the product of half a century of optimisations and refinements to the original theory that was first conceived of in the 1970s and 80s (Perri & Cameron 1974; Mizuno et al. 1978; Bodenheimer & Pollack 1986). It has reached a degree of sophistication where it is able to explain and reproduce many observationally established demographic patterns of

the exoplanet population and predict characteristics that are yet to be detected (Mordasini et al. 2009b).

Gravitational instability model: Throughout the first two decades after the initial construction of the CA framework, the model was afflicted by a serious incongruity conventionally referred to as the "timescale-problem" (Mordasini et al. 2008). Simply put, the time required to form a gaseous giant planet exceeded the expected and later measured lifetimes of protoplanetary discs (see e.g. Haisch et al. 2001). Cutting short the gas accretion phase would in many cases inhibit the formation of Jupiter-like giant planets (Hubickyj et al. 2005). Instead, one would expect CA formation to more likely result in Uranus-like planets, an inference that became ever more irreconcilable with the increasing number of hot Jupiter (HJ) detections in the mid to late 1990s (Ida & Lin 2004a). To add to this, refined estimates of Jupiter's and Saturn's core masses around the same time reinforced the emerging doubts as to the universality of the CA model (Stevenson 1982; Chabrier et al. 1992; Guillot et al. 1994). The new measurements appeared too low to trigger the runaway gas accretion phase so pivotal to the CA paradigm.

As mentioned in the above paragraph dealing with the CA model in detail, it should again be noted that since this period of scepticism about its applicability, the framework has been significantly refined and expanded to the point where it is now capable of resolving and dispelling the discrepancies raised in the 1990s (for some examples of these advances see Saumon & Guillot 2004; Klahr & Bodenheimer 2006; Fortier et al. 2007). Nevertheless, the uncertainties of that era coupled with significant advances in computational methods served as fruitful ground for other formation theories to be proposed and tested. The only such framework that has stood the test of time is the gravitational instability (GI) model as proposed in Boss (1997) and based on Kuiper (1951) and Cameron (1978).

While the CA framework describes a bottom-up view of planet formation with small objects clumping and gradually growing, the GI model mirrors the top-down paradigm of structure formation. It is based on the notion that instability mechanisms in the disc induced by self-gravity result in spiral arms and clumps of local over-densities that eventually collapse to form gaseous giant planets (e.g. Kratter & Lodato 2016). The common approach of outlining the GI mechanism in the literature assumes an initial axisymmetric, that is ring-like, density disturbance in the disc (Toomre 1981) that can be parametrised as

$$\delta p \propto e^{i\omega t \pm 2\pi a/\lambda},$$
 (1.8)

where p is the disc pressure at a radial distance, a, and  $\lambda$  is the perturbation wavelength in the radial direction. In this case,

$$\omega = \sqrt{\kappa^2 - \frac{4\pi^2 G\Sigma}{\lambda} + \frac{4\pi^2 c^2}{\lambda^2}}.$$
 (1.9)

In the above,  $\kappa$  is the oscillation frequency of a perturbed particle, also called the epicyclic frequency (Binney & Tremaine 2008), G is the gravitational constant,  $\Sigma$  is the local surface density of the gas and c is the speed of sound in the medium (D'Angelo et al. 2010). Two

distinct cases present themself: if  $\omega^2$  is positive, the exponent of Equation 1.8 is complex and the density wave propagates radially outwards; if instead  $\omega^2$  is negative,  $\omega$  is necessarily complex rendering the exponent real which in turn implies an exponential growth. In the second case the disc will be unstable. For this to happen, the second term within the square root in Equation 1.9 which can be attributed to the self-gravity of the disc has to dominate, hence the name "gravitational instability" (D'Angelo et al. 2010). Solving Equation 1.9 for  $\lambda$  while setting  $\omega = 0$  yields the Toomre Q parameter,

$$Q = \frac{c\kappa}{\pi G \Sigma}.\tag{1.10}$$

The parameter can be used to compute in which perturbation wavelength range the disc will be unstable. This is the case when Q falls below the critical value of 1 (Toomre 1964). While the above was derived for axisymmetrical discs, simulation studies demonstrated that even non-axisymmetric perturbations such as spiral waves cause the disc to become unstable for values as high as  $Q \leq 1.5$  (see e.g. Papaloizou & Savonije 1991). Thus, spiral waves can act as observational tracers of the GI mechanism (D'Angelo et al. 2010).

The eventual outcome of the instability depends on the heating and cooling processes at play in the disc. Indeed, the key determinant of whether the instability persists or subsides is the local disc temperature through its influence on the sound speed, c, and thus on the Toomre Q parameter via Equation 1.10. Unless the disc can dispose of the heat that builds up due to compression, shocks and e.g. turbulent dissipation (Nelson 2000), the speed of sound will increase and Q will return to the stable regime (Durisen et al. 2007). Starting with Gammie (2001), multiple simulations have shown that a bound gaseous clump that formed via the above described instabilities can be sustained if the disc cooling timescale,  $\tau_{\rm cool}$ , is comparable to the rotational timescale,  $\tau_{\rm rot}$ . Thus, enduring clump formation occurs if the so-called fragmentation criterion

$$\frac{\tau_{\rm cool}}{\tau_{\rm rot}} < f_{\rm frag} \tag{1.11}$$

is met (D'Angelo et al. 2010). While dependent on the gas equation of state employed in a given simulation and other factors, the constant  $f_{\rm frag}$  on the right hand side of the inequality is generally found to lie between 1 and 2 (Rice et al. 2003; Mejía et al. 2005; Clarke et al. 2007). It is in these over-densities within the fragmented disc where giant gaseous protoplanets (GGPPs; Boss 1997) are expected to form and thereafter evolve into the giant planets we can observe in extrasolar planetary systems. An visual example of a fragmented disc that is in the process of developing clumps is depicted in the right hand panel of Fig. 1.7.

One of the key differences between the CA and the GI model is that the latter functions on much shorter timescales, especially in the outer regions of the disc where the time required for a CA-like formation scenario far exceeds the expected disc lifetime (Boss 1997). The flip side of this argument is that the GI framework is incapable of explaining formation at shorter separations from the nascent host (Kratter & Lodato 2016). In fact, the GI mechanism is believed to be limited to separations larger than several tens of AU (D'Angelo

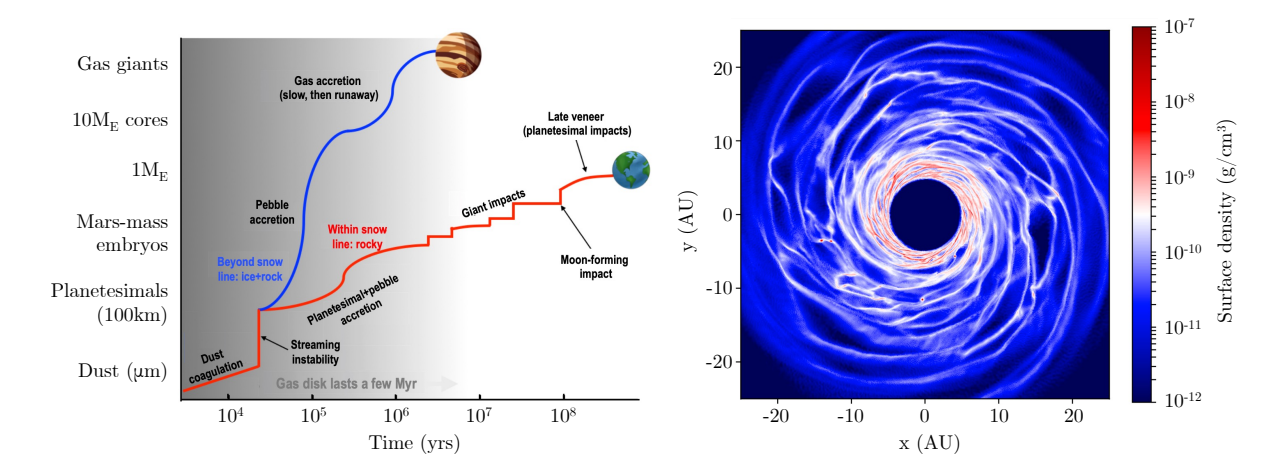


Figure 1.7: Left: Schematic of the core accretion formation model that distinguishes between formation within and beyond the snow line depicted in red and blue, respectively. Figure adapted from Meech & Raymond (2020). Right: Magnetohydrodynamical simulation of a gravitationally unstable disc that has begun to fragment. Two clumps are visible at four and six o'clock. Figure adapted from Deng et al. (2021).

et al. 2010). This dichotomy suggests that the two models do not necessarily compete with one another but can be viewed as complementary (Helled et al. 2014). Further caveats of the GI model include a certain nebulosity as to the initial triggers of the disc perturbations even though clumpy infall onto the disc as well as disruptions by binary companions or close stellar encounters have been proposed, and the contested ability of formed clumps to survive the dynamic disc environment (see Durisen et al. 2007 for a comprehensive discussion of these uncertainties).

Direct observational evidence of GI leading to the formation of exoplanets is still limited. A disc-embedded clump caught red-handed in the act of accreting material and contracting into a GGPP has yet to be observed. Nevertheless, the unique capabilities of the Atacama Large Millimeter/submillimeter Array (ALMA) now enable us to probe for kinematic signatures that are predicted to be the outcome of the GI mechanism (Hall et al. 2020). For instance, Speedie et al. (2024) have recently detected a wiggle in the velocity map of the disc surrounding AB Aurigae that can be directly attributed to GI being present in the disc. In the following paragraph we will have a closer look at further examples of such direct as well as more circumstantial evidence for GI as a pathway to planet formation.

**Fingerprints of formation:** Inference as to whether a given planet likely formed according to the CA or GI scenario requires theory to suggest observables that can act as discriminators between the two.

As it turns out, the two pathways give rise to distinguishable populations for a set of parameters on a demographic scale. Firstly, the – now observationally established –

circumstance that the metallicity of a star is strongly linked to the occurrence of orbiting giant planets (Fischer & Valenti 2005), was a key prediction of the CA model (Ida & Lin 2004b). This confirmation of theory is seen as a strong argument in favour of CA while GI models do not anticipate this specific correlation (Ida & Lin 2005). On the contrary, the GI formation mechanism is predicted to result in an anti-correlation between metallicity and occurrence, that is not observed (Cai et al. 2006). Similarly, only the CA model is successful in reproducing the diminished occurrence of giant planets around M dwarfs (Laughlin et al. 2004). A more qualitative line of evidence is afforded by the separation distribution of exoplanets. Here, the detection of giant planets several tens of AU from their respective hosts by means of direct imaging studies poses a challenge to the CA model. As was explained above, developing a more complete description of the physics at play in the disc served to resolve the timescale-problem of the 1990s for planets assembling at small separations. Nevertheless, CA formation at large distances from the host still presupposes timescales that far exceed the disc lifetime (Lambrechts & Johansen 2012). In this sense, imaged planets on wide orbits represent qualitative observational evidence of GI formation having taken place (Dodson-Robinson et al. 2009; Kratter et al. 2010). The detection of massive planets around very young stars can be viewed in the same way.

While a definitive conclusion as to which formation processes were at play is difficult to reach for a single specimen, there is a set of discriminators that can be invoked for a preliminary assessment. A common approach to constraining a given planet's formation history is to compare its measured or inferred mass, its luminosity and its age to theoretical models of how planetary characteristics evolve as a function of time, so-called evolutionary models (Baraffe et al. 2003). Marley et al. (2007) first proposed to distinguish between "hot" and "cold start" scenarios depending on the specific entropy, S, they deposit in a planet immediately after it has completed its formation. This entropy per unit of planetary mass determines the evolutionary behaviour the planet will undergo while it matures and is itself governed by the efficiency of the accretion shock experienced by the gas infalling onto the forming planets (Spiegel & Burrows 2012). An efficient shock, commonly associated to the CA model, will lead to a larger fraction of the potential energy being radiated away thereby affecting a cold start. More inefficient shock scenarios on the other hand allow a larger fraction of energy to be retained by the forming planet resulting in the hot start case typically linked to the GI formation mechanism (Mordasini et al. 2012). Additionally, the concept of "warm" start models as intermediate cases between the hot and cold models have since been proposed (Marleau & Cumming 2014). As such, precisely determining a given planet's bulk parameters can enable constraints on its specific entropy and thus its likely formation channel. The measurements required to follow through on this strategy can be acquired applying different methods. Firstly, the planet's age can often be estimated from detailed observations of the host star (see Soderblom 2010) or exploiting the system's potential membership of a particular stellar association of known age (Bell et al. 2015). Furthermore, the planet's luminosity needs to be gauged. This procedure is mainly limited to directly imaged planets since – contrary to the other methods introduced in Sect. 1.2.1 – the nature of the observational technique provides a direct measurement of the companion's luminosity. Likewise, if imaged during several epochs throughout a sufficient fraction of 1.3 Gaia 23

its projected trajectory about the host, orbital fitting can yield constraints on the planet's model-independent dynamical mass (e.g. Blunt et al. 2020). Chapters 2 and 3 present examples of how such dynamical masses of substellar companions can be measured with varying degrees of precision.

Thus, the imaging technique appears to be uniquely suited to investigate the boundary conditions, contributing processes and applicability of the different formation channels on the basis of young planets shortly after their formation phase is complete. In Sect. 2, we shall investigate whether determining the likely formation channel of a particular substellar companion, HIP 99770 b, is possible on the basis of observational data.

## 1.3 Gaia

On the 15th of January 2025, the European Space Agency's *Gaia* satellite ceased science observations, marking the end of a transformative mission that collected data over a period of more than ten years. In this section we will provide a short overview of this revolutionary space telescope, its functionality as well as its applicability to exoplanet science and lay out its relevance to this thesis.

## 1.3.1 Design and functionality

Originally conceived of as a space interferometer called the Global Astrometric Interferometer for Astrophysics (GAIA), the mission's functionality was overhauled at an early design stage, to operate on a set of telescope—detector subsystems that were not linked interferometrically (Perryman et al. 2001). While the acronym was discarded, the name endured, being altered only slightly to the now familiar *Gaia*. Likewise, the original science goals remained unchanged: the mission was intended as a successor to the High Precision Parallax Collecting Satellite (Hipparcos; see Schuyer 1985) and thus designed to map the entire celestial sphere, monitoring the exact positions of Solar System objects, stars and galaxies over a period of several years. Among other things, such a time-series astrometric data set is an excellent resource for identifying the parallax of stars (see Bessel 1838 for the first successful attempt of this measurement), thereby revealing their distances to unprecedented accuracy (e.g. Bailer-Jones 2015). In this way, *Gaia* promised to provide the most detailed and extensive three-dimensional map of the Milky Way.

To this end, *Gaia* was equipped with two telescopes that share a common focal plane populated by 106 Charge-Coupled Devices (CCDs). The intricate CCD layout consisted of subfields dedicated to metrology, sky mapping, astrometry, low-resolution spectro-photometry and spectroscopy functions (Gaia Collaboration et al. 2016). Given the specific applications of *Gaia* data in this thesis, we will here concentrate on the astrometric field (AF) which in total consists of nine columns à seven rows of CCDs. As the satellite rotated, point sources within the FoVs of both telescopes down to a magnitude of 20.7 in the white-light *Gaia* G-band jointly moved across and were registered by the AF (Hodgkin et al. 2021). Similar to the functionality of a classical meridian circle, the AF CCDs

didn't actually measure the on-sky position of a given source but the precise time when its point-spread function (PSF) crossed a pre-defined line on each detector (Brown 2021). In post-processing, these timing measurements could then be converted into one-dimensional, so-called along-scan (AL) position measurements using auxiliary data collected by the sky-mapping module and by referring to the Gaia scanning law, the pre-defined pointing strategy specifying the orientation of the two FoVs at any given moment in time (see Hoyer et al. 1981 and e.g. Gaia Collaboration et al. 2016 for a concise overview). While facilitating exceptionally precise astrometric measurements in the AL-direction, the accepted downside of this strategy is a significantly looser precision in the across-scan (AC) direction<sup>5</sup>. To compensate for this directional precision-disparity, each source must necessarily be observed multiple times under different scan-angles. Fortunately, the Gaia scanning law dictates an average of 12 and a minimum of 6 visits, that is observations, of each source visible to the Gaia instrumentation per year (Gaia Collaboration et al. 2016). Thus, the final astrometric time-series of a given source will consist of several dozen measurements exhibiting elongated error ellipses and collectively tracing out the source's on-sky trajectory over a period of more than ten years. Fitting this trajectory with a model of stellar motion (see e.g. Lindegren et al. 2012), the source's parallax, proper motion and – in cases where an unseen companion induces a noticeable stellar reflex motion – even its orbital motion about its system's barycentre can be constrained (see related paragraph in Sect. 1.2.1 in general and Fig. 1.2 in particular).

According to some estimates, the full end-of-mission Gaia astrometric data set should reveal several thousands of exoplanets with masses between 1 and  $15\,\mathrm{M_{Jup}}$  (Perryman et al. 2014). A similar number is expected for companion BDs (Holl et al. 2022). The end-of-mission Gaia legacy archive data release (DR) is not expected to be published before the end of the decade. How we can already hunt for these companions today will briefly be discussed in the following sections.

# 1.3.2 Hunting planets with Hipparcos & Gaia

Published in June 2022, Gaia DR3 is the most recent and complete set of data obtained by the mission that is currently available to the public (Gaia Collaboration et al. 2023b). While it has enabled significant advances in various fields of astronomy, like DR1 and DR2 it still lacks the time-series astrometric epochs Gaia observed for over a billion stars. Once published, this final, raw catalogue will serve as the key resource for exoplanet detection and characterisation. Nevertheless, the parallax and proper motion measurements resulting from fits to the unreleased astrometric epochs are already available. The stellar proper motions in particular offer an opportunity for exoplanet hunters. By themselves they are of no particular interest to the community, merely describing the motion of stars as projected onto the plane of the sky. Combined with an additional measurement obtained at an earlier epoch, however, they can reveal perturbations where the two vectors do not line

<sup>&</sup>lt;sup>5</sup>The actual numerical precision achieved in both directions also depends on the observed source's magnitude in the *Gaia* G-band. According to Lindegren et al. 2018, in the AL direction it can be as small as 60 µas per CCD observation.

1.3 Gaia 25



**Figure 1.8:** Gaia flight model undergoing a deployment test of its foldable sunshield while in Kourou, French Guiana, awaiting launch in December 2013. The engineers in the foreground provide a sense of the satellite's size. Image credit: ESA–M. Pedoussaut, 2013.

up. Such proper motion anomalies (PMa), as they are commonly called, are indications that an acceleration has taken place, an occurrence that can be induced by the presence of an orbiting companion (see e.g. Kervella et al. 2019b). Besides being the first to ever successfully measure a trigonometric stellar parallax, it was again Friedrich Wilhelm Bessel who originally proposed the PMa method of inferring unseen companions (Bessel 1844). Kervella et al. (2022) and Brandt (2021) offer two independently processed catalogues listing stars identified as a perceptibly anomalous between the Hipparcos and Gaia DR3 catalogues. In Chapter 2, we shall closely examine the first potentially planetary object detected on the basis of its host's deviant proper motion, HIP 99770 b.

Given the 26-year-long temporal baseline between Hipparcos and Gaia DR3, the companions that can be inferred by this technique must reside on wide, long period orbits (Kervella et al. 2022). This methodological bias suggests applying the PMa strategy as a precursor for DI follow-up observation. As such, the procedure can serve as a way of progressing beyond the essentially blind DI campaigns at present merely focusing on stars of a particularly young age towards a semi-targeted and thus more efficient approach where only the anomalous subset of which is scrutinised. Here, we use the prefix "semi" to indicate that – while a detected PMa can reveal stars of interest – this method is mostly incapable of constraining the inferred companion's position relative to the host. In the following, we will explore how it may be possible to further improve upon these already formidable capabilities.

# 1.3.3 Hunting planets with Gaia DR3?

Parallaxes and proper motions are far from the only products processed from the timeseries astrometric epochs available in DR3. For instance, an additional orbital solution is provided for a curated subset of approximately 170 000 *Gaia* sources (Halbwachs et al. 2023). These orbits are published as orbital elements, their associated uncertainties as well as a correlation matrix, all resulting from fitting a two-body orbit model to the time-series

astrometric data. They are listed in the Non-Single-Star (NSS) two-body orbit catalogue. On the one hand, this table can be viewed as a preview of what will be possible once *Gaia* DR4 is published (for some examples of science cases relevant to this thesis that will be unlocked by DR4, see Sect. 6.3). When combined with the respective stellar and companion mass estimates contained in the DR3's Binary Masses Table (Gaia Collaboration et al. 2023a), on the other hand, the NSS two-body orbit catalogue is already capable of informing direct follow-up observations aimed at confirming the first *Gaia*-inferred substellar companions.

The power of the NSS two-body orbit catalogue lies in the realisation that it can be used as a predictive tool enabling us to compute a given Gaia source's position relative to the respective system's barycentre at any given moment in time. With this goal in mind, we need to make two justified assumptions. First, we hypothesise that the stellar orbital motion is induced by a single companion. Second, we presume that for such system's where the estimated companion mass is in the substellar regime according to the DR3 Binary Masses Table, the flux contributed by said companion is negligible. Thus, since the vast majority of the flux registered by Gaia originates from host, we can approximate that the measured photocentre position coincides with the actual stellar position. Assuming the contribution of a substellar companion to be negligible appears justified given the exponential nature of the mass—luminosity relationship valid for even the lowest-mass host stars (Benedict et al. 2016). Having thus established the capability of predicting a star's position at a given time of observation, we can convert this information to the relative position of the perturbing companion.

This technique differs in several key aspects from the PMa method outlined in Sect. 1.3.2. For one thing, it does not rely on the significantly lower astrometric precision of the Hipparcos data set (see Chapter 2 for an example of how the large relative uncertainties of the Hipparcos–Gaia PMa can frustrate efforts to constrain a companion's dynamical mass). Secondly, the Gaia-only approach does not share the PMa technique's bias for wide, long-period orbits. Instead, it is capable of informing direct observations of planets residing at much closer separations down to a few AU. This capability appears particularly promising in light of the giant planet pile-up expected at these orbital distances (see Sect. 1.2.2).

The above is a quick and much simplified summary of the strategy that forms a key component of this thesis. As we shall see in substantially more detail in Chapter 3, the development and application of this novel technique that predicts the perturber's on-sky position, will enable us to take another step forward in terms of DI survey efficiency. In contrast to the PMa technique which has facilitated semi-targeted studies, this method will allow for fully-targeted DI follow-up campaigns. At the risk of giving away some of the results presented in Chapter 3, the question of whether – apart from orbiting BDs – the NSS two-body orbit catalogue might even be capable of guiding successful confirmations of planetary companions will be explored in Chapter 4.

Before we can apply this novel technique, however, we need to prepare the stage for another actor destined to play a central role in this thesis. Classical coronagraphic imaging instruments will not be capable of detecting the planets and BDs inferred from the NSS two-

body orbit catalogue. Confirming these companions, hiding at such close separations from the star, will require a different kind of observational technique: optical interferometry.

# 1.4 Fringe science: optical interferometry

Optical interferometry as conducted using the GRAVITY instrument at ESO's VLTI (see Sect. 1.5) is one of the pillars on which this thesis stands. The technique itself can still be considered as in its infancy. While immensely promising in what it can offer to many science cases from the characterisation of exoplanets to the probing of active galactic nuclei, many astronomers still shy away from employing interferometric observations in the optical and near-infrared. This might be due to its relative novelty, the notoriety of its complicated theoretical underpinnings or the scarcity of observational facilities actually supporting interferometric instruments. Whatever the reasons, the following overview of the main differences to conventional optical and near-infrared observational astronomy and brief summary of the theoretical background and the main interferometric observables should provide an adequate basis to understand the content of this thesis even for readers who do not happen to be expert interferometrists.

## 1.4.1 The yoke of the Rayleigh criterion

Depending on the pursued science case, an astronomer may demand different things from their observational data. To conduct an exoplanet transit search for instance, one would require highly accurate stellar photometry measurements and a high cadence of observations. Other sub-branches of astronomy depend on the capability to confidently resolve astrophysical features or precisely measure an object's position in the sky. The achievable angular resolution is thus a key characteristic of any telescope. It is defined as the smallest angular separation at which two objects can still be distinguished unambiguously from one another. Since any point source of light viewed through a telescope with a circular aperture will create a characteristic Airy pattern in the focal plane (Airy 1835), the smallest resolvable separation between two objects is reached if the centre of the first source's Airy pattern aligns with the first minimum of that of the second source. First described by Lord Rayleigh (Rayleigh 1880), this condition is commonly known as the Rayleigh criterion and can be written as

$$\theta = 1.22 \frac{\lambda}{D},\tag{1.12}$$

where  $\theta$  is the smallest angle resolvable by a telescope of diameter, D, at a wavelength,  $\lambda$ .  $\theta$  is also called the diffraction limit. From Equation 1.12 it naively follows that increasing the size of one's aperture, D, will translate to a gain in angular resolution. In general, however, a telescope with an aperture larger than approximately 50 cm is not diffraction-but seeing-limited in the optical and near-infrared. Seeing is the observational phenomenon that the image of a star or other celestial object seems to flicker randomly over short time spans. We have already briefly encountered this effect in the Direct Imaging paragraph in

Sect. 1.2.1. It is brought about by convective turbulence in the atmospheric layers that the astronomical light traverses while on its way to our telescope. The effect depends on a multitude of observing conditions such as the humidity, temperature and wind conditions at the observatory site. Hence, alongside other important considerations such as the amount of ambient light pollution, the locations at which the world's foremost observatories are built are chosen such as to optimise seeing conditions. Yet, if uncorrected for, even the most advanced telescopes situated at the most favourable locations on Earth are seeing-limited. For instance, the site mean seeing on Cerro Paranal measured 0.73 arcsec with a standard deviation of 0.31 arcsec in  $2024^6$ .

Despite this limit in angular resolution, telescopes built throughout the last century continued to grow in aperture size. This development was mainly driven by the associated increase in light collecting power that such larger telescopes facilitated. In other words, the goal of building ever larger optical telescopes was not the achievable angular resolution but the attainable sensitivity. The 100-inch Hooker telescope at Mount Wilson Observatory had held the record as the largest telescope in the world for more than 30 years when it was dethroned by the 200-inch Hale telescope at Palomar Observatory in 1948. At the time of writing, the Gran Telescopio Canarias (Alvarez et al. 1998) is the largest telescope in the world by diameter.

With the significant advances in computing power that enabled the development and implementation of AO systems in the 1990s (once more, see the Direct Imaging paragraph in Sect. 1.2.1 and references therein), it was finally possible to correct for atmospheric turbulence and overcome the seeing limitation for a large fraction of the sky. As a result, AO-equipped optical telescopes such as the VLT, Keck or Gemini North and South are essentially diffraction-limited. They can make full use of the angular resolution facilitated by their respective aperture sizes in accordance with Equation 1.12.

In principle, further increases in telescope aperture sizes will now also translate into an enhanced angular resolution. Yet, the trend towards gradually larger telescopes seen throughout the last century will not continue indefinitely. ESO's Extremely Large Telescope (ELT; Padovani & Cirasuolo 2023), which upon completion will be the largest ever built, employs a segmented primary mirror of 39 m in diameter. Manufacturing and transporting a monolithic mirror of this size being impossible, we may presume that the ELT will remain the largest telescope for the foreseeable future and surmise that – after decades of gradual improvements and the mitigation of the irksome seeing phenomenon – the angular resolution achievable by ground-based, single-telescope facilities may have reached an insurmountable limit.

# 1.4.2 Evading the diffraction limit

To understand how we can elude the resolution limit imposed by the Rayleigh criterion, we need to revisit one of the foundational experiments of modern physics: Young's double slit

<sup>&</sup>lt;sup>6</sup>see ESO's Paranal Astronomical Site Monitor: https://www.eso.org/sci/facilities/paranal/astroclimate.html

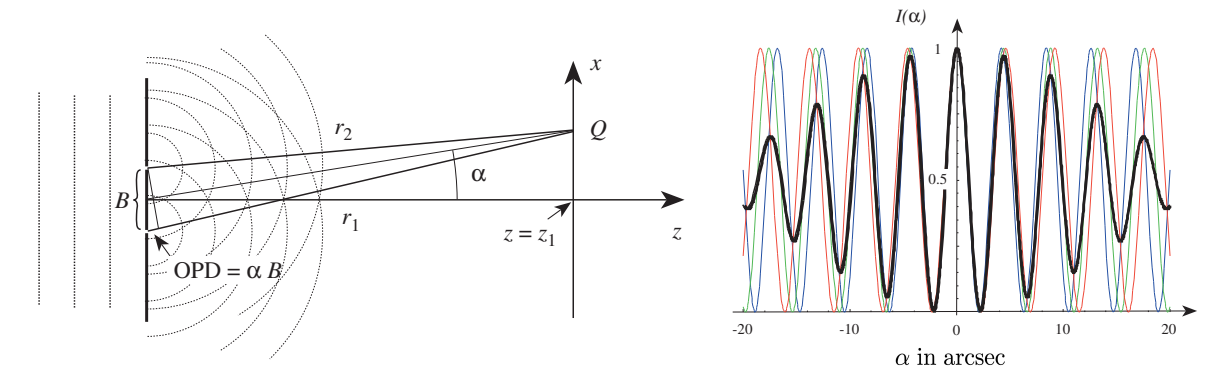


Figure 1.9: Left: Schematic of Young's double-slit experiment. A plane parallel light wave approaches a blind that contains two slits. Emerging from the slits, the light propagates spherically between the blind and a screen located at  $z=z_1$ . The light paths,  $r_1$  and  $r_2$ , required to reach a given point, Q, on the screen differ depending on the diffraction angle,  $\alpha$ , and the slit separation, B. This difference is called the optical path difference (OPD) and amounts to  $\alpha B$  for small angles,  $\alpha$ . Right: Interferometric pattern observed on the screen along the x-direction in the left hand panel given a slit separation of  $B=10\,\mathrm{cm}$ . The three colours correspond to the wavelengths 2.0, 2.2 and 2.4 µm while the black curve displays the resulting intensity. The maximum-to-minimum contrast declines with increasing absolute values of  $\alpha$ . Both figures adapted from Glindemann (2011).

experiment. Regarded as the original confirmation of the wave theory of light, it also serves as a fitting starting point for our foray into optical interferometry. As visualised schematically in the left hand panel of Fig. 1.9, Thomas Young observed that an approximately planar wavefront of light permitted to only pass through two parallel slits before reaching a screen will give rise to a well discernible sinusoidal intensity pattern. The effect can be explained by invoking the Huygens–Fresnel principle, deducing that in general the two spherical waves emerging from the slits will require different path lengths to reach a given point on the screen and concluding that they interfere constructively and destructively to produce a fringe pattern, that is a sequence of alternating maxima and minima, on the screen. Following Hecht & Zajac (1974), this irradiance distribution can be described via

$$I(\alpha) = 4I_0 \cos^2\left(\frac{\pi d \sin(\alpha)}{\lambda}\right),\tag{1.13}$$

where  $I_0$  is the irradiance per light wave emerging from the slits, d is the separation between the slits,  $\alpha$  is the angle subtended by the centre of the screen and the position of interest and  $\lambda$  is the wavelength of the monochromatic light used to conduct the experiment.

Not unlike the slits in this classic experimental setup, interferometric astronomical observations rely on at least two telescopes that are typically separated by distances that are much larger than the respective telescope apertures. This separation is called the interferometric baseline, B. The resolution achievable by such an interferometer is defined by half the angle between two neighbouring fringes, which – using Equation 1.13 – can be

$$\theta = \frac{\lambda}{2B}.\tag{1.14}$$

The power of the interferometric method becomes apparent when comparing this relation to the Rayleigh criterion defined in Equation 1.12: we can straightforwardly increase the angular resolution of our interferometer by extending its baseline, thereby avoiding disproportionate aperture diameters and the increased cost and effort they entail. To put it another way, an interferometer's resolution is governed by the distance between the involved telescopes, not their individual diameter. This considerable advantage over single telescopes comes at the price of a more intricate framework of observing modes as well as a set of less intuitive observables. In the following, we shall see how astronomical information can be gleaned from the complex interferometric patterns produced by combining two or more telescopes.

## 1.4.3 Turning fringes into precision measurements

To understand how an interferometer can provide measurements of a given target that are of scientific interest, it is instructive to consider an idealised instrumental setup. As visualised in Fig. 1.10, we assume our interferometer to consist of two apertures separated by the baseline vector,  $\vec{B}$ . They are observing an astronomical target along the line of light direction,  $\vec{s}(t)$ . The source can be considered sufficiently distant for its light waves to be planar once they arrive at our telescopes. The projected or effective baseline,  $\vec{B}_{\rm eff}(t)$ , is the component of  $\vec{B}$  that is oriented perpendicular to the viewing direction,  $\vec{s}(t)$ , and therefore parallel to the planar wavefront. Invoking Young's experiment outlined in Sect. 1.4.2 as an analogy, our two telescopes correspond to the slits while the effective baseline represents their separation. Our basic interferometer is also equipped with so-called delay lines, a set of mirrors mounted on moveable carts that can be used to reflect the light beam along precisely determined distances before allowing it to interfere with the light travelling along the other arm. This way, an accurate delay can be introduced into either or both arms of the interferometer. By varying the delay, we can effect an optical path difference (OPD) between the beams. Thus, the usage of delay lines allows us to sample and record the interference pattern for different OPDs. Such a delay mechanism was already employed in the very first successful optical interferometry demonstration by Labeyrie (1975).

The contrast between the resulting fringes is called visibility amplitude and corresponds to the absolute value of the complex visibility, V, the main interferometric observable. The second observable encoded in the complex visibility is the visibility phase,  $\Phi$ . It governs the position of the fringe maxima and minima on the detector and vanishes for a point source at the centre of the telescopes' FoVs. If the source is extended or off-axis, though, the visibility phase will assume a non-zero value. The capability of measuring this quantity represents a considerable advantage of the interferometric method as compared to using single telescopes. It is this specific ability that allows for measuring a given target's accurate on-sky position and in effect turns our interferometer into a tool for high precision astrometry (see Shao & Colavita 1992 and von der Lühe et al. 1995). The complex visibility

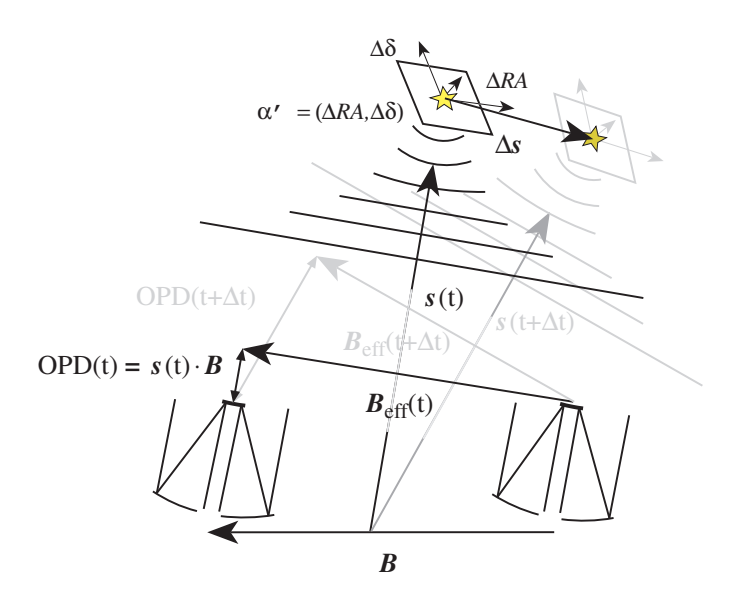


Figure 1.10: Interferometric observation of a moving target. The interferometer consists of two telescopes separated by the baseling vector,  $\vec{B}$ . The local coordinate system spanned by the  $\Delta RA$  and  $\Delta \delta$  axes is centred on the target and orthogonal to the viewing direction,  $\vec{s}(t)$ . Due to the large distance to the target, the wave front approaching the telescopes can be considered plane parallel and perpendicular to  $\vec{s}(t)$ . Likewise, the effective baseline,  $\vec{B}_{\rm eff}(t)$ , is the component of B that is oriented perpendicular to  $\vec{s}(t)$ . As the name implies, the optical path difference, OPD(t), is the difference in path length that the wave front needs to cover to reach the individual telescopes. At a second time of observation, here shown in grey, the target has moved. The shift in viewing direction translates to a change in  $\vec{B}_{\rm eff}$  and OPD. Figure adapted from Glindemann (2011).

can thus be written as

$$V(u,v) = |V|e^{-i\Phi}. (1.15)$$

Here, we have silently introduced a new coordinate system, the so-called u-v plane. It contains the projected baselines between the two telescopes during the respective observations and is parallel to the plane of the sky. u and v are called spatial frequency coordinates and measure the baseline as projected onto the plane of the sky along the East-West and North-South direction, respectively. Both are defined in units of wavelength at which the target is observed (Lawson 2000). Note that the u-v plane is not equivalent to the physical coordinate system of the observatory. Instead, u and v are difference-coordinates, in the sense that the spatial frequency probed at a given wavelength using the baseline B is identical to the one probed using the reversed baseline -B. Consequently, a complex visibility measurement corresponds to two data points within the u-v plane where one is the complex conjugate of the other.

The complex visibility is related to the properties of our on-sky target through the Van Cittert-Zernike theorem (van Cittert 1934; Zernike 1938). This fundamental proposition states that, for a distant, spatially incoherent target, the measured complex visibility is

equal to the Fourier transform of the two-dimensional on-sky intensity distribution, I(x, y), that is

$$V(u,v) = \frac{\iint I(x,y)e^{-2i\pi(xu+yv)}dxdy}{\iint I(x,y)dxdy}.$$
(1.16)

Here, the x and y coordinates specify a position on the plane of the sky in which our target's intensity distribution resides. It is equivalent to the  $\Delta \text{RA}-\Delta \delta$  system depicted in Fig. 1.10.

By varying the projected baseline as well as the wavelength of observation we can populate the u-v plane with complex visibility measurements. On the basis of multiple such observations, one can infer the target's intensity distribution. The intuitive way of conducting this operation is by applying the inverse of Equation 1.16, that is by obtaining multiple measurements of V, taking the Fourier transform and obtaining an actual image of the target's on-sky distribution. This process, commonly called interferometric imaging or image reconstruction, is challenging since it requires a dense sampling of the u-v plane which can only be achieved by measuring V at many different spatial frequencies (e.g. see Thiebaut & Giovannelli 2010). While this procedure is routinely applied in radio interferometry – perhaps most notably to image the circumstellar disc around HL Tau (ALMA Partnership et al. 2015) – implementing it for optical and near-infrared light is challenging. The main reason for this is the fact that measuring and recording the light phase at these wavelengths is currently impossible. Thus, the beams from the individual telescopes need to be combined physically and in situ at the observatory site. The beam transport infrastructure and delay line layout thus introduce a hard limit on the amount and length of the baselines involved in the setup, ultimately translating to a much more limited u-v plane coverage compared to the radio interferometry case where phases are measured directly, baselines are arbitrarily long and the interference is performed digitally. As a consequence, when working with sparsely sampled spatial frequencies, we usually resort to fitting models to the available interferometric data (e.g. see Mérand 2022). While not yielding an image of the astrophysical source, this technique still allows us to infer geometrical properties of the target's intensity distribution and take advantage of the unmatched angular resolution and astrometric capabilities that the interferometric method offers.

Since interferometric astrometry underpins most of the work presented in this thesis, it is worthwhile to examine the actual measurement procedure in more detail. In fact, obtaining the visibility phase is not as trivial as it may at first appear. As opposed to an ideal interferometer, a real instrument is plagued by non-trivial internal and external OPDs that will cause the pattern of maxima and minima to flicker, thereby introducing a visibility phase shift and either varying the measurable contrasts or erasing the fringes altogether. There are two major OPD sources that result in visibility phase shifts that are nigh impossible to measure directly but nevertheless – if left uncorrected – foil any attempt at measuring a meaningful visibility phase.

Firstly, we need to account for internal OPDs between the two arms of the interferometer, for instance resulting from temperature variations or vibrations affecting the delay lines. Of the two sources we discuss here, this is the more manageable effect since any confounding internal visibility phase contributions can be monitored by an inbuilt metrology system. This is a module that periodically measures the internal OPD by sending a laser beam backwards along the optical path of the respective interferometer arm all the way to the pupil plane where their interference pattern is registered by a set of diodes mounted on the spider holding the secondary mirror (e.g. Lippa et al. 2016).

Secondly, we need to deal with distorting external OPDs introduced by atmospheric turbulence along the line of sight (Roddier 1981). One way out of this dilemma is by measuring the closure phase instead of the absolute visibility phase. First introduced by Jennison (1958), this quantity is defined as the sum of phases measured along three baselines, that is

$$\Phi_{1,2,3} = \Phi_{1,2} + \Phi_{2,3} + \Phi_{3,1}, \tag{1.17}$$

where the digits in the indices refer to the telescopes involved in the individual phase measurements. The closure phase is a measure of the true astrophysical phase since the first order noise terms in Equation 1.17 as introduced by each telescope appear twice with different signs and thus cancel out. Hence, the closure phase is not affected by the malignant influences of the instrument and atmosphere. On the other hand, a closure phase measurement requires a minimum of three baselines.

Another viable method of correcting for disturbing external phase contributions is by applying a referencing technique (Shao & Colavita 1992). Similar to the functionality of an AO system, this approach amounts to selecting a reference source that is sufficiently bright and positioned close to the astrophysical source of interest such that we can assume the atmospheric distortions affecting the two sources to be similar. Periodic phase measurements of this reference source can then be used to correct the visibility phase of the science target (e.g. Lacour et al. 2019). As we shall see in Sect. 1.5, the GRAVITY instrument at the VLTI employs such a phase referencing technique to enable the visibility phase measurements that its astrometric capabilities rely on.

The combination of the internal and external OPDs can be corrected for by introducing an appropriate lag using the delay lines. This technique ensures that the measured fringes are stable and persist for sufficient periods to allow for adequate detector integration times.

The above describes a simple implementation of an interferometric facility and some of the methods that allow us to make sense of the observables involved. There is little doubt that this field of instrumentation will continue to prosper and play an ever more central role in observational astronomy. This thesis, however, is not directly concerned with the intricacies of optical interferometry. In fact, as we shall see in the chapters to come, we will use the technique as a means to an end rather than studying it for its own sake. Indeed, in this context it can be considered a tool that allows us to explore a new parameter space of the exoplanet population. As such, we will not delve any deeper into the theory of how interferometers work but refer to some of the well known publications and textbooks on the subject (e.g. Quirrenbach 2001; Monnier 2003; Glindemann 2011; Eisenhauer et al. 2023).

Nevertheless, before we can move on to apply this formidable tool we need to briefly introduce the instrument that makes these extraordinary feats possible in the first place.

## 1.5 VLTI and the GRAVITY instrument

The month of May, 2018, held a special event for astronomers interested in what was hiding in the very centre of the Milky Way. S2, one of the innermost stars of the Galactic centre, was scheduled to undergo its pericentre passage. Hurling past the unseen massive black hole candidate Sgr A\* at a mere distance of 120 AU and a velocity of approximately 3% of the speed of light, this occasion represented an ideal opportunity to test the predictions of general relativity and the nature of the central object (GRAVITY Collaboration et al. 2018). Given the star's orbital period of roughly 16 years, the event was better not to be missed.

As an input for orbital fitting routines, one of the coveted observables during pericentre passage was the star's precise astrometry. For the reasons outlined in Sect. 1.4, optical interferometry lent itself splendidly to this task. The opportunity afforded by S2's close passage of Sgr A\* thus motivated the development of a new interferometric instrument, GRAVITY (GRAVITY Collaboration et al. 2017). After years of designing, constructing and commissioning the instrument, it was ready in time to catch S2 at its pericentre, confirm several relativistic effects (GRAVITY Collaboration et al. 2018) and earn the group leading the project the Nobel Prize for Physics in 2020.

One year after S2's flyby of Sgr A\*, the instrument was used to observe an exoplanet for the first time (GRAVITY Collaboration et al. 2019). Although not designed with this specific goal in mind, the study demonstrated GRAVITY's applicability as a tool for diverse exoplanet science cases. This section aims to briefly introduce the VLTI facility, the GRAVITY instrument and the different observing modes employed in this thesis.

# 1.5.1 Design and functionality

ESO's VLT on Cerro Paranal consists of four 8.2 m Unit Telescopes (UTs) and four movable 1.8 m Auxiliary Telescopes (ATs). While each individual UT ranks amongst the largest optical telescopes in the world, it is the observatory's capability of interferometrically combining up to four apertures that makes it a truly unique facility. The ensemble of telescopes, delay lines and the beam combiner laboratory on Cerro Paranal is commonly called the Very Large Telescope Interferometer (VLTI). Figure 1.11 shows the observatory under construction and a bird's eye view schematic of the VLT platform illustrating the positions of the involved telescopes. The combination of four telescopes provides six baselines spanning up to 130 m in the UT case and over 200 m in the AT case. Before the arrival of GRAV-ITY, the VLTI had already hosted a series of interferometric instruments, among them the now decomissioned VINCI (Kervella et al. 2000), PRIMA (Quirrenbach et al. 1998), MIDI (Leinert et al. 2003) and AMBER instruments (Petrov et al. 2007). Today, there are three instruments in operation and available for usage by the astronomical community: PIO-

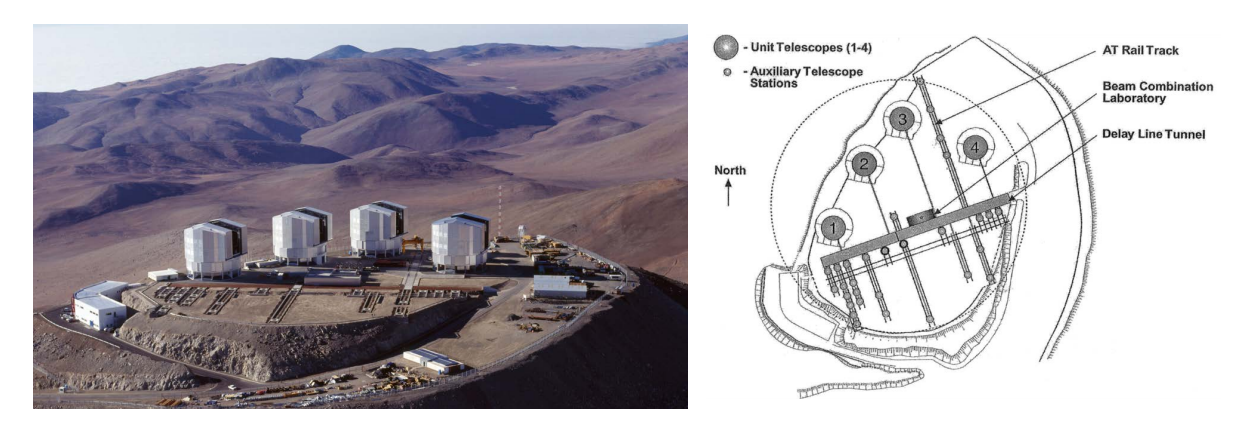


Figure 1.11: Left: Cerro Paranal during construction and commissioning of the Unit Telescopes in November, 1998. While the Auxiliary Telescopes were still missing at this time, the exposed underground tunnels – later used to guide their beams towards the delay lines and ultimately into the VLTI laboratory – can also be seen. Image credit: ESO. Right: Schematic showing a bird's eye view of Cerro Paranal including the fixed locations of the Unit Telescopes and the possible positions of the movable Auxiliary Telescopes. The underground delay lines run along the broad grey strip at the centre of the platform. Finally, the VLTI laboratory houses the interferometric instruments that combine the collected light. Figure adapted from Paresce et al. (2003).

NIER (Le Bouquin et al. 2011), MATISSE (Lopez et al. 2022) and GRAVITY (GRAVITY Collaboration et al. 2017).

GRAVITY itself is a beam combiner instrument working in the K-band, specifically in the wavelength range between 2.0 and 2.4 µm. It was designed to perform imaging observations as well as accurate astrometric measurements. For the latter it employs a phase referencing strategy (see Sect. 1.4.3) that relies on an inbuilt Fringe Tracker (FT; Lacour et al. 2019). This device monitors the visibility phase of a reference star at a high temporal frequency. In other words, the FT measures the OPD correction necessitated by confounding atmospheric fluctuations before feeding it to the delay lines. These rectify the accrued OPD by introducing an appropriate lag to the light collected by the individual telescopes, thereby facilitating stable fringes and detector integration times of up to several 100 s, provided the observing conditions are adequate (Nowak et al. 2024b).

While the FT monitors a reference star, the science target is observed by a second, independent interferometric combiner, the aptly named Science Combiner (SC). It has a higher resolution than the FT, ranging between R = 50 to 4000 depending on the adopted observing mode. This dual field capability, that is the ability of positioning both combiners individually resulting in two independent FoVs, is one of GRAVITY's key advantages since the interplay between the FT and SC allows for a measurement of the visibility phase that is offset by only one unknown quantity, the metrology zero-point,  $\Phi_{\rm ZP}$  (for a full derivation of this relation, see Nowak et al. 2024a). This zero-point can be measured in two different ways, namely by means of the on-axis and off-axis observation strategies which we will

both encounter in this thesis.

The on-axis mode builds on a choreographed sequence of observations: while the FT remains fixed on the reference target, the SC alternates between integrations of the reference and the science target. The simultaneous FT and SC observations of the reference can be used to determine  $\Phi_{\rm ZP}$  which is required to measure the relative astrometry between the two sources during the interlaced SC integrations on the science target. This observation mode is limited to angular separations of up to 600 mas between the two sources. Since it is especially applicable to sources in close proximity to one another (down to a separation of approximately 30 mas), the on-axis technique is ideally suited for the detection and characterisation of exoplanets and BDs on very close-in orbits. Its application requires the use of a so-called 50:50 beam-splitter. This device diverts the beams such that only 50 % of the collected light reaches each combiner entailing a loss of signal-to-noise ratio.

The off-axis mode on the other hand does not rely on an alternating observation strategy. Instead, a so-called "swap" observation of a well-known calibrator binary is performed where the targets observed by the FT and SC are exchanged (Nowak et al. 2024a). From the two inverted relative astrometry measurements one can extract  $\Phi_{\rm ZP}$  to obtain the calibrated relative astrometry. This strategy requires separations of more than 300 mas between reference and science target, a condition that stems from the usage of a triangular roof-mirror diverting the light towards the combiners. The fact that the roof-mirror does not have a perfectly sharp edge entails the lower separation limit. While it is therefore not suited to probe the immediate angular environment of a given host star, it can be applied for systems harbouring companions on wider orbits. On the other hand, using a roof-mirror instead of a beam-splitter, all of the collected light is diverted to combiners enabling higher signal-to-noise ratios than the on-axis observing mode. We shall see the off-axis technique employed for an observation of HIP 99770 b at approximately 400 mas from its host in Chapter 2.

As stated above, the nuances of GRAVITY observations are not a theme of this thesis. Instead, throughout the different chapters, we relied on the nominal ESO instrument pipeline as well as the dedicated ExoGRAVITY pipeline to handle the data reduction up to the point where we were left with the precision astrometry and extracted K-band spectrum of a given science target. For a more detailed description of the on- and off-axis observing strategies, see Nowak et al. (2024a).

## 1.6 Thesis outline

Direct imaging as a means of exoplanet detection and characterisation is still a fairly novel technique plagued by a low yield and limited applicability, currently confined to massive companions on wide orbits of several dozen AU. Equally important, we are only slowly adding new discoveries to our pool of imaged planets and even when we succeed in doing so, their large separations come back to haunt us: after years of monitoring, we are often left with a negligible orbital coverage, forcing upon us the unenviable task of characterising their atmospheres and inferring their formation histories without adequate

1.6 Thesis outline 37

knowledge of their most basic and far-reaching property, namely their mass. At the same time, the method is currently poorly suited for application at closer separations where a more thorough characterisation would be possible. Here, we are limited by the inner working angle of coronagraphic imagers concealing the immediate angular environment of any prospective host.

In this thesis I aim to lay the groundwork for a new method that is capable of piercing this figurative "bubble" around potential host stars, enabling the study of planets at separations never before accessed by direct detection techniques. At the heart of this new approach lies a symbiosis between two observational techniques. We will explore how the combination of the large astrometric database obtained by the *Gaia* mission and precision follow-up observations using VLTI/GRAVITY enables us to transition from time-consuming blind imaging campaigns, that often result in non-detections, to a highly-targeted, highly-efficient routine. Not only will this method confirm the existence of companions tentatively suggested by the astrometric data, it will yield highly precise dynamical masses and spectral as well as photometric data sets that will facilitate a thorough characterisation of the individual specimens. Thus, as we leverage the *Gaia*–GRAVITY synergy to push to ever closer separations and lower companion masses, the efficient nature of the approach will enable a population-level, demographic investigation into the make-up of planetary systems that begin to resemble our own Solar System.

This thesis is structured such that the gradual build-up of different methods and the respective science cases they serve blends into a coherent narrative. Chapter 2 deals with HIP 99770 b, the first companion identified as a planet that was directly detected on the basis of astrometric evidence as to its existence. In this sense, the discovery of HIP 99770 b can be viewed as a milestone towards a more efficient realisation of the direct imaging method. It demonstrated how astrometry can inform follow-up studies as to which stars are likely to host companions accessible to our instruments. While we did not perform the original detection, the companion serves as an instructive example of the complementarity between astrometry and imaging, motivating a renewed study of the object. In the course of our characterisation of the companion based on GRAVITY observations, we shall also encounter potential limitations of this synergetic approach.

The landmark discovery of HIP 99770 b raises the question whether we can go one step further: might it be possible to refine our targeting capabilities, moving from mere indications as to which stars are likely to host substellar companions towards predictions of the relative on-sky positions of these companions relative to their respective hosts. Chapter 3 introduces a method of combining *Gaia* with GRAVITY that can provide such predictions, thereby substantially simplifying the companion confirmation process and aiding our efforts at characterisation of the detected object. Developing and refining these predictive capabilities is essential if we are to use GRAVITY as a follow-up machine in the future, since the instrument only offers a small FoV of approximately 60 mas in diameter.

Having demonstrated the potential of the *Gaia*–GRAVITY synergy for BD companion detection and characterisation at small angular separations in Chapter 3, we might ask whether the technique can be applied to even lower mass companions. To put it another

way: can we use GRAVITY to confirm planet candidates hidden in the Gaia DR3 data set? This challenge is met in Chapter 4, where we present the outcome of an ambitious observing programme aimed at uncovering the first Gaia-inferred exoplanet<sup>7</sup>.

Throughout Chapters 2 to 4, the target selection process that precedes any follow-up observation is based on the wobble motion that prospective host stars display, be in in the long- (Hipparcos-Gaia PMa method; see Sect. 1.3.2 and Chapter 2) or in the short-term (Gaia-GRAVITY synergy; see Chapter 3). In Chapter 5, we put forward a procedure as to how we can apply this method to the planets themselves. By simulating the undulating trajectory of an moon-hosting planet around its host star, we investigate our current and future capabilities of robustly detecting exomoons, a class of objects that has so far evaded discovery. This search amounts to taking the next step in astrometric detection: we will move from Gaia inferring planets around gravitationally perturbed stars to GRAVITY detecting moons around wobbling planets.

The results presented in this thesis can be considered a stepping stone, a demonstration of different techniques that can be scaled efficiently in the future and have the potential of yielding population-level samples of previously unknown BDs and planets at short separations. As such, they provide the means for tackling a wide range of questions, some of which are presented in Chapter 6. There, we elaborate on how these methods may be expanded, what's next for some individual companions of interest and what resources and capabilities we may expect *Gaia* DR4 to add to this framework.

Finally, Chapter 7 gives a final assessment of the main results and central advances made throughout the preceding chapters. We conclude by placing the work presented in this thesis into the broader context of exoplanet research.

<sup>&</sup>lt;sup>7</sup>To clarify, while HIP 99770 b was discovered on the basis of *Gaia* data, the method hinged on comparison between Hipparcos and *Gaia* proper motion measurements (see Sect. 1.3.2). Here, we refer to confirming the first planet based solely on *Gaia* data. As we shall see in Chapter 3, by foregoing the Hipparcos data, we are able to access a different parameter space closer to the star, rendering this method more applicable for shorter-period companions.

# Chapter 2

# From blind to semi-targeted searches: HIP 99770 b

The content of this chapter is a reproduction of Winterhalder et al. (2025), a publication in Astronomy & Astrophysics, titled:

# Orbit and atmosphere of HIP 99770 b through the eyes of VLTI/GRAVITY

T. O. Winterhalder, J. Kammerer, S. Lacour, A. Mérand, M. Nowak, T. Stolker, W. O. Balmer, G.-D. Marleau et al.<sup>1</sup>

As first author of this publication, I was in charge of the data analysis, interpretation and writing process. J. Kammerer, S. Lacour and A. Mérand acted as supervisors. M. Nowak, T. Stolker, W. O. Balmer and G.-D. Marleau provided comments before submission to the journal. I have taken the liberty of adjusting the label font sizes in some figures where appropriate. The paper abstract can be found on the reverse of this page. The appendix as originally published in *Astronomy & Astrophysics* is reproduced in Appendix A of this thesis.

 $<sup>^{1}</sup>$ For brevity, the remaining, alphabetically sorted co-authors from the GRAVITY collaboration are abbreviated as et al.

#### Abstract

Context. Inferring the likely formation channel of giant exoplanets and brown dwarf companions from orbital and atmospheric observables remains a formidable challenge. Further and more precise directly measured dynamical masses of these companions are required to inform and gauge formation, evolutionary, and atmospheric models. We present an updated study of the recently discovered companion to HIP 99770 based on observations conducted with the near-infrared interferometer VLTI/GRAVITY.

Aims. Through renewed orbital and spectral analyses based on the GRAVITY data, we characterise HIP 99770 b to better constrain its orbit, dynamical mass, and atmospheric properties, as well as to shed light on its likely formation channel.

Methods. Upon inclusion of the new high-precision astrometry epoch, we ran an orbit fit to further constrain the dynamical mass of the companion and the orbit solution. We also analysed the GRAVITY K-band spectrum, placing it into context with literature data, and extracting magnitude, age, spectral type, bulk properties and atmospheric characteristics of HIP 99770 b.

Results. We detected the companion at a radial separation of 417 mas from its host. The new orbit fit yields a dynamical mass of  $17^{+6}_{-5}\,\mathrm{M_{Jup}}$  and an eccentricity of  $0.31^{+0.06}_{-0.12}$ . We also find that additional relative astrometry epochs in the future will not enable further constraints on the dynamical mass due to the dominating relative uncertainty on the Hipparcos–Gaia proper motion anomaly that is used in the orbit-fitting routine. The publication of Gaia DR4 will likely ease this predicament. Based on the spectral analysis, we find that the companion is consistent with spectral type L8 and exhibits a potential metal enrichment in its atmosphere. Adopting the AMES-DUSTY model to infer its age, within its dynamical mass constraint the companion conceivably corresponds to either a younger  $(28^{+15}_{-14}\,\mathrm{Myr})$  object with a mass just below the deuterium-burning limit or an older  $(119^{+37}_{-10}\,\mathrm{Myr})$  body with a mass just above the deuterium-burning limit.

Conclusions. These results do not yet allow for a definite inference of the companion's formation channel. Nevertheless, the new constraints on its bulk properties and the additional GRAVITY spectrum presented here will aid future efforts to determine the formation history of HIP 99770 b.

## 2.1 Introduction

Gas giant exoplanets that are accessible to direct-imaging studies are rare. Unbiased blind surveys have provided only a few detections (e.g. Nielsen et al. 2019; Vigan et al. 2021; Chomez et al. 2025; for a review, see Bowler 2016) and demonstrated that targeted studies, for instance informed by clues stemming from other detection techniques such as astrometric monitoring of potential host stars, are the only way to efficiently build a population-level sample of directly imaged exoplanets.

The source HIP 99770 was identified as exhibiting a significant proper motion anomaly (PMa; see Kervella et al. 2022; Brandt 2021), the discrepancy between the proper motion of a star as observed by the Hipparcos (Schuyer 1985) and Gaia missions (Gaia Collaboration et al. 2016). Such a PMa can be caused by an orbiting companion inducing reflex motion in the star that manifests itself in its projected movement on the sky plane, and thus, in its proper motion. A dedicated direct-imaging follow-up using SCExAO/CHARIS (Jovanovic et al. 2015; Groff et al. 2017) on the Subaru Telescope and Keck/NIRC2 revealed a substellar companion with a dynamical mass of  $16.1^{+5.4}_{-5.0} \,\mathrm{M_{Jup}}$  (Currie et al. 2023b). Hence, HIP 99770 was the first system to yield a detection of a companion identified as a planet after it was targeted specifically on the basis of tentative astrometric evidence that indicated the existence of an orbiting object. The loose mass constraint places the companion in close proximity to the deuterium-burning threshold, implying a need for further observations to pin down its mass<sup>1</sup>.

The necessity of follow-up studies of this object becomes all the more apparent when we consider the relative scarcity of what are loosely referred to as super-Jupiters (Carson et al. 2013), that is, substellar companions with masses at about the deuterium-burning threshold. These objects tend to defy the commonly proposed planet formation mechanisms. On the one hand, the disc-instability pathway, which posits that planets form via the gravitational collapse of the circumstellar disc (Cameron 1978; Boss 1997; Kratter & Lodato 2016), is predicted to form more massive companions well within the brown dwarf or even stellar mass regime (Forgan & Rice 2013). On the other hand, formation via core accretion in the outer disc is difficult to justify because the required timescales at these distances from the host are significantly longer than the typical disc-dissipation timescale (Lambrechts & Johansen 2012). The different pathways are expected to leave telltale imprints on the orbital geometry of the system implying that precisely constraining the orbital elements of a given companion can reveal clues as to its formation history (e.g. Bitsch et al. 2020; Marleau et al. 2019). Given its long period orbit (approximately 50 years; Currie et al. 2023b) and its recent discovery based on data collected between 2020 and 2021, the current orbit coverage of HIP 99770 b is limited. An extension of the

 $<sup>^1\</sup>mathrm{While}$  the deuterium-burning threshold, which is traditionally assumed to be located at  $13\,\mathrm{M_{Jup}}$  (e.g. Burrows et al. 2001; Spiegel et al. 2011; Mollière & Mordasini 2012), is the conventional choice of classifier between planets and BDs, others have been proposed. For instance, there is evidence that suggests that the turn-over mass of the companion mass function is located far beyond  $13\,\mathrm{M_{Jup}}$  in the region between 25 and  $40\,\mathrm{M_{Jup}}$  (e.g. Sahlmann et al. 2011; Ma & Ge 2014; Reggiani et al. 2016; Kiefer et al. 2019; Stevenson et al. 2023)

available astrometric baseline will help us improve the orbital solution.

An alternative and complementary route towards probing the formation history of a given companion is the characterisation of its atmosphere. Observables such as the atmospheric metallicity or elemental abundance ratios, which are accessible via a spectroscopic analysis of the flux emitted by the companion, can add to the conclusions drawn from orbital considerations (e.g. Mollière et al. 2022). For the specific case of HIP 99770 b, a recent high-resolution spectroscopic follow-up yielded constraints on the metallicity and elemental abundance ratios of the companion (Zhang et al. 2024). These were unable to exclude either formation pathway, however. In addition to these continuum-removed high-resolution K-band spectra, a new data set that preserves the continuum emission component of the companion (albeit at a lower resolution) can shed new light on the atmospheric properties of the companion.

Here, we present new VLTI/GRAVITY (GRAVITY Collaboration et al. 2017) observations of HIP 99770 b, describe how they facilitate constraints on the orbital geometry of the system and act as yet another window into the companion atmosphere. GRAVITY is a near-infrared interferometric instrument at the European Southern Observatory's Very Large Telescope (VLT). Previous studies using the instrument for exoplanet observations have demonstrated an astrometric accuracy of 50 μas (GRAVITY Collaboration et al. 2019).

This paper is arranged as follows: Section 2.2 gives an overview of the observational data we used. The orbital and spectral analyses of the obtained data are presented and discussed in Sect. 2.3 and 2.4, respectively. The conclusions of our study are laid out in Sect. 2.5.

## 2.2 Observations and data reduction

### 2.2.1 Previous observations

This work draws upon data that were collected by previous studies of the HIP 99770 system. We used the astrometric epochs and the photometric and spectral data obtained by Currie et al. (2023b). The CHARIS spectrum contained therein consists of 22 channels covering the wavelength range between 1.16 and 2.37 µm at a resolution of approximately 20. Additionally, the orbital fit performed in Sect. 2.3 is partially based on the host star absolute astrometry as listed in the Hipparcos–Gaia Catalogue of Accelerations (HGCA; Brandt 2021).

# 2.2.2 VLTI/GRAVITY

We observed HIP 99770 b with the GRAVITY instrument on 31 May and 2 July 2023. These observations were obtained on technical time and in the framework of the Exo-GRAVITY Large programme (ESO ID 1104.C-0651 Lacour et al. 2020). An observation log for both epochs can be found in Table 2.1. Notably, they were taken using different

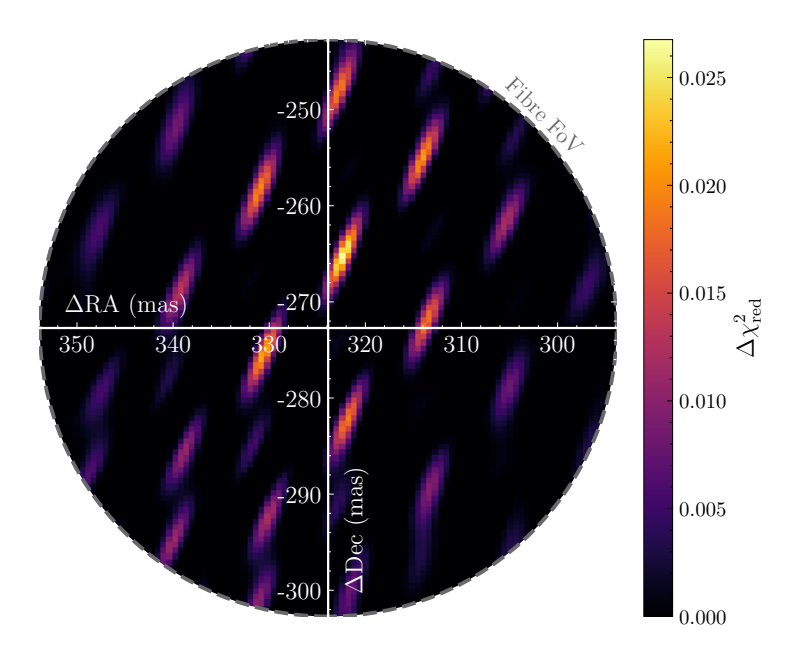


Figure 2.1: Detection of HIP 99770 b on 31 May 2023. The circular panel indicates the field of view of the GRAVITY science fibre. The map within visualises the  $\Delta\chi^2_{\rm red}$  over a two-dimensional grid of positions relative to the host star, which is located at the origin of the axes, and thus, outside the field of view. Each  $\Delta\chi^2_{\rm red}$  value is the difference between how well a model with and without a coherent point source of light at a given position ( $\Delta {\rm RA}, \Delta {\rm Dec}$ ) describes the interferometric observables. Thus, the strongest peak within the field of view corresponds to the position of the companion, while the secondary peaks (the so-called side lobes) are typical for interferometric observations and mostly depend on the u-v plane coverage.

observing modes. For the first epoch, we used the dual-field on-axis mode, while the second epoch was obtained in dual-field off-axis mode. Importantly, the latter mode enables a higher signal-to-noise ratio (S/N) because the entire light of the sources that is collected by the four unit telescopes is injected into the fringe tracker and science fibre channels by means of a rooftop mirror. This is not the case for on-axis observations, where a beam splitter directs only half the light into the different channels. A comprehensive comparison of the two observing modes is given by Nowak et al. (2024a). For both observations, the placement of the science fibre was informed by orbital fits applied to the available direct detections of the companion (see Sect. 2.2.1 and Table 2.2).

We used the ESO GRAVITY instrument pipeline 1.6.4b1 for the data reduction. This yielded the so-called "astroreduced" byproduct, from which the relative astrometry between host and companion can be extracted following the standard exoplanet dual-field data processing outlined in Appendix A of GRAVITY Collaboration et al. (2020). The first detection on 31 May 2023 is visualised in Fig. 2.1, the resulting relative astrometry epoch is listed in Table 2.2. Because the off-axis observation mode was employed for the second epoch, the collected data necessitated a special reduction procedure. To measure

the metrology zero point, we performed a swap observation of a calibration binary, which in this case was HD 196885 AB. The binary observation was based on a poor relative position prediction, and the pointing of the single-mode fibres was therefore off by approximately 35 mas. The field aberrations resulting from this pointing deviation (GRAVITY Collaboration et al. 2021) caused a bias in the zero-point estimate of up to 30 degrees. As a consequence, the astrometric measurement of the science target HIP 99770 b was uncertain, which caused us to discard this astrometric epoch from our orbital analysis.

For each epoch, we also obtained a K-band companion-to-host contrast spectrum ranging from 1.97 to 2.48  $\mu$ m at a resolution of R = 500. Depending on the angular distance between the astrometric position of the companion and the centre of the science fibre, we needed to correct the spectra for throughput losses. A detailed description of how this is accounted for is provided in Appendix A.1. To convert the companion contrast spectra measured by GRAVITY into companion flux spectra that could be used for the atmospheric analysis and modelling, we first multiplied them with the flux spectrum of the amplitude reference source, that is, the host star HIP 99770 A for the on-axis, and the binary (swap) calibrator HD 196885 AB for the off-axis epoch. To obtain model spectra of these targets, we fitted a BT-NextGen and a BT-Settl (CIFIST) solar metallicity stellar model atmosphere (Allard et al. 2012) to archival photometric data from Gaia and Tycho using the species toolkit (Stolker et al. 2020). Additionally, we included the Gaia XP spectrum of HIP 99770 A and HD 196885 AB in these fits. When we also incorporated 2MASS photometry, the inferred stellar model parameters did not change by more than  $1\sigma$ . Based on PyMultiNest (Feroz & Hobson 2008; Feroz et al. 2009; Buchner et al. 2014), the nested-sampling approach implemented within species enables the inference of the posterior distributions of the individual model parameters. Following Cardelli et al. (1989), we also accounted for extinction by the interstellar medium that might affect HIP 99770 A by setting the V-band extinction parameter,  $A_V$ , to 0.043 mag (Murphy & Paunzen 2017). To further guide the spectral fits to physically plausible solutions, we invoked Gaussian priors on the mass of HIP 99770 A of  $M=1.8\pm0.2~{\rm M}_{\odot}$  (Currie et al. 2023b) and on the effective temperatures and masses of the two binary components of HD 196885 AB using the values and uncertainties reported in Table 1 of Chauvin et al. (2023)  $(T_{\rm eff,A} = 6340 \pm 19 \, {\rm K},$  $T_{\rm eff,B} = 3660 \pm 190 \text{ K}, M_{\rm A} = 1.3 \pm 0.1 \text{ M}_{\odot}, M_{\rm B} = 0.45 \pm 0.01 \text{ M}_{\odot}).$  We converted the M1±1 spectral type constraint of component B that is reported in this table into an effective temperature constraint using Table 5 of Pecaut & Mamajek (2013). For more details on the conversion of contrast to flux, we refer to Appendix A.2. The mass and effective temperature values of HIP 99770 A inferred from our fit are within  $2\sigma$  of the value reported by Murphy & Paunzen (2017), those of HD 196885 AB are within  $3\sigma$  of the values reported by Chauvin et al. (2023).

The resulting on- and off-axis flux spectra normalised by the respective amplitude references are significantly offset relative to each other. Since the off-axis reference (swap) binary HD 196885 AB was observed with a significant mispointing of the fibre, a lower throughput is expected (estimated at  $\approx 45\%$  in Table 2.1). This biased our photometric calibration. The on-axis observations of HIP 99770 b, on the other hand, were calibrated quasi-simultaneously as a result of the continuous monitoring of the host star spectrum,

Target	Start	End	NEXP/NDIT/DIT(s)	Airmass	$ au_0$	Seeing	Fibre placement		$\gamma$
	(UTC)	(UTC)			(ms)	(arcsec)	$\Delta RA \text{ (mas)}$	$\Delta \mathrm{Dec}\ (\mathrm{mas})$	
31st May									
HIP 99770 A	09:19:59	09:25:04	2/96/0.5	2.19	8.2	0.62	0.0	0.0	100 %
${\rm HIP}$ 99770 b	09:27:53	09:39:12	2/32/10	2.25	7.2	0.63	323.87	-272.72	96.3%
2nd July 2023									
HIP 99770 b	07:05:36	07:32:34	3/12/30	2.22	2.9	0.55	323.6	-261.6	99.8 %
HD 196885 AB	07:43:03	07:56:17	4/32/3	1.31	2.4	0.91	285.0	430.0	44.8%

**Table 2.1:** GRAVITY observation log of the target HIP 99770 b and of the swap calibrator HD 196885 AB.

Notes. The reported start and end times indicate the duration of the full observation, consisting of a series of NEXP exposures, each subdivided into NDIT detector integrations per exposure, that were taken over a duration of DIT.  $\tau_0$  is the mean atmospheric coherence time during the observation, and the fibre placement columns display where the centre of the science fibre was located relative to the host star at the time of observation. The positions are given as on-sky Cartesian coordinates in separation relative to the host star along the right ascension axis,  $\Delta$ RA, and the declination axis,  $\Delta$ Dec. The last column lists the normalised coupling efficiency,  $\gamma$ , by which the respective contrast spectrum needs to be divided to correct for the throughput loss resulting from an imperfect alignment of the fibre centre and the companion (see Appendix A.1).

with GRAVITY science spectrometer observations interspersed between the planet observations. The on-axis spectrum is therefore more reliable, and we opted for scaling the off-axis companion flux spectrum such that it matched the on-axis spectrum best. The best-fitting scale factor was found to be 61%.

Finally, we combined the companion flux spectra for the two epochs into a single covariance-weighted mean spectrum that we used for the analysis presented in Sect. 2.4. The spectral reduction process is visualised in Fig. 2.2. This is the first time a GRAVITY exoplanet off-axis spectrum without an on-axis amplitude reference is published.

# 2.3 Orbital analysis

To obtain constraints on the companion mass and orbital parameters, we performed an orbit fit of the relative astrometry epochs presented in Table 2.2 using the orbitize! package (Blunt et al. 2020). Its MCMC sampling routine allowed us to include the absolute astrometry of the host star collected by the Hipparcos and Gaia missions (conveniently presented by Brandt 2021). The orbitize! sampling procedure is an implementation of ptemcee (Vousden et al. 2016), a parallel-tempered affine-invariant Markov chain Monte Carlo (MCMC) algorithm based on emcee (Foreman-Mackey et al. 2013). It was carried out using 20 temperatures and 100 walkers taking  $4 \times 10^4$  burn-in steps and another  $4 \times 10^4$  actual sampling steps each. These walkers were let loose on nine free parameters, namely the semi-major axis, a, the eccentricity, e, the inclination, i, the argument of periastron,  $\omega$ ,

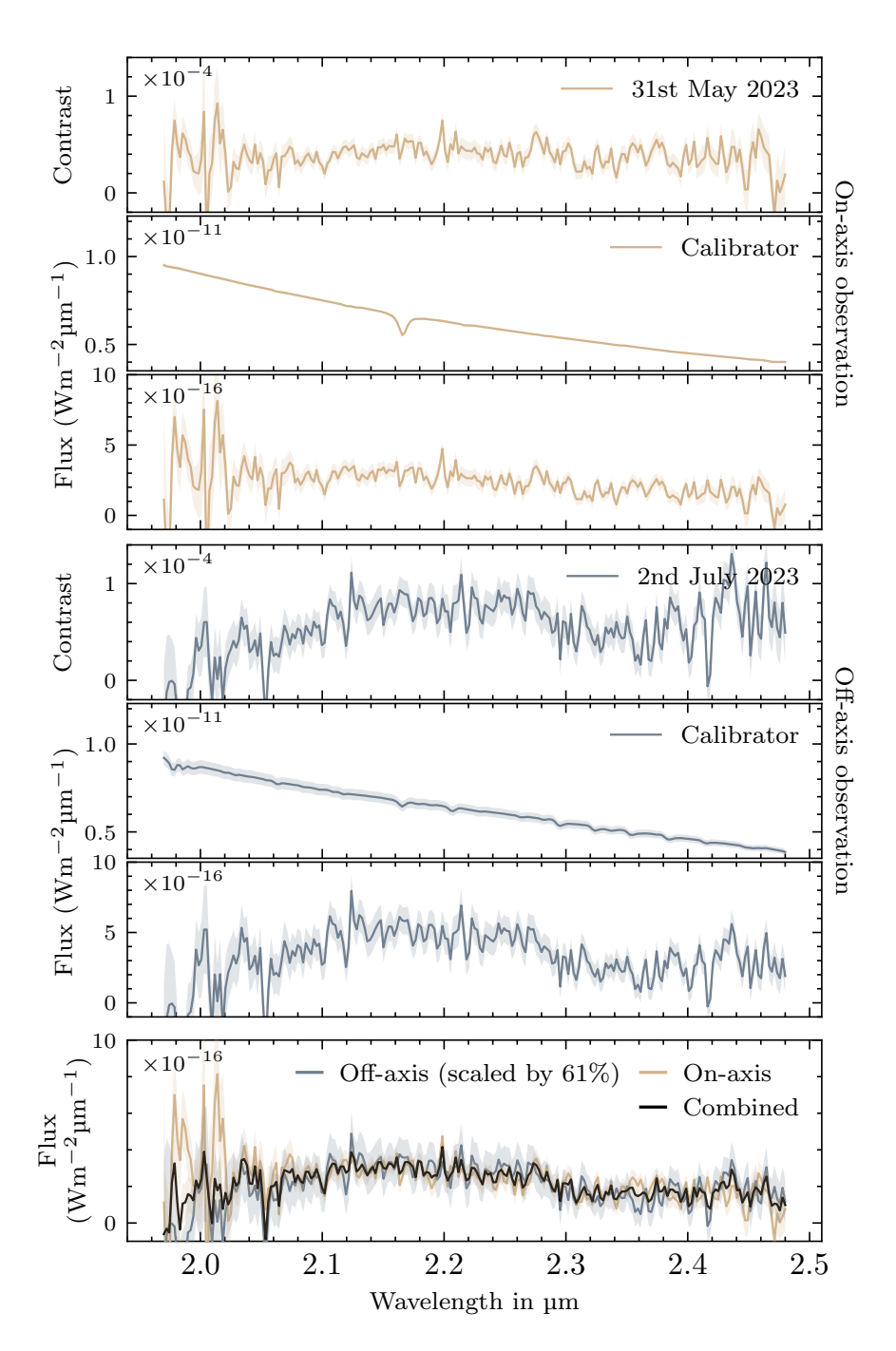


Figure 2.2: Ingredients and outcome of the spectral data reduction. The top three panels show the GRAVITY on-axis contrast spectrum, the associated stellar calibration flux spectrum, and the resulting companion flux spectrum. The same is visualised for the off-axis observation in the three middle panels. Finally, the bottom panel shows the on-and off-axis companion flux spectra alongside the combination of the two. This K-band spectrum of HIP 99770 b is used in Sect. 2.4.

MJD (days)	Instrument	$\Delta RA$ (mas)	$\Delta \mathrm{Dec}$ (mas)	ρ
59059	CHARIS	$(263 \pm 4)$	$(-367 \pm 5)$	
59093	CHARIS	$(263 \pm 5)$	$(-366 \pm 5)$	
59353	CHARIS	$(280 \pm 4)$	$(-343 \pm 4)$	
59368	NIRC2	$(286 \pm 6)$	$(-337 \pm 6)$	
59408	CHARIS	$(286 \pm 4)$	$(-338 \pm 4)$	_
59504	CHARIS	$(292 \pm 4)$	$(-327 \pm 4)$	
$60095.40$ $60127.31^*$	GRAVITY GRAVITY	$(322.27 \pm 0.10)$ $(322.21 \pm 0.36)$	$(-265.09 \pm 0.18)$ $(-260.66 \pm 0.49)$	-0.88 $-0.88$

Table 2.2: Astrometric detections of HIP 99770 b.

Notes. The astrometric position of the companion relative to the host star at each epoch is presented as separation components along the right ascension axis,  $\Delta RA$ , and the declination axis,  $\Delta Dec.$  The CHARIS and NIRC2 epochs were originally published by Currie et al. (2023b). For these, the time of observation is rounded to the nearest full day. The GRAVITY data we present also comprise a correlation coefficient,  $\rho$ , between  $\Delta RA$  and  $\Delta Dec.$ 

the longitude of the ascending node,  $\Omega$ , the relative epoch of periastron<sup>2</sup>,  $\tau$ , the parallax,  $\pi$ , the stellar mass,  $M_{\text{host}}$ , and the companion mass,  $M_{\text{comp}}$ . The priors we chose for the individual free parameters are listed in Table 2.3. We carried out two separate sampling runs. The first run was performed using the Hipparcos–Gaia stellar astrometry and the previous astrometric companion detections (Currie et al. 2023b) only. We then resampled the posterior distributions upon inclusion of our own GRAVITY detection from 31 May 2023. With the two resulting posterior samplings in hand we investigated how the addition of a GRAVITY detection changed the inferred parameter values and their uncertainties. By means of visual inspection of the chain traces for the individual parameters, we confirmed that the walker chains converged for all parameters and for both runs. The two posterior samplings of the orbital parameters are shown in Fig. 2.4. A random subset of the posterior sampling was used to visualise the projection of the companion orbit onto the sky plane in Fig. 2.3.

The bottom right panel of Fig. 2.4 shows that the resampling procedure resulted in a slightly increased companion mass of  $16.7^{+6.0}_{-4.8} \,\mathrm{M_{Jup}}^3$ .

To investigate the extent to which this result is driven by the uniform companion mass prior, we ran an additional sampling procedure using a log-uniform prior distribution instead. This yielded a lower posterior mass of  $13.5^{+5.2}_{-4.4} \,\mathrm{M_{Jup}}^3$ , a behaviour consistent with the findings by Currie et al. (2023b). Along the same lines, we examined the dependence

<sup>\*</sup> Since this astrometric epoch is corrupted, it was not used anywhere in this study.

<sup>&</sup>lt;sup>2</sup>Using the relative epoch of periastron,  $\tau$ , is a sleight of hand that simplifies setting the prior range boundaries. In combination with a reference epoch ( $t_{\rm ref} = 58\,849\,{\rm MJD}$ ) and the orbital period, P, it relates to the actual time of periastron passage,  $t_{\rm p}$ , via  $\tau = (t_{\rm p} - t_{\rm ref})/P$  and is thus a dimensionless quantity.

<sup>&</sup>lt;sup>3</sup>These values have not been rounded to their respective significant figures to facilitate better comparison.

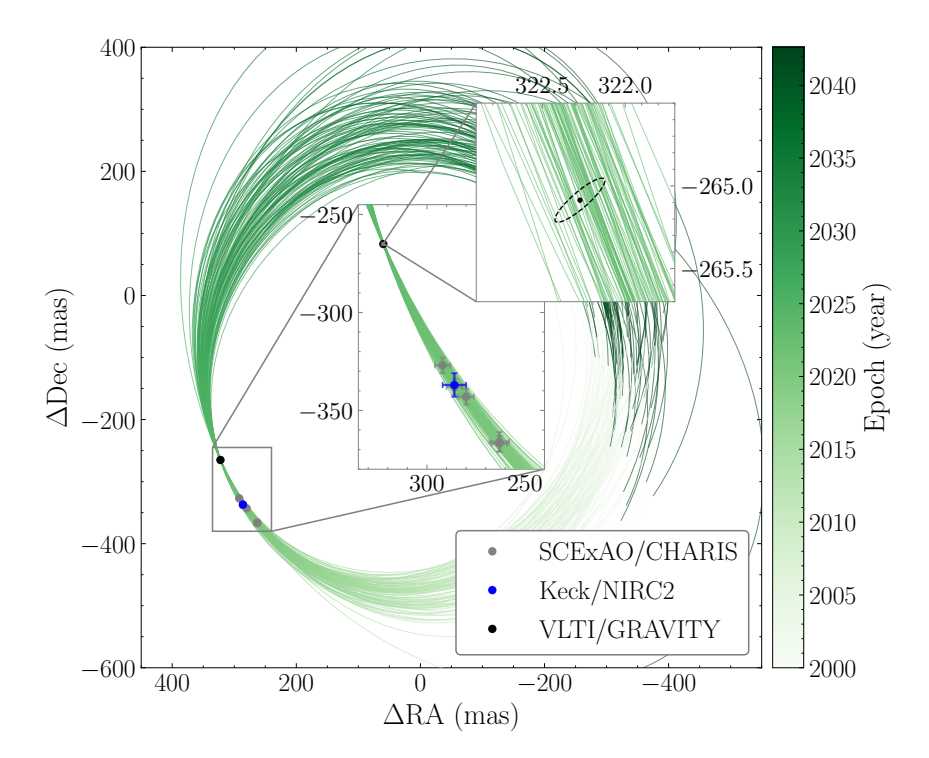


Figure 2.3: Orbit of HIP 99770 b relative to its host, i.e., fixed at the origin. The visualised orbits were generated from a random subset of 100 parameter sets drawn from the posterior sampling. While the previously available astrometric epochs obtained by SCExAO/CHARIS and Keck/NIRC2 are shown along with their respective uncertainties in  $\Delta$ RA and  $\Delta$ Dec, knowledge of the correlation coefficient,  $\rho$ , allowed us to visualise the VLTI/GRAVITY epoch as a 1  $\sigma$  confidence ellipse.

of the inferred companion mass on the stellar mass prior. Retaining the standard deviation of  $0.2\,\mathrm{M}_\odot$ , we performed further posterior samplings based on underlying Gaussian priors that were shifted from the original 1.8 to 1.7 in the first and  $1.9\,\mathrm{M}_\odot$  in the second run. These modifications resulted in a companion mass of  $14.7^{+5.0}_{-4.4}\,\mathrm{M}_\mathrm{Jup}^3$  (decrease of 12%) and  $16.8^{+5.7}_{-5.3}\,\mathrm{M}_\mathrm{Jup}^3$  (increase of 0.5%), respectively. A comparison between the resulting posterior mass distributions is shown in the top right panel of Fig. A.3. Since these adjustments to the shapes and positions of the priors affect larger posterior displacements than the inclusion of the GRAVITY astrometry epoch, the slight shift in companion mass evident in Fig. 2.4 does not necessarily amount to a robust inference of a higher dynamical mass.

The manifest inability to further constrain the companion mass comes as somewhat of a surprise given the high angular resolution of the new GRAVITY astrometry epoch. It is, however, not driven by the individual astrometric epochs or the amount thereof, but by the large relative uncertainty of the Gaia-Hipparcos PMa. Following Kervella et al. (2019a), we computed the PMa as the difference between the Gaia DR3 proper motion vector,  $\mu_{G3}$ , and the long-term Hipparcos-Gaia DR3 proper motion vector,  $\mu_{HG3}$ , which both consist

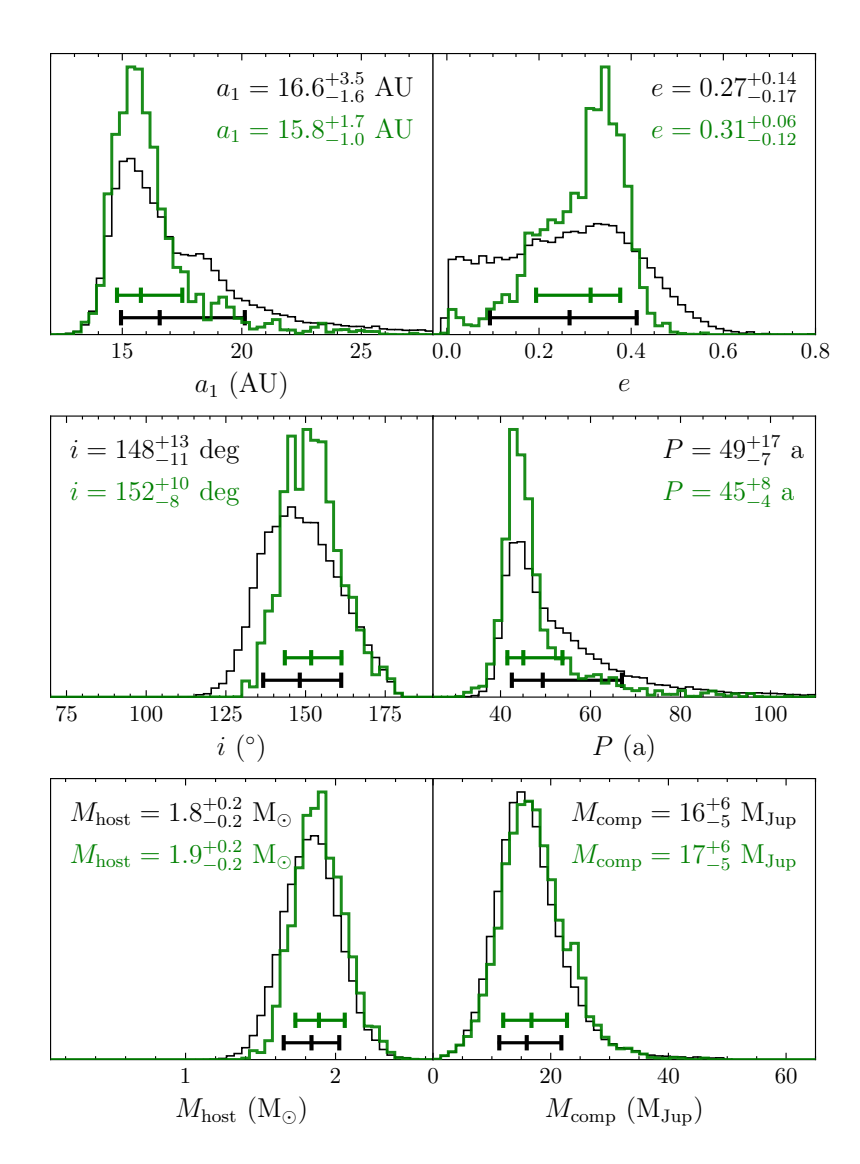


Figure 2.4: Marginalised posterior distributions of a subset of the fitted orbital parameters. The black posteriors were sampled considering the previously available data only, while the green posteriors result from the inclusion of the new GRAVITY epoch from 31 May 2023. The median values and intervals between the 16th and 84th percentiles of the distribution are indicated by the horizontal bars. The inferred values resulting from the two runs, which were rounded to the respective significant figure, are displayed at the top of each panel. While technically not one of the parameters explored by the walkers during the sampling procedure, we also plot the period, P, as computed from the other posteriors via Kepler's third law. The full posterior samplings can be found in Appendix A.3.

of a right ascension and declination component. Carrying the respective uncertainties, we found the PMa to be

$$(\vec{\mu}_{G3} - \vec{\mu}_{HG3}) = \begin{pmatrix} 68.09 \pm 0.12 \\ 69.40 \pm 0.14 \end{pmatrix} - \begin{pmatrix} 68.236 \pm 0.012 \\ 69.671 \pm 0.012 \end{pmatrix}$$
$$= \begin{pmatrix} 0.15 \pm 0.12 \\ 0.27 \pm 0.14 \end{pmatrix},$$

where all components are given in units mas/yr, and the proper motion values were taken from Brandt (2021). Thus, the relative uncertainties on the RA and Dec components are approximately 80 and 51%, respectively. This large PMa uncertainty dominates so thoroughly that even additional GRAVITY epochs in the future would not help constrain the companion mass further. Tighter error bars on the mass can therefore only be obtained once a more precise PMa will be available in *Gaia* DR4. To substantiate this finding, we performed several orbital resampling runs including varying numbers of mock GRAVITY epochs predicted from the current best fit. While these additional artificial epochs served to narrow down the posterior distributions of the remaining orbital parameters, they likewise fail to further constrain the companion mass. For instance, when we iteratively generated an additional three GRAVITY astrometric mock epochs based on the newly obtained orbit solution, we found an improvement of approximately 1% in relative uncertainty of the companion semi-major axis, but no such gain is achieved in the precision of its mass.

While the addition of the GRAVITY astrometry epoch yielded no improved constraints on the companion mass, it did pin down the orbital semi-major axis at  $15.8^{+1.7}_{-1.0}$  AU and the eccentricity at  $0.31^{+0.06}_{-0.12}$ . The strong constraint on the orbital eccentricity is a marked improvement on the previously available solution. While a circular orbit was conceivable prior to the GRAVITY detection (Currie et al. 2023b), this configuration is now decisively ruled out. HIP 99770 b therefore joins a growing number of substellar companions exhibiting elevated eccentricities. Examples of other recently detected eccentric companions are 51 Eri b (Macintosh et al. 2015) with  $e = 0.57^{+0.08}_{-0.06}$  (Dupuy et al. 2022) and Eps Ind A b (Feng et al. 2019) with  $e = 0.40^{+0.15}_{-0.18}$  (Matthews et al. 2024).

# 2.4 Spectral analysis

# 2.4.1 Spectral classification

We folded the GRAVITY K-band spectrum with the Paranal/SPHERE.IRDIS\_B\_Ks, IRDIS\_D\_K12\_1, and IRDIS\_D\_K12\_2 filter profiles to position HIP 99770 b in a colour-magnitude diagram (CMD) and thereby place it in the context of a literature population of companion and free-floating brown dwarfs and exoplanets. This folding procedure yielded absolute companion magnitudes of  $M_{\rm Ks} = ((12.460 \pm 0.014))$  mag,  $M_{\rm K2} = ((12.34 \pm 0.02))$  mag, and  $M_{\rm K1} = ((12.56 \pm 0.02))$  mag. The resulting CMD is shown in Fig. 2.5 and indicates that HIP 99770 b is compatible with a late L- to early T-type object. We also folded the GRAVITY spectrum with the MKO/NSFCam.Ks filter profile and

Parameter	Prior type and range	Posterior
Semi-major axis (AU)	Log uniform $[10^{-5}, 10^3]$	$15.8^{+1.7}_{-1.0}$
Eccentricity	Uniform $[0, 1)$	$0.31^{+0.06}_{-0.12}$
Inclination (deg)	Sine $[0, \pi)$	$152^{+10}_{-8}$
Argument of periastron (deg)	Uniform $[0, 2\pi)$	$210^{+90}_{-50}$
Long. of ascending node (deg)	Uniform $[0, 2\pi)$	$190^{+120}_{-30}$
Relative epoch of periastron $^2$	Uniform $[0, 1)$	$0.36^{+0.06}_{-0.06}$
Parallax (mas)	Gaussian $(24.55 \pm 0.09)^*$	$24.56^{+0.08}_{-0.08}$
Stellar mass $(M_{\odot})$	Gaussian $(1.8 \pm 0.2)^{\dagger}$	$1.9_{-0.2}^{+0.2}$
Companion mass $(M_{Jup})$	Uniform $[1, 50]$	$17^{+6}_{-5}$

**Table 2.3:** Orbital parameter priors and posteriors.

**Notes.** For the log uniform and uniform distributions, the square and rounded brackets denote inclusive and exclusive boundaries, respectively. The reported values were rounded to their significant figures. They correspond to the marginalised posterior distribution median and its differences to the 84th and 16th percentiles in superscript and subscript, respectively (see Fig. 2.4 and Appendix A.3 for the marginalised posteriors).

References. \* Gaia Collaboration et al. (2023b) † Currie et al. (2023b)

obtained an absolute magnitude of  $(12.544 \pm 0.013)$ , which lies within the 68 % confidence interval of the discovery paper measurement of  $(12.61 \pm 0.09)$  (Currie et al. 2023b).

To achieve a more quantitative classification, we used the empirical spectral type fitting routine implemented in species. Based on minimising the goodness-of-fit statistic,  $G_k$ (Cushing et al. 2008), this procedure compares the spectrum of a given object to nearinfrared reference spectra of low-mass stars, brown dwarfs, and exoplanets within the SpeX Prism Library. We first performed this fit on the composite spectrum, consisting of the GRAVITY and CHARIS spectra. The latter was obtained with the original discovery of the companion (Currie et al. 2023b). To ensure that the two spectra were consistent with one another, we computed a GRAVITY scaling factor using the CHARIS spectrum as a calibration baseline. Rebinning the GRAVITY spectrum onto the CHARIS wavelength solution using SpectRes (Carnall 2017) allowed us to directly compare the two spectra in the wavelength region in which they overlap (2.00 to 2.37 µm). We applied a simple scaling factor,  $\alpha$ , to the GRAVITY spectrum and subsequently compared it to the CHARIS spectrum by minimising a mutual chi-squared metric. This suggested a scaling factor of  $\alpha = 0.86$  to facilitate the best agreement. Fig. 2.6 shows that for the composite CHARIS and GRAVITY spectrum, the  $G_k$ -minimum is reached at a spectral type of L8. To explore the effect of only having access to a narrower wavelength coverage, we performed another spectral classification run that only considered the higher-resolution GRAVITY spectrum. In addition to preferring the earlier spectral type of L6, the GRAVITY K-band spectrum by itself proved less capable of excluding other, especially earlier spectral types. Whereas

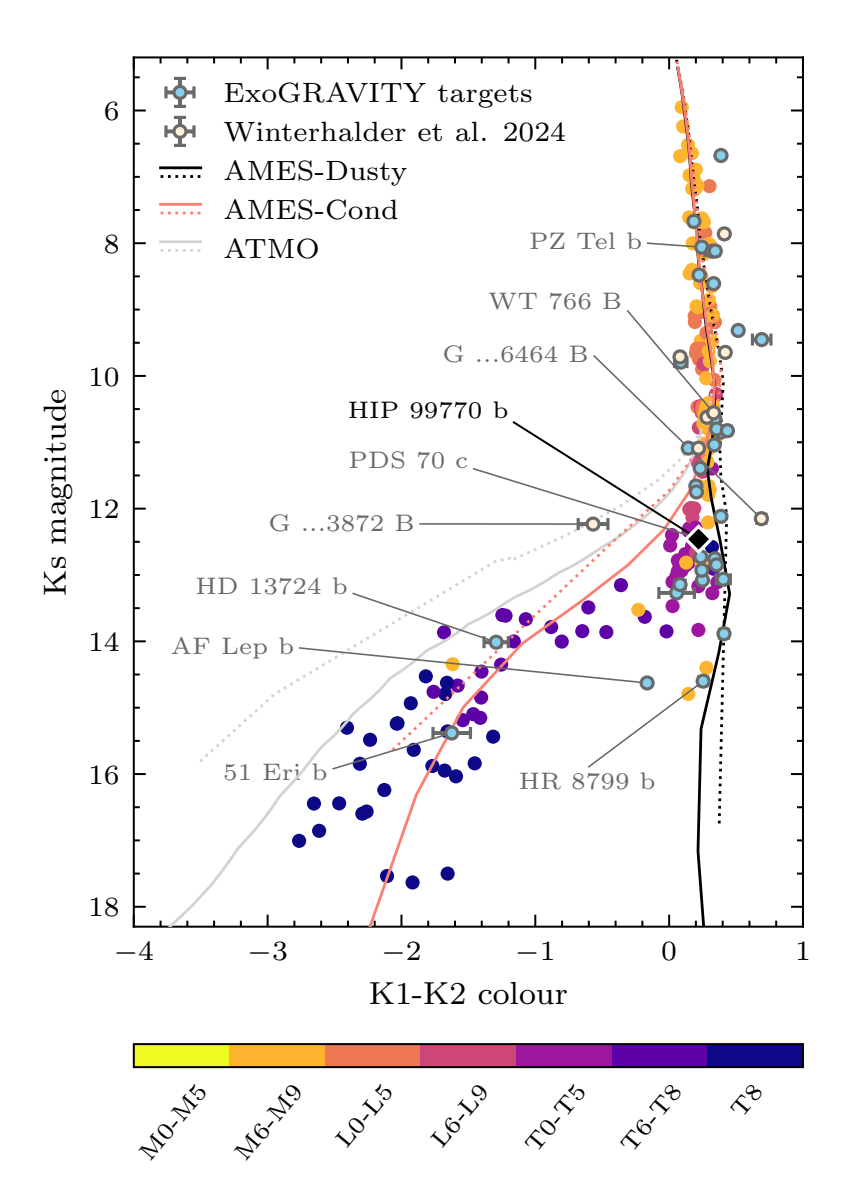


Figure 2.5: Colour-magnitude diagram showing HIP 99770 b, indicated by the black diamond, in relation to a literature population of low-mass stars, brown dwarfs, and exoplanets (see Appendix C of Bonnefoy et al. 2018 and references therein). All ExoGRAVITY targets (ESO ID 1104.C-0651; Lacour et al. 2020) and the companions so far detected via the Gaia-GRAVITY synergy (Winterhalder et al. 2024) are shown in light blue and ochre, respectively. Additionally, isochrones computed using the AMES-Dusty (Chabrier et al. 2000; Allard et al. 2001), AMES-Cond (Allard et al. 2001; Baraffe et al. 2003), and ATMO (Phillips et al. 2020) evolutionary models are shown for two ages: 1 Gyr (solid lines), and 100 Myr (dotted lines). The filters we used to extract these magnitudes and colours from the spectra are Paranal/SPHERE.IRDIS B Ks, IRDIS D K12 1, and IRDIS D K12 2.

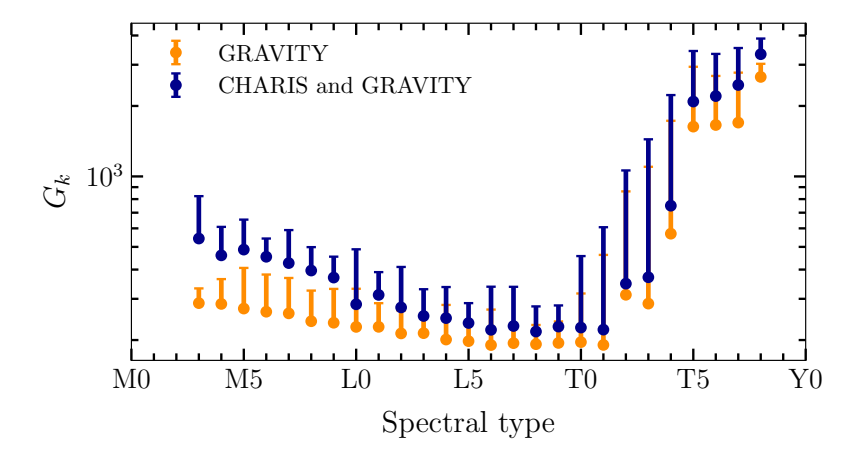


Figure 2.6: Goodness-of-fit statistic,  $G_k$ , (Cushing et al. 2008) as a function of spectral type when comparing the CHARIS and GRAVITY spectra together and the GRAVITY spectrum alone to empirical spectra. The minimum  $G_k$  value in each spectral type bin is indicated by the coloured circles, the error bars display the full  $G_k$  range resulting from all empirical spectra within the respective bin.

in the GRAVITY-only run, these types showed an only minimally higher and thus only marginally less appropriate goodness-of-fit statistic than the L8 bin, they were significantly disfavoured in the composite CHARIS and GRAVITY run. As a consistency check, we repeated the spectral classification using the SpeX Prism Library Analysis Toolkit (SPLAT; Burgasser & Splat Development Team 2017), which likewise yielded L8 for CHARIS and GRAVITY data and L6 for the GRAVITY spectrum alone.

# 2.4.2 Constraining the system age

In Sect. 2.4.1, the companion was shown to correspond to a late L- to early T-type, which implies a cloudy atmosphere. This circumstance needs to be accounted for when selecting an appropriate evolutionary model. As is evident from Fig. 2.5, based on their physics and cloud prescriptions, the models can vary in their applicability to different objects. While the AMES-Cond (Allard et al. 2001; Baraffe et al. 2003) and ATMO (Phillips et al. 2020) models appear to be poorly suited to describing objects just above the L-T transition, the AMES-Dusty model (Chabrier et al. 2000; Allard et al. 2001) captures the position of HIP 99770 b on the CMD reasonably well. It is thus a suitable model for constraining the system age. To this end, we used the companion Ks-band filter magnitude of ((12.460  $\pm$  0.014)) mag obtained by folding the GRAVITY K-band spectrum with the IRDIS\_B\_Ks filter profile. This approach clearly yielded an unrealistically precise magnitude since merely propagating the errors on the flux measurements in each wavelength channel did not take the calibration offset into account that was determined relative to the CHARIS spectrum in Sect. 2.4.1. Based on the scaling factor  $\alpha = 0.86$ , we adopted a systematic error of 14% which (at an IRDIS\_B\_Ks filter magnitude of 12.46 mag) translates into an error of 0.15 mag.

Figure 2.7 places this filter magnitude in context with a set of AMES-Dusty grid isochrones in the vicinity of the dynamical mass of the companion. For any given mass-magnitude pair, we can compute the corresponding age as implied by the model by minimising a loss function that compares the measured magnitude to a given AMES-Dusty isochrone magnitude at the mass in question. By thus finding the isochrone that best describes the mass-magnitude pair, we obtained the best-fitting age. We applied this bootstrapping procedure to  $10^6$  mass-magnitude pairs drawn from the dynamical mass posterior distribution and a Gaussian IRDIS\_B\_Ks distribution,  $\mathcal{N}(12.46\,\mathrm{mag}, 0.15\,\mathrm{mag})$ , which takes the dominant systematic calibration error into account. This yielded the age distribution visualised in the small panel in the bottom right corner of Fig. 2.7.

The bimodal nature of the age distribution is a direct consequence of the circumstance that HIP 99770 b occupies a region in the mass-magnitude plane in which deuterium can affect the cooling of the companion as it ages. The mass-dependent position of the deuterium-burning shoulder in the cooling (luminosity) curves at constant mass as a function of time (e.g. Burrows et al. 2001; Saumon & Marley 2008; see a similar feature in Hinkley et al. 2023) causes a ripple, or a peak<sup>4</sup>, in the isochrones that is clearly visible in Fig. 2.7.

Computation of the median and 68% confidence intervals of both modes yielded the two possible age scenarios of  $a_{\rm y}=28^{+15}_{-14}\,{\rm Myr}$  and  $a_{\rm o}=119^{+37}_{-10}\,{\rm Myr}$ , where y and o denote younger and older, respectively. The older scenario is strongly preferred in terms of its statistical power. There is also a non-zero probability that the companion occupies a position between the two modes in close proximity to the deuterium shoulder (see also Fig. 8 of Burrows et al. 2001). Using ATMO (Phillips et al. 2020) as the underlying evolutionary model to convert the companion K-band magnitude and dynamical mass into an age, we found similar results. The two modes are located at  $a_{\rm y}^{\rm ATMO}=23^{+20}_{-11}\,{\rm Myr}$  and  $a_{\rm o}^{\rm ATMO}=96^{+36}_{-13}\,{\rm Myr}$ . Currie et al. (2023b) placed the age of this system between 40 and 400 Myr, but emphasised that a self-consistent treatment similar to what we outlined above suggests an age between 115 and 200 Myr, which broadly agrees with our older scenario. More precise knowledge of the companion mass would disambiguate between the two modes of our age distribution. Thus, the main hindrance preventing a firmer age constraint is again the looseness of the dynamical mass constraint.

The above analysis and age constraint hinges on the validity of the evolutionary model for HIP 99770 b. Several aspects warrant caution. Firstly, instances in which evolutionary models deviate from the observed characteristics of exoplanets are well documented, an example being the tensions exhibited by older substellar companions with constrained dynamical masses (e.g. Dupuy et al. 2009; Kuzuhara et al. 2022; Franson et al. 2023a). Secondly, and perhaps more importantly for HIP 99770 b, for young objects, an uncertainty persists as to whether the onset of companion formation is simultaneous or delayed relative to the disc and host formation (e.g. Franson et al. 2023b; Zhang et al. 2023; Balmer et al.

<sup>&</sup>lt;sup>4</sup>Not to be confused with a deuterium flash, which is a sudden rise, on a logarithmic scale, in the luminosity of an object that begins to burn deuterium only late (e.g. Bodenheimer et al. 2013; Marleau & Cumming 2014).

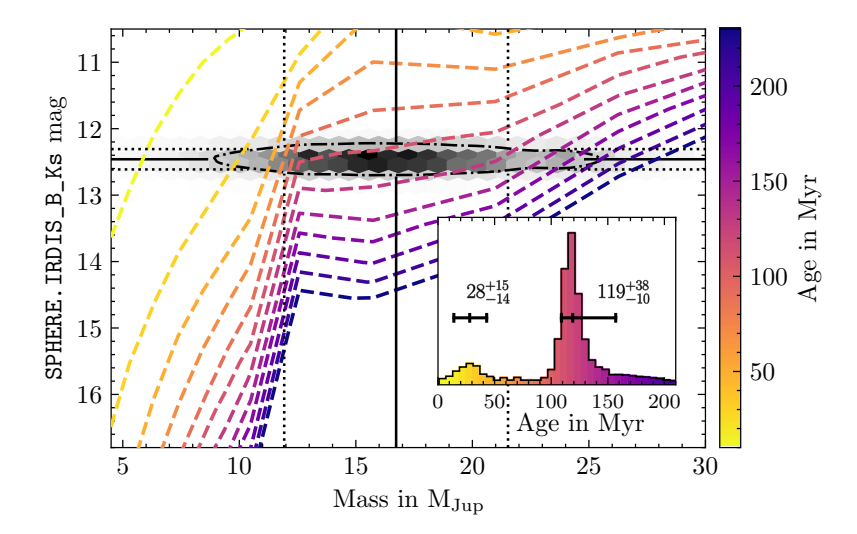


Figure 2.7: Isochrones from the AMES-Dusty model grid (Chabrier et al. 2000; Allard et al. 2001) in the mass-magnitude plane. The colours indicate the respective age. The solid black lines show the dynamical mass of the companion and the IRDIS\_B\_Ks filter magnitude, the dotted lines delineate the 16th and 84th percentiles. For the filter magnitude, we adopted a conservative systematic error (see text). The grey colour map in the background visualises the two-dimensional distribution of randomly drawn masses and magnitudes from their respective distributions. The dash-dotted line encircles 68% of all draws. The shoulder in the isochrones in this particular region of the mass-magnitude plane is caused by the onset of deuterium burning and the mass dependence of its time evolution. The panel in the bottom right corner shows the companion age posterior obtained by bootstrapping the drawn mass and magnitude pairs onto the age manifold as defined by the isochrones.

2025). Because especially at young ages, evolutionary models imply strong gradients in the bulk parameters of companions as a function of time, erroneous assumptions regarding the onset of companion formation can result in flawed inferences.

# 2.4.3 Atmospheric forward modelling

Using species, we performed a suite of atmospheric grid-model fits to the entirety of the spectral and photometric data available for HIP 99770 b. As was the case for the orbit sampling procedure in Sect. 2.3, every sampling run described below was performed with an underlying Gaussian parallax prior,  $\mathcal{N}(24.55\,\mathrm{mas},0.09\,\mathrm{mas})$ , which corresponds to the host parallax angle as listed in Gaia DR3 (Gaia Collaboration et al. 2023b). In all fitting procedures, each wavelength channel across both spectra was weighted equally. Additionally, we accounted for correlations between the GRAVITY wavelength channels using the covariance matrix provided by the data reduction pipeline. According to Currie et al. (2023b), the covariance matrix associated with the CHARIS spectrum is dominated by

spatially and spectrally uncorrelated noise, which likely renders its inclusion insignificant. Similar to the approach outlined in Sect. 2.4.1, we included an additional factor,  $\alpha$ , as a free parameter to allow for a relative flux calibration between the CHARIS and GRAVITY spectra.

Cloudless models such as Sonora Bobcat (Marley et al. 2021) or Saumon & Marley Clear (2008) (Saumon & Marley 2008) did not result in adequate fits. Instead, these models tended to overestimate the spectral energy distribution below 1.9 µm. This was especially the case for the two prominent broad-band spectral features surrounding the water absorption signature at 1.4 µm. The muted nature of these features suggests a cloudy atmosphere. We therefore proceeded to fit the spectral energy distribution using a set of cloudy models. The full corner plots showing the posteriors resulting from sampling linearly interpolated grids of the DRIFT-PHOENIX (Woitke & Helling 2003; Helling & Woitke 2006; Helling et al. 2008), BT-Settl (Allard et al. 2012), Sonora Diamonback (Morley et al. 2024), and Saumon & Marley Cloudy (2008) (Saumon & Marley 2008) models using 1000 live points can be found in Appendix A.4. As compared to the dynamical mass obtained from the refined orbital solution in Sect. 2.3, the BT-Settl and Sonora Diamonback models performed poorly in that they inferred significantly lower masses. This is a cause for concern. We therefore conducted an additional posterior sampling run, this time employing a Gaussian companion mass prior,  $\mathcal{N}(17\,\mathrm{M_{Jup}}, 6\,\mathrm{M_{Jup}})$ , that reflects the dynamical mass constraint obtained in Sect. 2.3. The posteriors resulting from this informative mass prior are shown alongside the initial non-informative, that is, uniform, mass prior run in Appendix A.4. For the problematic models, the inclusion of the informative mass prior was evidently not effective in forcing the walkers to sample a solution within the dynamical mass constraint. Both the Sonora Diamondback and the BT-Settl posterior samplings showed little to no reaction to the application of the informative prior. We conclude that the dynamical mass constraint is too loose to effect a strong and physically accurate pull on the posteriors. Subsequent tests with artificially reduced dynamical mass uncertainties, and thus, stronger, more informative mass priors indeed resulted in the desired forcing confirming that the low current precision of the prior is the cause for its futility. The DRIFT-PHOENIX and Saumon & Marley Cloudy (2008) models, on the other hand, yielded reasonable posterior masses in both the non-informative and informative companion mass prior cases. To assess the performance of the different models and the inferred results on the basis of a consistent set of priors, we only consider the informative mass prior sampling runs hereafter. Figure 2.8 shows the spectra associated with the most likely parameter sets for each of the chosen models. The median posterior parameter values and  $68\,\%$  confidence intervals are presented in Table 2.4. The reduced chi-squared values,  $\chi^2_{\rm red}$ , of these best-fitting parameter sets also to be found in Table 2.4 are acceptable for all models. This quantitatively confirms the qualitative impression that the models manage to capture the overall shape of the spectral energy distribution in Fig. 2.8. However, the model posteriors in Table 2.4 and Appendix A.4 reveal that the inferred parameter values can differ significantly between the individual models.

The median effective temperatures of the companion are spread across a range spanning from approximately 1300 to 1770 K with the Sonora Diamondback and DRIFT-PHOENIX

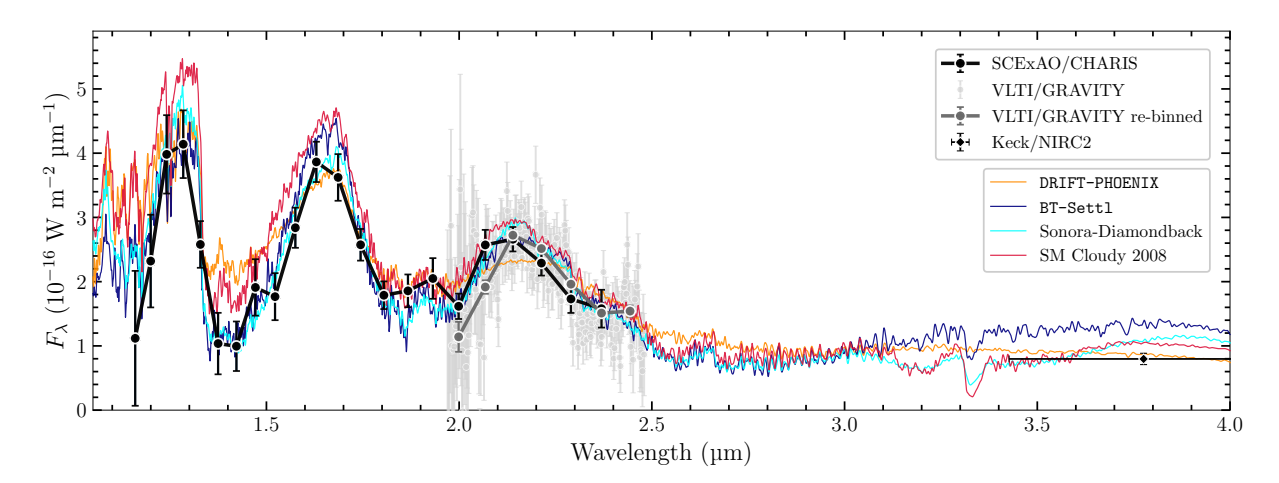


Figure 2.8: Spectral energy distribution of HIP 99770 b. The black points encircled by a white border and connected by a black line show the CHARIS spectrum taken from Currie et al. (2023b). The light grey points depict the combination of the on- and off-axis GRAV-ITY spectra. For visualisation purposes, a rebinned lower resolution GRAVITY spectrum is shown in dark grey encircled by a white border and connected by a dark grey line. Additionally, the mid-infrared photometry data point in the NIRC2.Lp filter is shown as a black diamond encircled by a white border (Currie et al. 2023b). The associated horizontal error bar indicates the FWHM of the filter transmission profile. The spectra resulting from the most likely parameter sets determined by the posterior sampling processes are shown for four different atmospheric forward models. SM Cloudy 2008 denotes the cloudy ( $f_{\rm sed} = 2$ ) Saumon & Marley (2008) model.

models yielding the lowest and highest temperatures, respectively. The surface gravity also varies significantly, with the Sonora Diamondback chain converging on the edge of the prior range at  $\log(q) = 3.6$ , while DRIFT-PHOENIX places it at approximately 5.0. While BT-Settl and Sonora Diamondback agree on a radius of approximately  $1\,R_{Jup}$ , Saumon Marley and DRIFT-PHOENIX converge on 1.5 and  $0.6\,R_{\mathrm{Jup}},$  respectively. The flux scaling factor,  $\alpha$ , which is required to reconcile the GRAVITY with the CHARIS spectrum and was derived in Sect. 2.4.2, is recovered to within  $2\sigma$  by all fits. Finally, sampling the companion atmosphere metallicity is only supported by the DRIFT-PHOENIX and Sonora Diamondback models. With an inferred metallicity of  $[Fe/H] = 0.25^{+0.03}_{-0.06}$ , the chain converges close to the edge of the DRIFT-PHOENIX grid at 0.3. The value agrees well with the somewhat looser  $[Fe/H] = 0.27^{+0.12}_{-0.12}$  obtained using the Sonora Diamondback model, however, which is defined over a wider grid that extends to 0.5. Furthermore, they are both consistent with the metallicity measurement of  $[M/H] = 0.26^{+0.24}_{-0.23}$  reported by Zhang et al. (2024). An extension of the spectral coverage into the mid-infrared, for instance by means of JWST observations, is likely to further constrain the posteriors, and would thus enable a tighter hold on the companion metallicity and elemental abundance ratios (e.g. see Miles et al. 2023).

Following the analysis presented by Nasedkin et al. (2024) and Balmer et al. (2025),

Model	$\chi^2_{\rm red}$	$T_{\rm eff}$ (K)	$\log(g)$	$R (R_{Jup})$	$M  (\mathrm{M_{Jup}})$	[Fe/H]
DRIFT-PHOENIX	2.06	$1772^{+11}_{-11}$	$5.03^{+0.08}_{-0.06}$	$0.587^{+0.011}_{-0.009}$	$15^{+3}_{-2}$	$0.25^{+0.03}_{-0.06}$
BT-Settl	1.25	$1380^{+20}_{-20}$	$3.95^{+0.02}_{-0.02}$	$0.99^{+0.04}_{-0.03}$	$3.5^{+0.2}_{-0.2}$	-
Sonora-Diamondback	1.06	$1300^{+20}_{-20}$	$3.62^{+0.15}_{-0.08}$	$1.05^{+0.04}_{-0.04}$	$1.8^{+0.7}_{-0.3}$	$0.27^{+0.12}_{-0.12}$
SM Cloudy $2008^*$	2.08	$1539_{-27}^{+17}$	$4.16^{+0.07}_{-0.06}$	$1.5_{-0.3}^{+0.3}$	$13^{+4}_{-4}$	-

Table 2.4: Atmospheric forward modelling posteriors.

**Notes.** The values were rounded to their significant figure. They correspond to the median of the marginalised posterior distribution and its differences to the 84th and 16th percentiles in superscript and subscript, respectively. These results stem from the sampling runs employing an informative underlying companion mass prior (see corner plots in Appendix A.4 for uninformative mass prior posteriors).

we can contextualise this result with other planetary metallicity measurements. To this end, we converted the metallicity relative to the solar value into a metallicity ratio of the companion and the host. There are different metallicity constraints for HIP 99770 in the literature: Paunzen et al. (1999) placed it at  $[Fe/H]_{host} = ((-1.3 \pm 0.2))$ , Paunzen et al. (2002) estimated ( $(-1.46 \pm 0.08)$ ), while Villaume et al. (2017) inferred -0.8 (no uncertainty reported). These estimates, however, might be superficial since HIP 99770 has been classified as a chemically peculiar  $\lambda$  Boo star (Murphy & Paunzen 2017). Despite the apparent metal depletion suggested by their iron underabundances, these stars are in fact expected to possess bulk solar abundances (e.g. Murphy et al. 2020). Since the companion metallicity inferred using DRIFT-PHOENIX ( $[Fe/H]_{comp} = 0.25^{+0.03}_{-0.06}$ ) is based on a chain that converged towards the edge of the defined grid range, we only considered the estimate obtained using the Sonora Diamondback model  $(0.27^{+0.12}_{-0.12})$ . This yielded a metallicity ratio of companion and host of  $1.9^{+0.6}_{-0.4}$ , which would be consistent with the mass-metallicity relation derived by Thorngren et al. (2016). How these results compare to other companions with measured metallicity ratios as well as the aforementioned empirical relation is visualised in Fig. 2.9.

The main caveat for assessing the derived metallicity ratios is their dependence on the loosely constrained stellar metallicity. To illustrate, if we had instead used a host metallicity of  $[Fe/H]_{host} = ((-1.46 \pm 0.08))$ , as suggested by Paunzen et al. (2002), the metallicity ratio would have amounted to  $50^{+30}_{-20}$ , which would indicate strong metal enrichment in the companion. This conclusion might be interpreted in terms of the sequence of formation phases that have led to the current state of the companion. Indeed, the high metallicity of many giant planets as compared to their host stars suggests that they have accreted a significant amount of solid material after their initial formation process, a mechanism referred to as late accretion (e.g. Mousis et al. 2009; Franson et al. 2023b; Zhang et al. 2023; Balmer et al. 2025).

 $f_{\text{sed}} = 2 \text{ model of Saumon & Marley (2008)}.$ 

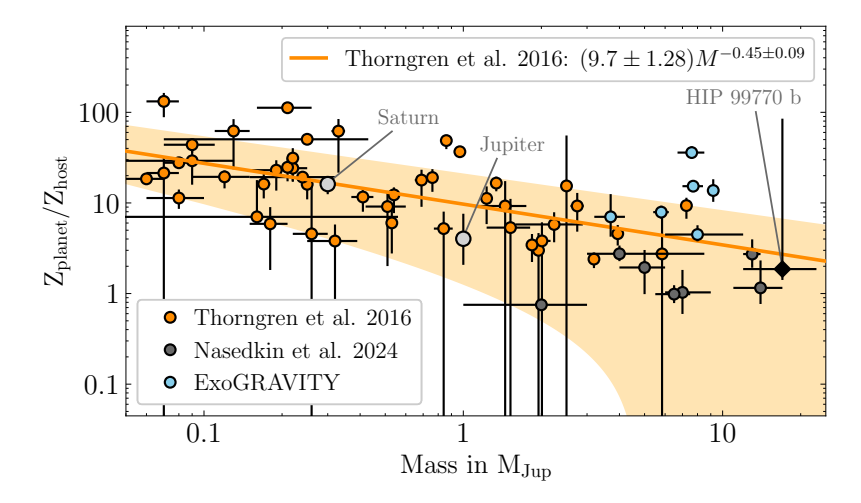


Figure 2.9: Mass-metallicity plane populated with companions from different samples, adapted from Thorngren et al. (2016), Nasedkin et al. (2024) and Balmer et al. (2024). The orange points show transiting giant exoplanets from Thorngren et al. (2016). The grey points illustrate a set of directly detected planets, and the blue points show a subset that was observed using VLTI/GRAVITY. Both samples were compiled by Nasedkin et al. (2024) and references therein. For context, Jupiter and Saturn are included with the metallicity measurements taken from Guillot (1999). The orange line and confidence interval trace the empirical relation between mass and metallicity for giant exoplanets presented by Thorngren et al. (2016). The black diamond indicates the ratio derived for HIP 99770 b when assuming a solar metallicity for the host. We took the higher metallicity ratios obtained from the host metallicity estimates by Paunzen et al. (1999, 2002), and Villaume et al. (2017) into account by presenting the data point with an inflated error bar that reflects a skewed systematic error encompassing the 68% confidence interval of the highest encountered ratio.

# 2.4.4 Comparing evolutionary and atmospheric modelling

To assess whether the bulk parameter values inferred using atmospheric models to fit the spectral energy distribution as discussed in Sect. 2.4.3 are physically plausible, we compared them to the values implied by self-consistent evolutionary models. To this end, the relations between the companion effective temperature,  $T_{\rm eff}$ , and its radius, R, as well as between its effective temperature and surface gravity,  $\log(g)$ , at constant ages (isochrones) and constant masses (evolutionary tracks) as suggested by the AMES-Dusty model are plotted alongside the respective values resulting from sampling the different atmospheric model grids in Fig. 2.10. We also highlight the  $T_{\rm eff}$ -R and  $T_{\rm eff}$ - $\log(g)$  regions consistent with the AMES-Dusty model at the dynamical mass and age of HIP 99770 b (via its Ks-band magnitude, as explained in Sect. 2.4.2).

Comparison of these self-consistently inferred parameter regions with the values from the atmospheric modelling implies a poor agreement between the two independent methods. Notably, the DRIFT-PHOENIX results are farthest removed from those of AMES-Dusty in both cases. Fig. 2.10 reveals that the DRIFT-PHOENIX radius of approximately  $0.6\,R_{\mathrm{Jup}}$  is unrealistic at the ages suggested by both the older and the younger scenario outlined in Sect. 2.4.2. Similarly, the surface gravity inferred by DRIFT-PHOENIX would necessitate a far more massive body, which we know to be impossible from the orbital analysis in Sect. 2.3. The effective temperature is reasonably well recovered by the three remaining atmospheric models. However, the radius and surface gravity values from the atmospheric models both show a significant degree of scatter around the feasible parameter regions implied by AMES-Dusty. Seeing that it overlaps with the AMES-Dusty model in both panels, of the three, the Saumon & Marley Cloudy (2008) model performs best, while BT-Sett1 and Sonora-Diamondback underestimate both radius and surface gravity. Thus, even in cases where the dynamical mass is only loosely constrained around the deuterium-burning threshold, the radius, surface gravity, and effective temperature of the companion as derived from self-consistent evolutionary models still exhibit less scatter than the scatter that is encountered between different atmospheric models.

Going forward, the CHARIS, GRAVITY and NIRC2 observations at hand constitute a suitable data set for testing and gauging atmospheric models in comparison to self-consistent evolutionary models.

# 2.5 Conclusions

Here, we have presented an updated study of the directly imaged super-Jupiter HIP 99770 b on the basis of two new data sets obtained by the near-infrared interferometric instrument VLTI/GRAVITY. These additional observations added a highly precise astrometric epoch of the companion position relative to its host and extended the temporal coverage available for the system. In addition to confirming the results reported by Currie et al. (2023b), the combination of these gains also served to further constrain the orbital solution of the companion. Due to the large relative uncertainty of the host PMa, the resulting companion dynamical mass constraint is still comparatively loose at  $17^{+6}_{-5}\,\mathrm{M_{Jup}}$ . We showed that this situation cannot be remedied by the addition of further relative astrometric epochs. Thus, when its relative uncertainty is large, the dominant nature of the PMa in the orbital sampling procedure prevents further constraints on the dynamical mass of the companion. The only viable method of gaining a firmer grasp on it in the foreseeable future is to exploit the time-series astrometry to be published in Gaia DR4.

While it was unable to strongly constrain the companion mass, the orbital resampling resulted in a significant detection of a non-vanishing eccentricity at  $0.31^{+0.06}_{-0.12}$ . Although this moderately elevated eccentricity was conceivable even before inclusion of the GRAVITY epoch, the CHARIS and NIRC2 epochs by themselves were also consistent with a low or even vanishing orbital eccentricity, which is now positively ruled out. Instead, HIP 99770 b appears more eccentric than most directly imaged exoplanets.

Comparing the GRAVITY K-band magnitude and dynamical mass of the companion to an evolutionary model, we found them to be consistent with two scenarios. The first implies a planetary mass object at an age of  $28^{+15}_{-14}$  Myr, the second suggests a more massive

2.5 Conclusions 61

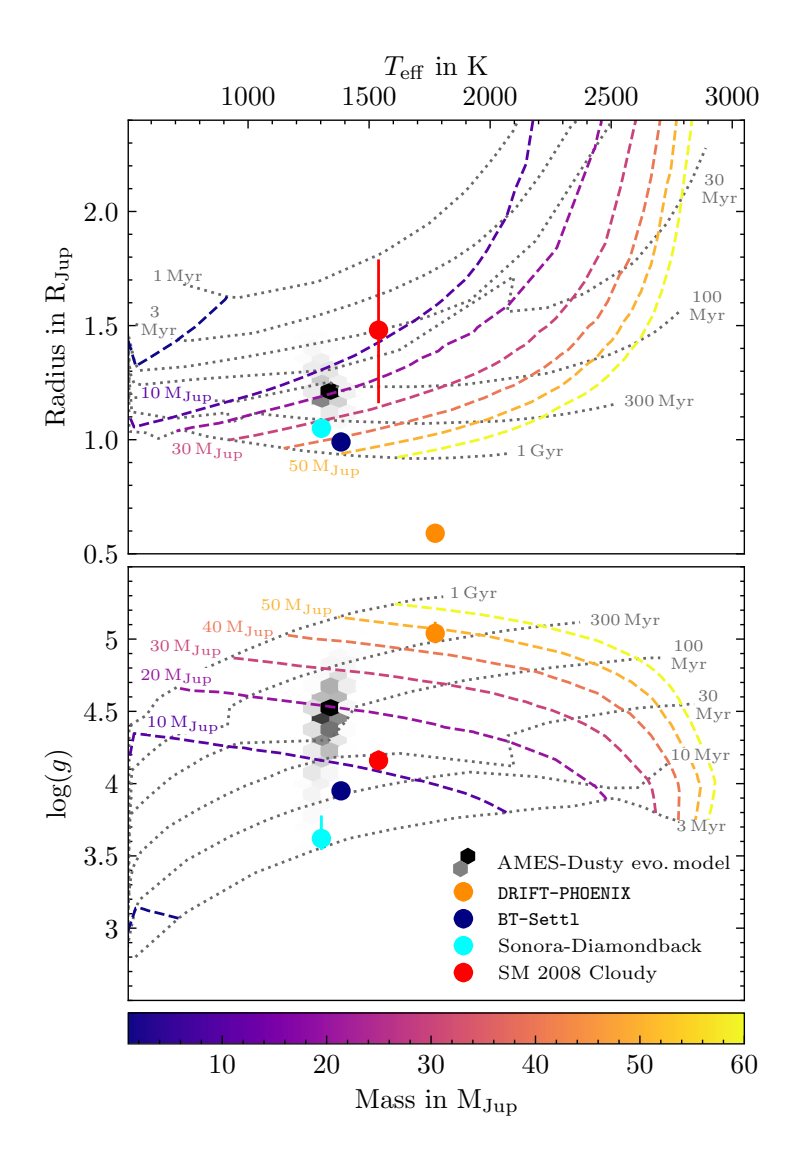


Figure 2.10: Companion radius, R, and surface gravity,  $\log(g)$ , as a function of effective temperature,  $T_{\rm eff}$ . The dotted grey lines indicate isochrones of different ages, the dashed lines illustrate evolutionary tracks, i.e. how a companion of a certain mass evolves over time. The specific masses that the tracks correspond to are indicated by their respective colours. Both the isochrones and the evolutionary tracks are taken from the AMES-Dusty model grid (Chabrier et al. 2000; Allard et al. 2001). The hexagonal bin map in the background shows where a sample of pairs drawn from the mass and K-band magnitude distributions falls when propagated into the parameter planes depicted in the two respective panels using AMES-Dusty. Finally, the values obtained through the atmospheric models applied to the spectral energy distribution of the companion are marked as circles of different colours.

object beyond the deuterium-burning threshold at an age of  $119^{+37}_{-10}\,\mathrm{Myr}$ . The full spectral energy distribution of the companion is best described by an empirical L8 type object. This agrees with the location of the body on a CMD as compared to a literature population of brown dwarfs and exoplanets.

Next, we fitted the observed spectrum of the companion using different atmospheric models. While each model performed well in terms of its reduced  $\chi^2$  squared value, the inferred parameter values varied significantly. The use of an informative mass prior based on the dynamical mass of the companion was implemented, but proved ineffective due to its comparative looseness. Employing a firmer dynamical mass constraint as a prior would effect a stronger pull on the posteriors. The inferred enriched metallicity of the companion relative to the solar value is consistent across different models and with the results presented by Zhang et al. (2024).

Finally, the radii, surface gravities, and effective temperatures inferred from the atmospheric models were compared to the results obtained from a self-consistent evolutionary model. This approach revealed the DRIFT-PHOENIX results to be inconsistent with companion's mass and age for both the younger and older scenario outlined above. While the other models yielded values more in line with the evolutionary approach, this agreement is feeble and we encountered considerable scatter between the models. Despite its current looseness, the dynamical mass of the companion reveals significant incongruities between self-consistent evolutionary and atmospheric models. Not only do the latter infer numerical parameter values that are at odds with the known physics of substellar companions, they are also inconsistent with each other.

The results laid out in this work do not permit us to infer the formation history of HIP 99770 b. That being said, the provided astrometric and spectroscopic data as well as the new constraints they facilitated will support endeavours to do so in the future.

# Chapter 3

# From semi- to fully-targeted searches: the Gaia-GRAVITY synergy

The content of this chapter is a reproduction of Winterhalder et al. (2024), a publication in Astronomy & Astrophysics, titled:

# Combining Gaia and GRAVITY: Characterising five new directly detected substellar companions

T. O. Winterhalder, S. Lacour, A. Mérand, J. Kammerer, A.-L. Maire, T. Stolker, N. Pourré, C. Babusiaux, A. Glindemann et al.<sup>1</sup>

As first author of this publication, I was in charge of the data analysis, interpretation and writing process. S. Lacour, A. Mérand, J. Kammerer and A. Glindemann acted as supervisors. A.-L. Maire, T. Stolker, N. Pourré and C. Babusiaux provided comments before submission to the journal. I have taken the liberty of adjusting the label font sizes in some figures where appropriate. The paper abstract can be found on the reverse of this page. The appendix as originally published in *Astronomy & Astrophysics* is reproduced in Appendix B of this thesis. It should also be noted that a minor part of Winterhalder et al. (2024), specifically the detection of *Gaia* DR3 2728129004119806464 B, was presented as a demonstration of a new GRAVITY observing technique in Pourré et al. (2024).

The publication of this work was accompanied by an ESA press release on 20th of June 2024 titled "Scientists spot hidden companions of bright stars".

 $<sup>^{1}</sup>$ For brevity, the remaining, alphabetically sorted co-authors from the GRAVITY collaboration are abbreviated as et al.

<sup>&</sup>lt;sup>1</sup>Link to article: https://www.esa.int/Science\_Exploration/Space\_Science/Gaia/Scientists\_spot\_hidden\_companions\_of\_bright\_stars

#### Abstract

Precise mass constraints are vital for the characterisation of brown dwarfs and exoplanets. Here we present how the combination of data obtained by Gaia and GRAVITY can help enlarge the sample of substellar companions with measured dynamical masses. We show how the Non-Single-Star (NSS) two-body orbit catalogue contained in Gaia DR3 can be used to inform high-angular-resolution follow-up observations with GRAV-ITY. Applying the method presented in this work to eight Gaia candidate systems, we detect all eight predicted companions, seven of which were previously unknown and five are of a substellar nature. Among the sample is Gaia DR3 2728129004119806464 B, which – detected at an angular separation of  $(34.01 \pm 0.15)$  mas from the host – is the closest substellar companion ever imaged. In combination with the system's distance and the orbital elements, this translates to a semi-major axis of  $(0.938 \pm 0.023)$  AU. WT 766 B, detected at a greater angular separation, was confirmed to be on an orbit exhibiting an even smaller semi-major axis of  $(0.676 \pm 0.008)$  AU. The GRAVITY data were then used to break the host-companion mass degeneracy inherent to the Gaia NSS orbit solutions as well as to constrain the orbital solutions of the respective target systems. Knowledge of the companion masses enabled us to further characterise them in terms of their ages, effective temperatures, and radii via the application of evolutionary models. The inferred ages exhibit a distinct bias towards values younger than what is to be expected based on the literature. The results serve as an independent validation of the orbital solutions published in the NSS two-body orbit catalogue and show that the combination of astrometric survey missions and high-angularresolution direct imaging holds great promise for efficiently increasing the sample of directly imaged companions in the future, especially in the light of Gaia's upcoming DR4 and the advent of GRAVITY+.

3.1 Introduction 65

#### 3.1 Introduction

The knowledge of a given substellar companion's mass is key to understanding its formation history, interior evolution, and atmosphere (e.g. Mordasini 2013; Marleau & Cumming 2014; D'Angelo et al. 2010; Bowler 2016). Masses being one of the main exoplanetary observables, they are also of central importance for mapping the demographics of the exoplanet and brown dwarf population (e.g. Nielsen et al. 2019; Vigan et al. 2021; Fontanive et al. 2023; Kirkpatrick et al. 2024; Gratton et al. 2024). Estimates of a given companion's mass are commonly obtained by applying its approximate age and measured luminosity to evolutionary models (e.g. Chabrier et al. 2000; Baraffe et al. 2003; Baraffe et al. 2015). Such indirect mass constraints must, however, be treated with the utmost care since – in the absence of a large sample of reliably measured masses – the underlying models are as of yet insufficiently benchmarked and do not always agree with one another (Marley et al. 2007; Mordasini 2013). There is thus an urgent need for more directly measured masses of substellar companions. Examples of such dynamical masses obtained for objects in the brown dwarf mass regime are HD 206893 B (Kammerer et al. 2021), HD 72946 B (Maire et al. 2020), and HD 136164 Ab (Balmer et al. 2024). Measured dynamical masses of planetary companion objects, that is, companions with masses below 13 M<sub>iup</sub>, include PDS 70 b (Wang et al. 2021),  $\beta$  Pictoris c (Nowak et al. 2020), HR8799 e (Brandt et al. 2021b), AF Lep b (Mesa et al. 2023; Franson et al. 2023b; De Rosa et al. 2023), and HD 206893 c (Hinkley et al. 2023). A subset of the cited studies make use of the astrometric data collected by ESA's Hipparcos and Gaia satellites (Gaia Collaboration et al. 2016). Potential proper motion anomalies, the difference in a star's proper motion as measured by the two missions, can be suggestive of the presence of an orbiting companion. Catalogues of such anomalous stars can be found in Brandt (2021) or Kervella et al. (2022).

Directly imaging substellar companions is still to unfold its great potential in terms of the number of its successful applications (see The LUVOIR Team 2019; Gaudi et al. 2020; Kasper et al. 2021; Quanz et al. 2022). Yet, even today it can help constrain dynamical masses in a rapid manner. This is the case when it is applied to candidate or confirmed companions whose positions relative to their host stars can be predicted reasonably well and are favourable for such observations. Such an approach has been made possible by Gaia Data Release (DR) 3 (Gaia Collaboration et al. 2023b), opening up a new avenue for searches for substellar companions in Gaia data that do not include the use of proper motion anomalies. As showcased in this work, the synergies between Gaia and GRAVITY (GRAVITY Collaboration et al. 2017) makes this instrument ensemble uniquely suited to pursue this new line of attack.

Gaia is a space-based survey telescope orbiting the Sun at the Sun-Earth Lagrange point L2, mapping the positions, velocities, spectra, and other characteristics of stars in the solar neighbourhood and beyond. Its astrometric accuracy has been shown to be sufficient to detect the reflex motions that stars exhibit as a consequence of orbiting bodies (Perryman et al. 2014; Gaia Collaboration et al. 2023a). In this work, we use the orbits of such host stars to predict the momentary position of the perturbing companion.

The GRAVITY instrument is a near-infrared interferometer at the Very Large Telescope

(VLT) on Cerro Paranal. When employed for exoplanet observations, it has been shown to achieve an astrometric accuracy of 50 µas (GRAVITY Collaboration et al. 2019). We used it to follow up on and directly image eight targets identified in the *Gaia* Non-Single-Star (NSS) catalogue.

The paper is structured as follows: How the *Gaia*-informed GRAVITY observations are prepared and conducted is described in Sect. 3.2. The combination of the two data sets as well as further analysis of the GRAVITY observation is presented in Sect. 3.3. The obtained results are then discussed in Sect. 3.4, and we present our conclusions in Sect. 3.5.

## 3.2 Observations

## 3.2.1 Using Gaia as a signpost

This work makes use of data obtained by the *Gaia* satellite. The mission's third data release (DR3) (Gaia Collaboration et al. 2023b) contains the NSS two-body orbit catalogue – a collection of hundreds of thousands of orbital solutions of point sources of light that can but are not guaranteed to correspond to individual stars. In principle, they can constitute the combination of two or more unresolved sources and are thus referred to as photocentres. A subset of the photocentre orbits are based on astrometric time-series observations taken by Gaia over several years. The original astrometric measurements in their raw format are not accessible in DR3. Instead, curated orbital fits are presented as sets of Thiele-Innes (TI) elements, which are directly – if not linearly – related to the classical sets of Campbell elements. Additionally, each orbital solution comes with uncertainties associated with the individual elements as well as a correlation matrix. We used nsstools<sup>2</sup> (Halbwachs et al. 2023) to perform the conversions between the TI and Campbell space. Dealing with substellar companions, the assumption that the flux seen by Gaia originates entirely from the host star is justified for the targets discussed in this work. The validity of such a zero-companion-Gaia-flux hypothesis, as we shall henceforth call it, is corroborated by the eventual GRAVITY detection of the selected companions and – more substantially – by the later calculation of their synthetic G band magnitudes by means of evolutionary models. As a consequence of the zero-companion-Gaia-flux hypothesis, the photocentre coincides with the position of the host star, and the NSS orbital solution can be interpreted as the star's orbit around its system's centre-of-mass (COM). This enables us to compute the Gaia-informed position of the star relative to the COM at any given time. Accordingly, the unresolved companion must be located along the axis connecting the star and the COM and behind the COM as seen from the star. Its exact placement along this axis is determined entirely by the companion-to-host mass ratio. Reflecting on two extreme cases serves as an instructive exercise to make sense of the situation. If the mass ratio approaches 1 (that is the companion has the same mass as the host; the initial zero-companion-Gaiaflux hypothesis would break down for this extreme case) one would expect the companion to be situated at the opposite side of and at the same distance from the COM as the

<sup>&</sup>lt;sup>2</sup>https://www.cosmos.esa.int/web/gaia/dr3-nss-tools

3.2 Observations 67

host. If instead the mass ratio approaches 0, we must expect the companion to be far removed from the host. Thus, lower mass ratios imply greater separations between host and companion. Both estimates for the host star and companion mass are provided by *Gaia*. From the DR3 Binary Masses Table (Gaia Collaboration et al. 2023a), we retrieve the host star's mass with associated uncertainties. The companion mass is given in the form of an upper and lower limit. Following the reasoning above, by adopting the lower limit as the companion mass we ensure that our eventual host-companion separation is an upper estimate.

Filtering the NSS catalogue according to predefined conditions on different parameters, we can identify favourable targets for a GRAVITY follow-up. Possible filtering conditions are constraints on the RA and Dec positions of the host, its distance, its mass, the companion's lower mass estimate, or the host-companion separation. Age is another possible criterion. It was not applied in the target selection performed for this work, however. We discuss the consequences of this in Sect. 3.4.1. The above method enabled us to compile a list of eight target systems viable for a follow up: Gaia DR3 2728129004119806464, Gaia DR3 4986031970629390976, CD-50 869, HD 17155, WT 766, Gaia DR3 4739421098886383872, Gaia DR3 4858390078077441920, and StKM1-1494. Among this sample, only the HD 17155 system is known to host a companion (detected via RV monitoring; see Barbato et al. 2023). For brevity, we shall henceforth shorten the Gaia DR3 IDs to the format G ...wxyz, where wxyz are the last four digits of the ID. To account for the uncertainties of the orbital elements and the correlations between them, we employed a randomisation procedure for each of the companion position predictions. Drawing  $N_{\rm rand} = 5 \times 10^5$  different sets of orbital parameters from the multivariate distribution in TI space, converting them to Campbell sets, and evaluating the resulting companion position at a defined time of observation, we obtain  $N_{\rm rand}$  different position predictions for each companion candidate. These can be visualised in a two-dimensional histogram of the sky plane as shown for each target system in Fig. 3.1. We can further quantify the degree of constraint on the companion position prediction by defining a significance metric for the orbital solution. Such a metric can be written as

$$(S/N)_{orbit} = \sqrt{\mathbf{T}\mathbf{I}_{Gaia}^{T} \cdot \mathbf{COV}_{TI, Gaia}^{-1} \cdot \mathbf{T}\mathbf{I}_{Gaia}},$$
 (3.1)

where  $\mathbf{TI}_{Gaia}$  is the vector containing the TI elements A, B, F, and G as reported by Gaia, and  $\mathbf{COV}_{TI, Gaia}$  is the covariance matrix associated with the four elements. The obtained results are presented in the respective panels of Fig. 3.1.

# 3.2.2 Following-up with GRAVITY

The targets selected from the *Gaia* NSS two-body orbit catalogue were followed up with GRAVITY between July 2022 and October 2023. Initial observations were conducted on technical time, to demonstrate the validity of the technique. Subsequent observations were conducted within the framework of the ExoGRAVITY Large Programme (ESO ID 1104.C-0651 Lacour et al. 2020) and within a dedicated open time programme (ESO ID 111.253E,

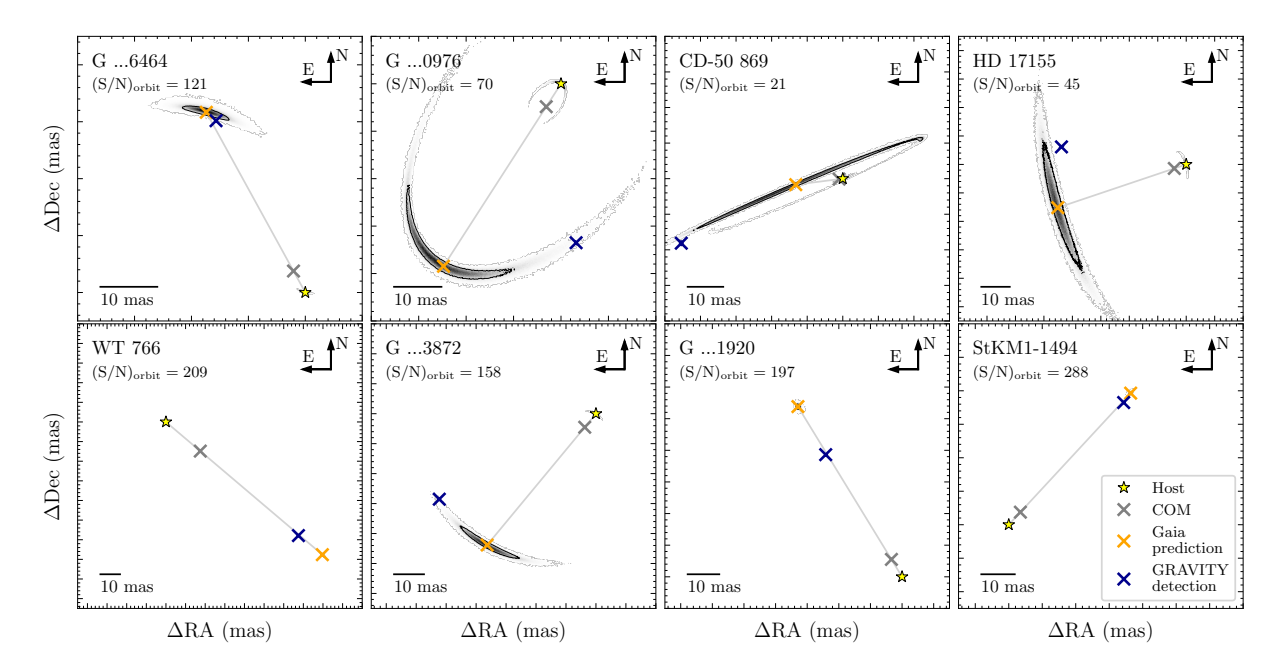


**Figure 3.1:** Position probability maps at the time of observation for the observed systems as computed from the respective orbital solutions listed in the Gaia NSS catalogue. The orange cross indicates the mean companion position relative to the mean host position, which is marked by the yellow star. The system's COM is shown by the grey cross. Randomising the host and companion positions on the basis of the parameter uncertainties and correlations (while keeping the mass ratio, q, fixed to the lower limit; see the main text) yields the predicted spread around the respective mean positions. The contour line encircles 68% of the randomised companion positions. The grey axis connects the mean host position with the mean companion position to visualise the separation's dependence on the mass ratio, q. The position at which the companion was detected with GRAVITY is shown as the dark blue cross. For targets that were observed more than once, we show the companion position prediction corresponding to the first epoch and the resulting initial detection. The dark blue uncertainty ellipses associated with the GRAVITY detections are too small to be seen at these scales. The ticks along the panel axes are spaced by 10 mas. Finally, the significance of the individual orbital solutions, (S/N)<sub>orbit</sub>, is given below the target system name in the top-left corner of each panel.

3.2 Observations 69

Target	$t_{\rm obs}~({\rm MJD})$	$\Delta RA \text{ (mas)}$	$\Delta \mathrm{Dec}\ (\mathrm{mas})$	$\rho$	$(F_c/F_*)_{ t 2MASS.Ks}$
Gaia DR3 2728129004119806464	59892.1	$(15.68 \pm 0.14)$	$(30.18 \pm 0.15)$	-0.94	$(0.335 \pm 0.006) \%$
Gaia DR3 4986031970629390976	59893.1	$(-3.19 \pm 0.15)$	$(-33.5 \pm 0.4)$	0.93	$(35.98 \pm 0.12)\%$
CD-50 869	59782.4	$(45.4 \pm 0.4)$	$(-18.1 \pm 0.6)$	0.05	$(0.481 \pm 0.007) \%$
HD 17155	59782.3	$(43.8 \pm 0.7)$	$(6.2 \pm 0.4)$	-0.93	$(0.472 \pm 0.005) \%$
	59810.4	$(44.61 \pm 0.05)$	$(2.03 \pm 0.10)$	-0.68	$(0.2890 \pm 0.0015) \%$
WT 766	59809.2	$(-67.50 \pm 0.05)$	$(-57.89 \pm 0.05)$	0.48	$(6.406 \pm 0.009) \%$
Gaia DR3 4739421098886383872	60128.4	$(52.3 \pm 0.4)$	$(-28.6 \pm 0.4)$	0.56	$(0.299 \pm 0.007) \%$
	60244.3	$(63.28 \pm 0.05)$	$(-7.1 \pm 0.4)$	0.46	$(0.173 \pm 0.019) \%$
Gaia DR3 4858390078077441920	60156.4	$(24.15 \pm 0.07)$	$(38.62 \pm 0.04)$	-0.44	$(1.988 \pm 0.006) \%$
StKM1-1494	60072.2	$(-34.32 \pm 0.06)$	$(36.49 \pm 0.19)$	-0.72	$(0.470 \pm 0.003) \%$

**Table 3.1:** Astrometric epochs of the respective companions obtained with GRAVITY.

Notes. The astrometric companion position components  $\Delta RA$  and  $\Delta Dec$  are given relative to the respective host as detected with GRAVITY at the time of observation,  $t_{\rm obs}$ .  $\rho$  denotes the correlation between the two astrometric components while the rightmost column shows the companion over host contrast,  $(F_c/F_*)$ , in the K band after folding with the 2MASS/2MASS.Ks filter profile. Note the high K band contrast in the G ...0976 system.

PI A.-L. Maire). An observation log containing observation dates, conditions, exposure times and the fibre placement for each target is presented in Table B.1.

All targets were observed using the dual-field on-axis observation mode comprehensively described in (GRAVITY Collaboration et al. 2019). To summarise, this technique places the first instrument fibre on the host star to track fringes (Lacour et al. 2019). The science fibre, on the other hand, alternates between the host and the companion. As this project progressed the observing technique changed slightly. To begin with, the science fibre was placed at the position at which the companion was predicted to be located (as described in Sect. 3.2.1). Later, we decided to position it slightly off-centre to gain in contrast capabilities (this so-called fibre off-pointing technique is comprehensively discussed in Pourré et al. 2024). The flip side of such an approach is the loss of a fraction of the companion flux. How this throughput loss is corrected for is described in Appendix B.1.

The data reduction was performed using the ESO GRAVITY Instrument Pipeline 1.6.4b1, from which we obtained the astro-reduced byproduct. The astrometry from these files was then obtained using the standard exoplanet dual field data processing described in Appendix A of GRAVITY Collaboration et al. (2020). The separations in RA and Dec relative to the hosts at which the companions were detected are shown in Table 3.1. Also note that a metrology jump that occurred on Unit Telescope 3 during the observation of the StKM1-1494 system was corrected for.

One of the detections presented in this work (that of G ...6464 B) as well as a preview of the analysis undertaken below was briefly showcased in Pourré et al. (2024) in order to demonstrate a successful application of the fibre off-pointing observation technique.

# 3.3 Methods

# 3.3.1 Making Gaia and GRAVITY 'talk'

The synergies between Gaia and GRAVITY are not confined to using the NSS catalogue as a signpost to inform follow-up observations and facilitate detections. By combining the two data sets we can obtain tighter constraints on the orbital elements, break the degeneracy between the host and companion mass that is an inherent feature of Gaia NSS orbital solutions and confirm the initial zero-companion-Gaia-flux hypothesis. To this end, we employed a Bayesian approach. In this sense we can interpret the orbital solution provided by Gaia as the likelihood information from which the posterior distributions of the orbital elements follow. The GRAVITY detection and concomitant relative astrometry measurement can be viewed as an additional likelihood, upon inclusion of which we can update the posteriors. This amounts to re-sampling the posterior distributions by performing a Markov Chain Monte Carlo (MCMC) run through the multivariate parameter space, spanned by nine free parameters, namely the TI elements A, B, F, and G, the eccentricity, e, the period, P, the time of periastron passage relative to the Gaia epoch,  $t_{p,rel}$ , the parallax,  $\pi$ , and the total mass of the system,  $M_{\rm tot}$ . To avoid external and non-physical constraints on the individual parameters, we defined a broad, uniform prior range for each of them, virtually ranging from minus infinity to infinity. Next, a set of  $N_w = 100$  walkers were initialised. We assigned a unique set of orbital parameter values to each of them. The actual placement was performed by assuming Gaussian distributions around the Gaia NSS orbital elements. To adopt a more conservative initialisation approach and loosen the dependence on the Gaia values, we inflated the distributions' standard deviations by a factor of two. This introduces a greater spread ensuring that the prior range is more thoroughly sampled by the initial set of walkers. It should be noted that the total mass is initialised around the host mass estimate,  $M_1^{\text{Gaia}}$ , listed in the Gaia DR3 Binary Masses Table. Considering the significantly higher mass of the host compared to the companion, this placement appears reasonable.

The MCMC run and actual building of the posterior sampling was performed using emcee (Foreman-Mackey et al. 2013). At the heart of this procedure lies an In-likelihood function that reads

$$\ln(\mathcal{L}) = -\frac{1}{2} \left[ \chi_{\text{Gaia}}^2 + \chi_{\text{GRAVITY}}^2 \right], \tag{3.2}$$

where  $\chi^2$  denotes different chi-squared contributions. The first term,  $\chi^2_{\text{Gaia}}$ , compares the individual sets of free parameters sampled by the walkers to the set listed in the *Gaia* NSS catalogue under consideration of the provided covariance matrix. It is thus defined as

$$\chi_{\text{Gaia}}^2 = (\boldsymbol{\theta}_{\text{Sample}} - \boldsymbol{\theta}_{\text{Gaia}})^{\text{T}} \cdot \mathbf{COV}^{-1} \cdot (\boldsymbol{\theta}_{\text{Sample}} - \boldsymbol{\theta}_{\text{Gaia}}). \tag{3.3}$$

Here,  $\theta_{\text{Sample}}$  denotes the parameter set vector sampled by the walker,  $\theta_{\text{Gaia}}$  is the *Gaia* parameter set as retrieved from the NSS catalogue and **COV** represents the covariance matrix that follows from the correlation matrix yet again presented in the NSS catalogue.

3.3 Methods 71

The second term,  $\chi^2_{\text{GRAVITY}}$ , introduces the GRAVITY astrometry into the ln-likelihood function and is defined as

$$\chi_{\text{GRAVITY}}^{2} = \sum_{n=1}^{N_{\text{G}}} \left( \boldsymbol{\zeta}_{n}^{\text{Sample}} - \boldsymbol{\zeta}_{n}^{\text{G}} \right)^{\text{T}} \cdot \mathbf{COV}_{n}^{-1} \cdot \left( \boldsymbol{\zeta}_{n}^{\text{Sample}} - \boldsymbol{\zeta}_{n}^{\text{G}} \right), \tag{3.4}$$

where  $N_{\rm G}$  is the number of GRAVITY observations and thus astrometric epochs. The vector  $\boldsymbol{\zeta}_n^{\rm G}$  contains the host-companion separation components in RA and Dec measured during the n-th GRAVITY observation.  $\boldsymbol{\zeta}_n^{\rm Sample}$ , on the other hand, represents the separation components resulting from the parameter set probed by the walker. Finally,  $\mathbf{COV}_n^{-1}$  describes the covariance matrix associated with the n-th GRAVITY observation. Running the MCMC procedure through a burn-in phase of  $N_{\rm burn}=2000$  iterations and building the chain in the actual sampling phase over  $N_{\rm iter}=10\,000$  iterations yields the posteriors.

A word of caution: due diligence is required when applying MCMC methods to data from the Gaia NSS two-body orbit catalogue. The orbital solutions contained in the catalogue are presented as sets of TI elements. Related to the classical Campbell elements by a set of non-linear equations (Binnendijk 1960), the TI elements are known to exhibit strong degeneracies and even circular correlations for circular and quasi-circular orbits. This can lead MCMC procedures astray. Local linear approximation (LLA) methods offer a safe way of utilising Gaia NSS orbital solutions (Babusiaux et al. 2023). Information such as the skewness of a posterior distribution or potential multi-modalities, however, is lost when limiting oneself to these inherently Gaussian procedures. Thus, it is desirable to combine the NSS orbital solutions with MCMC methods for such targets where this is possible without misinterpreting the data. We strongly recommend ascertaining the equivalence of LLA and MCMC methods for every target individually. To this end, we used BINARYS (Leclerc et al. 2023), a dedicated LLA implementation specifically designed to handle Gaia NSS orbit solutions in combination with relative astrometry measurements, to compute an independent set of posteriors under inclusion of all available data. The thus obtained consistent results suggest that the NSS solutions for the targets at hand are suitable to be treated with MCMC procedures.

Finally, it should be noted that the procedure as outlined above cannot be applied to the G ...0976 system. This is due to G ...0976 B's high K band flux relative to its host (see Table 3.1). Even though the system's G band flux ratio can be expected to be lower it does not seem reasonable to uphold the zero-companion-Gaia-flux hypothesis. Without it, however, we lose the convenient advantage of assuming the photocentre to coincide with the host. In the absence of a measurement of the system's G band flux ratio, it is impossible to convert the photocentre orbit into the host orbit.

#### 3.3.2 Orbital refinements

The MCMC method outlined in Sect. 3.3.1 is applied twice. First, we ran it while only including the Gaia term,  $\chi^2_{Gaia}$ , in the ln-likelihood function defined in Eq. 3.2. By not considering  $\chi^2_{GRAVITY}$ , we are ignoring the GRAVITY astrometry. We then ran the MCMC procedure taking both terms into account. This let us visualise the constraining power

achievable by the inclusion of GRAVITY data, since we can compare the initial Gaia-only posteriors to the updated ones. Once the two samplings have been created, we conveyed the individual parameter sets from TI to Campbell space. The resulting full corner plots showing both the initial and the updated posteriors are to be found in Appendix B.3. The marginalised posterior distributions of the free parameters are shown in Fig. 3.2. The inferred median values and associated uncertainties are listed in Table B.4. The refinements to the orbital solutions also manifest in the orbits' appearances as projected onto the sky plane. Figure 3.3 shows how the updated orbits compare to the initial Gaia-only orbits.

## 3.3.3 Nailing down dynamical masses

A given host star's movement around its system's COM can conceivably be induced by different combinations of the companion's mass and separation (and when disregarding the zero-companion-Gaia-flux hypothesis also by the host-companion flux ratio). For this reason, the Gaia astrometric time-series data of the host and the resulting orbital fits by themselves are inherently degenerate in terms of the two bodies' dynamical masses. The columns to the right of Fig. 3.2 reveal that in addition to enabling significant constraints to be placed on the orbital parameters of target systems, the inclusion of a GRAVITY data point facilitates the breaking of the mass degeneracy. Indeed, one detection suffices to put tight constraints on both absolute masses. Again, the inferred median masses as well as their associated uncertainties are listed in Table B.4.

#### 3.3.4 Photometric characterisation

Apart from precise relative astrometry measurements between companion and host, the GRAVITY observations of the different target systems also provide so-called contrast spectra in the K band. These measure the flux ratio between companion and host as a function of wavelength. The individual spectra can be found in Fig. B.3. Convolving such a spectrum with a given filter yields the contrast between companion and host as it would appear through the chosen filter. The contrast can then be converted to a magnitude difference. We used species (Stolker et al. 2020) to fit the BT-Settl (CIFIST) atmospheric model (Allard et al. 2003) to stellar photometry from the literature listed in Table B.2. From the resulting fit we then generated a synthetic stellar magnitude in the chosen filter. Finally, the companion magnitude is arrived at by adding the companion-to-host magnitude difference to the synthetic stellar magnitude.

The knowledge of the companion's dynamical mass alongside its filter magnitude allows us to estimate the object's age by comparing its position on the mass-magnitude plane with isochrones generated using evolutionary models as shown in Fig. 3.4. In other words, this procedure amounts to turning the conventional application of evolutionary models to substellar companions on its head. Typically, they are used to obtain mass estimates from a companion's measured magnitude and its inferred age, which most often is assumed to be similar to that of the stellar association the host belongs to (Bowler 2016). As explained above, in our case we can instead obtain constraints on the companion's age from its

3.3 Methods 73

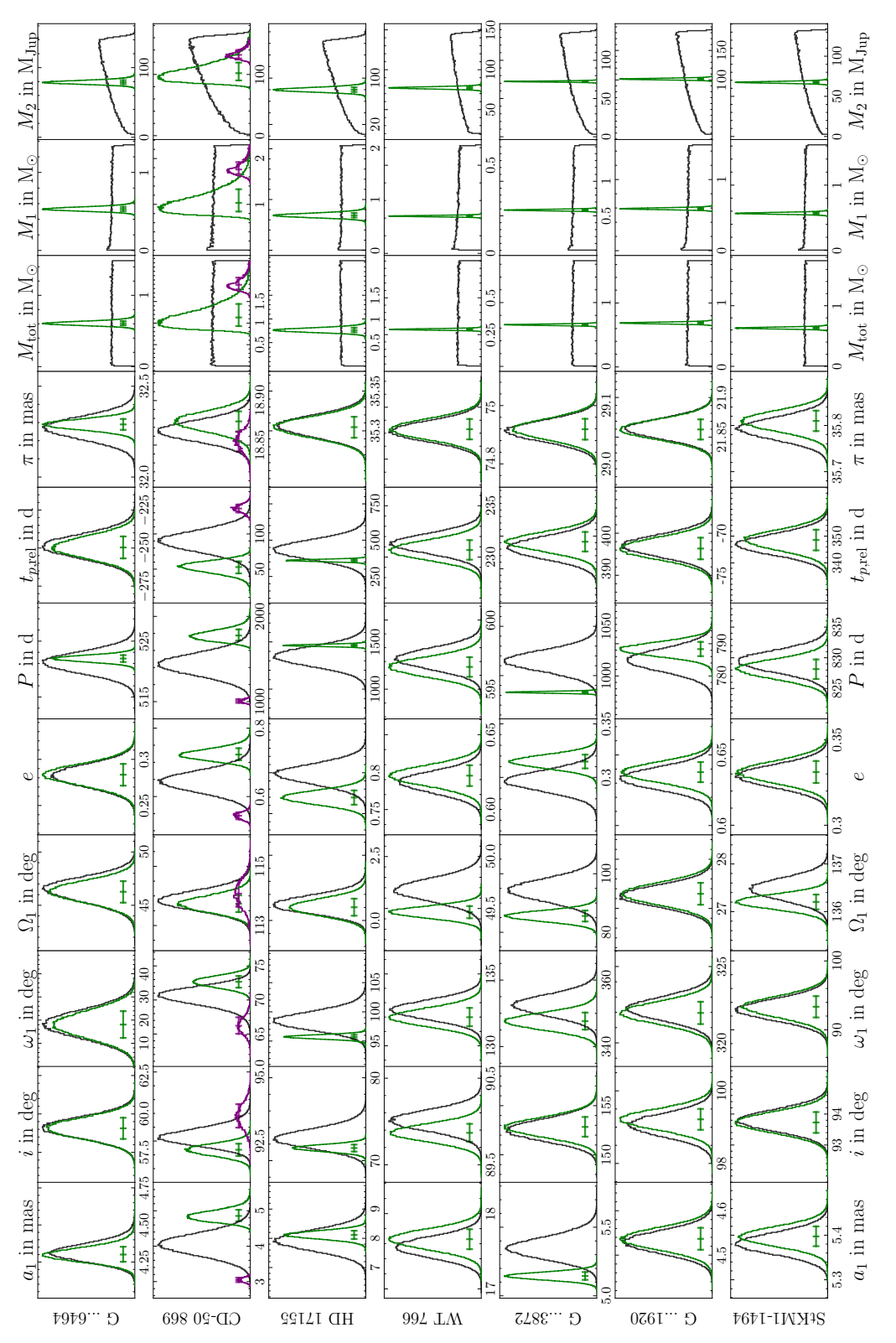


Figure 3.2: Marginalised posterior distributions of the systems' orbital parameters for the Gaia-only run (in black) as well as the Gaia-plus-GRAVITY run (in green). Note that the Gaia-plus-GRAVITY chain converges on two different and the secondary solution (purple). The indices 1 denote that the shown parameters describe the host star's orbit around orbital solutions for the CD-50 869 system. The bimodal posterior distribution was separated into the preferred (green) the respective system's COM.

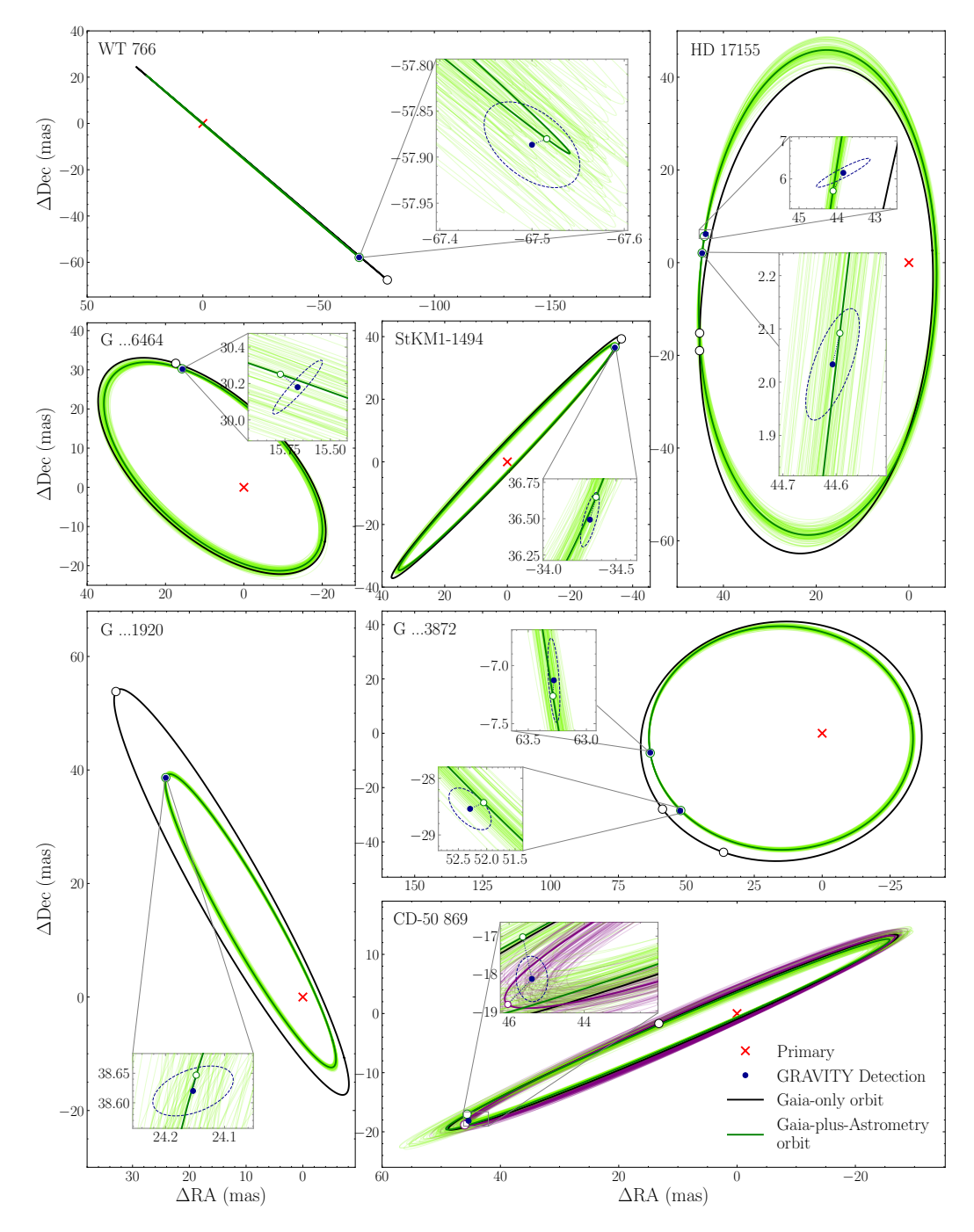
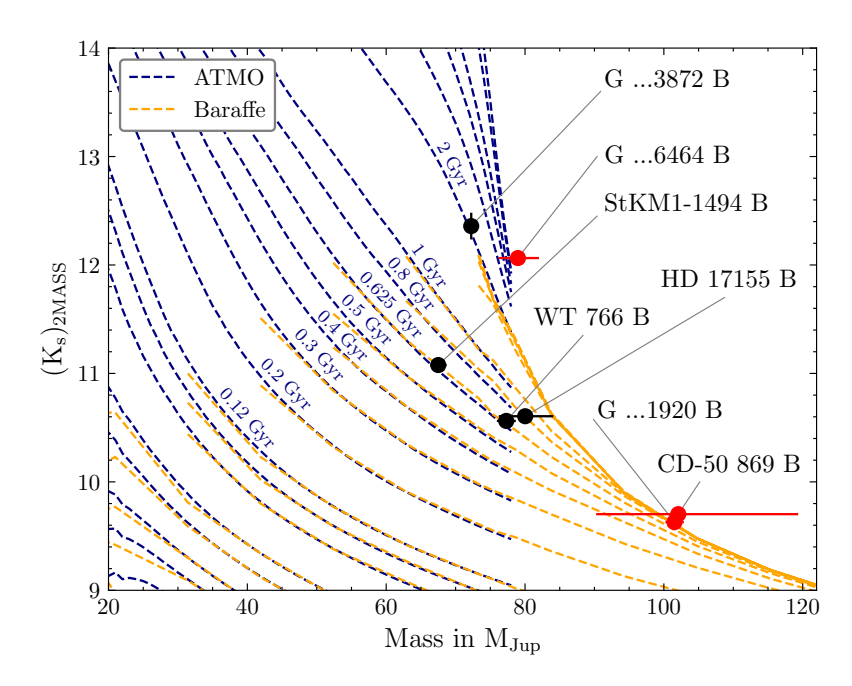


Figure 3.3: Orbits of the individual companions relative to their respective host. The black line indicates the orbit as suggested by the orbit solution listed in the *Gaia* NSS catalogue (assuming the lower companion mass estimate). The black circle shows where the companion was predicted to be located at the time of observation. The blue dot and its uncertainty ellipse indicate where the GRAVITY detection was made. The thick green orbit is based on the median parameter values of the posterior distributions after combining the *Gaia* and GRAVITY data as described in Sect. 3.3.1. The thin light green lines show 100 orbits drawn at random from the posterior distribution. Note that CD-50 869's posterior orbit sampling was separated into a primary and secondary mode, shown here in green and purple, respectively.

3.3 Methods 75



**Figure 3.4:** Mass-magnitude plane with the companions detected in this work and isochrones taken from the ATMO and Baraffe model grids in blue and orange, respectively. Both the data points and the isochrones are presented as 2MASS/2MASS.Ks filter magnitudes. The three potentially under-luminous companions, G ...6464 B, CD-50 869 B, and G ...1920 B, are marked in red.

magnitude and measured mass. Again, we used species to interpolate isochrones from the ATMO model grid (Phillips et al. 2020). Some companions exhibiting masses above the conventional brown dwarf domain, we included the Baraffe et al. (2015) model to cover the entire mass range of our target sample.

To eventually arrive at a meaningful age estimates, we propagated the posterior distributions in mass and magnitude by means of a bootstrapping method. To this end we interpolated linearly between the isochrones using scipy.interpolate.griddata (Virtanen et al. 2020). This method enables the rapid age determination of mass-magnitude samples randomly drawn from the respective posterior distributions. Computing the ages resulting from  $N_{\rm boot}=10\,000$  mass-magnitude samples for each target yields the age posteriors shown in the left column of Fig. 3.5 and listed in Table B.4. To showcase the power of possessing a high-precision dynamical mass estimate, we can bootstrap the mass and age sampling further into other parameter spaces. Thus, we can repeat the above procedure to obtain posteriors of the companions' effective temperatures and radii. The results are shown in the middle and right column of Fig. 3.5 and are listed in Table B.4.

To further contextualise the detected companions we placed them on a colour-magnitude diagram spanned by the Paranal/SPHERE.IRDIS\_B\_Ks filter magnitude and the colour between Paranal/SPHERE.IRDIS\_D\_K12\_1 and Paranal/SPHERE.IRDIS\_D\_K12\_1. Such a colour-magnitude diagram, populated with a template dwarfs from the literature (for de-

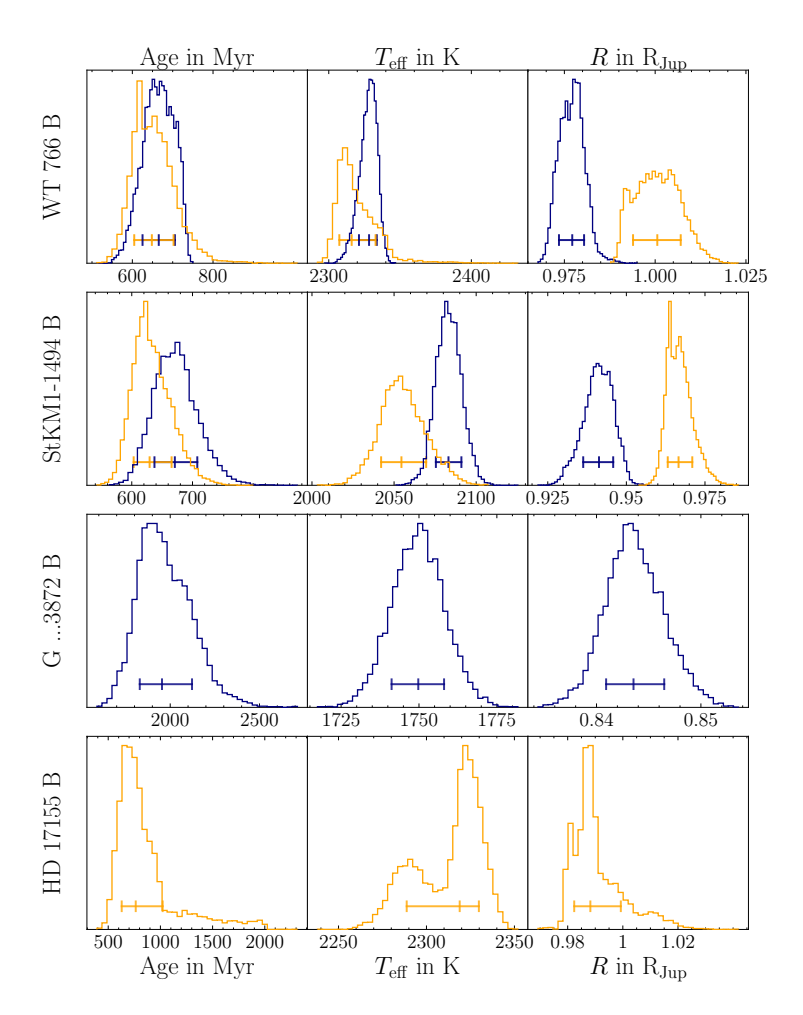


**Figure 3.5:** Age, effective temperature, and radius constraints for the individual companions as obtained using the ATMO and Baraffe models in blue and orange, respectively. The horizonal bars show the  $1\sigma$  environment around the median of each distribution.

tails see Appendix C of Bonnefoy et al. 2018) and the companion sample presented here, can be found in Fig. 3.6.

# 3.4 Discussion

# 3.4.1 On the Gaia-GRAVITY synergy

In the previous sections we showed that the orbit solutions contained in the *Gaia* NSS catalogue can be used to inform follow-up observations with a high-precision direct imaging instrument such as GRAVITY. The *Gaia*-based position predictions proved to be sufficiently accurate to facilitate the placement of the GRAVITY science fibre in such a way that the exceedingly small field of view contained the sought-after companion. In this way, we were able to detect and confirm all eight predicted companions.

3.4 Discussion 77

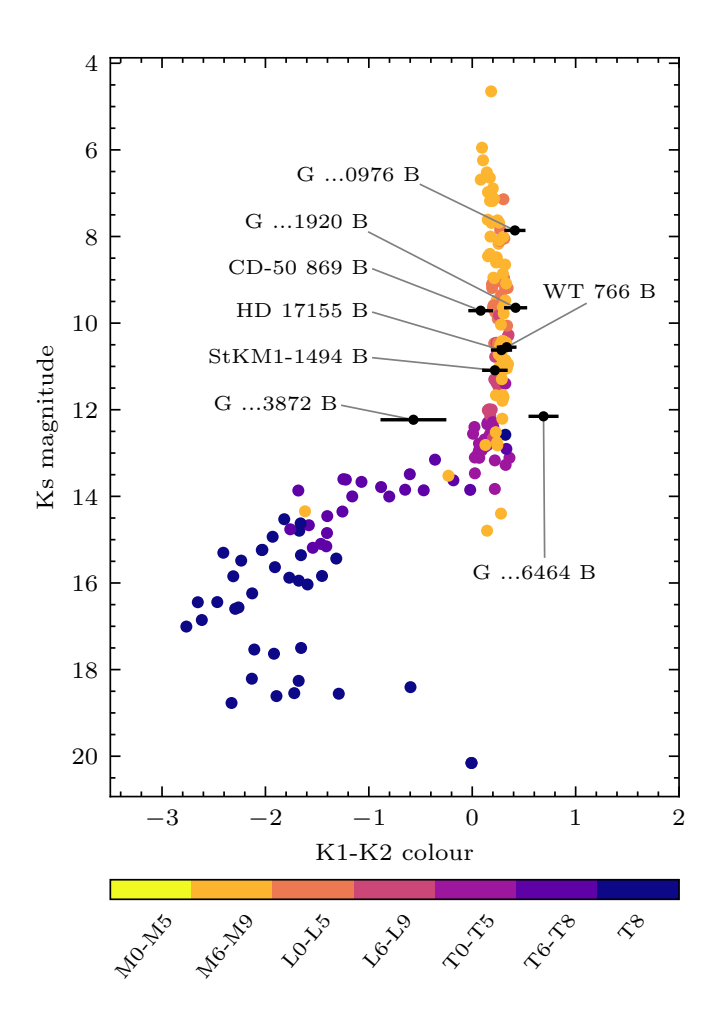


Figure 3.6: Colour-magnitude diagram showing a template dwarf population compiled in Bonnefoy et al. (2018, for details, see their Appendix C) as well as the companion sample discussed in this work. The colour indicates the spectral type of a given object.

The complete lack of non-detections is worthy of a short discussion. As the reader will recall, young age was not used as a criterion for target selection. Thus, one would naïvely assume that such an allowance for old targets would cause some of the observations to result in non-detections of the respective companions since the companion-to-host contrast decreases with age. A simple estimation of the companion magnitude at high ages resolves the conundrum. Given the inferred masses, we could compute the magnitudes from evolutionary models. Furthermore, we could compute the limiting magnitude up to which detection with GRAVITY can be achieved for each target system. To this end, we evaluated the GRAVITY contrast curve (Pourré et al. 2024) at the detection separation of each companion and converted the resulting limiting contrasts to a magnitude difference. In combination with the respective K band magnitudes of the hosts this yields the limiting companion magnitudes. Comparison with the companion magnitudes from the evolutionary models reveals that they are all observable independent of their ages. This

is a consequence of investigating companions located towards the upper end of the brown dwarf mass range. We are dealing with objects that are sufficiently bright to facilitate successful detection regardless of their age. This is a luxury not afforded to those who plan to apply the procedures outlined here to less massive and therefore fainter companion targets. In such cases one is forced to include age as a selection criterion.

Substellar companions in the NSS catalogue typically reside at separations of a few dozen mas. This makes follow-up observations with classical direct imaging instruments such as SPHERE (Beuzit et al. 2019) or GPI (Macintosh et al. 2014) challenging for the vast majority of these objects due to the inner working angle of their coronagraphs. It is only by the means of GRAVITY and its unique angular resolution that these low-separation companions can be accessed. This will be even more relevant for the numerous Gaia-inferred companions in the planetary-mass regime, which are predicted to be found at even smaller separations (Perryman et al. 2014). To illustrate this point, it is worth noting that among the sample of detected companions presented here is Gaia DR3 2728129004119806464 B, which, observed at a radial separation of 34 mas from the host star, is the closest ever directly detected substellar companion. The inferred companion orbit puts the semi-major axis at  $(0.938 \pm 0.023)$  AU. Another noteworthy example is that of WT 766 B's orbit, which exhibits a semi-major axis of  $(0.676 \pm 0.008)$  AU. The semi-major axes of the entire companion sample are presented in Table 3.2.

The independent companion detections by GRAVITY provide a rare opportunity to validate and assess the orbital solutions published in the Gaia DR3 NSS two-body orbit catalogue. One way of doing so is by assessing the statistic validity of the Gaia uncertainties. To this end we compared the companion position prediction based on the NSS orbital solutions to the GRAVITY detection. Since the radial separation component depends on the initially unconstrained mass ratio between companion and host, we removed it from the analysis by only considering the position angle component,  $\varphi$ . If the Gaia uncertainties are statistically robust approximately 68% of the detections should be made at position angles within a 1 $\sigma$  confidence interval around the median of the Gaia-based position angle prediction,  $\varphi_{\rm med}$ . Figure B.2 shows said position angle distribution for each target system as well as the respective GRAVITY detection position angle,  $\varphi_{\rm det}$ . By taking the absolute difference,  $\Delta \varphi = |\varphi_{\rm det} - \varphi_{\rm med}|$ , between the distribution's median and the detection value and scaling it by the respective uncertainties,  $\sigma_{\varphi, \rm det}$  and  $\sigma_{\varphi, \rm med}$ , according to

$$I = \frac{\Delta \varphi}{\sqrt{\sigma_{\varphi, \, \text{det}}^2 + \sigma_{\varphi, \, \text{med}}^2}},\tag{3.5}$$

we can compute an inflation factor, I, that quantifies by how much the Gaia uncertainties need to be 'blown up' to make the  $1\,\sigma$  position angle confidence interval encompass the detection. The resulting inflation factors for the individual systems are showcased in Table 3.2. They indicate that – with the exception of G ...6464 B – all companions were detected outside the respective Gaia-based  $1\,\sigma$  position angle confidence interval, suggesting that the Gaia uncertainties are underestimated. We note that as can be seen in Fig. B.2 the inflation factor found for the CD-50 869 system results from a non-Gaussian position angle distribution rendering the value unusable.

3.4 Discussion 79

#### 3.4.2 Orbital refinements and dynamical masses

By means of a Bayesian inference framework conducted using an MCMC procedure, we were able to combine the orbit solution provided by *Gaia* with the GRAVITY astrometry measurement. Visual inspection confirmed that, apart from the mass chains, all chains of the *Gaia*-only runs as well as all chains of the *Gaia*-plus-GRAVITY runs converged for every target system. The inclusion of the GRAVITY detection resulted in tighter constraints on the orbital elements and the breaking of the mass degeneracy inherent to the NSS orbit solution. With the exception of CD-50 869 B and G ...1920 B, which have both been shown to be of stellar nature, the resulting dynamical masses lie within the respective mass constraints listed in the DR3 Binary Masses Table (Gaia Collaboration et al. 2023a). While the dynamical mass of CD-50 869 B carries a relative uncertainty of 15 %, those of the other targets vary between 0.9 and 5 %.

Furthermore, the posterior sampling of the CD-50 869 system is of bimodal nature. A possible explanation of this circumstance can be found in the geometry of the orbit and epoch of the GRAVITY detection. In order to minimise leakage of the host star flux into the science fibre and the resulting speckle noise it was decided to observe this companion at its furthest separation from the host. In combination with the orbit being almost edgeon, the MCMC chain converges on two different solutions that place the companion before and after the projected turning point, respectively. Such a configuration serves to show the limitation of this method. By observing at the largest separation and thereby maximising the chances of detection, one runs the risk of obtaining an inconclusive posterior due to bior even multi-modality. It should be noted, however, that the acquisition of an additional GRAVITY epoch of the companion at a different position along its orbit would likely kill the bimodality and pin down the orbital solution at or close to the primary mode obtained here. Finally, when allowing for additional evidence from proper motion anomaly studies, CD-50 869's entry in the catalogue put forward in Kervella et al. (2022) suggests a host star mass of  $(0.90 \pm 0.04) \,\mathrm{M}_{\odot}$ . This estimate is covered by the primary mode's host mass constraint of  $1.03^{+0.32}_{-0.19}$  M $_{\odot}$ . Moreover, using surface brightness to colour relations and the system's parallax they also obtain a host star radius estimate of  $(0.87\pm0.04)$  R<sub>Sun</sub>, which is incompatible with the secondary mode's large host mass. The only other system presented here that is also contained in the Kervella et al. (2022) proper motion anomaly catalogue is HD 17155.

While more constrained, on the whole the updated orbit posteriors visualised in Fig. 3.2 agree with the *Gaia* NSS orbital solutions. The largest discrepancy between the posteriors before and after inclusion of the GRAVITY astrometry can be seen in the orbital period of G ...3872 B. We note that this period value is particularly large, suggesting that the period estimate presented in the NSS catalogue might have been underestimated due to insufficient orbital coverage.

The almost exactly edge-on orbit of WT 766 B was already indicated by the orbital solution listed in the *Gaia* NSS catalogue. The updated orbit elements substantiate this orbit configuration and suggest the possibility of observing this substellar companion in transit. The transit probability can be calculated on the basis of the maximum opening

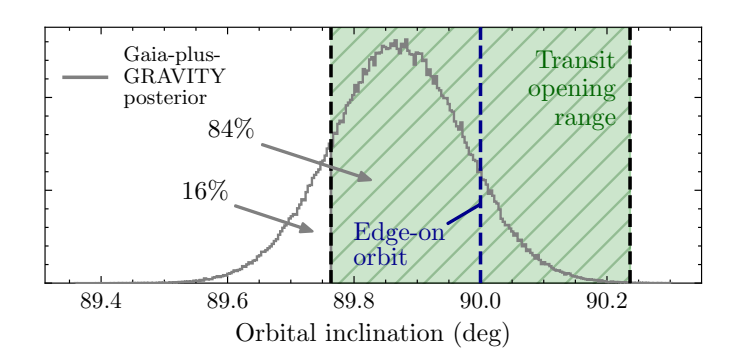


**Figure 3.7:** WT 766 B's *Gaia*-plus-GRAVITY inclination posterior compared to the angular transit opening range indicated by the hatched green region. The dashed blue line shows a perfectly edge-on orbit. The percentage values specify the posterior sampling fractions falling within and outside the opening range.

angle,  $\vartheta$ . If a given companion's orbit exhibits an inclination within the range  $90^{\circ} - \vartheta < i < 90^{\circ} + \vartheta$  it will show a transit. Based on the derivation in Beatty & Seager (2010) the maximum opening angle,  $\vartheta$ , for an eccentric companion orbit can be computed via

$$\vartheta = \arcsin\left(\frac{R_*}{a} \cdot \frac{1 + e\sin(\omega)}{1 - e^2}\right),\tag{3.6}$$

where  $R_*$  is the stellar radius and a, e, and  $\omega$  are the companion orbit's semi-major axis, eccentricity, and argument of periastron, respectively. For WT 766 B this yields a maximum opening angle of  $\vartheta = (0.236 \pm 0.007)^{\circ}$ . How this compares to the companion's inclination posterior is visualised in Fig. 3.7. Integrating the posterior within the angular transit opening range around 90° yields a transit probability of 84%.

According to the orbital solution posterior the next transit will occur in February 2025. The symmetry of the orbit as projected onto the sky plane makes it impossible to determine whether this will constitute a primary or secondary eclipse, however. Upon observation it should be fairly obvious which phenomenon is observed, breaking the degeneracy in the orbit symmetry. Alternatively, an additional RV measurement of the system on top of the one listed in Gaia DR3 should enable the derivation of the systematic velocity and in turn resolve the orbit's directional degeneracy. In any case, such an observation would constitute the first application of imaging and transit techniques to the same object.

In the respective panels of Fig. 3.3 we can observe that the orbital constraints resulting from the inference procedure also manifest in changes to the geometry of some of the orbits. To prepare for computing reduced chi-squared values of the refined orbits we ran an additional gradient descent procedure starting at the most probable parameter sample as determined by the MCMC run. The minima identified by the gradient descent procedure were then used to compute the chi-squared values presented in Table 3.2.

3.4 Discussion 81

Table 3.2:	Semi-major	axes,	inflation	factors	and	reduced	chi-squared	values	for	the
detected com	npanions.									

Target	a in AU	I	$\chi^2_{\rm red}$
Gaia DR3 2728129004119806464 B	$(0.938 \pm 0.023)$	0.4	0.04
Gaia DR3 4986031970629390976 B	_ a	2.9	_ a
CD-50 869 B	$(2.73 \pm 0.28)$	$0.2^{\ b}$	3.67
HD 17155 B	$(2.07 \pm 0.07)$	1.6	2.52
WT 766	$(0.676 \pm 0.008)$	2.9	1.84
Gaia DR3 4739421098886383872 B	$(1.500 \pm 0.019)$	3.0	2.19
Gaia DR3 4858390078077441920 B	$(1.265 \pm 0.016)$	1.4	0.54
StKM1-1494 B	$(1.329 \pm 0.014)$	1.3	0.92

Notes. The semi-major axes, a, shown here result from the Gaia-plus-GRAVITY orbital posteriors. The inflation factors, I, are required to make the  $1\,\sigma$  position angle confidence interval encompass the detection. The presented reduced chi-squared values of the best-fit orbital solution were found by means of a gradient descent from the most probable parameter set in the MCMC posterior sampling.

# 3.4.3 Inferring ages from evolutionary models

The first notable feature of Fig. 3.4 is the potential under-luminosity observed in three of the detected companions, namely G ...6464 B, CD-50 869 B, and G ...1920 B. For two of these (G ...6464 B and CD-50 869 B) the error bars on their dynamical mass estimates still overlap with the oldest isochrones. This is not the case for G ...1920 B, which is significantly removed from the isochrones. Under-luminosity in old brown dwarf companions is a known problem in the literature (e.g. Brandt et al. 2021c). Invoking the possibility of companion binarity offers a potential explanation as to the observed lack in luminosity. A companion to the companion would distort the mass of the primary companion since the treatment as put forward here accounts for the putative pair of bodies as a single point mass located at the astrometric position measured by GRAVITY. This would move the respective companion's data point in Fig. 3.4 towards the right into a domain where it appears to be under-luminous when instead its mass was misjudged by assuming the companion system to be a single body.

The presence of a secondary companion could be observable by obtaining several GRAV-ITY epochs. If the astrometric data can be shown to deviate from the expected orbit and to follow a trajectory that exhibits features reminiscent of epicycles, this would strongly suggest companion binarity. The magnitude of such a feature would depend on the mass ratio between the primary and the secondary companion, which can be estimated to the first order by measuring the excess mass in Fig. 3.4. Such a follow-up study could not

<sup>&</sup>lt;sup>a</sup> Note that G ...0976 B lacks values for the semi-major axis as well as the reduced chi-squared since the posterior could not be sampled for this companion.

<sup>&</sup>lt;sup>b</sup> The inflation factor found for the CD-50 869 system results from a non-Gaussian position angle distribution rendering the value unusable.

be conducted within the framework of this work since the host-companion separations of the targets at hand have already dropped into a range at which even GRAVITY observations are impossible. Once the separations have sufficiently increased again, a dedicated follow-up should be able to shed light on the question of companion binarity.

A note on the filter magnitudes shown in Fig. 3.4: to present the isochrones of both evolutionary models in the same filter system, we converted the ATMO isochrones from APO/NSFCam.MKO\_K to 2MASS/2MASS.Ks magnitudes (for details on the conversions between the two filter systems, see Hawarden et al. 2001 and Carpenter 2001). The slight divergence of the isochrones towards lower masses can be explained by the fact that the filter system conversion was derived using stellar photometry. It should be noted, however, that the conversion was only performed for visualisation purposes within Fig. 3.4. The subsequent bootstrapping, which was conducted in the APO/NSFCam.MKO\_K and 2MASS/2MASS.Ks filter magnitude space for the ATMO and Baraffe models, respectively, is therefore not affected by any potential isochrone divergence.

Since WT 766 B and StKM1-1494 B lie in a the region of the mass-magnitude plane where both evolutionary models are defined, we were able to use both to infer age, effective temperature and radius. Figure 3.5 and Table B.4 show that the ages inferred using both models match. While the effective temperature posteriors agree for WT 766 B this is not the case for StKM1-1494 B. Furthermore, the radius posteriors from both models disagree for both targets. For G ...3872 B and HD 17155 B only one model could be used for the characterisation. Due to their placement on the mass-magnitude plane, no such analysis could be conducted for the three potentially under-luminous targets G ...6464 B, CD-50 869 B, and G ...1920 B.

The clustered and thus degenerate nature of isochrones describing older objects within the mass-magnitude plane is reflected in the age posteriors of some of the targets. Their samplings are skewed towards older ages. In general the obtained ages for our target sample companions are remarkably low. This comes as a surprise seeing that the stellar age distribution in the solar neighbourhood peaks at a significantly higher value (at  $\sim 5\,\mathrm{Gyr}$  according to Gondoin 2023). This bias towards young ages could be caused by an observational overestimation of the companion flux amounting to a photometric calibration error of the GRAVITY data. Investigation into whether or not this is the cause of the observed bias is outside the scope of this work. If confirmed, however, correcting for the resulting magnitude offset would exacerbate the aforementioned under-luminosity observed in three of the companions.

Having acquired the companions' dynamical masses as well as their ages, we could apply the same evolutionary models as above to generate synthetic companion magnitudes in different wavelength bands. This serves two goals. On the one hand it enables us to verify that our initial zero-companion-Gaia-flux hypothesis was justified, closing the loop and ascertaining that the mass constraints on the hosts and companions are trustworthy. On the other hand these magnitudes will be informative for potential future follow up observations of the companions with other instruments working in different wavelength ranges. The respective synthetic companion magnitudes are listed in Table B.3. Inspection of the G band flux ratio of the target systems for which it could be computed affirms that

3.5 Conclusion 83

they are indeed negligible.

Figure 3.6 establishes that the majority of new companions presented here are spread out along the L-dwarf branch with G ...0976 B, G ...1920 B, and CD-50 869 B consistent with M-L transition bodies (Kirkpatrick et al. 1999). G ...3872 B and G ...6464 B are the only companions discussed here that appear removed from the literature population. In the case of G ...6464 B this could constitute another hint at companion binarity. Alternatively, as Faherty et al. (2014) point out, the strong red colour of G ...6464 B might indicate a thick cloud deck in its atmosphere. G ...3872 B on the other hand sits above the L-T (Kirkpatrick 2005) transition possibly indicating a methane rich atmosphere.

Finally, it is worth remembering that we detected an additional companion, which – judging by its large K band flux relative to its host – is likely of stellar nature. The high contrast was the reason G ...0976 B could not be included in the analysis since the crucial zero-companion-Gaia-flux hypothesis could not be upheld. Since the orbit listed in the Gaia NSS two-body orbit catalogue did facilitate a successful detection, however, there is every reason to expect that such a Gaia-informed observation can be repeated. Obtaining additional epochs of this companion will enable further constraints to be placed on its orbit and thereby its mass, potentially solving the question as to why it is so bright in the K band.

## 3.5 Conclusion

In this work we have demonstrated the synergies between Gaia and GRAVITY by showcasing how the astrometry-based orbital solutions contained in the NSS two-body orbit catalogue can be used to inform high-angular-resolution follow-up observations. We detected and confirmed eight companions, of which seven were previously unknown. Every conducted observation resulted in the successful detection at or close to the predicted position of the inferred companion. It is important to note that the unprecedentedly precise nature of the astrometric data collected by Gaia makes it difficult to follow up on or challenge using other currently available instruments. In most cases, the high contrasts and small angular separations between hosts and companions as suggested by the orbits listed in the NSS catalogue are inaccessible to today's direct imaging facilities. From this point of view, GRAVITY offers a unique opportunity to test the orbits put forward in the NSS two-body orbit catalogue. We can conclude that the results presented here – both in terms of the 100% success rate in detecting the inferred companions and in terms of how the two data sets can be combined – constitute an independent validation of the Gaia NSS orbital solutions as well as the Gaia binary mass estimates. Applying the Gaia-GRAVITY ensemble to companion candidates of planetary nature will be an intriguing next step in exploring the two instruments' joint potential.

Combination of the *Gaia* and GRAVITY data by means of a Bayesian approach revealed more refined orbital solutions as well as tight constraints on the host and companion masses. They suggest that five companions of the sample can be categorised as brown dwarfs, while two, CD-50 869 B and G ...1920 B, are of a stellar nature. The same can be expected for

#### G ...0976 B.

The GRAVITY K band spectra were investigated to further characterise the companions. To this end, evolutionary models were used to obtain constraints on their age, effective temperature, and radius. The possibility of probing for companion binarity by means of a high-resolution astrometric time series with GRAVITY is discussed here and should be considered for the potentially under-luminous targets G ...6464 B, CD-50 869 B, and G ...1920 B. Comparison with a template population from the literature further contextualises the companion sample and indicates that they are consistent with L- to T-type brown dwarfs.

The potential of this method in confirming candidates suggested by *Gaia* astrometry cannot be overestimated. Rapid direct detections of the inferred companions render the breaking of the mass degeneracy between host and companion a matter of routine. The resulting tight constraints on the companion masses can shed light on formation processes and interior evolution.

The procedures showcased in this work are not confined to brown dwarf companions but can readily be applied to planetary candidates as well. Such candidates are still scarce in DR3 but should be forthcoming in DR4, which is expected to be published in 2026. The astrometric time-series data to be released therein will amount to a treasure trove of planetary candidates accessible with GRAVITY. And finally, with the imminent arrival of GRAVITY+, the possibility of accessing companions at even smaller contrasts bodes well for the future synergies between *Gaia* and GRAVITY as well as direct imaging in general.

# Chapter 4

# Surveying the planetary frontier: pushing Gaia - GRAVITY to the limit

This chapter describes the preparations and outcome of an ESO Director's Discretionary Time (DDT) observing programme (ID: 113.27R5). None of its content was published before.

# 4.1 Motivation for the observing programme

#### 4.1.1 A logical next step

In the wake of the successful demonstration of the synergy between Gaia and GRAVITY outlined in Chapter 3, it comes as an instructive exercise to consider how to expand upon this technique. In terms of angular separation from the star, we are already scraping against the lower limit of what is possible with GRAVITY: at a separation of approximately 34 mas (which, for this target, translates to a linear distance of less than 1 AU), the closest companion detected in Chapter 3 is Gaia DR3 2728129004119806464. At even closer angular separations, the leakage of star light into the GRAVITY science fibre increasingly inhibits robust companion detections and the achievable contrast worsens dramatically (Pourré et al. 2024). Instead, aiming to detect less massive companions is a more straightforward direction in which to grow this technique and our detection capabilities. Naturally, targeting gradually less massive companions is an intriguing prospect since – if a continuous reduction is possible – our detection domain will eventually overlap with the planetary regime. Routinely obtaining dynamical masses of exoplanet companions alongside a snapshot of their spectral and photometric appearances in the K-band at the low cost of a single GRAVITY epoch, would constitute a major step towards building a truly demographic sample of the exoplanet population at separations comparable to the gas giants in the Solar System. In this sense, pushing for companions with lower masses can be considered the logical next step in the development of the Gaia-GRAVITY synergy. Here, we present an effort at leapfrogging the low-mass BD regime and immediately pursuing the detection of Gaia-inferred planets, instead. The mass-semi-major axis domain where we pursue these discoveries is highlighted in Fig. 4.1. While this ambitious approach represented a formidable challenge, adopting this strategy forced a definitive answer to the question of whether there are planets hiding in the Gaia DR3 catalogue that lend themselves to direct detection with GRAVITY.

# 4.1.2 A matter of timing

This planet-hunting project was initially conceived of in early 2024. At the time, the several-year-long GRAVITY+ upgrade had just been initiated (Gravity+ Collaboration et al. 2022). In the context of this programme, the AO-system used by the instrument when observing in UT-mode was scheduled to be overhauled. As planned, the MACAO system (Arsenault et al. 2003) was decommissioned in July 2024 to be replaced by the GRAVITY+ Adaptive Optics system (GPAO). Once complete, the new infrastructure will include wavefront sensors and laser guide stars (LGS) on all four UTs. It will provide an up to 2.5 times higher Strehl ratio for bright objects, reduce speckle noise and enable so-called dark-hole techniques (Bourdarot et al. 2024). However, in the short-term, the staged nature of the commissioning process resulted in a stricter magnitude limits for the natural guide stars (NGS) the AO system is working with. Until the LGS become available and GPAO will thus be fully operational in 2026, it is limited to NGS brighter than 12.5 mag

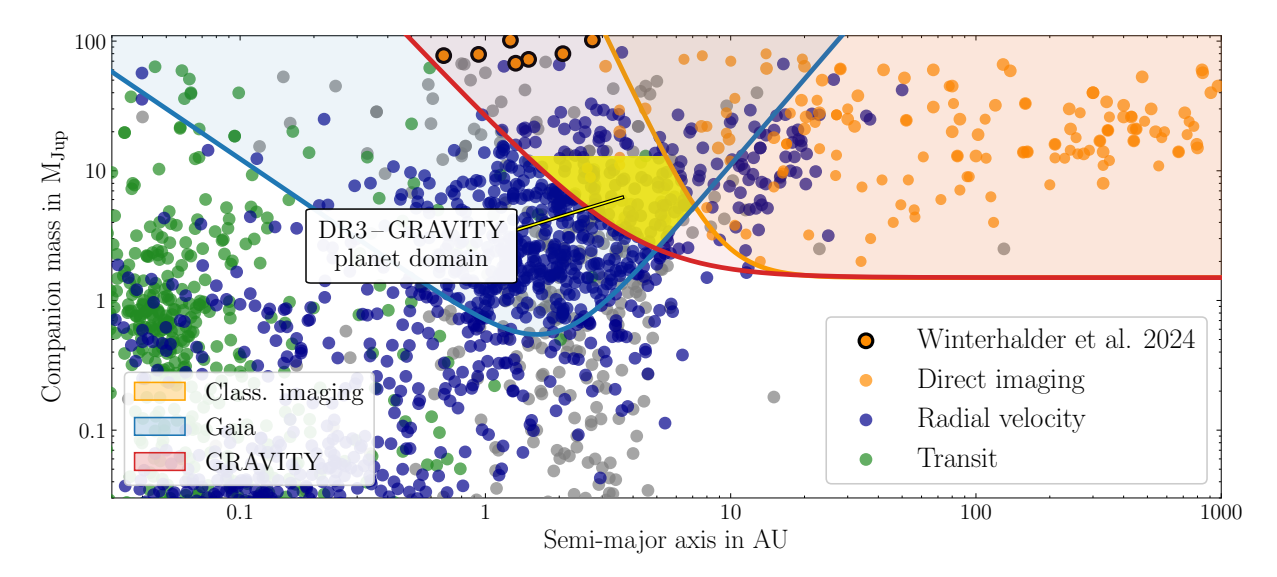


Figure 4.1: Same as Fig. 1.4 but including the companions detected by Winterhalder et al. (2024) and where the Gaia–GRAVITY planet detection domain is located. The sensitivity ranges of different methods and instruments are indicated by the shaded regions. The blue Gaia detection region corresponds to the 5 year mission estimates around a  $0.4 \,\mathrm{M}_{\odot}$  at 25 pc (Sozzetti & de Bruijne 2018). The red and orange lines delineate the detection regions of GRAVITY and classical direct imaging instruments, respectively. They are approximations of the contrast curves shown in Pourré et al. (2024). Classical direct imaging is not sensitive in the aimed for detection domain, that partially overlaps with the RV planet population.

in the R-band. Observing with GRAVITY in dual-field on-axis mode, we typically use the respective host as the FT reference source. As we shall see in Sect. 4.2, the list of exoplanet candidates in the *Gaia* NSS two-body orbit catalogue shrinks to a handful of targets viable for a GRAVITY follow-up. However, the only prospective planet-hosts we could identify did not meet the provisional GPAO R-band magnitude condition. Therefore, to hunt for planets in the DR3 version of the *Gaia* NSS two-body orbit catalogue, we were effectively forced to make use of the soon-to-be-decommissioned MACAO system, compelling us to conduct this observing campaign in the framework of a DDT programme.

# 4.2 Target selection

# 4.2.1 Preliminary filtering

To begin with, the target selection process that preceded our attempt at confirming Gaia-inferred companions of planetary nature followed the procedure outlined in Sect. 3.2.1. First, we applied straightforward cuts to the full list of candidates in the NSS two-body orbit catalogue. By querying the Binary Masses Table (Gaia Collaboration et al. 2023a) we filtered out any candidates exhibiting minimum masses greater than 15  $M_{Jup}$ . We fur-

ther constrained this planetary sample by removing candidates that are not observable from Paranal during the period until the decommissioning of the MACAO system. These uncomplicated filtering steps were followed by a slightly more intricate selection condition. For the remaining candidates we computed the position of the prospective planet companion relative to the host at different observing dates spanning the period until July 2024. Only such candidates that exhibited angular companion-to-host separations larger than 25 mas are retained. This removed all companions that remain concealed within the effective inner working angle of GRAVITY in the period until MACAO decommissioning.

### 4.2.2 Age filtering

Contrary to the procedure in Sect. 3.2.1, we were here forced to include the age of candidate systems as a selection criterion. Whereas the age is irrelevant for the detectability of BD companions, it is critically important for candidates in the planetary mass regime. In this domain, only young planets are bright enough to satisfy the separation-dependent GRAVITY contrast limit between companion and host (Pourré et al. 2024). Since the literature does not provide age constraints for any of the potential host stars in our list we needed to estimate their ages manually. There are different methods that can be invoked to estimate the age of a given system.

A first attempt was made to identify young candidate systems by their potential membership to a known young stellar association (Zuckerman & Song 2004). To this end, we employed Banyan  $\Sigma$ , a Bayesian analysis tool that estimates the probability of a given star to be a member of different stellar associations (Gagné et al. 2018). We compiled a set of young associations to be considered in our analysis. This list consisted of the  $\beta$  Pictoris moving group (Zuckerman et al. 2001a), TW Hydrae (de la Reza et al. 1989; Kastner et al. 1997), Tucana-Horologium (Torres et al. 2000; Zuckerman et al. 2001b), Carina (Torres et al. 2008), Argus (Makarov & Urban 2000) and Columba (Torres et al. 2008). None of the candidates appeared to be members of the young associations listed above.

Compelled to resort to a different age dating technique, we decided to conduct a gyrochronological examination of the candidate list. Briefly put, the rapid rotation exhibited by young stars can manifest itself as detectable variations in their photometric signal. Periodicities in the light curves of stars can therefore be used as a proxy for their ages (Barnes 2003, 2007b). Since the sources contained in the *Gaia* data set are often uncatalogued stars that have not been studied in any detail before, we decided to make use of the rich photometric all-sky back catalogue established by the Transiting Exoplanet Survey Satellite (TESS; Ricker et al. 2015). Querying the TESS archive using lightkurve package (Lightkurve Collaboration et al. 2018), we retrieved all photometric data available for the remaining host candidates. Since TESS surveys the sky by repeatedly observing pre-defined sectors, it is possible that the obtained data exhibits long temporal gaps. Observations stemming from different sector visits not sharing a common calibration, makes identifying periodic patterns in the full light curves almost impossible. We therefore searched for signals that repeat at periods of several days within the light curves collected during individual sector visits. Computing Lomb-Scargle periodograms (Lomb 1976; Scargle 1982) for

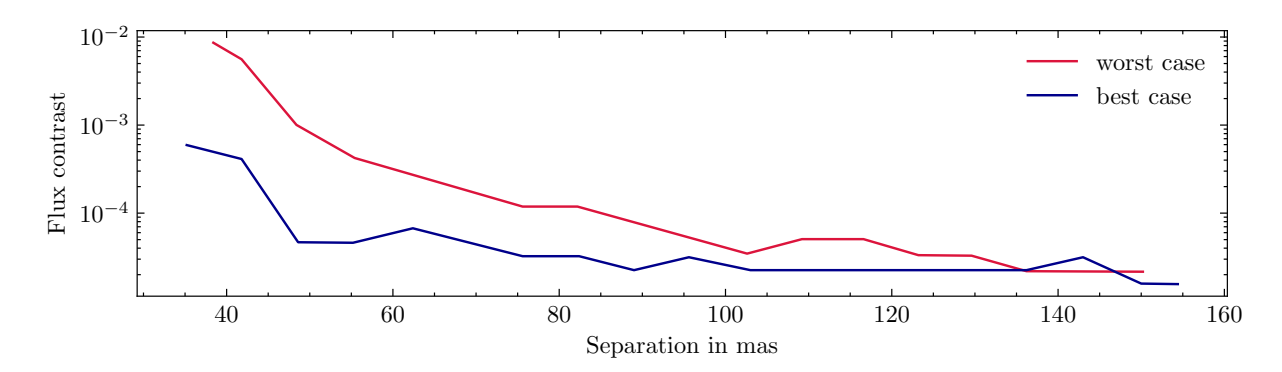


**Figure 4.2:** Contrast achievable with GRAVITY as a function of host-to-companion separation. The worst and best cases correspond to a perpendicular and parallel alignment of the separation vector with the longest projected VLTI baseline, respectively.

each light curve and extracting the maximum power below an upper limit of six days, we obtained a rough estimate of a potential short-term period, P, in each light curve. Since the resulting periodograms are dominated by noise, it should be noted, that most of these periods can be expected to be spurious, however. Ideally, one would only retain systems that can confidently be classified as rapidly rotating. Given the small sample size of planetary candidates potentially accessible by GRAVITY until MACAO decommissioning, this luxury was not afforded to us, however. We therefore decided to hold on to all period estimates resulting from the periodogram analysis and converted them to stellar ages via

$$\log (t_{\text{gyro}}/\text{Myr}) = \frac{1}{n} [\log (P/d) - \log a - b \log (B - V - 0.4)], \qquad (4.1)$$

where  $n=(0.519\pm0.007)$ ,  $a=(0.773\pm0.011)$ ,  $b=(0.601\pm0.024)$  and B-V is the measured stellar colour (Barnes 2007b). Taking the mean of the ages computed on the basis of the different light curves and propagating the errors through each step, we obtained the gyrochronological age estimates for the different candidate systems.

To assess the detectability of the remaining companions we needed to impose a contrast condition: at their respective gyrochronological age, would the contrast with their respective host be large enough to make a detection with GRAVITY viable? Such an assessment requires the knowledge of the contrast limit of the instrument. This depends on the angular host-to-companion separation and the viewing angle during the observation. If the separation vector is oriented parallel to the longest projected VLTI baseline the contrast capability is maximised, while a perpendicular orientation puts a tighter limit on the achievable contrast. We extracted both these best and worst cases from Fig. 9 of Pourré et al. (2024). They are visualised in Fig. 4.2.

Interpolating both curves and evaluating the achievable contrasts for the best and worst cases at the predicted host-to-companion separations (see Sect. 4.2.3), we obtained the two thresholds for each candidate. These contrasts were then converted to magnitude differences, which – upon addition to the host magnitudes in the K-band – yielded the respective companion magnitude limits. If the companions are fainter than their respective

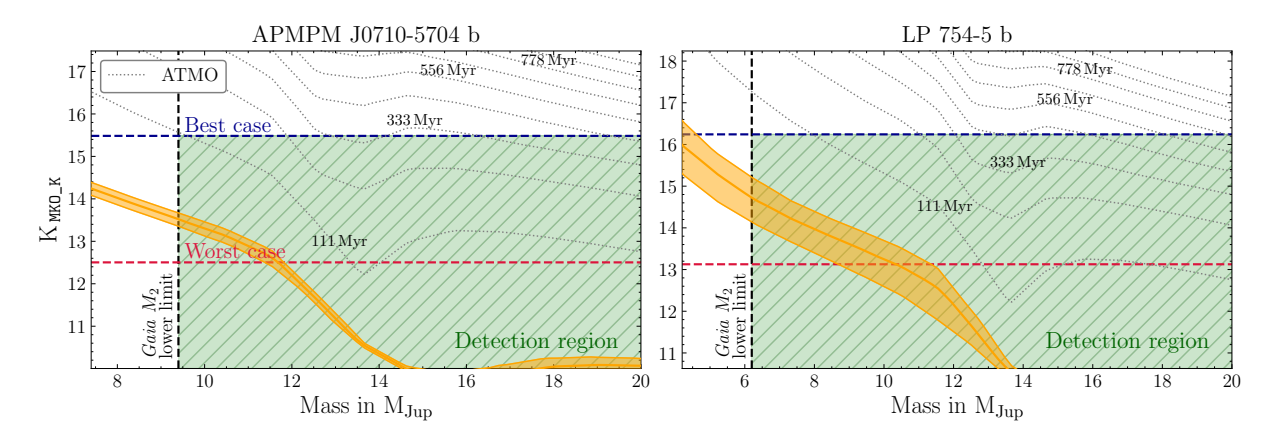
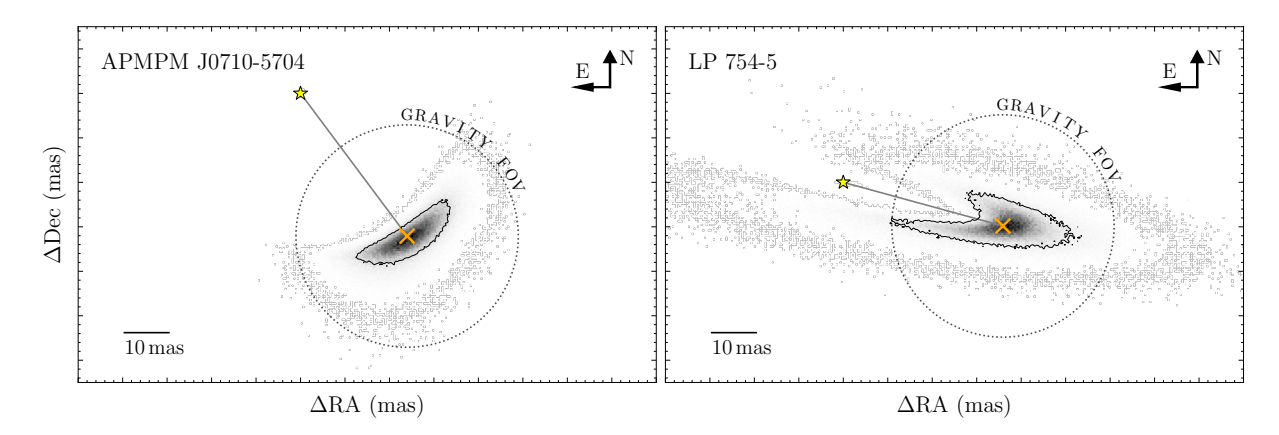


Figure 4.3: K-band magnitudes of the two Gaia-inferred planets feasible for a GRAV-ITY follow-up as a function of mass. The orange lines and shaded regions show the ATMO isochrones (Phillips et al. 2020) and their 68% confidence intervals at the systems' respective gyrochronological ages. Other isochrones are shown as dotted lines with every other bearing an annotation indicating the age value. The horizontal dashed lines show the best and worst case contrast limits effectively defining how faint a given candidate can be to still be detectable using GRAVITY depending on the orientation of the longest VLTI baseline. The vertical dashed line indicates the lower companion mass estimate listed in the DR3 Binary Masses Table. These are the only candidates potentially young enough such that their isochrones overlap with the detection region that is shaded green.

best or worst thresholds depending on the orientation of their separation vector, they will not be detectable using GRAVITY. Thus, the last ingredient we required to gauge which candidates were viable for a follow-up were their expected magnitudes. Using the gyrochronological age estimates in combination with the Phillips et al. (2020) evolutionary model we computed the theoretical magnitudes we can expect the prospective planetary companions to exhibit. Since the Gaia Binary Masses Table only provides lower and upper companion masses we computed these model magnitudes as a function of different masses. Comparison of the magnitude values with the respective limits revealed that only two planet candidates appeared feasible for a follow-up with GRAVITY, namely APMPM J0710-5704 (b)<sup>1</sup> and LP 754-5 (b). The gyronchronological approach outlined above yielded ages of  $(32 \pm 3)$  and  $(33.0 \pm 0.8)$  Myr, respectively. These estimates should be treated with extreme caution. In the absence of other, more reliable age constraints and without the option to conduct auxiliary observations due to the looming MACAO decommissioning, we were compelled to submit the DDT based on the two thus identified targets. Their magnitudes at their respective gyrochronological ages as a function of mass in comparison with the best and worst GRAVITY contrast limit cases are presented in Fig. 4.3.

 $<sup>^{1}</sup>$ We enclose the planet identifier "b" in brackets to indicate that these objects are unconfirmed candidate planets.



**Figure 4.4:** Position predictions for the planet candidates in the two viable target systems for observations on the 29th of April and 28th of May 2024, respectively. These dates were chosen to maximise the host-to-companion separation during the period until MACAO decommissioning. The yellow star indicates the position of the host, the orange cross marks the mean companion position at the time of observation. The black contour encircles the 68 % of all position predictions indicated by the grey colourmap. The dotted circle visualises the GRAVITY science fibre FoV, here conservatively defined as 50 mas in diameter.

### 4.2.3 Position predictions

For the two potentially viable target systems we computed the companion positions relative to the respective host by randomising over the solutions listed in the *Gaia* NSS two-body orbit catalogue. In the same manner as in Sect. 3.2.1, we accounted for correlations between the different orbit elements so as to obtain more constrained companion positions. Only such companions exhibiting a sufficiently constrained position prediction to be covered by the FoV of the GRAVITY science fibre are feasible targets for a follow-up. As is evident from the position probability maps depicted in Fig. 4.4, this condition is met for both planet candidates.

### 4.3 Results of the observing programme

### 4.3.1 Missing APMPM J0710-5704 (b)

To pursue the science case outlined above, we submitted a DDT proposal on the 19th of April 2024. In principle, this allowed for enough time to utilise the next VLTI observing run scheduled for the period between the 24th and 29th of April. Incidentally, this was the last window during which our first target system, APMPM J0710-5704, was observable from Paranal. Unfortunately, approval of our proposal was only issued on the 30th of April, rendering an observation impossible and effectively removing 50 % of our target sample. A follow-up and potential confirmation of APMPM J0710-5704 (b) must therefore wait until

Target	Start (UTC)	NEXP/NDIT/DIT(s)	Airmass	$\tau_0$ (ms)	Seeing (arcsec)	Fibre pl $\Delta RA \text{ (mas)}$	acement $\Delta \text{Dec (mas)}$
		2nd	June 2024	:			
LP 754-5 LP 754-5 (b)	05:04:46 05:15:54	5/8/0.7 24/8/0.7	1.25 1.25	6.5 7.3	0.53 0.48	0 -54.74	0 -15.35
		3rd	June 2024				
LP 754-5 LP 754-5 (b)	09:12:45 09:31:34	5/8/0.7 8/8/0.7	1.13 1.15	5.8 6.0	0.36 0.36	0 -54.74	0 -15.35

**Table 4.1:** GRAVITY observation log of LP 754-5.

Notes. See notes to Table 2.1.

GPAO is fully operational and equipped with LGS systems. Like many other potential host stars identified by *Gaia*, APMPM J0710-5704 is too faint to serve as an NGS with GPAO.

### 4.3.2 Unveiling LP 754-5 (b)'s true identity

The delay in DDT approval left us with only one viable target system, LP 754-5. Aiming to detect a planetary companion, we observed the target in dual-field on-axis mode on the 2nd and 3rd of June 2024. Table 4.1 logs the observing strategy and conditions during both nights. The achieved u-v plane coverage during both nights is visualised in Fig. C.1.

As in Chapters 2 and 3, we used the ESO GRAVITY instrument pipeline 1.6.4b1 for the initial data reduction. Subsequent reduction steps (see Appendix A of GRAVITY Collaboration et al. 2020) did not yield a clear detection. Evidently, a more thorough analysis of the interferometric observables was required to make sense of the data. Upon closer inspection of the data, it became evident that the flux ratio between the two detected objects is close to 1 hinting at the detection of a stellar binary. This necessitated a different data analysis approach compared to the routine employed for exoplanet observations. Discarding the off-axis SC integrations on the position predictions of the putative planetary target to only retain the interspersed on-axis observations obtained while both fibres were pointed at the host (see Sect. 1.5.1), we opted for a classic interferometric modelling analysis of the visibility amplitude and closure phase data.

Using the PMOIRED package (Mérand 2022) we proceeded to fit an unresolved binary model to the data. Specifically, we modelled the host and its putative companion as two point sources with the flux of the latter as a fraction of that of the former and handled as a free parameter. Moving the companion disc to different positions around the host that was fixed at the origin, we found the observed closure phase and visibility amplitude to be best described by a stellar binary system as opposed to an exoplanet-hosting star. The closure phase and visibility amplitude data together with the best fitting models are shown in Fig. C.2 and C.3, respectively. The posterior samplings, presented as corner plots in Fig. C.4, indicate that the flux ratio between the two binary components is consistent with

Fitting parameter	2nd June	3rd June
Flux ratio	$0.64 \pm 0.07$	$0.49 \pm 0.01$
$\Delta RA \text{ (mas)}$	$-41.97 \pm 0.08$	$-41.51 \pm 0.02$
$\Delta \mathrm{Dec}\ (\mathrm{mas})$	$-5.38 \pm 0.13$	$-5.75 \pm 0.03$

Table 4.2: Parameter posteriors obtained from the PMOIRED fitting routine.

**Notes.** The flux ratio is here defined as the ratio between the flux of the secondary divided by the flux of the primary binary component.

a stellar companion. The numerical results of the fitting procedure for both nights is also presented in Table 4.2.

The astrometry of the secondary binary components differs significantly between the two nights in both  $\Delta RA$  and  $\Delta Dec$  indicating a tentative detection of orbital motion among the two objects. The variation of the flux ratio between the two nights of observation, on the other hand, is not expected and unlikely to be astrophysical. There are several potential explanations for this inconsistency. Firstly, no calibration source was observed for this observation. This is standard procedure when observing exoplanets but can cause offsets in the closure phase. Secondly, we need to account for the fact that the Gaia-based orbit solution that the observation planning was based on does not correspond to the orbit of the host star since for stellar binaries the photocentre is shifted according to the flux ratio. Therefore, the zero-companion-Gaia-flux hypothesis that we introduced in Chapter 3 breaks down, implying that the positioning of the FT was inaccurate. As mentioned in Chapters 2 and 3, observing a target in such an off-centre manner will cause flux throughput losses that need to be accounted for (see Appendix A.1 and B.1). Left uncorrected for, this loss of fibre throughput can cause an inconsistent flux ratio between the two nights. Finally, it should be noted that the instrument transfer function could conceivable cause the flux ratio inconsistency stemming from resulting offsets in the closure phase and factors in the visibility amplitude. Accordingly, we allowed for the transfer function to be fit alongside the binary model following an approach first implemented in Deshmukh et al. (2025). This procedure gives more confidence in the measured flux ratio, hence reinforcing the notion that the variations we see are due to the FoV effects outlined above.

In the absence of additional data, conclusively interpreting the GRAVITY epochs and deciphering this target system is challenging. An RV monitoring campaign may shed light on its orbital geometry. Combining the linear semi-major axis measurement obtained from such an RV follow-up with the angular semi-major axis constrained from the interferometric observation would also yield a refined distance measurement. Given the non-trivial dependency of the photocentre on the system configuration, the *Gaia* parallax is likely unreliable. A preliminary check using the Exposure Time Calculator provided by ESO indicates that the system should be observable with VLT/CRIRES+ (Kaeufl et al. 2004; Follert et al. 2014) at high S/N within a few minutes given the infrared brightness of the target. Even without such a follow-up, we can conclude on the basis of the GRAVITY data

alone that the LP 754-5 system does not host the potentially directly detectable planet inferred by *Gaia*. Instead, it is a stellar binary masquerading as a planet-hosting star and thus belongs to a class of *Gaia*-sources referred to as "imposter binaries".

### 4.4 Gaia follow-up observations in context

By itself, the non-detection resulting from our observing programme is of limited use for inferring how common the imposter binaries mentioned above truly are. To assess the degree of false-positive contamination within the Gaia DR3 NSS two-body orbit catalogue, we need to place the result into context with other, more extensive follow-up campaigns. The obvious comparison is be drawn is the one with the results outlined in Chapter 3 (and Winterhalder et al. 2024). There we presented the follow-up of eight Gaia-inferred substellar companion candidates. At first glance, the fact that all of these observations yielded successful detections contrasts starkly with the non-detection outlined in this chapter. Far from being incompatible, however, the yield discrepancy can be attributed to the inherently different target selection procedure employed by the two programmes, in that we only considered high-mass BD companion candidates in Chapter 3. Indeed, upon confirmation and the constraining of their dynamical masses, some of the detected companions initially deemed substellar might rather be classified as low-mass stars. In general, such high-mass substellar companions induce stellar reflex motions that are registered by Gaia at a higher significance than planetary companions. The resulting NSS orbital solutions are thus more reliable than those provided for companion candidates inferred in the planetary mass regime.

The results reported in Marcussen & Albrecht (2023) substantiate this conclusion. Their analysis of archival high-resolution spectra and RV time-series observations of the planetary companion candidates listed in the NSS two-body orbit catalogue implies a large fraction of false-positives contaminating the data set. A similar conclusion is reached by Stefánsson et al. (2025), whose dedicated RV follow-up programme of 28 Gaia-inferred substellar companion candidates did result in two planet confirmations, objects now referred to as Gaia-4 b and Gaia-5 b, but also unmasked 21 of the targets as stellar binaries. Both works note the possibility of identifying imposters by double-line signatures in highresolution spectra. A single spectrum obtained at precisely those orbital phases at which the two lines of such spectroscopic binaries overlap can be misleading, but several epochs should suffice to rule out an SB2 nature of a given target system. Naturally, imposter binaries orbiting each other in a face-on orientation as projected onto the plane of the sky will successfully evade such preventive diagnosis attempts. Sahlmann & Gómez (2025) suggest that machine learning approaches may provide a potential way forward by identifying reliable Gaia candidates on the basis of the source catalogue alone without the need for an expensive and protracted vetting process. A large training set of validated and refuted candidates is essential for such a procedure to work dependably, highlighting not only the need for more Gaia-based direct confirmations but also the fact that there is scientific merit in non-detections like the one we have presented in this chapter.

### Chapter 5

# Taking the next step: hunting exomoons with optical interferometry

The content of this chapter is a reproduction of an article submitted to Astronomy & Astrophysics on the 31st of July 2025, titled:

### Planetometric<sup>1</sup> exomoon detection via optical interferometry

T. O. Winterhalder, A. Mérand, J. Kammerer, S. Lacour, W. O. Balmer, G. Bourdarot, A. Glindemann, Th. Henning, G.-D. Marleau, M. Nowak, N. Pourré, E. Rickman

As first author of this publication, I was in charge of the analysis, interpretation and writing process. A. Mérand, J. Kammerer, S. Lacour and A. Glindemann acted as supervisors. The rest of the authors list provided comments before submission to the journal. I have taken the liberty of adjusting the label font sizes in some figures where appropriate. The paper abstract can be found on the reverse of this page.

<sup>&</sup>lt;sup>1</sup>In this chapter, I use the word "planetometric" to mean position measurements of a planet relative to its host, in order to differentiate them from "astrometric", that is stellar, position measurements. Note, however, that most authors in the literature use the word "astrometric" for both stellar and planetary position measurements.

#### Abstract

Context. With no conclusive detection to date, the search for exomoons, satellites of planets orbiting other stars, remains a formidable challenge. Detecting these objects, compiling a population-level sample and constraining their occurrence will inform planet and moon formation models and shed light on moon habitability.

Aims. Here, we demonstrate the possibility of a moon search based on "planetometric" time series data, repeated measurements of the position of a given planet relative to its host star. The perturbing influence of an orbiting moon induces a potentially detectable planetary reflex motion. Methods. Based on an analytical description of the planetometric signal amplitude, we place the expected signatures of putative moons around real exoplanets into context with our current and future planetometric measurement precision. Modelling the orbital perturbation as a function of time, we then simulate the detection process given different target system configurations, instrumental measurement precisions and numbers of observational epochs to obtain the first planetometric exomoon sensitivity curves.

Results. The planetometric technique already allows for the detection and characterisation of binary planets and favourable moons around giant exoplanets and brown dwarfs. Since the detection sensitivity of this method is mainly governed by the achievable planetometric precision, long-baseline interferometry lends itself ideally to this pursuit. We find that, on the basis of 12 epochs obtained with VLTI/GRAVITY, it is already today possible to infer the presence of a  $0.14\,\mathrm{M_{Jup}}$  satellite at a separation of  $0.39\,\mathrm{AU}$  around AF Lep b. Future facilities offering better precision will refine our sensitivity in both moon mass and separation from the host planet by several orders of magnitude.

Conclusions. The planetometric method of exomoon detection, especially when applied to interferometric observations, provides a promising avenue towards making the detection of these elusive objects a reality and efficiently building a sample of confirmed specimens. With a future facility that achieves a planetometric precision of  $1 \,\mu$ as, probing for Earth-like moons within the habitable zone of a given star will become a realistic proposition.

5.1 Introduction 99

### 5.1 Introduction

With the number of confirmed detections growing steadily, the field of exoplanet research is in the process of branching out into a diverse set of subdisciplines, ranging from formation modelling to the atmospheric characterisation of individual specimens. Another such ongoing pursuit is the search for low-mass companions to exoplanets, bodies conventionally called exomoons<sup>1</sup>. With the exception of Mercury and Venus, every planet (and even some dwarf planets) in our Solar System harbours at least one moon. It is thus plausible that planets orbiting other stars are accompanied by their own satellites. A successful detection of such an object in an exoplanetary system would be the first step towards assessing the prevalence of exomoons around different types of host planets and building a populationlevel moon sample, which can help calibrate our models of moon formation, whether via capture (Hansen 2019), impact (Barr & Bruck Syal 2017) or in-situ within the circumplanetary disc (Moraes & Vieira Neto 2020). Such knowledge will provide vital clues that can inform formation and evolutionary models (e.g. Peale & Canup 2015; Batygin & Adams 2025), the selection of follow-up targets deemed potentially habitable (Martínez-Rodríguez et al. 2019; Dobos et al. 2022) and the interpretation of putative biosignature detections in the future (Rein et al. 2014).

Since first articulated in detail by Kipping (2009), the detection of exomoons by means of planetary transit observations has been the main focus of the community. Both photometric effects as well as transit timing and duration variations as a result of the presence of a moon orbiting a given planet have been proposed and modelled. So far, however, no bona fide detection has been made (candidates include Kepler-1625 b-i and Kepler-1708 b-i; Teachey & Kipping 2018; Heller et al. 2019; Kreidberg et al. 2019; Teachey et al. 2020; Kipping et al. 2022; Heller & Hippke 2024; see also Kenworthy et al. 2023).

More recent studies simulating the survival rate of moons around planets at different orbital separations from their hosts are suggestive of why there has not yet been a confirmed detection. The sensitivity of transit studies – inherently biased to short orbital periods and hence small separations between host and planet – appears to be limited to a parameter space where moons are prone to being ejected or tidally disrupted (see e.g. Dobos et al. 2021). To put it another way, exomoons are unlikely to survive in orbit around the planets accessible to transit observations. On the other hand, these simulations suggest that moons around far-out, long period exoplanets of the kind accessible to direct imaging studies have a high likelihood of remaining in orbit for several Gyr. Here, however, our current contrast, sensitivity and resolution capabilities do not allow for detecting the presence of such moons directly. Spectroastrometric detections may be a way forward, but as Agol et al. (2015) point out, pursuing this strategy requires a next-generation space telescope.

A "middle ground" between the two extremes is to hunt for moons around planets orbiting their host stars every few hundred days. In this window of opportunity, we expect the survival rate to be large enough to make a discovery possible, while also possessing

<sup>&</sup>lt;sup>1</sup>While a strict definition of the term is yet to be agreed upon, we will use the word "exomoon" to mean a body gravitationally bound to a given exoplanet. Depending on the mass ratio between the two components, the term "binary planet" may be more appropriate, however.

the means of performing such a detection in the first place. As we shall show in this paper, precisely monitoring a given planet's position over time can reveal deviations from the expected Keplerian trajectory, that is a higher-order epicyclic or "wobble" motion, induced by the presence of an orbiting moon. Such a detection would amount to applying the astrometric method of planet detection by monitoring the periodic movement of a star to a planet-moon pair. Such a "planetometric" technique represents a readily applicable strategy towards making the first extrasolar satellite detection a reality. The convenient possibility of constraining the mass and orbital elements of the moon from the planetometric time-series renders this method especially compelling.

At the heart of this new drive towards dynamic moon detection lies the unprecedented planetometric precision of the near-infrared interferometer GRAVITY at ESO's Very Large Telescope Interferometer (VLTI; GRAVITY Collaboration et al. 2017). With a planetometric precision of 50  $\mu$ as (GRAVITY Collaboration et al. 2019), the instrument has already facilitated remarkable constraints on the dynamical masses and orbital solutions of a large sample of directly detected planets. Notably, GRAVITY enabled an independent dynamical detection and characterisation of  $\beta$  Pic c based solely on its perturbations to the orbit of  $\beta$  Pic b (Lacour et al. 2021) and provided the key data set used to resolve the first known brown dwarf, Gliese 229 B, into two near equal-mass binary components (Xuan et al. 2024; Whitebook et al. 2024).

Here, we present an analytical modelling effort that aims to determine our current plane-tometric exomoon detection sensitivity and explore how future interferometric instruments and facilities might aid the hunt for these elusive objects. This paper is structured as follows: in Sect. 5.2 we outline how to calculate the planetometric signal amplitude of a moon and to simulate its variation as a function of time. Sect. 5.3 deals with current and future capabilities of planetometric exomoon detection on the basis of several exemplary systems and the case of a putative moon around  $\beta$  Pic b in particular. The modelling of detection attempts based on multiple planetometric epochs is described in Sect. 5.4 before the derived sensitivity curves are presented in Sect. 5.5. We conclude our study in Sect. 5.6.

### 5.2 The planetometric signal

The concept of a planetometric exomoon detection essentially amounts to a re-application of the astrometric method of planet detection. As we shall see, the main differences and additional challenges with respect to the planet detection science case are the circumstance that the observable perturbation amplitudes are orders of magnitude smaller and the fact that we are required to perform the position measurements on the planets themselves. To aid future target selection and observation planning, it is therefore crucial to understand the behaviour of the observable as a function of different parameters. Here, we briefly introduce the planetometric signal amplitude and variability in time.

### 5.2.1 Planetometric signal amplitude

To assess the detectability of a given star–planet–moon configuration, we are interested in the planet's deviation from a Keplerian orbit around the host as a consequence of being orbited by a moon. Projected onto the plane of the sky, one can picture this perturbation as a time-dependent offset from the expected planetary position. While varying periodically in right ascension (RA) and declination (Dec) according to the orbital parameters of the planet–moon system, we are initially mostly interested in the maximum radial deviation, a quantity we shall call the planetometric signal amplitude  $\mathcal{P}$  and which we can estimate via

$$\mathcal{P} = \left(\frac{G}{4\pi^2}\right)^{1/3} \left(\frac{P}{M_{\rm pl} + M_{\rm m}}\right)^{2/3} \frac{M_{\rm m}}{d} = \frac{a_{\rm m}}{d} \frac{M_{\rm m}}{M_{\rm pl} + M_{\rm m}},\tag{5.1}$$

where G is the gravitational constant, P is the orbital period of the planet–moon orbit, d is the distance of the target system and  $M_{\rm pl}$  and  $M_{\rm m}$  are the masses of the planet and moon, respectively (Sahlmann et al. 2013b; Quirrenbach 2010). For the second equality, we used Kepler's third law to substitute P with an expression that includes the semi-major axis of the moon,  $a_{\rm m}$ . In general, Equation 5.1 is an approximation that holds only for circular moon orbits.

To reiterate, the quantity  $\mathcal{P}$  is an amplitude and is therefore only a snapshot of the deviant wobble movement exhibited by the planet. In this sense, it is comparable to the radial velocity (RV) semi-amplitude, K. This analogy to the RV method for exoplanet detection extends even further: when hunting for planets using the RV method, we do not rely on a single measurement. To sample a large fraction of the phase-folded RV curve, many observations often spanning several orbital periods are required. This ensures two things: (1) ideally, the full radial velocity amplitude is registered and (2) the large number of epochs increases the detection significance. The same is true for the astrometric method of planet and planetometric method of moon detection: while we do not know at which moment in time the planet shows the largest deviation and the measurement precision of our current instrumentation may not suffice to make a significant detection based on only a small number of observations, an extensive time-series of multiple planetometric epochs will solve both of these problems. We therefore require not just an estimate of the perturbation amplitude as provided by Equation 5.1, but also its behaviour in time. In the following, we shall briefly explain how this modulation can be computed analytically.

### 5.2.2 Simulating the signal variation in time

To investigate the behaviour of the orbital perturbation experienced by the planet as a function of different parameters and thus its detectability with current and future instruments in more detail, we need to analytically describe the time variation of the signal. To this end, we defined two models.

### The star-planet model

First, we implemented an analytical two-body orbit model that is capable of integrating the trajectories of the host star and planet around their mutual centre of mass as a function of nine orbital parameters, namely the system's parallax,  $\varpi$ , the stellar and planetary masses,  $M_{\rm s}$  and  $M_{\rm pl}$ , respectively, the semi-major axis of the planet,  $a_{\rm pl}$ , its inclination,  $i_{\rm pl}$ , eccentricity,  $e_{\rm pl}$ , longitude of ascending node,  $\Omega_{\rm pl}$ , argument of periastron,  $\omega_{\rm pl}$ , and time of periastron passage,  $t_{\rm peri,pl}$ . In broad terms, this is an algorithm that converts a given time of observation to a mean anomaly, solves Kepler's equation iteratively, performs a series of three-dimensional space rotations and scales the resulting stellar position by the planet—star mass ratio to obtain the planetary position. Performed for a series of time steps, this procedure yields the orbital trajectory of the two bodies as projected onto the plane of the sky. Clearly, this model forms the baseline case of our investigation: a system devoid of a moon exhibiting perfect Keplerian two-body orbits.

### The star-planet-moon model

On top of the star-planet model, we needed to simulate the system's behaviour under the influence of a moon in orbit around the planet. To this end, we employed the same framework as above but extended it by seven additional orbital parameters: the moon mass,  $M_{\rm m}$ , semi-major axis,  $a_{\rm m}$ , inclination,  $i_{\rm m}$ , eccentricity,  $e_{\rm m}$ , longitude of ascending node,  $\Omega_{\rm m}$ , argument of periplanet,  $\omega_{\rm m}$ , and time of periplanet passage,  $t_{\rm peri,\,m}$ . Thus, the star-planet-moon model incorporates 16 free parameters.

Whereas in the star–planet model we assumed the dynamical mass of the companion object or system to be entirely locked in the planet, we are here supposing that it is actually the sum of the planet and moon masses. Thus, the trajectory obtained from the star–planet model can be reused as the trajectory of the planet–moon barycentre. Superimposing the trajectories of the planet and moon in their own reference frame onto this barycentric trajectory yields the space motions of the planet and moon around the barycentre of the entire system. While this nested strategy avoids cumbersome three-body numerical integrations, it neglects higher-order gravitational interaction terms between star, planet and moon. Such a simplification appears reasonable, however, given that we intend to apply this model to stable systems exhibiting wide planetary orbits and for only negligible timescales compared to long-term orbital disruption and ejection processes. As Kipping (2010) points out, this approach is justified provided the considered semi-major axis of the moon is smaller than 0.531 times the planet's Hill radius,  $R_{\rm Hill,\,pl}$ . The latter is defined as

$$R_{\text{Hill, pl}} = a_{\text{pl}} \left(\frac{M_{\text{pl}}}{3M_{\text{s}}}\right)^{1/3},$$
 (5.2)

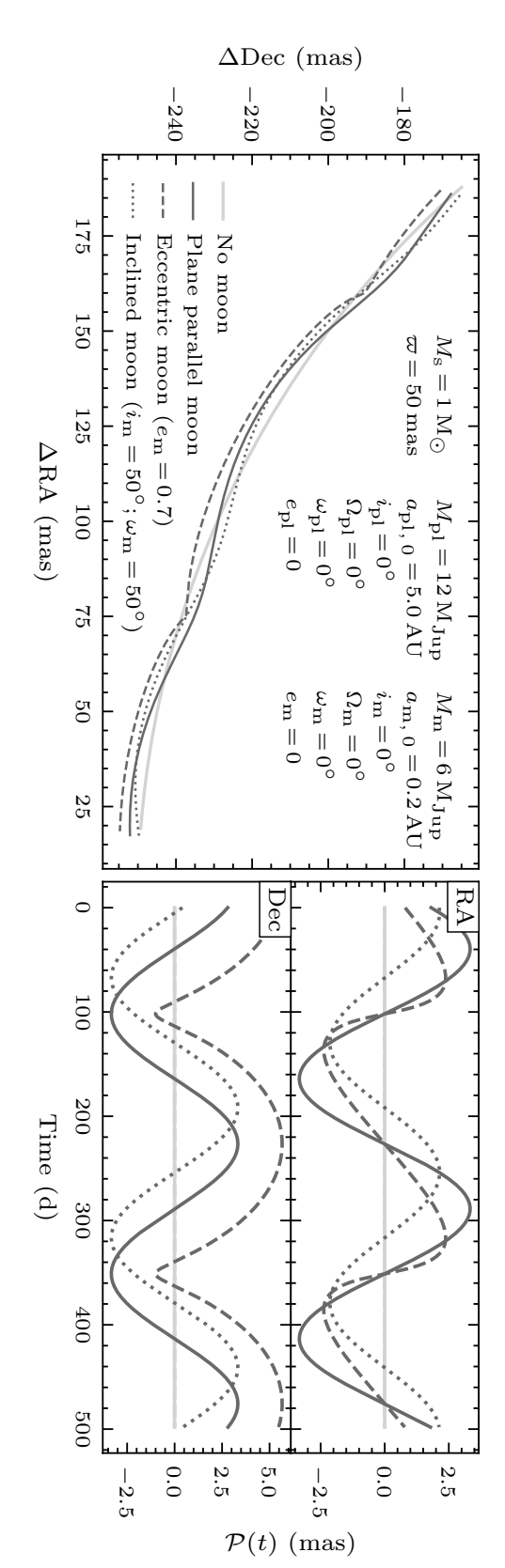
where  $a_{\rm pl}$  is the semi-major axis of the planet around the star and  $M_{\rm pl}$  and  $M_{\rm s}$  are the planetary and stellar mass, respectively (e.g. Murray & Dermott 1999)

#### Extracting the wobble

Comparing the trajectories simulated using the star-planet and the star-planet-moon models yields the orbital deviation resulting from the presence of a moon. This perturbation can be visualised by plotting the orbital trajectories of the planet for both cases. The left hand panel of Fig. 5.1 shows the resulting planetary wobble for a fictitious example system. The shape of the wobble depends on the system configuration and can be deconstructed into RA and Dec components presented in the right hand panels of Fig. 5.1. Unlike the simplified description of the planetometric signal amplitude given in Equation 5.1, the star-planet and star-planet-moon models that underpin the parametrisation of the visualised wobble are capable of handling eccentric planet and moon orbits. The Saturnian moons provide an example of eccentric moons in the Solar System. Titan, Saturn's most massive moon, presents an eccentricity of approximately 0.03 (Jacobson 2022).

# 5.3 Expected signals in the context of measurement uncertainties

While, in general, an exomoon cannot be detected by a single planetometric measurement, it can be instructive to compare to our current planetometric measurement capabilities the theoretical perturbation in planet position as a consequence of an orbiting body. To illustrate this, Table 5.1 lists multiple known exoplanets and the planetometric signal amplitudes they would present for a series of assumptive companion moons. Here, we have varied both the mass and semi-major axis of the moon. While the former assumes three distinct values for each case, for the reasons outlined in Sect. 5.2.2, the latter is coupled to the respective Hill radius of the planet,  $R_{Hill, pl}$ . Apart from ensuring the applicability of the nested two-body framework we employed as an approximation of the three-body situation we are in reality confronted with, restricting the semi-major axis of the moon to values below a constant critical fraction,  $\chi_{\rm crit}$ , of the respective Hill radius also safeguards against modelling system configurations that are dynamically unstable. Amongst other things,  $\chi_{\rm crit}$  depends on the eccentricity and obliquity of the planetary orbit (e.g. Holman & Wiegert 1999). Different estimates of the critical distance fraction include  $\chi_{\rm crit} \approx 0.36$  and  $\chi_{\rm crit} \approx 0.49$  for prograde (Barnes & O'Brien 2002; Domingos et al. 2006) and  $\chi_{\rm crit} \approx 0.93$ for retrograde orbits (Domingos et al. 2006). To meet both the two-body approximation and the dynamical stability conditions, we therefore chose the two representative values of  $\chi = 0.5$  and 0.1 to compute the case-dependent semi-major axes according to  $a_{\rm m} = \chi R_{\rm Hill,pl}$ . The demonstrated and predicted planetometric measurement uncertainties associated with a set of current and future instruments listed in the bottom of Table 5.1 place the computed signal amplitudes for the different system configurations into context. At present, GRAVITY is the only instrument capable of robustly resolving the perturbations predicted for a large subset of cases presented in Table 5.1. Classical imaging instruments, on the other hand, cannot be expected to be capable of detecting any but the most extreme cases, where the moon-to-planet mass ratios are unlikely large.



are the sums of the semi-major axes of the respective hosts and orbiting bodies around their mutual centre of mass. Since orbital trajectory of the moon-hosting planet relative to the star at the origin for different configurations, the right panels component remains unaffected. we define the inclination of the moon to be 0° and 90° for face-on and edge-on orbits as projected onto the plane of the semi-major axes indicate that these values correspond to the separation between the two bodies, that is between the using the adjusted orbital elements specified in the brackets in the bottom left of the panel. The "0" in the indices of to the configuration given in the top right of the left hand panel. The eccentric and inclined examples were computed purposes, the mass ratio between moon and planet,  $M_{
m m}/M_{
m pl}$ , used in these examples is unrealistically high to the point display the corresponding planetometric signals in right ascension and declination as a function of time. For visualisation Figure 5.1: Orbital wobble caused by the perturbing gravitational influence of an exomoon. The left panel shows the planetometric signal in the declination component while - as is evident in the bottom right panel - the right ascensionthe sky, respectively, simply increasing the inclination results in a dampening and eventual complete suppression of the planet-moon barycentre and the host star as well as between the moon and the planet, respectively. In other words, they that the system would more fittingly be described as a "binary planet". The plane parallel moon case corresponds exactly better distinguish the different cases We also adjusted the argument of periastron to add a phase shift in the signal so as to

**Table 5.1:** Planetometric signal amplitudes for different case examples in the *top* and the approximate planetometric measurement precision of different current and future instruments in the *bottom*.

Planet	System parameters	$M_{\rm m}~({ m M_{Jup}})$	χ	$\mathcal{P}$ ( $\mu$ as)	
	$\varpi = (50.93 \pm 0.15) \mathrm{mas}^{-1}$ $M_{\mathrm{s}} = (1.83 \pm 0.04) \mathrm{M_{\odot}}^{-2}$	1.0	0.5 0.1	$3000 \pm 600$ $600 \pm 130$	
β Pic b	$M_{\rm pl} = 9.3^{+2.6}_{-2.5} \mathrm{M_{Jup}}^{2}$	0.1	$0.5 \\ 0.1$	$330 \pm 70$ $65 \pm 15$	
	$a_{\rm pl} = (10.26 \pm 0.10) \text{AU}^2$ $R_{\rm Hill,  pl} = (1.20 \pm 0.11) \text{AU}$	0.01	0.5 0.1	$33 \pm 8$ $6.6 \pm 1.5$	
	$\varpi = (24.46 \pm 0.05) \text{mas}^{-1}$ $M_{\rm s} = 1.51^{+0.38}_{-0.24} \text{M}_{\odot}^{-3}$	1.0	$0.5 \\ 0.1$	$3800 \pm 900$ $770 \pm 180$	
HR 8799 d	$M_{\rm pl} = (10 \pm 3)  \rm M_{\rm Jup}^{4}$	0.1	$0.5 \\ 0.1$	$420 \pm 110$ $80 \pm 20$	
	$a_{\rm pl} = (26.97 \pm 0.73) \text{AU}^{-3}$ $R_{\rm Hill,  pl} = (3.5 \pm 0.4) \text{AU}$	0.01	~ ~	$42 \pm 11$ $8 \pm 2$	
	$\varpi = (24.53 \pm 0.04) \text{mas}^{-1}$ $M_{\rm s} = 1.32^{+0.07}_{-0.05} \text{M}_{\odot}^{-5}$	1.0	0.5 0.1	$460 \pm 30$ $92 \pm 7$	
HD 206893 c	$M_{\rm pl} = 12.7^{+1.2}_{-1.0} \rm M_{\rm Jup}^{-5}$	0.1	$0.5 \\ 0.1$	$49 \pm 4$ $9.8 \pm 0.7$	
	$a_{\rm pl} = 3.53^{+0.08}_{-0.06} \text{AU}^{5}$ $R_{\rm Hill,  pl} = (0.51 \pm 0.02) \text{AU}^{5}$	0.01	0.5 0.1	$5.0 \pm 0.4$ $0.99 \pm 0.07$	
SPH	IERE GPI GRAVITY	PLANETES*	MICA	ADO† KBI <sup>††</sup>	
$\sigma_{\mathcal{P}}$ (µas) 150	00 <sup>6</sup> 1000 <sup>7</sup> 50 <sup>8</sup>	10 <sup>9</sup>	40	$0^{9}$ < $1^{10}$	

**Notes.** In the top,  $\varpi$ ,  $M_s$ ,  $M_{pl}$  and  $a_s$  are the system's parallax, stellar mass, planetary mass and semi-major axis, respectively.  $R_{Hill,\,pl}$  is the Hill radius that results from the system parameters according to Equation 5.2 when propagating the uncertainties associated with the different quantities involved. The semi-major axis of the moon used to compute the signal amplitude,  $\mathcal{P}$ , via Equation 5.1, is the respective Hill radius scaled by the constant fraction,  $\chi$ . Again, all uncertainties were propagated until arriving at the signal amplitude. In the bottom,  $\sigma_{\mathcal{P}}$  is the approximate planetometric measurement uncertainty achievable with different instruments.

\* Future VLTI instrument (see Sect. 5.3); † First-generation ELT instrument (Davies et al. 2021); †† Future kilometre baseline interferometric facility (Bourdarot & Eisenhauer 2024) **References.** <sup>1</sup> Gaia Collaboration et al. (2023b); <sup>2</sup> Brandt et al. (2021a); <sup>3</sup> Zurlo et al. (2016); <sup>4</sup> Marois et al. (2008); <sup>5</sup> Hinkley et al. (2023); <sup>6</sup> Maire et al. (2021); <sup>7</sup> Wang et al. (2016); <sup>8</sup> GRAVITY Collaboration et al. (2019); <sup>9</sup> priv. comm.; <sup>10</sup> Bourdarot & Eisenhauer (2024)

Clearly, the system configurations envisaged in Table 5.1 are entirely imaginative and serve to illustrate how the signal strength changes for a set of exemplary cases. If one were to attempt a planetometric exomoon detection in earnest, however, one would ideally

want to avoid having to resort to a blind search around an arbitrary planet. This is due to the prolonged period of time throughout which planetometric epochs need to be collected for in order to achieve a positive detection. Instead, an additional line of evidence that hints towards the potential existence of an orbiting body should be the starting point of an efficient planetometric moon hunt. In this regard, the case of  $\beta$  Pic b warrants further attention. Recently, Poon et al. (2024) have argued that the planet's potentially increased obliquity (to be confirmed by future observations) could be explained by the perturbing influence of an exomoon. They also give estimates as to the moon mass and semi-major axis required to induce the observed planetary obliquity. Hereafter, we use the shorthand "P24-moon" to refer to objects that comply with these constraints.

To understand whether our current instrumentation is capable of picking up on the planetometric signal of such a P24-moon, we can compute the expected amplitude in the vicinity of the moon mass and semi-major axis constraints using the models defined in Sect. 5.2.2. This region of the parameter space is visualised in the right panel of Fig. 5.2. It demonstrates that a P24-moon would induce a planetometric wobble amplitude of 10 to 20  $\mu$ as. Despite its unprecedented planetometric precision of 50  $\mu$ as, such a perturbation would likely be difficult to detect using GRAVITY. However, plans are already underway to improve the planetometric accuracy of the existing GRAVITY instrument by addressing certain limitations (e.g., optical aberrations in GRAVITY Collaboration et al. 2021), as well as by halving the operational wavelength – observing in the Y- and J-bands instead of the K-band. These efforts are part of the VLTI/PLANETES technological development program at ESO<sup>2</sup>. A future instrument developed under this program would be expected to achieve a precision of 10  $\mu$ as (as predicted in Lacour et al. 2014), providing the capability to search for a P24-moon around  $\beta$  Pic b.

The unique potential inherent to the planetometric method is reinforced by the comparison to the detection capabilities of other methods. For one thing, strategies that hinge on observations of the planet transiting the stellar disc are not applicable to this nontransiting planet. What is more, Poon et al. (2024) point out that transits of the putative moon in front of the planet are unlikely. An alternative avenue towards eventual detection might lie in a comprehensive RV monitoring programme of the exoplanet (Ruffio et al. 2023; Vanderburg & Rodriguez 2021). To gauge whether such a strategy is feasible for detecting a P24-moon, we visualised the expected RV semi-amplitude, K, as a function of moon mass and semi-major axis in the left hand panel of Fig. 5.2. As expected, the sensitivity gradient of the RV method is opposite to that of the planetometric technique: while both signals increase with the moon mass, the planetometric signal is stronger for larger semi-major axes, whereas the RV semi-amplitude decreases with larger separations. To probe the entire parameter space region predicted for the P24-moon requires an RV precision of approximately 75 m/s. Recent studies have already demonstrated measurements of planetary RVs to be possible when coupling an adaptive optics system with a high-resolution spectrograph. Denis et al. (2025) could constrain the RV of AF Lep b to within approximately 1 km/s using VLT/HiRISE (Vigan et al. 2024), while Parker et al.

<sup>&</sup>lt;sup>2</sup>Funded by the European Research Council: https://cordis.europa.eu/project/id/101142746/fr

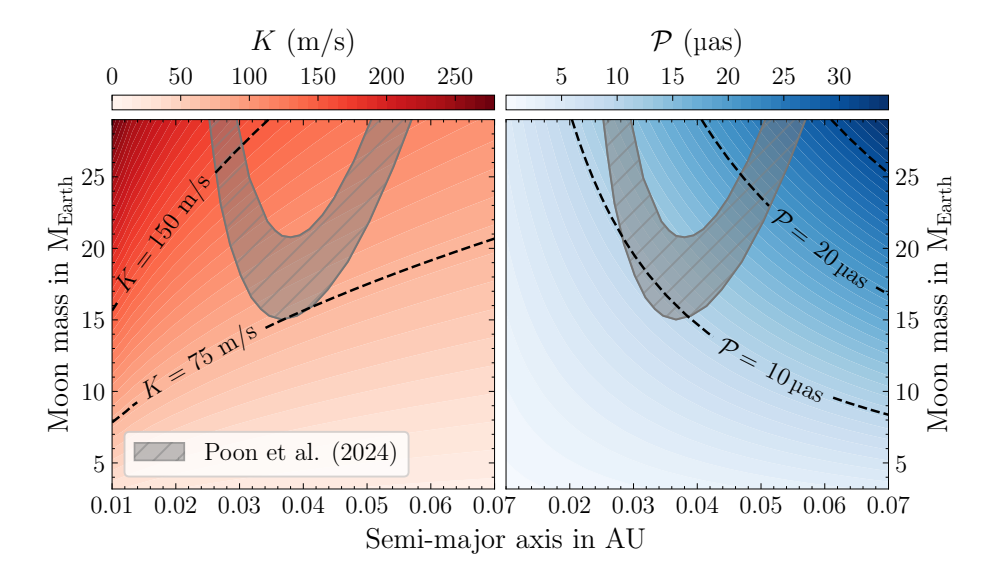


Figure 5.2: Signal amplitudes in the vicinity of the putative exomoon around  $\beta$  Pic b suggested by Poon et al. (2024) as a function of moon mass and semi-major axis for RV studies on the *left* and planetometric searches on the *right*. The grey shaded region is the parameter space where a P24-moon is likely to reside if it is indeed real. The dashed lines indicate contours delineating the indicated signal strength.

(2024) and Landman et al. (2024) achieved measurements of  $\beta$  Pic b with uncertainties of approximately  $2 \, \text{km/s}$  and  $300 \, \text{m/s}$ , respectively. Using KPIC (Delorme et al. 2021), Horstman et al. (2024) was able to obtain RV epochs of GQ Lup B with precisions ranging from 400 to  $1000 \, \text{m/s}$ . Notwithstanding these promising results that will stimulate further development of the involved techniques and instruments, the attainable planetary RV precision does not yet suffice to detect the putative P24-moon.

Regardless of whether one pursues an RV or planetometry-based strategy, a single epoch will never suffice for detection. Instead, extensive monitoring of the planet is necessary to reveal its periodic reflex motion. Accordingly, the study of a simulated time series of mock epochs is the logical next step towards assessing what is required to planetometrically detect an exomoon.

### 5.4 Modelling multi-epoch detection attempts

To probe which kind of systems a given instrument is sensitive to, we need to establish different observation sampling strategies, implement a procedure of generating mock planetometric epochs, provide safeguards against over- or underestimating the signal of a given moon, and define a robust way of computing the significance for any combination of instrument, observing strategy and system configuration. In the following, these points will be addressed individually.

### 5.4.1 Defining observing strategies

The chosen observational cadence is of consequence for the system configurations one is most sensitive to. First, it is important to note that there is no one optimal strategy. Instead, the approach one adopts would ideally be informed by the target and the period one suspects the moon to exhibit. Assessing which sampling strategy is ideal for which system is a far-reaching problem by itself. Avoiding aliasing and achieving an efficient sampling of the planetometric curve are key concerns that need to be addressed (see Madore & Freedman 2005). Doing so is beyond the scope of this work, however. We shall instead confine our study to investigating how the attainable sensitivity of different instruments behaves as a function of the number of planetometric epochs. Second, most targets are not observable throughout the entire year from most locations on Earth. The chosen observatory and target system position thus impose a second constraint on the observing strategy. Finally, there might be special boundary conditions set by the operational processes and time allocation procedure of the chosen observatory. For instance, on Cerro Paranal, the VLTI observation windows are scheduled to coincide with the full moon and typically last for five days each. Since at the moment there is little to no possibility of deviating from this fixed schedule we shall consider it a hard condition in the analysis to follow. Bearing the above in mind, we define two basic strategies:

- 1. 12 epochs: A sequence of evenly spaced observations with a cadence of one synodic month, that is approximately 29.5 days. Once six epochs have been obtained, we pause for a period of six months during which the target is assumed to be unobservable, before observing for another six months in a row.
- 2. 18 epochs: Same as above but including a second pause and third sequence of six epochs.

Naturally, these approaches only represent a small subset of all possible strategies and are mainly geared towards investigating the sensitivity gain obtained from an additional set of six planetometric epochs. Beyond the above approaches, one could adopt a higher-frequency tactic where a planetometric epoch is obtained during every night of several consecutive VLTI windows. Such a "rapid-fire" strategy would be especially suited to hunt for short-period moons. As mentioned above, however, we defer a thorough signal-processing-based identification of optimal sampling strategies for different system configurations to future works.

### 5.4.2 Creating the planetometric mock epochs

Based on the chosen number of epochs, we next need to generate a mock planetometric data set. To this end, we can use the models introduced in Sect. 5.2 as our underlying fiducial models. They provide the exact on-sky positions of the star, planet and moon relative to the system barycentre for any given time of observation. By extracting the planetary position according to the two models at a series of pre-defined observing times,

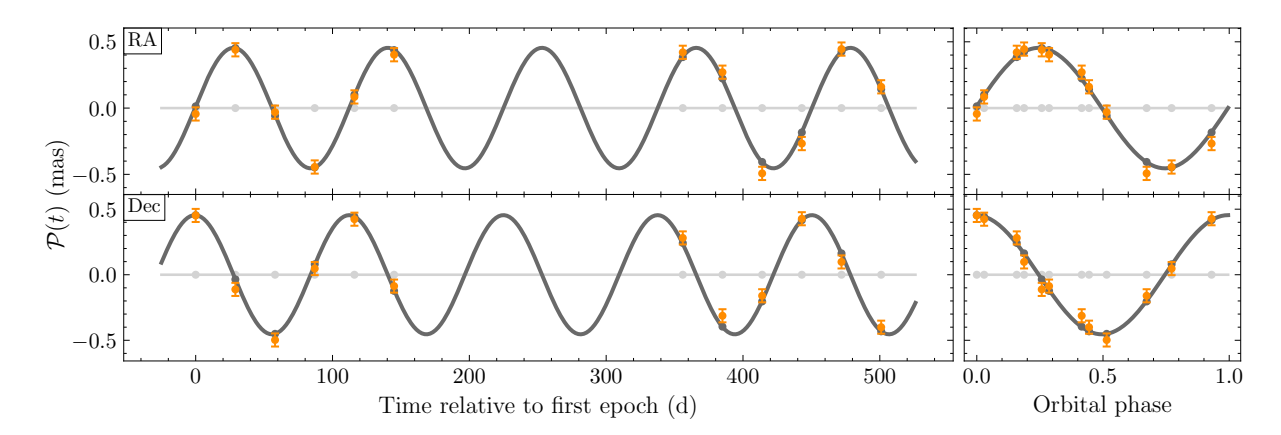


Figure 5.3: Fiducial planetometric signal in RA and Dec as a function of time for an exemplary system configuration ( $M_{\rm s}=1.5\,{\rm M}_{\odot},\,M_{\rm pl}=10\,{\rm M}_{\rm Jup},\,M_{\rm m}=1\,{\rm M}_{\rm Jup},\,\varpi=50\,{\rm mas},\,a_{\rm m,0}=0.1\,{\rm AU},\,i_{\rm m}=0\,^{\circ},\,e_{\rm m}=0$ ). The dark grey curve indicates the fiducial signal computed using the star–planet–moon model described in Sect. 5.2.2, while the light grey line shows the zero-signal expected in the absence of a moon. The light and dark grey circles show the fiducial momentary signals in RA and Dec when employing the 12 epoch strategy defined in Sect. 5.4.1. In orange we indicate the associated GRAVITY mock epochs generated according to the procedure outlined in Sect. 5.4.2. The right hand panels show the same data but phase-folded by the fiducial orbital period.

we obtain our fiducial planet positions. These are not the positions that our instrument will measure, however. Shifting them in both RA and Dec by a noise component drawn from the Gaussian distribution  $\mathcal{N}(0, \sigma_{\mathcal{P}})$ , where  $\sigma_{\mathcal{P}}$  is the measurement uncertainty of the chosen instrument, turns the fiducial planet positions into our mock planetometric epochs. Figure 5.3 shows the fiducial signal and generated GRAVITY mock epochs as a function of time in RA and Dec for an exemplary system configuration.

### 5.4.3 Randomising the time of periplanet passage

The fact that the planetometric signal varies periodically over time holds the danger of significantly misjudging the achievable detection significance. In case the epochs are taken at regular intervals and the chosen cadence coincides approximately with a multiple of  $P_{\rm m}/2$ , where  $P_{\rm m}$  is the orbital period of the moon, one runs the risk of consistently sampling the wobble at the same angular deviation. For instance, one could conceivably "be lucky" and systematically observe the planet at its largest deviation from the Keplerian trajectory or "be unlucky" and catch it at just the moments when the planetometric signal is minimal. To avoid this pitfall when hunting for moons in earnest, it is therefore advisable to refrain from employing an evenly spaced observing strategy in cases where one expects the moon orbit to be of a similar period. In our simulation, however, we can additionally counteract the issue by randomising the time of periplanet passage,  $t_{\rm peri,m}$ . This effectively entails a randomisation of the planet—moon orbital phase such that an evenly spaced observing

sequence can still coincidentally align with the planetary wobble for a single run but not for the entire sample of  $N_{\rm rand}$  runs. Another consequence of this manoeuvre is that for a given star–planet–moon configuration we will be left with a distribution of detection significances.

### 5.4.4 Estimating the detection significance

The last ingredient required to assess our current and future detection capabilities is a framework that allows us to quantify in which parameter spaces the star–planet–moon model performs significantly better at explaining the mock planetometric epochs than the mere star–planet model.

The two models are nested in the sense that the star-planet-moon model transitions into the star-planet model when the moon mass becomes negligible. That being said, the star-planet-moon model requires more free parameters, which implies that any approach to be used to compare the performance of the two models must be capable of penalising such increased complexity. Since it computes the Bayesian evidence, a nested sampling approach (see e.g. Feroz & Hobson 2008; Buchner 2021) would enable us to account for the number of free parameters in a given model. As we are planning to compute the significance achievable by different instruments using various observing strategies over a grid of target system parameters, while also randomising the time of periplanet passage for each grid point (see Sect. 5.4.3), such a strategy would require inordinate computational effort. Given the general character of this work as an initial feasibility assessment, we decided to defer the implementation of a nested sampling routine to a future study and focus the sensitivity estimates on comparing the  $\chi$ -squared values presented by the two models at the fiducial parameter settings. This approach presumes that the fiducial solution can be converged upon using a suitable fitting routine, an assumption that is justified for the cases we are most interested in: the ones where  $\Delta \chi^2_{\rm red}$ , the difference in  $\chi^2_{\rm red}$  between the two models, is significant. Starting from the fiducial parameter set we ran a gradient descent routine to ensure the minimum was stable. The  $\chi$ -squared values used throughout the remainder of the analysis presented here are based on these converged-upon parameter sets.

To quantify the relative performance of the two models, we applied a variant of the F-test based on the Fisher-Snedecor distribution (see e.g. Eadie et al. 1971). Following Band et al. (1997), a given  $\Delta \chi^2_{\rm red}$  value was converted to an F-value according to

$$F = \frac{\Delta \chi^2 / \Delta \nu}{\chi_{\text{moon}}^2 / \nu_{\text{moon}}},\tag{5.3}$$

where  $\Delta\nu$  is the difference in the degrees of freedom  $\nu = N_{\rm data} - N_{\rm fp} + 1$  between two models. Here,  $N_{\rm data}$  and  $N_{\rm fp}$  are the number of data points and free parameters, respectively. To account for the fact that each planetometric epoch corresponds to a measurement in RA and Dec, we used  $N_{\rm data} = 2N_{\rm epoch}$ . The quantities in the denominator of Equation 5.3 are the  $\chi$ -squared and degrees of freedom of the more complex model, that is the one including

the moon. From the resulting F-values, we computed the corresponding p-values via its survival function. Finally, we converted the p-values into a significance via the quantile function. Both operations were handled using the respective **scipy** methods (Virtanen et al. 2020).

We thus possess all the tools required to collapse the  $\chi$ -squared values resulting from the comparison of the two models with a set of noisy mock data obtained by a given instrument employing a certain observing sequence of a specific star–planet–moon configuration into a single detection significance.

### 5.5 Multi-epoch sensitivity curves

We applied the procedure outlined above to estimate the detection significance achievable using VLTI/GRAVITY, VLTI/PLANETES and a hypothetical future interferometric facility with a 3 km baseline (see Table 5.1 for the respective planetometric measurement uncertainties), each employing the two observing strategies described in Sect. 5.4.1. To facilitate comparability with a large fraction of the directly imaged planet population, the fictional star-planet-moon system this investigation is based on was deliberately configured as general as possible. Accordingly, we chose a  $10 \,\mathrm{M_{Jup}}$  planet revolving around a  $1.5\,\mathrm{M}_{\odot}$  star on a circular, face-on orbit  $(i=0\,^{\circ})$  with a semi-major axis of 10 AU and at a distance of 20 pc. The moon orbit was assumed circular and co-planar with the planetary orbit, that is also face-on. The planetary Hill radius resulting from these fiducial parameter settings amounts to approximately 1.2 AU. These parameters remained fixed throughout the grid exploration of a two-dimensional plane spanned by the moon semi-major axis and moon mass axes, which were logarithmically sampled by 15 values from  $10^{-2}$  to 1 AU and  $10^{-2}$  to  $1 \,\mathrm{M_{Jup}}$ , respectively. Each grid point was sampled 100 times, generating a new set of mock epochs with a randomly drawn noise term, respectively. This ensures adequate sampling of the underlying  $\chi$ -squared statistic and sufficient randomisation of the time of periplanet passage which was drawn anew for each sample (see Sect. 5.4.3). Accordingly, this yielded a sampling of 100  $\chi$ -squared values per model fit performed.

At this point, one could choose between retaining the minimum, median or maximum  $\chi$ -squared value (and associated significance computed via the F-test routine) depending on whether one is interested in extracting the least favourable, median or most favourable detection scenario, respectively. To arrive at a realistic assessment of our detection capabilities we opted to retain the median  $\chi$ -squared value for each model and grid point. The  $5\,\sigma$  detection contours resulting from the different combinations of instruments and observing strategies are visualised in Fig. 5.4.

Besides the number of obtained epochs, the detection significance at a given grid point in Fig. 5.4 is mainly governed by the expected planetometric signal amplitude. In Equation 5.1, we found that  $\mathcal{P} \propto a_{\rm m}/d$  and  $\mathcal{P} \propto M_{\rm m}/(M_{\rm pl}+M_{\rm m})$ . By appropriately folding in the fiducial distance, d, and the total mass,  $M_{\rm pl}+M_{\rm m}$ , of the fictional underlying planetmoon system, we rescaled the axes in Fig. 5.4 providing the resulting alternate axes along the right and top side of the panel. These rescaled axes enable comparison of the obtained

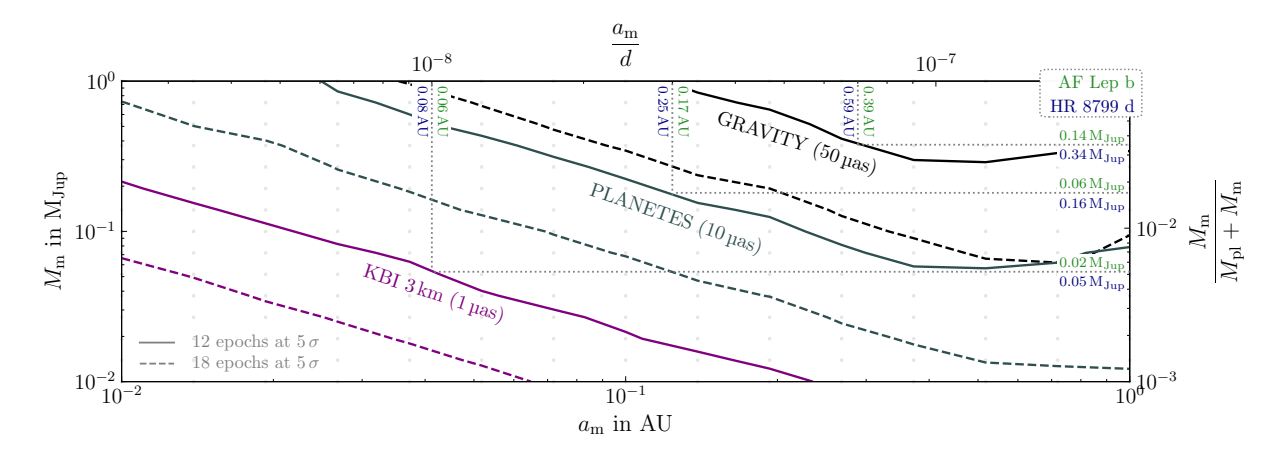


Figure 5.4: Sensitivity curves of different current and future interferometric instruments capable of planetometric measurements. The solid and dashed lines indicate the 5  $\sigma$  detection limits based on 12 and 18 epochs, respectively. The grey dots in the background mark the probed grid points. The rescaled axes in the top and on the right provide a parametrisation where the fiducial target system distance, d, and planet mass,  $M_{\rm pl}$ , have been folded in. They can thus be used to estimate the moon detection significance achievable for a genuine exoplanet of interest. Three exemplary moons detectable around ( $M_{\rm pl} = (3.27 \pm 0.25) \, {\rm M_{Jup}}$ ; Balmer et al. 2025) and HR 8799 d ( $M_{\rm pl} = (9.3 \pm 0.5) \, {\rm M_{Jup}}$ ; Zurlo et al. 2022) are indicated by the dotted lines. The corresponding moon masses and semi-major axes are provided.

sensitivity contours with genuine exoplanets that might be considered for a follow-up aimed at unveiling an exomoon.

To give two illustrative examples, we included the cases of AF Lep b  $(M_{\rm pl}=(3.27\pm$  $0.25) \,\mathrm{M_{Jup}}; \,\mathrm{Balmer} \,\mathrm{et} \,\mathrm{al}.\,\,2025) \,\mathrm{and} \,\mathrm{HR} \,8799 \,\mathrm{d} \,(M_{\mathrm{pl}} = (9.3 \pm 0.5) \,\mathrm{M_{Jup}}; \,\mathrm{Zurlo} \,\mathrm{et} \,\mathrm{al}.\,\,2022).$ Multiplying the values along the rescaled semi-major axis axis with the distance of a target system yields the physical semi-major axis values corresponding to the significance contours. Likewise, using the mass of an exemplary target planet, one can convert the values along the mass ratio axis into the corresponding moon masses. Doing so, we find that 12 planetometric GRAVITY epochs suffice to detect a moon of  $0.34\,\mathrm{M_{Jup}}$  at a separation of  $0.59\,\mathrm{AU}$  around HR 8799 d with a confidence of  $5\,\sigma$ . Targeting the lower mass AF Lep b, 12 epochs could reveal a  $0.14\,\mathrm{M_{Jup}}$  moon at a separation of  $0.39\,\mathrm{AU}$ . Both of these hypothetical moons would reside within  $0.5R_{\text{Hill, pl}}$  of their respective planetary hosts. Since more massive or more distant moons would induce a larger planetometric signal, they would manifest themselves in the data at even higher significances. Conversely, if none is present, 12 epochs would be adequate to rule out the existence of such moons around AF Lep b and HR 8799 d. The arrival of PLANETES at the VLTI will amplify our sensitivity such that moons of  $0.06 \,\mathrm{M_{Jup}}$  at  $0.17 \,\mathrm{AU}$  and  $0.16 \,\mathrm{M_{Jup}}$  at  $0.25 \,\mathrm{AU}$  were detectable at  $5\,\sigma$  around AF Lep b and HR 8799 d, respectively. Finally, a future 3 km baseline interferometric facility will be capable of detecting moons of  $0.02\,\mathrm{M_{Jup}}$  at  $0.06\,\mathrm{AU}$  and  $0.05\,\mathrm{M_{Jup}}$ at 0.08 AU around the two planets at the same confidence. These scenarios, indicated by

the grey dotted lines in Fig. 5.4, are only three example cases for two arbitrary exoplanets. Note that 0.02 and  $0.05\,\mathrm{M_{Jup}}$  translate to approximately 6 and  $16\,\mathrm{M_{Earth}}$ , respectively. At larger moon semi-major axes the detectable masses can be substantially lower. Similarly, at higher moon masses the instruments would be capable of probing smaller semi-major axes. Evidently, the moon masses attainable with a kilometric baseline facility (or any facility achieving a planetometric precision of  $1\,\mathrm{\mu as}$ ) lie in a regime where these objects can well be compared with Super-Earth or even Earth-like exoplanets. Targeting potential host planets in their respective circumstellar habitable zones may eventually teach us how prevalent habitable Earth-like exomoons are.

As long as they are comparable to the underlying fiducial system configuration on which the significance contours are based (far-out, circular, face-on orbit planets), Fig. 5.4 can be used to estimate the attainable instrument-dependent detection significance for any planet of interest. Star-planet-moon configurations and viewing angles that differ from the underlying fiducial system such as eccentric or edge-on orbits warrant dedicated simulations. Intuitively, for edge-on or near-edge-on cases the signal amplitude would remain the same, even if the reflex motion of the planet were confined to tracing out a line as projected onto the plane of the sky. With the publication of the astrometric time series data in *Gaia* DR4, we can expect to confirm dozens of planet candidates using GRAVITY. The combination of *Gaia* astrometry and the direct detection will yield a large sample of narrowly constrained orbital solutions and precise dynamical masses (see Winterhalder et al. 2024) that will lay the groundwork for a planetometric exomoon hunt.

Broadly speaking, based on 12 or 18 epochs, GRAVITY and PLANETES are sensitive at  $5\,\sigma$  to moons between 0.1 and a few per cent of the mass of their planetary host. According to Canup & Ward (2006), moons that have formed in-situ, that is in orbit around the planetary host, should not exceed a moon-to-planet mass ratio of approximately  $10^{-4}$ . There thus does not exist an overlap between our current and near-future planetometric exomoon detection capabilities and the regime where these regular moons are expected to reside. Judging by Fig. 5.4, a kilometric baseline facility might begin to tackle this limit – at least for comparatively large moon semi-major axes. So-called irregular moons, that is ones that were either captured by or formed as a result of an impact with their host, do not abide by this upper mass-ratio limit. Probing for a moon around a sufficiently massive host, we could therefore already today hunt for Earth-mass objects orbiting habitable-zone planets.

To assess the potential of a planetometric search for exomoons, it is of interest what expenditure in observation time such a study would entail. Based on experiences drawn from observations conducted within the framework of the ExoGRAVITY Large Programme (ESO ID 1104.C-0651 Lacour et al. 2020), obtaining one GRAVITY epoch can be assumed to require a total of 2 hours of telescope time including overheads. Data sets comprising 12 and 18 epochs, such as the ones the sensitivity curves in Fig. 5.4 are based on, would therefore carry a cost between 20 and 40 hours of VLTI UT-mode time. While this is a non-negligible investment, a potential moon discovery would make such a project highly worthwhile. Risk mitigation can be achieved by an informed target selection that hinges on clues as to the potential existence of an orbiting moon from auxiliary studies. The spec-

troscopic data products that result from a GRAVITY observation can act as contingency science cases in the event that no moon is present or detectable: time-series observations of exoplanet and brown dwarfs can be probed for variability or combined into a single high signal-to-noise spectrum.

Finally, a note on distinguishing between perturbations caused by a planet-orbiting moon and a star-orbiting interior planet, since, in general, both object classes would manifest themselves as a planetometric wobble. The expected periods are significantly different, however. Whereas the sought-after moons are expected to impart signals with periods of days to months, inner planets can be assumed to complete their orbits on typical timescales of several years. There does exist an overlap between the two cases, however: undetected hot Jupiters would induce a stellar reflex motion that could mimic the signature of a moon since our planetometric epochs correspond to relative separation measurements between the host star and the targeted planet. Such niche cases could easily be handled by obtaining an RV data set of the star. If present, a signal of a similar period would strongly suggest an inner planet causing the observed planetometric wobble. An exomoon, on the other hand, would not impart any measurable stellar RV modulation.

### 5.6 Conclusions

In this feasibility study, we have demonstrated the potential of hunting for exomoons and binary planets by means of a planetometric time series. The unprecedented precision of interferometric instruments such as VLTI/GRAVITY renders the technique not only viable, but also uniquely sensitive to low-mass moons around far-out directly imaged planets, a regime where moons are expected to survive over long periods. While, contrary to the RV method, the planetometric signal drops for target systems at greater distances, if successfully applied, the method can provide constraints on all orbital parameters including the absolute dynamical mass of the moon, the key parameter upon which any characterisation of the satellite object depends. The first dedicated GRAVITY search for an exomoon targeting HD 206893 B is currently being conducted with the results expected to be published soon (Kral et al. in prep). We showed that, a next-generation instrument like VLTI/PLANETES will likely be capable of probing for the putative exomoon around β Pic b suggested by Poon et al. (2024).

The sensitivity curves obtained from modelling the planetometric signatures expected for different target system configurations quantify our current and future capabilities and provide a compelling science case for pursuing kilometre-baseline interferometric facilities. Future studies should concentrate on implementing a fitting framework based on a nested sampling routine in order to robustly assess the degree to which a genuine planetometric time-series suggests the existence of an exomoon around a given planet. Moreover, the signal-processing conundrum of how to optimally sample a planetometric signature of a given period should be examined. In particular, such an investigation would help answer the question of whether the strict monthly VLTI observation window allocation inhibits the detection of short-period signals and whether the current scheduling system should be

5.6 Conclusions 115

reconsidered.

On the whole, planetometric time-series observations provide an excellent means of detecting moons around gas giant exoplanets. Their sensitivity extends to sufficiently low masses such that finding and characterising truly habitable exomoons might soon become an ambitious but viable proposition of potentially far-reaching consequence.

## Chapter 6

### Outlook

In this chapter I present a brief summary of where the developed techniques and obtained results outlined in Chapters 2 to 4 may lead in the future. First, we discuss how it may be possible to resolve some of the open questions regarding HIP 99770 b, the companion we encountered in Chapter 2. We then explore what kind of discoveries the rich data set published in *Gaia* DR3 may still offer and how we can best extract new insights from it while we wait for the arrival of DR4 in late 2026. A short preview of the treasures within that long-awaited release is given, before we present a possible follow-up strategy of the almost edge-on WT 766 B. Finally, we consider possible next steps towards making planetometric exomoon detections a reality.

Some of the content of this chapter is partially based on observing proposals I have developed under the supervision of S. Lacour and A. Mérand. None of it was published before.

### 6.1 Quo vadis, HIP 99770 b?

The conclusions we were able to draw about the characteristics and likely formation history of HIP 99770 b in Chapter 2 were limited. Nonetheless, the super-Jupiter status (Carson et al. 2013) of this companion and the scarcity of comparable specimens with masses around the threshold between planets and BDs justify continued observations of this target in the future. The results presented in Sect. 2.3 suggest that a firmer constraint on the dynamical mass of the companion is near-impossible to obtain when basing the orbital fitting routine on the imprecise PMa that is currently available. This difficulty will only be resolved once a more precise PMa will become available with the arrival of DR4. Alternatively, depending on the eventual data quality, basing the orbital fits on the time-series astrometric data also to be published in DR4 could supersede the PMa approach entirely (see e.g. Kiefer et al. 2024).

Aside from their inability to provide a firmer grasp on the dynamical mass, additional epochs would facilitate tighter constraints of the orbital eccentricity. In the context of the population-level eccentricity distributions already published (Bowler et al. 2020; Nagpal et al. 2023) or forthcoming (Roberts et al., in prep.), a precise eccentricity estimate might provide some indication as to whether the companion is more fittingly described as a planet or a brown dwarf. The current orbital solution enables companion position predictions sufficiently constrained to allow for GRAVITY follow-up observations until several years from now. A set of exemplary predictions is provided in Fig. 6.1.

Until the publication of DR4, additional spectroscopic data sets, especially at longer wavelengths, would help constrain the atmospheric properties of HIP 99770 b. Observations in the L, M or N-bands would likely serve to pin down the effective temperature and metallicity of the companion. These characteristics will bolster the case in favour or against a given formation channel that will eventually be made once a firm dynamical mass constraint breaks the age bimodality visualised in Fig. 2.7 and provides us with an answer as to whether the companion is burning deuterium in its core or not.

### 6.2 Untapped resources in Gaia DR3

As briefly mentioned in Sect. 3.4.3, a phenomenon commonly referred to as underluminosity is starting to emerge for directly detected BD companions. These anomalous objects appear to be fainter than expected by evaluating evolutionary models at their dynamical mass and age estimates. Companion binarity can serve as an interpretation of this tension between observations and theory. Recently, GRAVITY observations played a key part in resolving Gl 229 B into two distinct BD objects (Xuan et al. 2024; Whitebook et al. 2024). The original dynamical mass estimate of approximately  $70\,\mathrm{M_{Jup}}$  (Brandt et al. 2021c; Howe et al. 2023) was shown to be the sum of two components of approximately  $35\,\mathrm{M_{Jup}}$  each, thus resolving the significant and long-standing luminosity tension observed for this object. As such, the underluminosity phenomenon can be recast as an equivalent over-massiveness. Identifying more anomalies like Gl 229 B and probing them for potential binarity will shed

120 6. Outlook

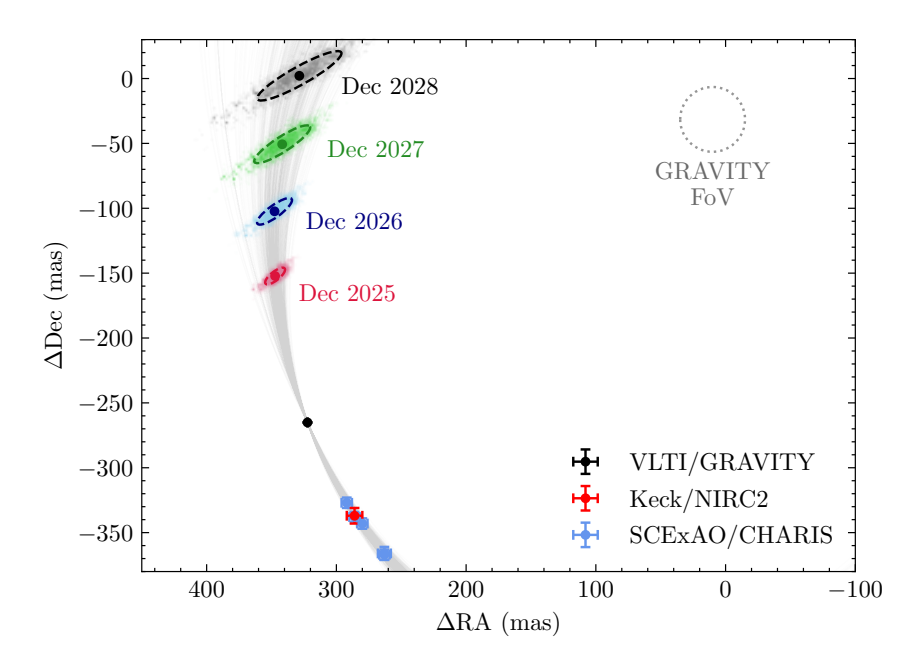


**Figure 6.1:** Position predictions for HIP 99770 b for the 1st of December of each year from the time of writing until 2028. For comparison, the effective FoV of the GRAVITY science fibre with a radius of 25 mas is visualised in the top right hand corner. The epochs obtained with different instruments correspond to the ones listed in Table 2.2.

light on the true nature of individual objects and patterns within the substellar companion population as a whole.

Reaching an underluminosity diagnosis for a given companion requires high-precision measurements of its luminosity and dynamical mass to be made. Scarce as these estimates used to be, the results presented in Winterhalder et al. (2024) and Chapter 3 demonstrated the potential of the Gaia-GRAVITY synergy in this regard. The highly-targeted nature of these follow-up observations combined with the narrow constraints on the companion magnitudes and dynamical masses they facilitate, render the technique uniquely suited to efficiently probe for underluminous objects. Far from being exhausted of detectable BD companions, the DR3 version of the NSS two-body orbit catalogue still contains a multitude of candidates viable for confirmation using GRAVITY. Thus, while it did not provide us with the hoped-for directly observable planetary companions – as we were forced to conclude in Chapter 4 – the current NSS catalogue can still serve as a basis on which a thorough and large-scale effort at expanding the sample of underluminous BD companions can be built.

Shortly before submission of this thesis, we received confirmation that our observing proposal based on the arguments outlined above and titled "Unveiling underluminosity in uncharted parameter spaces: a Gaia–GRAVITY brown dwarf hunt" (ID: 116.29AA) had been approved. On the basis of 22 h of VLTI observation time during the P116 semester, we will attempt to confirm eleven previously unknown Gaia-inferred BD companion candidates, to precisely measure their dynamical masses and luminosities and to assess whether

they warrant further attention on the grounds of being underluminous. The parameter space this project seeks to populate is presented in the lower panel of Fig. 6.2. It can be considered a continuation of and expansion upon the pilot study presented in Chapter 3.

### 6.3 What Gaia DR4 will bring to the table

The most important implication of the *Gaia*–GRAVITY synergy developed in Chapter 3 is its extended applicability to the astrometric time-series data to be published in *Gaia* DR4. In this section, we explore a selection of science cases set to be impacted by its long-awaited release.

# 6.3.1 Pushing for an overlap between radial velocity and direct imaging

The results presented in Chapter 3 were based on the orbital solutions listed in the DR3 NSS two-body orbit catalogue (Gaia Collaboration et al. 2023b). The entire third data release contained a grand total of 72 exoplanet candidates (Marcussen & Albrecht 2023; Gaia Collaboration et al. 2023a), most of which – if not indeed all, as we learned in Chapter 4 – are inaccessible to direct follow-up campaigns. Upon publication of the next Gaia data release, these meagre numbers are predicted to increase to large candidate samples, however (Perryman et al. 2014). The raw astrometric data collected over five and a half years of observation time will represent a treasure trove for a diverse set of communities. While we are sure to see a sudden rise in confirmed planet detections via the astrometric method (DR4 will contain a catalogue of astrometrically detected exoplanets identified and confirmed by Gaia), it is the catalogue's complementarity with direct detection methods we are most interested in here.

Once the data becomes available, there are two ways forward. Filtering the DR4 version of the NSS two-body orbit catalogue will likely provide a sufficiently large set of candidates such that a subset of them will be accessible for direct follow-up observations. But the large-scale harvesting of planets will be enabled by mining the raw astrometric time-series data. Fitting a single-star model based on the proper motion and parallax of a given star will facilitate the identification of anomalous targets that show large residuals and potential periodicities. In Sect. 1.2.1, we discussed how such higher-order motion can be indicative of an orbiting companion. The recently published GaiaPMEX tool (Kiefer et al. 2024) is already capable of a similar procedure based on DR3 data. While currently limited to the PMa, astrometric excess noise and re-normalised unit weight error (AEN and RUWE¹, respectively) of a given star, the release of the underlying astrometric data will unlock the full potential of this method.

An example of how astrometric detections based on *Gaia* time-series data may be performed is given by the recent discovery of *Gaia* BH3 (Gaia Collaboration et al. 2024).

<sup>&</sup>lt;sup>1</sup>AEN and RUWE are two metrics provided in the *Gaia* DR3 source catalogue that measure the quality of the single-star model fit to the astrometric time-series (Lindegren et al. 2021).

122 6. Outlook

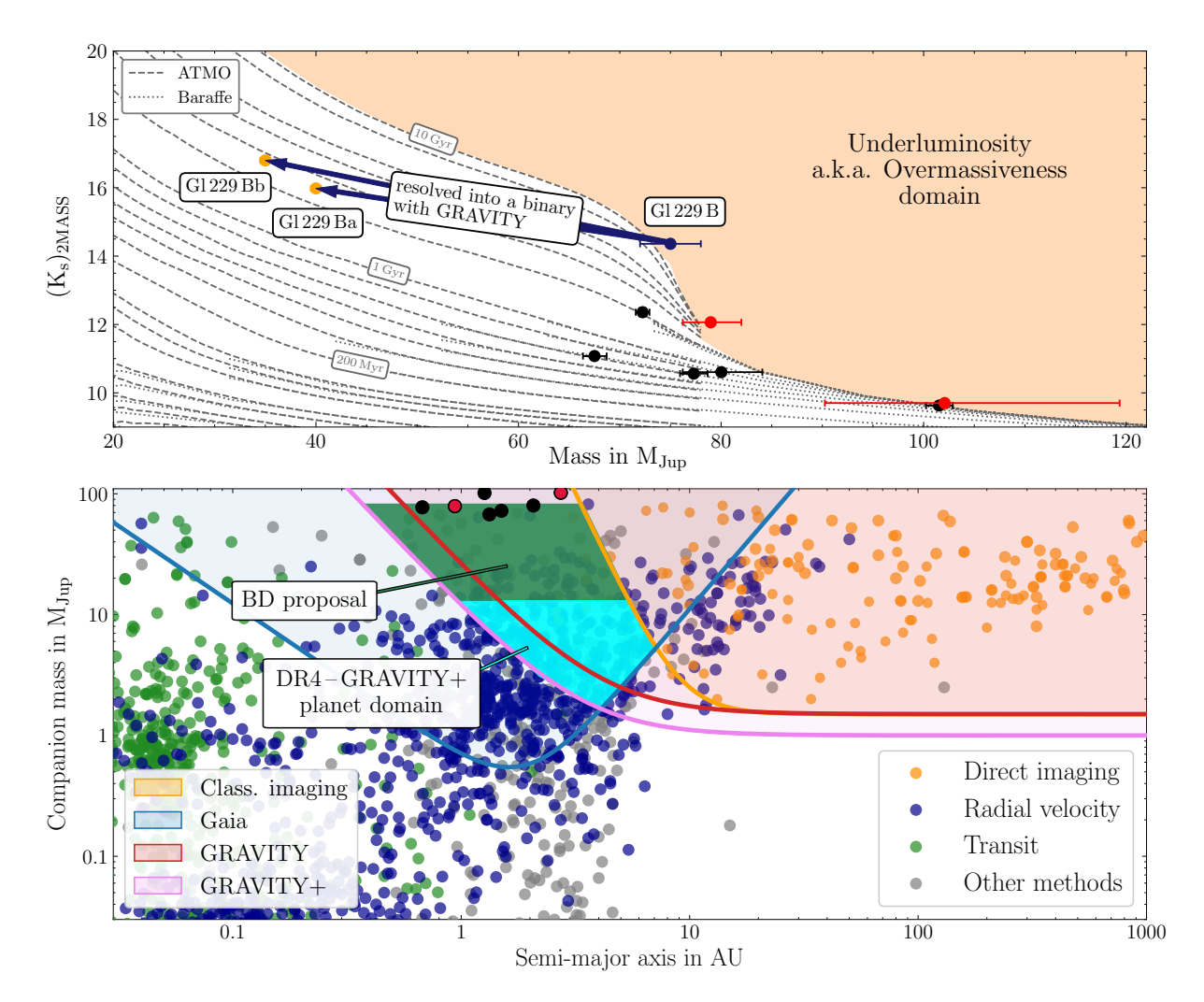


Figure 6.2: Top: Variation of Fig. 3.4 showing the BD sample detected in Chapter 3 and isochrones from the ATMO (Phillips et al. 2020) and Baraffe (Baraffe et al. 2003, 2015) models. The 200 Myr, 1 Gyr and 10 Gyr isochrones are annotated with labels. The two potentially anomalous companions straddling the underluminoisty domain are marked in red. Additionally, the original position of Gl 229 B and the two components it was resolved into are shown in dark blue and orange, respectively. Bottom: Similar to Fig. 1.4 and 4.1, highlighting the detection region aimed for in the BD follow-up observing programme described in Sect. 6.2 and the planet domain to be probed once Gaia DR4 is published as described in Sect. 6.3. The companions marked in black and red correspond to the sample presented in the top panel. Like the orange and red lines indicating the classical imaging and GRAVITY sensitivity limits, the violet margin delineating the GRAVITY+ detection region is based on Pourré et al. (2024).

Figure 2 of the announcement paper serves as a visualisation of the method. The publication of this result included the raw time-series astrometry, marking the first time such unprocessed *Gaia* data was made available. In this sense, *Gaia* BH3 can be viewed as a harbinger of the discoveries to be made on the basis of the next data release.

For an efficient direct detection follow-up of *Gaia*-inferred substellar companions to be possible, we will need to be capable of robustly estimating the age of a given target system. While the attempt in Chapter 4 proved unsuccessful, gyrochronology (Barnes 2003, 2007b) remains a viable option for arriving at such an estimate for a subset of the DR4 candidates. Cross-matching target lists with catalogues containing age measurements such as Zari et al. (2018) or El-Badry et al. (2021), assessing their potential membership to a young stellar associations (Zuckerman & Song 2004) or probing high-resolution spectra of the respective hosts for the 6708 Å lithium line (e.g. Soderblom et al. 1990) are alternative avenues towards reliable age estimates. The outcome of Chapter 4 demonstrates that the implementation of the age criterion as an element of the target selection process is key to performing successful follow-up observations.

The imposter binaries that contaminate the DR3 candidate sample (Marcussen & Albrecht 2023) and are likely to still be present in the DR4 catalogue constitute another challenge that needs to be tackled in order to make the eventual follow-up as efficient as possible. While an RV screening prior to a direct detection follow-up attempt is possible, such a strategy would introduce a long delay to the commencement of the direct observations. Cross-matching potential targets with binary star catalogues such as the Washington Double Star Catalog (Mason et al. 2001) or  $S_{B^9}$  (Pourbaix et al. 2004) and performing an additional candidate vetting step using machine-learning tools based on relevant observables in the *Gaia* source catalogue (Sahlmann & Gómez 2025) are alternative preventive strategies. They can provide a more immediate if less reliable diagnosis as to the binarity of a given target.

Provided the challenges outlined above can be met, the parameter region we will be sensitive to when also accounting for the improved contrast capabilities of the upgraded GRAVITY+ is visualised in the lower panel of Fig. 6.2. The extent of this domain illustrates what the future holds for the interplay of these two facilities: with *Gaia* DR4 and GRAVITY+ we will be able to establish true overlap between the RV and directly detected planet populations. As these advanced targeting techniques push our direct detection capabilities to shorter separations we are approaching a regime where we expect a pile-up of planets around the ice line (see Sect. 1.2.2 and references therein). Unleashing both the RV and direct detection techniques on this large reservoir of exoplanets will enable a more thorough characterisation than previously possible, furnish us with the most precise dynamical mass estimates to date and potentially allow us to uncover as of yet undetected population-level trends.

### 6.3.2 Additional avenues to pursue

Apart from achieving significant overlap between the RV and direct detection populations of exoplanets, there are a series of science cases connected to the general theme of directly

124 6. Outlook

following-up on Gaia companion candidates and confirmed detections.

Gaia astrometry is expected to yield hundreds of multi-planet system detections (Casertano et al. 2008; Wallace et al. 2025). On top of this, precise planetometry, for instance obtained with GRAVITY, can reveal additional, undetected inner planets. As briefly mentioned in Chapter 5, Lacour et al. (2021) have already demonstrated this method on the basis of perturbations observed in the orbit of  $\beta$  Pic b. With the plethora of directly observable planets Gaia DR4 will likely bestow upon us and the precise orbital solutions resulting from a GRAVITY follow-up, the identification of further such cases, and indeed ones where the sought-for perturber is not known or confirmed a-priori, will become a possibility. The similar nature of the methods make this science case highly complementary with the exomoon detection technique put forward in Chapter 5. Pursuing one of these cases will by default enable the other, even though the mass and separation sensitivity of the eventual data set for inner planets differs significantly from that for exomoons. An extensive sample of well-characterised multiple-planet systems will enable the study of formation scenarios (e.g. Mordasini et al. 2009a), migration histories (e.g. Kley & Nelson 2012), coplanarity (e.g. Fang & Margot 2012) and dynamical interactions (e.g. Lissauer et al. 2011) to name only a few examples of how these ensembles can act as astrophysical laboratories. To date, such analysis was confined to close-in planetary systems detected through transit observations. Astrometric and direct observation techniques may soon expand the orbital separations at which these studies can be conducted.

The first population-level study of eccentricities presented by directly detected substellar companions as conducted by Bowler et al. (2020) found two distinct distributions for BDs and exoplanets. While the exact shape of the underlying eccentricity distribution for exoplanets was called into question by Nagpal et al. (2023), its distinct nature as compared to the BD distribution now appears probable (see Sect. 1.2.2). While the BD population is likely to possess a broad peak at elevated eccentricities, the main bottleneck that has prevented these studies from drawing definitive conclusions as to the underlying planetary distribution is the small sample size of sufficiently constrained eccentricity posteriors stemming from direct detections. The hierarchical Bayesian approach employed in these investigations benefits from an increase in both the amount of eccentricity estimates as well as their precision. It follows that the detection and orbital characterisation of new substellar and especially planetary companions will have strong implications for these efforts. In a current study by Roberts et al. (in prep) these same procedures are already re-applied to an expanded and up-to-date planet sample that includes the back catalogue of eccentricity constraints enabled by GRAVITY planetometry. Yet again, this is a field of research that will benefit from the abundance of direct detections that DR4 will enable and the precise orbital solutions the Gaia-GRAVITY synergy will provide as a matter of routine and on the basis of a single follow-up detection.

#### 6.4 Companion on the brink: the tale of WT 766 B

The number of benchmarked brown dwarfs, that is objects with precisely determined bulk parameters such as mass and radius combined with a broad coverage of their spectral appearance that offers insights into their atmospheric makeup, is still limited to a handful of objects (see Rickman et al. 2024 and references therein). Yet, these objects act as vital empirical anchors for calibrating evolutionary and atmospheric models, which – in the absence of observational data – mostly rely on the theory of physical processes in the interior of BDs and exoplanets (Marley et al. 2007; Baraffe et al. 2003, 2015; Marleau & Cumming 2014; Marley et al. 2021). Compiling a sample of benchmarked companions will gauge these models, test their validity and reveal where refining is required.

The biases intrinsic to the different methods of exoplanet and BD detection and characterisation (see Sect. 1.2.1) render the combination of these techniques challenging. Transit observations, for instance, allow for measuring the radius of a given substellar companion, while fitting an orbital trajectory to direct companion detections facilitates estimates as to their dynamical masses. The transit and direct detection method are hardly ever applicable to the same object, however. This incompatibility of different methods is one reason why benchmarked objects are rare.

Presenting a semi-major axis of approximately  $0.6\,\mathrm{AU}$  and an orbital inclination of  $(89.87\pm0.10)\,\mathrm{deg}$ , the BD companion WT 766 B, which we encountered in Chapter 3, may offer an opportunity to achieve overlap between the population of transiting and directly imaged companions. Its remarkably edge-on orbit, depicted in the top left panel of Fig. 3.3 the left hand panel of Fig. 6.3, implies that a well-timed follow-up observation may allow us to catch it in transit. If successful, such an observation would mark the first transit observation of a directly detected substellar companion. The resulting radius measurement and transmission spectrum would add to our precise dynamical mass estimate and K-band GRAVITY spectrum and serve to elevate WT 766 B to the status of one of the most thoroughly benchmarked BD companions available to the transit and direct imaging communities.

To prepare for such an observation it is vital to confirm the transiting behaviour of WT 766 B and constrain the exact timing of the event. Both these needs can be addressed by one or more additional GRAVITY epochs of the companion. The additional data may sufficiently constrain the orbit inclination posterior such that it lies entirely within the transit opening angle of the system and pin down the period and time of periastron passage, the orbit parameters that govern the predicted transit time. To assess the effect of additional GRAVITY epochs, we used the refined posterior sampling obtained in Chapter 3 and visualised in Fig. B.7, to forecast the position of the companion relative to the host star at different times of observation. The resulting position predictions, shown in the left hand panel of Fig. 6.3, are sufficiently constrained to allow for GRAVITY follow-up observations. Fig. 6.3 reveals another qualitative detail about the optimal timing for such an undertaking: after reversing its projected orbital motion in the beginning of December 2025, the companion commences its projected approach towards the host. As its velocity projected onto the plane of the sky increases, the position predictions become more blurry

126 6. Outlook

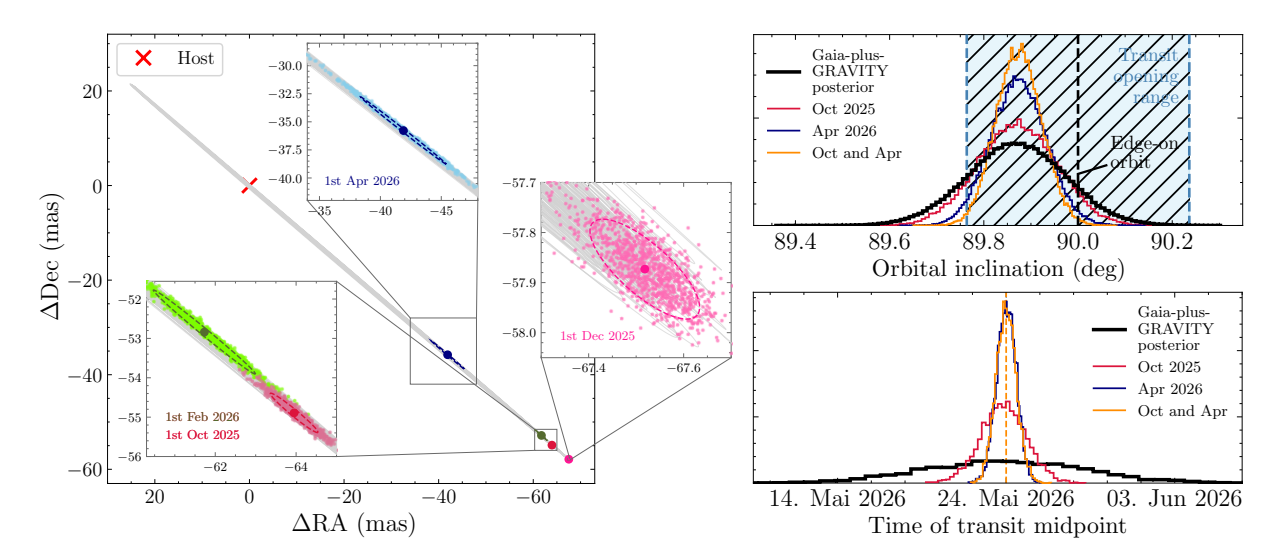


Figure 6.3: Left: Orbit of WT 766 B as projected onto the plane of the sky. The dots of different colours indicate companion position predictions for different observing dates with the bold circles marking the mean position and the dashed contours encompassing 68% of all predictions. Top right: Orbit inclination posterior based on the currently available Gaia and GRAVITY data. The different colours show how the posterior would change if the companion were detected at the positions marked by the bold dots of the respective colour in the left hand panel. For comparison, the blue hatched region visualises the transit opening angle on the system. Bottom right: Time of transit midpoint estimates based on the currently available data as well as assuming mock detections at the bold dots of the respective colour in the left hand panel. The most constrained posterior presents a median transit time on the 24th of May 2026, indicated by dashed line.

and elongated along the orbital trajectory, an effect best visible for the April 2026 prediction. Detecting the companion during this approach phase would yield stronger constraints on its orbital period and time of periastron passage. The time span between the direct follow-up and potential transit would also be shorter, enabling more precise transit timing estimates.

Adding mock GRAVITY epochs obtained at the mean position predictions to the already available data, we resampled the orbit posteriors to assess the constraining power of one or more additional follow-up detections at different times of observation. As is evident from the resulting inclination posteriors shown in the top right panel of Fig. 6.3, two well-timed additional GRAVITY epochs provide sufficient constraining power to confirm the transiting nature of WT 766 B<sup>2</sup>. As can be seen from the bottom right panel of Fig. 6.3, a

<sup>&</sup>lt;sup>2</sup>The additional data may also make the transit hypothesis less likely or rule it out entirely, depending on the position at which the companion is actually detected. In the absence of genuine epochs, we can only assess the constraining power of additional observations, not whether they might pull the posteriors in a different direction. This is why the posteriors and transit time estimates presented in Fig. 6.3 are centred on the currently available distributions.

significant constraint on the time of transit midpoint can also be obtained by re-observing the companion with the current prediction ointing towards the 24th of May 2026<sup>3</sup>. The precision to which this forecast can be made depends on the number and timing of the follow-up observations. Without additional data, the prediction is likely accurate to within twenty days. Detections of WT 766 B in October 2025 and April 2026 enable a constraint to within 29 hours.

If, after the follow-up, WT 766 B is indeed deemed likely to transit, a transit timing estimate within 29 hours will suffice to pursue a dedicated transit observing programme. With an expected transit depth of approximately  $1.2\,\%$  based on the current companion radius estimate (around  $1\,R_{Jup}$ ; see Fig. 3.5) and the characteristics of the host, using the CHEOPS satellite (Benz et al. 2021) or the Next Generation Transit Survey (NGTS; Wheatley et al. 2018) on Cerro Paranal are both viable options. Benchmarking WT 766 B in this way would – for the first time – bridge the gap between the transiting and direct imaging communities and provide a strong anchor for our models of substellar evolution and atmospheric makeup.

#### 6.5 What's next for exomoons?

The exomoon and binary planet sensitivity curves derived in Chapter 5 provide an intuitive sense about what kind of objects are detectable around a given planet using a certain instrument. More importantly, however, they prepare us for the next step towards making an exomoon detection reality. Knowledge about the limits of a given observation setup are critically important for an informed and well-refined target selection process.

With this key tool in hand, we can move towards conducting further studies into the intricacies of the observation planning and eventual data reduction. In particular, we need to explore different sampling techniques and establish the optimal observing strategy given a suspected signal period (Madore & Freedman 2005). Investigating which fitting routine based on what shape of priors works most efficiently and – more importantly – most reliably is another key line of inquiry.

Once these topics are sufficiently well understood, an efficient and goal-oriented detection effort can be embarked upon. Most likely such an undertaking will be rooted in an external and auxiliary line of evidence that points towards the existence of a moon around a given planet. An example of such additional clues is the inference of a moon around  $\beta$  Pic b on the basis of obliquity considerations as presented in Poon et al. (2024). On top of these external considerations there is a clear-cut case for selecting a close-by, massive and far-out substellar companion as the target of an exomoon-driven observation campaign. This would serve to maximise the planetometric signal-amplitude which decreases with the distance of the target system and ensure a high signal-to-noise planet detection for each

<sup>&</sup>lt;sup>3</sup>This date was computed by minimising the projected companion-to-host separation. Whether it corresponds to the primary or secondary transit is unclear. Two auxiliary RV epochs of the star would break this degeneracy, however.

128 6. Outlook

observation, thereby ruling out the loss of any epoch and facilitating a set of high-precision planetometric measurements.

Considering the myriad of comparable objects in our own Solar System, the first conclusive detection of an exomoon is only a matter of time. If followed through, the roadmap outlined above represents a promising avenue towards achieving this goal by means of the planetometric method.

## Chapter 7

## Summary & Conclusions

In this thesis, I have presented a technique that allows for a more efficient direct follow-up of substellar companions and enables detections at previously inaccessible orbital separations close to their respective hosts. To illustrate the evolution of our targeting capabilities, progressing from mostly blind to fully-targeted follow-up campaigns, and indeed my own perspective on how these topics fit into the field of exoplanet detection and characterisation, I have structured the investigated topics in a deliberate and sequential manner, presenting the conducted work as a coherent narrative.

Chapter 2 dealt with HIP 99770 b, the substellar companion whose detection by Currie et al. (2023b) can be considered a milestone in the development of our targeting capabilities: instead of pursuing blind direct detection campaigns, we are now demonstrably able to target specific stars on the grounds of their anomalous long-term proper motion behaviour indicating the presence of a previously unknown companion. On the basis of two GRAVITY observations of this companion that sits at the cusp between planets and BDs, we were able to characterise its orbit and atmosphere by conducting a thorough analysis of the new detections and spectra in the context of already available data. While unable to infer a definitive formation scenario for this companion, we were able to further constrain its eccentricity and atmospheric metallicity. These new results will aid future studies of HIP 99770 b and may help shed light on its true nature as well as its formation history.

In **Chapter 3**, we progressed from the semi-targeted method facilitated by the Hipparcos-Gaia PMa measurements to a fully-targeted technique that draws on Gaia data only. We demonstrated that the orbit solutions based on Gaia astrometry and presented in the NSS two-body orbit catalogue are of sufficient accuracy to allow for a prediction of not only which stars are likely to host substellar companions but where those companions are likely to be found relative to the star. While such an ability may seem irrelevant, since direct imaging instruments are able to probe the entire vicinity of a star, it is actually critically important for follow-up observations using instruments that only offer a small FoV such

as GRAVITY.

Combining the *Gaia* data with the GRAVITY detections was then shown to be a powerful method of constraining orbital parameters and dynamical masses. The synergetic nature of the *Gaia*–GRAVITY ensemble allows for pinning down the dynamical masses, typically to within relative uncertainties of a few per cent, on the basis a single GRAVITY epoch. Such efficiency will be especially valuable for building a large sample of directly detected companions with precisely determined masses once the publication of *Gaia* DR4 provides a plethora of directly detectable substellar candidates.

Our current limitation to the DR3 orbit solutions does not imply that hunting for planets needs to wait for the publication of the astrometric time-series data in DR4. In **Chapter 4**, we filtered the currently available data to select those putative planetary companions viable for follow-up, ultimately concluding that only two candidates could conceivably be targeted with GRAVITY at the time. Missing the first and resolving the second into a stellar imposter binary, we were forced to conclude our attempt at expanding the technique into the planetary mass regime without a detection. The study substantiated the critical importance of a robust target selection and age estimation as well as the conviction that avoiding imposter binaries that masquerade as planet-hosting systems is one of the major challenges of this field.

Observational exomoon research is a novel field of study that still awaits its first conclusive detection. In **Chapter 5**, we investigated the potential of searching for moons by unleashing the unparalleled planetometric precision of interferometric observing techniques and instruments on this topic. Simulating the gravitational perturbations that moons can inflict on the orbital trajectories of far-out exoplanets, we established the first sensitivity curves in the moon mass—separation plane and established that hunting for binary planets and favourable exomoons is already possible with the GRAVITY today. This study can be viewed as an indication of what lies ahead and can act as a prime science case for the near-infrared and optical interferometry community: if developed further, these techniques will likely allow for the detection and characterisation of a comprehensive sample of exomoons, objects that can act as probes of formation processes, shed light on the dynamic evolution of planetary systems and expand our search horizon for habitable worlds and extraterrestrial life in the nearby Galaxy.

Finally, in **Chapter 6** we dared to take a look at where the presented themes and developed techniques may lead in the future. One by one, we revisited the main topics encountered throughout this thesis, discussing possible next steps towards a better understanding of HIP 99770 b, remaining science cases facilitated by the *Gaia* DR3 source catalogue, future avenues to pursue on the basis of DR4, the follow-up of an unlikely edge-on substellar companion and the key steps required to make planetometric exomoon detections a reality.

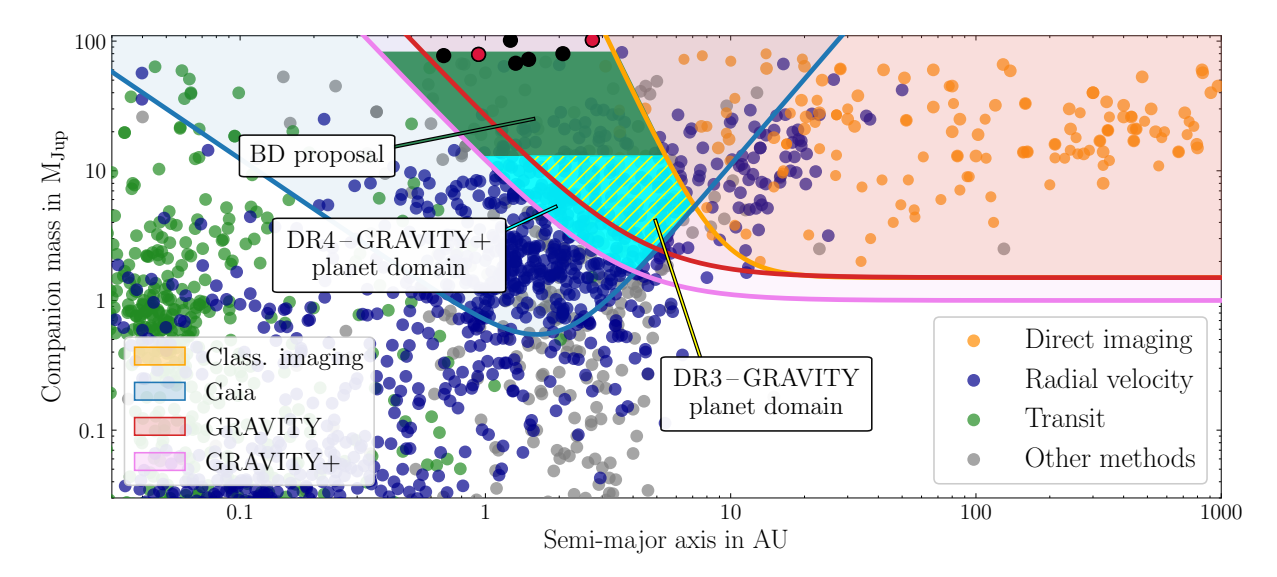


**Figure 7.1:** Combined version of Fig. 1.4, 4.1 and 6.2 visualising different elements discussed in this thesis: the high-mass BDs detected through the *Gaia*–GRAVITY synergy in Chapter 3 shown as black points with the two potentially underluminous companions shown in red, the DR3 planet hunting region aimed for in Chapter 4 visualised as the yellow hatched region and the BD proposal and DR4–GRAVITY+ target regions described in Chapter 6 shown in green and light blue, respectively.

Throughout Chapters 1 to 6, we have encountered different versions of a plot showing the planetary mass—separation plane occupied by different populations and instrument sensitivities, each variant highlighting the detections made or parameter space targeted in a given project or proposal. A combined version of all these diagrams (Fig. 1.4, 4.1 and 6.2) is shown in Fig. 7.1. This final edition combines the building blocks we have compiled throughout this thesis – the different biases of our detection methods and resulting diverse planetary populations as described in Chapter 1, the successful BD detections at high masses in Chapter 3, the unsuccessful hunt for planets in Chapter 4 and the regions aimed for in our BD underluminosity observing programme as well as future DR4-based planet hunting endeavours, both described in Chapter 6 – and serves as a visual summary of the progress made and science cases developed throughout this thesis.

#### Concluding remarks

Since exoplanet research began in earnest twenty-five years ago, many surprising lessons about their nature, the systems we tend to find them in and their atmospheres have been learned. Landmark missions like Kepler and Gaia have changed – or are about to change – the way we think about these distant worlds as well as our own home planet. The rapid

pace of new discoveries in this field shows no signs of slowing down. These are exciting times for exoplanet science. With the James Webb Space Telescope currently dedicating a large fraction of its observing time to planet-related programmes and the arrival of the ELT approaching fast, we are bound to uncover new surprises on the way to better understanding the formation, atmospheres and evolutionary behaviour of exoplanets.

Optical interferometry in general, and the VLTI in particular, will partake in this journey, with current instruments like GRAVITY already filling a niche that no other facility can serve. Future VLTI instruments or whole new facilities will increase the foothold this technique has already established within the exoplanet community. From close-in planets to ultra-precise dynamical mass estimates, all the way to exomoon detections, we have encountered several of the potential science cases throughout this thesis. Indeed, the work presented here, paves the way to more efficient direct detection campaigns and establishing overlap between the RV and directly detected planet populations in a region of the parameter space, where we expect a large reservoir of detectable companions to reside. Routinely detecting these planets resembling those found in our own Solar System will enhance our understanding of its formation and ultimately help answer the question as to how we got here.



**Figure 7.2:** Artist's impression of a BD companion, taken from the ESA press release dealing with the results presented in Chapter 3. These high-mass but Jupiter-sized objects orbit their hosts at distances of a few AU, comparable to the planetary semi-major axes found in the Solar System. Image credit: ESA.

## Appendix A

## Appendix to Chapter 2

#### A.1 Correcting for throughput losses

Misplacement between the centre of the GRAVITY science fibre and the target aimed for (in our case the companion) leads to a loss of flux throughput when observing in dual-field mode. To correct for this, we divided the contrast spectra by the normalised coupling efficiency,  $\gamma$ , of the respective observations. These values can be found in Table B.1. The coupling efficiency, visualised in Fig. A.1, varies between 1 and 0 and is a function the angular separation between the fibre centre and the target. A comprehensive derivation of its analytic description can be found in Wang et al. (2021).

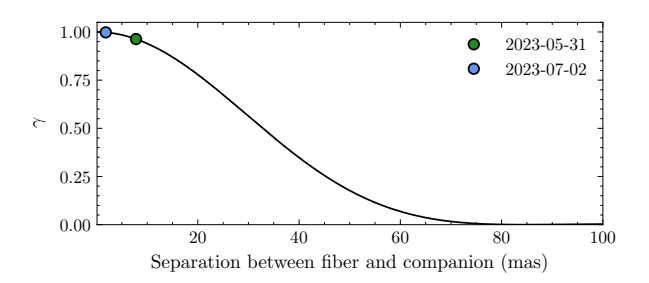


**Figure A.1:** Normalised coupling efficiency,  $\gamma$ , as a function of the misplacement between the centre of the science fibre and the target. The  $\gamma$ -values used to correct for the throughput losses incurred during the two observations are indicated.

#### A.2 Reduction of GRAVITY on and off-axis spectra

As described in Sect. 2.2.2, eventually arriving at the combined companion flux spectrum used in the analysis presented in Sect. 2.4 required converting the contrast spectra into companion flux spectra. This involved multiplying the contrast spectra by calibrator spectra that describe the reference targets (HIP 99770 A and the binary HD 196885 AB for the on and off-axis observations, respectively). In Fig. A.2, we present plots visualising the

fitting procedure yielding the best-fit stellar models with Table A.1 listing the parameter values associated to the highest-likelihood sample. We did not account for a potential variability of the star. If present, such variability can impact the goodness of our fits.

These best fitting stellar models,  $F_{\text{host}}^{\text{model}}$  for HIP 99770 A as well as  $F_{\text{A}}^{\text{model}}$  and  $F_{\text{B}}^{\text{model}}$  for the binary components of HD 196885 AB, are the calibrator spectra that were used to convert the observed contrast spectra, C, into companion flux spectra,  $F_{\text{comp}}$ , for both epochs via

$$F_{\text{comp, on-axis}} = C \cdot F_{\text{host}}^{\text{model}}, \quad F_{\text{comp, off-axis}} = C \cdot \langle F_{\text{host}}^{\text{FT}} \rangle \cdot \sqrt{\frac{F_{\text{A}}^{\text{model}} \cdot F_{\text{B}}^{\text{model}}}{\langle F_{\text{A}}^{\text{model}} \rangle \cdot \langle F_{\text{B}}^{\text{model}} \rangle}}, \quad (A.1)$$

where the operator  $\langle \rangle$  denotes the averaging over the GRAVITY bandpass. The flux average of the host star  $\langle F_{\text{host}}^{\text{FT}} \rangle$  that is required in Eq. A.1 is obtained from the simultaneous GRAVITY fringe tracker (FT) observations of the host at low spectral resolution. The covariances provided by the GRAVITY pipeline and stellar model uncertainties obtained by taking the standard deviation over 100 randomly drawn samples from the respective posteriors were propagated through each reduction step.

**Table A.1:** Inferred stellar model atmosphere parameters.

Star	$T_{\rm eff,A}$ (K)	$\log g_{\mathrm{A}}$	$R_{\rm A}~({ m R}_{\odot})$	$T_{\rm eff,B}$ (K)	$\log g_{\mathrm{B}}$	$R_{\rm B}~({\rm R}_{\odot})$	$\pi$ (mas)	$A_V \text{ (mag)}$	$f_{K_{ m s}}$
HIP 99770	$8085^{+33}_{-35}$	$4.09^{+0.05}_{-0.06}$	$1.96^{+0.01}_{-0.01}$				$24.54^{+0.06}_{-0.07}$	0.043*	
HD 196885	$6294_{-18}^{+17}$	$4.29_{-0.03}^{+0.03}$	$1.36^{+0.01}_{-0.01}$	$3648^{+129}_{-126}$	$4.65^{+0.06}_{-0.06}$	$0.52^{+0.04}_{-0.03}$	$29.41^{+0.02}_{-0.02}$	0	$0.059 \pm 0.006$

**Notes.** The indices A and B denote the different binary components.  $f_{K_s}$  is the Paranal/SPHERE.IRDIS\_B\_Ks band contrast between the components as estimated from the GRAVITY observations.

References. \* Murphy & Paunzen (2017)

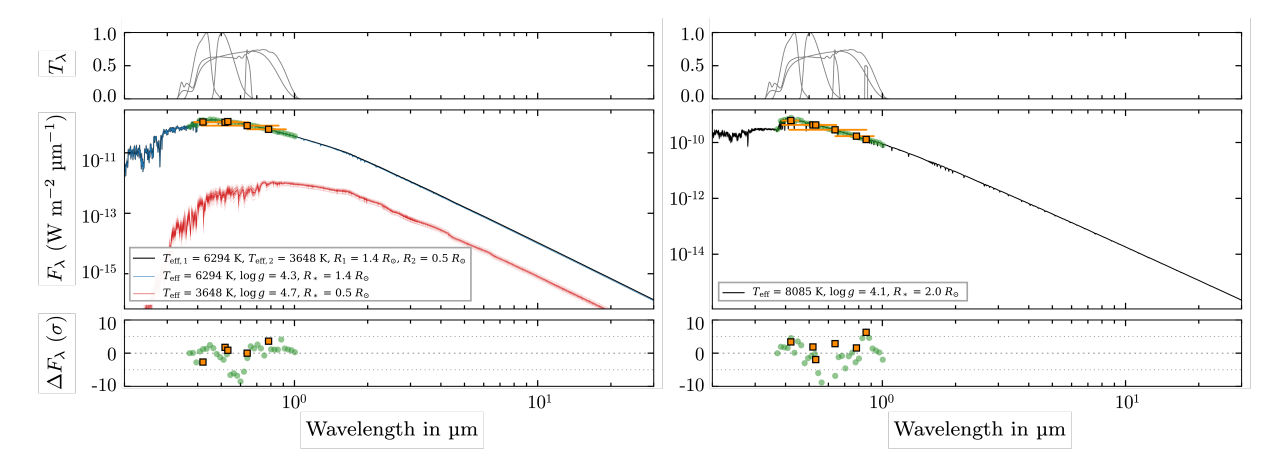


Figure A.2: Inferred stellar model atmospheres for HIP 99770 A (left) and HD 196885 AB (right). The inferred model atmospheres for the A and B components are shown in blue and red, respectively. The combined model is shown in black. The thin lines illustrate 30 randomly drawn samples from the posterior distribution. The photometry and the Gaia XP spectrum included in the fit are shown in orange and green. For greater clarity, only every 10th data point of the Gaia XP spectrum is shown. The top panel shows the filter transmission curve for each photometric point while the bottom panel presents the residuals between the data and the best fit model atmosphere.

#### A.3 Additional orbital fitting plots

Here, we present additional plots relating to the orbital analysis outlined in Sect. 2.3. The full corner plot showing how the inclusion of the GRAVITY astrometric epoch affects the posterior sampling of the orbital solution is shown in Fig. A.3.

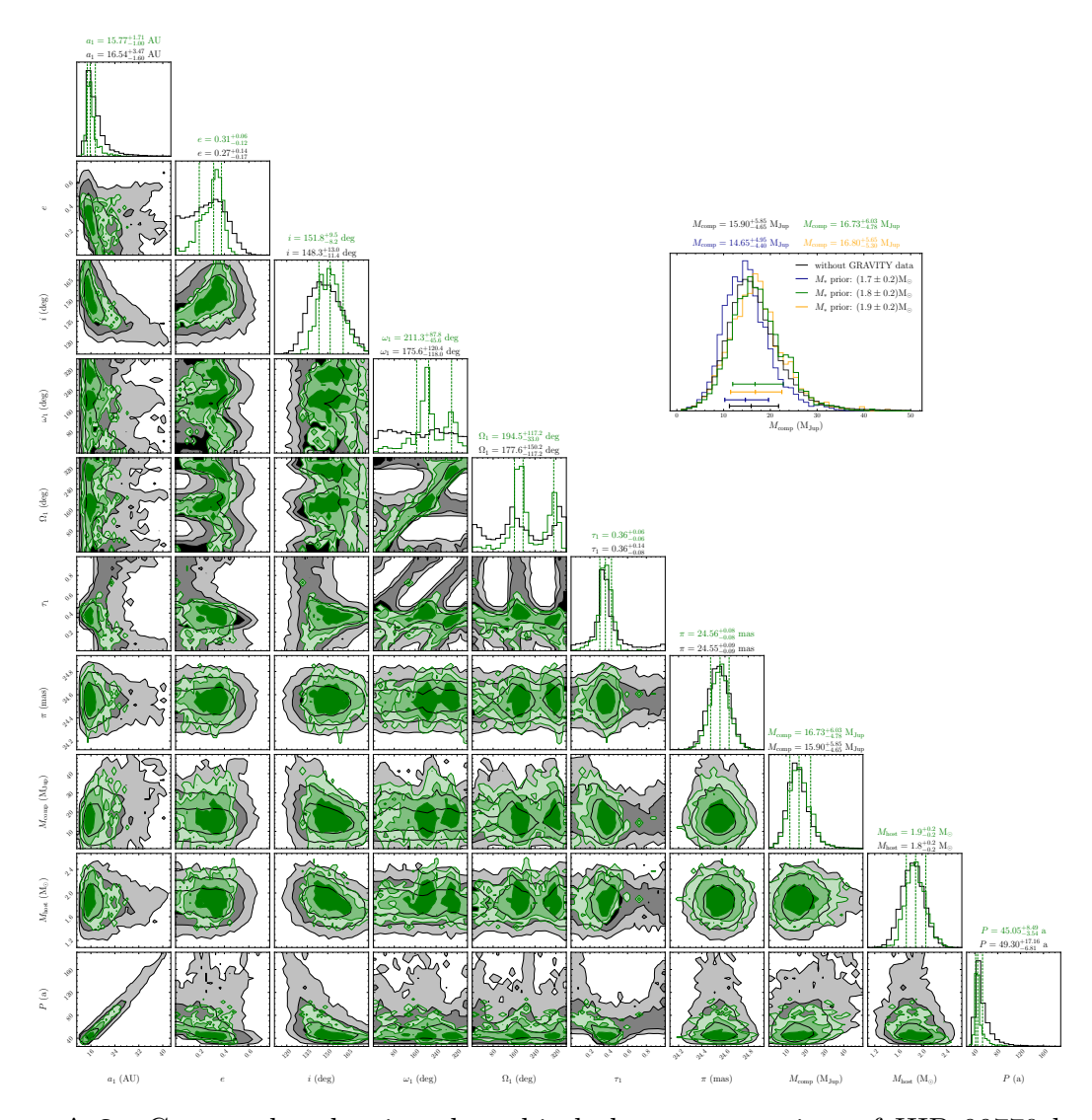


Figure A.3: Corner plot showing the orbital element posteriors of HIP 99770 b. The sampling resulting from only accounting for the previously available data and that obtained upon inclusion of the GRAVITY astrometric epoch (on-axis observation on 31 May 2023) are shown in black and green, respectively. The reported values above the panels showing the marginalised posterior distributions correspond to the median and boundaries of the 68% confidence intervals of the respective element in each sampling run. The top right panel shows companion mass posterior distributions sampled using Gaussian stellar mass priors whose centres were shifted from 1.8 to 1.7 and  $1.9\,\mathrm{M}_\odot$ , respectively.

#### A.4 Additional spectral fitting plots

Here, we present additional plots relating to the spectral analysis outlined in Sect. 2.4.

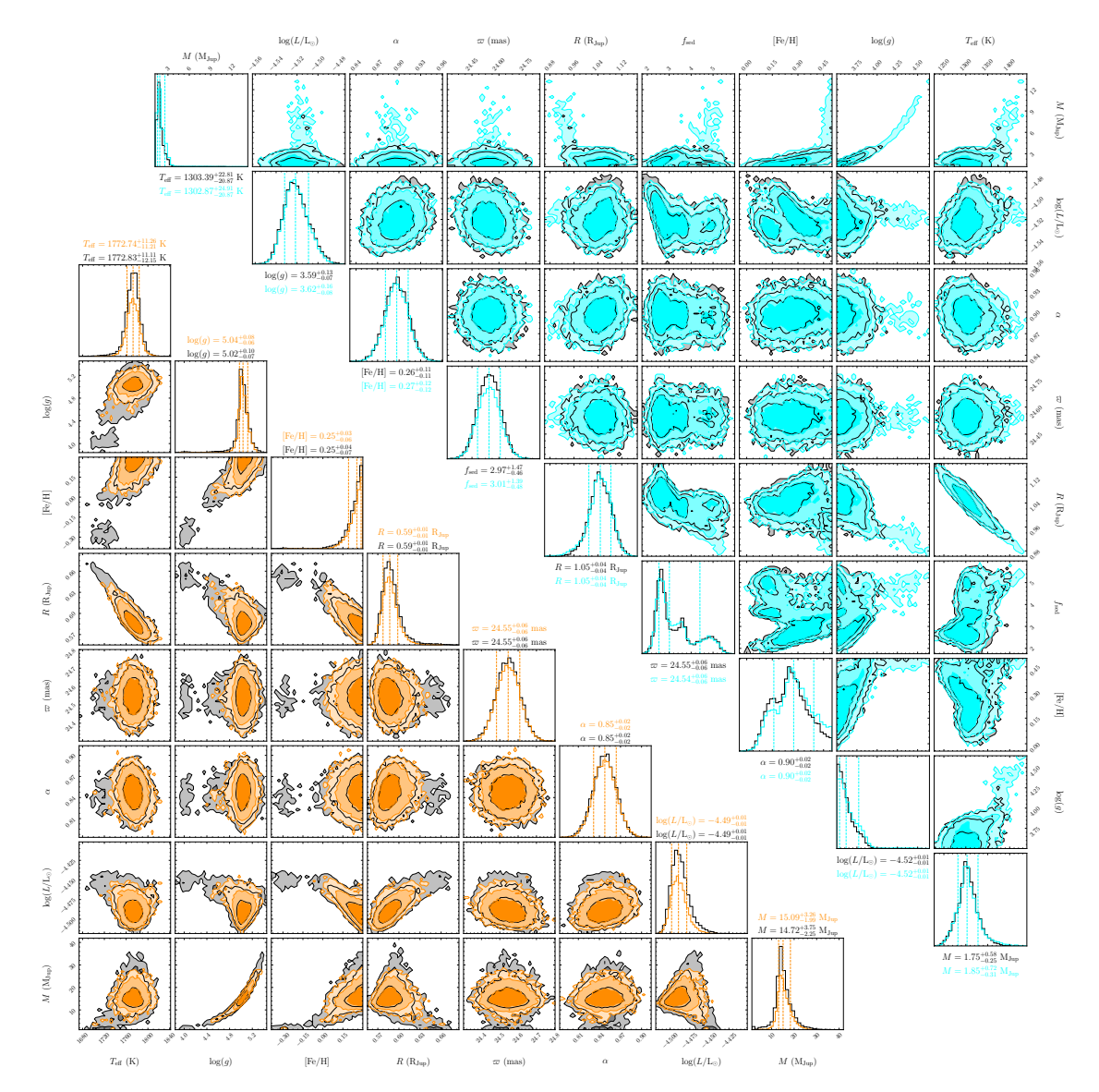
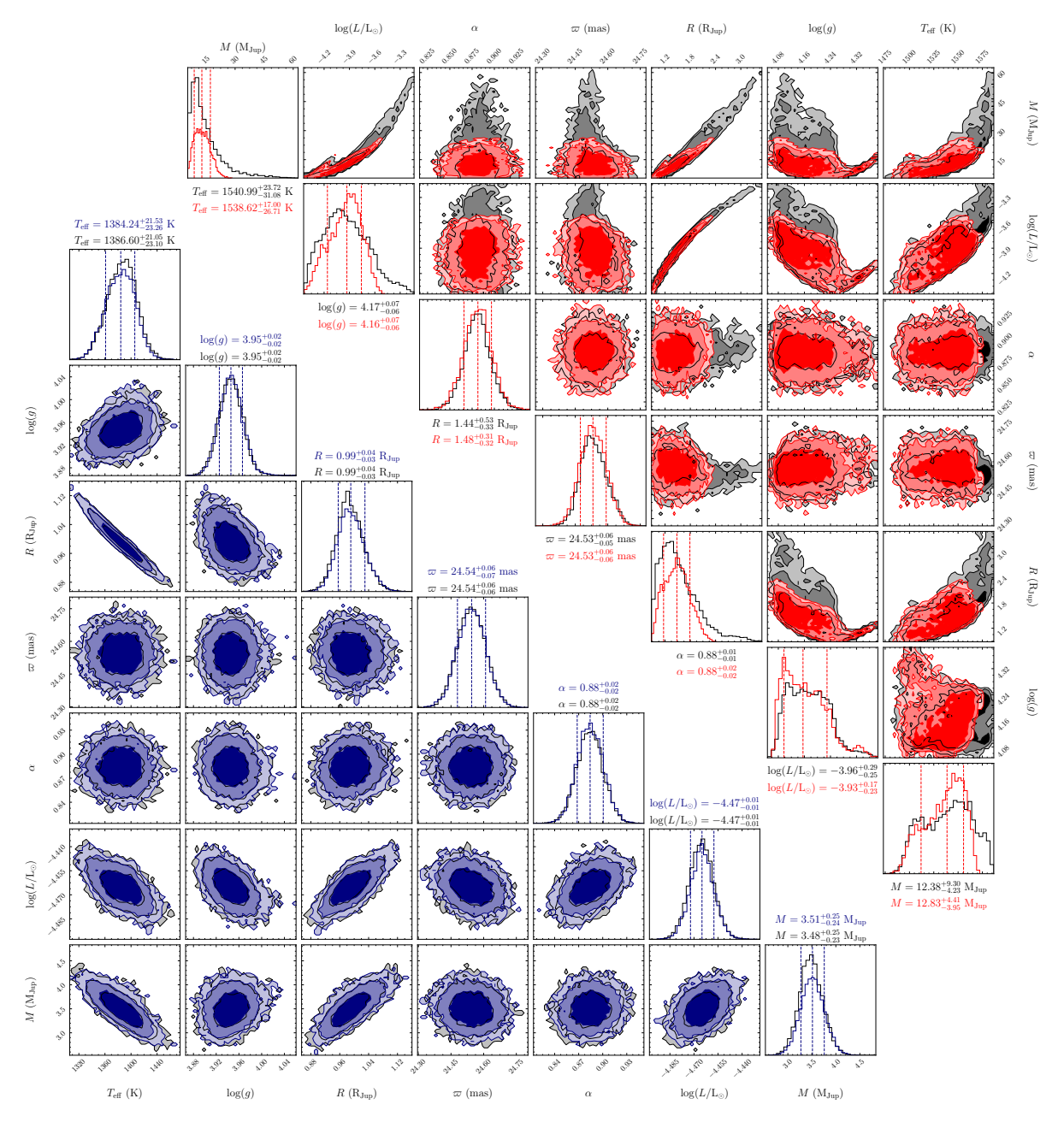


Figure A.4: Lower left: Corner plot showing the posterior sampling of the parameter grid when applying the DRIFT-PHOENIX model to the full set spectroscopic and photometric data presented in Sect 2.2. Two sampling runs were performed: the results obtained when using no mass prior, that is an uninformative uniform prior, and when using a Gaussian prior based on the dynamical mass obtained from the orbital fit (see Sect. 2.3) are shown in black and orange, respectively. Above the panels showing the marginalised posterior distributions we report their median values and their differences to the 84th and 16th percentiles in superscript and subscript, respectively. Upper right: Same as lower left for the Sonora Diamondback model grid.



**Figure A.5:** Same as Fig. A.4 for the BT-Settl and Saumon, Marley Cloudy (2008) model grids in the lower left and upper right panels, respectively.

## Appendix B

## Appendix to Chapter 3

### B.1 Correcting for throughput losses

When observing targets in the dual-field on-axis mode of GRAVITY, situations can arise where the companion body is separated from the centre of the science fibre by a certain angular distance. This can be case when the companion's position relative to the host cannot be constrained well enough to inform the proper placement of the fibre or when the observer deliberately moves the fibre in such a way that the target is not located at its centre anymore. This fibre off-pointing technique (Pourré et al. 2024) can facilitate contrast capability gains rendering it especially useful for such observations where one expects unfavourable contrast conditions between the companion and host. For both these reasons the observations conducted for this work exhibit angular separations between the eventually detected companions and the fibre-centre. Following the procedure outlined in Appendix A of Wang et al. (2021), we computed the normalised coupling efficiency,  $\gamma$ , as a function of the angular separation from the fibre centre. The relation as well as the respective companions' separations are presented in Fig. B.1. Dividing the observed contrast spectra by the respective coupling efficiency,  $\gamma$ , we can correct for the ensued throughput losses.

#### B.2 Inflation factors for *Gaia* uncertainties

As discussed in Sect. 3.4.1, the companion position angle predictions based on the *Gaia* NSS two-body orbit catalogue in combination with the true position angle measured with GRAVITY can be used to assess how robust the *Gaia* uncertainties are. In Fig. B.2 we present the comparison between prediction and detection for each target system.

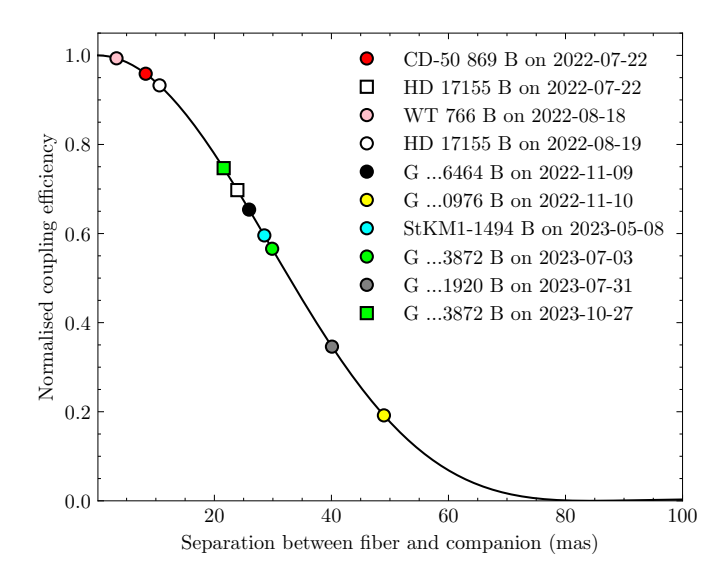


**Figure B.1:** Normalised coupling efficiency,  $\gamma$ , as a function of the angular separation between the fibre centre and the observed body.

#### B.3 Additional tables and plots

Here, we present additional relevant tables and plots. Table B.1 presents the observation log for every target observed with the GRAVITY instrument. Table B.2 lists the stellar magnitudes used for the spectral fits. Table B.4 showcases the inferred numerical results for each orbital parameter, the host and companion masses as well as the characteristics inferred from evolutionary models for each target system. Table B.3 lists synthetic companion magnitudes resulting from the application of the inferred ages and masses to evolutionary models. Figure B.3 shows the companion-to-host K band contrast spectra measured by GRAVITY. The full corner plots of the respective MCMC runs for each target system are presented in Fig. B.4 to B.10.

Target Name	Date	Start time (UT)	End time (UT)	$N_{\rm exp}$ / $N_{ m DIT}$ / DIT (s)	airmass	$\tau_0 \; (\mathrm{ms})$	seeing	$(\Delta RA, \Delta Dec)_{Fibre}$ (mas, mas)
G6464	2022-11-09	01:56:47	02:57:59	16 / 4 / 30	1.82	0.006	0.560	(28, 53)
G0976	2022-11-10	01:49:26	02:22:20	8 / 4 / 30	1.05	0.006	0.685	(38, -60)
CD-50 869	2022-07-22	08:55:04	09:56:35	8 / 32 / 10	1.24	0.002	1.288	(50, -25)
HD 17155	2022-07-22	07:31:51	08:29:51	8 / 32 / 10	1.44	0.002	1.26	(55, -15)
	2022-08-19	08:42:32	09:38:51	8 / 32 / 10	1.08	0.013	0.586	(54, 7)
WT 766	2022-08-18	04:34:07	05:00:46	4 / 12 / 30	1.12	0.003	1.23	(-70, -60)
G3872	2023-07-03	08:47:12	09:56:39	8 / 4 / 100	1.40	0.005	0.625	(65, -55)
	2023-10-27	06:12:01	06:47:37	4 / 8 / 30	1.27	0.002	1.176	(59, -28)
G1920	2023-07-31	09:17:12	10:30:54	8 / 4 / 100	1.14	0.003	0.749	(44, 73)
StKM1-1494	2023-05-08	06:11:37	07:19:57	8 / 4 / 100	1.06	0.002	0.976	(-54 58)

**Table B.1:** Observation log of the GRAVITY follow-up.

**Notes.**  $N_{\rm exp}$  denotes the number of exposures.  $N_{\rm DIT}$  is the number of detector integrations per exposure, while DIT is the detector integration time. The atmospheric coherence time during the observation is given by  $\tau_0$ .  $(\Delta {\rm RA}, \Delta {\rm Dec})_{\rm Fibre}$  describes the placement of the fibre centre relative to the host star.

**Table B.2:** Stellar magnitudes in different wavelength bands used for the spectral fits performed in Sect. 3.4.3.

Target Name	$GAIA3.G^{1}$	$GAIA3.Grvs^{1}$	$2MASS.J^2$	$2MASS.H^2$	$2MASS.Ks^2$	${ m WISE.W1^3}$	${ m WISE.W2^3}$	WISE.W3 <sup>3</sup>	$WISE.W4^3$
G6464	$(11.687 \pm 0.002)$	-	$(9.20 \pm 0.02)$	$(8.61 \pm 0.06)$	$(8.30 \pm 0.03)$	$(8.21 \pm 0.02)$	$(8.11 \pm 0.02)$	$(8.00 \pm 0.02)$	$(7.9 \pm 0.2)$
G0976	$(13.708 \pm 0.003)$	_	$(10.86 \pm 0.02)$	$(10.35 \pm 0.02)$	$(10.08 \pm 0.02)$	$(9.90 \pm 0.02)$	$(9.73 \pm 0.02)$	$(9.56 \pm 0.03)$	$(8.6 \pm 0.3)$
CD-50 869	$(9.463 \pm 0.003)$	_	$(8.07 \pm 0.02)$	$(7.68 \pm 0.06)$	$(7.53 \pm 0.02)$	$(7.39 \pm 0.03)$	$(7.53 \pm 0.02)$	$(7.486 \pm 0.017)$	$(7.59 \pm 0.10)$
HD 17155	$(8.709 \pm 0.003)$	_	$(7.14 \pm 0.02)$	$(6.62 \pm 0.03)$	$(6.49 \pm 0.03)$	$(6.47 \pm 0.08)$	$(6.46 \pm 0.02)$	$(6.486 \pm 0.015)$	$(6.45 \pm 0.05)$
WT 766	$(11.985 \pm 0.003)$	$(10.177 \pm 0.008)$	$(9.12 \pm 0.03)$	$(8.48 \pm 0.03)$	$(8.19 \pm 0.02)$	$(8.03 \pm 0.02)$	$(7.83 \pm 0.02)$	$(7.671 \pm 0.018)$	$(7.45 \pm 0.14)$
G3872	$(11.364 \pm 0.003)$	=	$(9.01 \pm 0.03)$	$(8.35 \pm 0.04)$	$(8.14 \pm 0.03)$	$(7.98 \pm 0.03)$	$(7.97 \pm 0.02)$	$(7.857 \pm 0.018)$	$(7.63 \pm 0.11)$
G1920	$(11.688 \pm 0.003)$	_	$(9.52 \pm 0.02)$	$(8.85 \pm 0.03)$	$(8.68 \pm 0.02)$	$(8.54 \pm 0.02)$	$(8.51 \pm 0.02)$	$(8.40 \pm 0.02)$	$(8.5 \pm 0.2)$
StKM1-1494	$(10.535 \pm 0.003)$	_	$(8.30 \pm 0.02)$	$(7.71 \pm 0.03)$	$(7.45 \pm 0.03)$	$(7.34 \pm 0.03)$	$(7.34 \pm 0.02)$	$(7.268 \pm 0.018)$	$(7.17 \pm 0.10)$

References. (1) Gaia Collaboration et al. (2023b); (2) Cutri et al. (2003); (3) Cutri et al. (2021).

**Table B.3:** Synthetic absolute magnitudes of the different companions.

Target Name	$MKO.J^1$	MKO.H <sup>1</sup>	MKO.K <sup>1</sup>	MKO.Lp <sup>1</sup>	${ m MKO.Mp}^1$	WISE.W12	WISE.W2 <sup>2</sup>	WISE.W3 <sup>2</sup>	WISE.W4 <sup>2</sup>	GAIA3.G <sup>3</sup>	$(F_c/F_*)_{ t GAIA3.G}$
G6464 B	-	-	-	-	-	-	-	-	-	-	=
G0976 B	_	_	_	_	_	_	_	-	_	-	-
CD-50 869 B	_	_	_	_	_	_	_	_	_	_	-
HD 17155 B	_	_	_	_	_	-	_	-	_	$16.0_{-4}^{+7}$	$(0.014 \pm 0.008) \%$
WT 766 B	$11.45^{+0.09}_{-0.07}$	$10.85^{+0.07}_{-0.08}$	$10.55^{+0.08}_{-0.07}$	$9.83^{+0.05}_{-0.06}$	$10.44^{+0.09}_{-0.09}$	$10.27\substack{+0.07 \\ -0.05}$	$10.21\substack{+0.08 \\ -0.07}$	$9.70^{+0.05}_{-0.05}$	$9.69^{+0.05}_{-0.06}$	$16.11\substack{+0.20 \\ -0.15}$	$(1.3 \pm 0.2)\%$
${\rm G}$ 3872 ${\rm B}$	$12.88^{+0.11}_{-0.09}$	$12.23^{+0.13}_{-0.11}$	$12.24^{+0.18}_{-0.13}$	$11.14^{+0.13}_{-0.11}$	$11.55^{+0.06}_{-0.06}$	$12.05^{+0.17}_{-0.16}$	$11.29\substack{+0.07 \\ -0.07}$	$10.49\substack{+0.05 \\ -0.05}$	$10.38^{+0.05}_{-0.04}$	-	_
G1920 B	-	-	-	-	-	-	-	-	-	-	_
StKM1-1494 B	$11.98^{+0.09}_{-0.09}$	$11.33^{+0.08}_{-0.08}$	$11.09^{+0.10}_{-0.10}$	$10.19^{+0.08}_{-0.08}$	$10.91^{+0.08}_{-0.07}$	$10.74^{+0.11}_{-0.10}$	$10.63^{+0.08}_{-0.07}$	$9.96^{+0.05}_{-0.04}$	$9.94^{+0.04}_{-0.04}$	$17.28^{+0.20}_{-0.18}$	$(0.026 \pm 0.004)\%$

Notes. The GAIA3.G magnitude was computed via the Baraffe et al. (2015) model, while the ATMO model grid Phillips et al. (2020) was utilised to calculate the other magnitudes. Where the companion mass lies outside of the mass range for which one or the other model is defined, only one model could be used. No magnitudes could be computed for targets lacking age (G ...6464 B, CD-50 869 B and G ...1920 B) or both age and dynamical mass (G ...0976 B). The rightmost column shows the companion-to-host flux ratio in the GAIA3.G band, which is of importance for the zero-companion-Gaia-flux hypothesis.

References. (1) Tokunaga et al. (2002); (2) Cutri et al. (2021); (3) Gaia Collaboration et al. (2023b).

Table B.4: Orbital and evolutionary model parameters of the respective target systems.

	G6464	G0976	CD-50 869	HD 17155	WT 766	G3872	G1920	StKM1-1494
$a_1 \text{ (mas)}$	$4.30^{+0.05}_{-0.05}$	_	$4.85^{+0.18}_{-0.16}$	$8.12^{+0.14}_{-0.14}$	$17.66^{+0.14}_{-0.13}$	$5.15^{+0.03}_{-0.03}$	$4.54^{+0.03}_{-0.02}$	$5.40^{+0.02}_{-0.02}$
i  (deg)	$59.0^{+0.7}_{-0.7}$	_	$92.2^{+0.2}_{-0.2}$	$71.5^{+0.4}_{-0.4}$	$89.87^{+0.11}_{-0.10}$	$152.8^{+1.0}_{-1.0}$	$99.2^{+0.3}_{-0.3}$	$93.7^{+0.3}_{-0.3}$
$\omega_1 \; (\mathrm{deg})$	$18^{+6}_{-6}$	_	$72.6_{-0.8}^{+0.8}$	$95.7^{+0.4}_{-0.4}$	$132.0_{-0.6}^{+0.6}$	$348^{+3}_{-3}$	$321.9_{-0.7}^{+0.7}$	$93.3^{+1.6}_{-1.5}$
$\Omega_1 \text{ (deg)}$	$46.2^{+1.0}_{-1.0}$	_	$113.7^{+0.3}_{-0.3}$	$0.5^{+0.4}_{-0.3}$	$49.46^{+0.06}_{-0.06}$	$85.6^{+1.9}_{-1.9}$	$27.3^{+0.2}_{-0.2}$	$136.20^{+0.15}_{-0.16}$
e	$0.284^{+0.011}_{-0.012}$	_	$0.722^{+0.019}_{-0.018}$	$0.770^{+0.009}_{-0.009}$	$0.623^{+0.007}_{-0.007}$	$0.315^{+0.006}_{-0.006}$	$0.638^{+0.007}_{-0.007}$	$0.331^{+0.006}_{-0.006}$
P (d)	$521.9^{+0.6}_{-0.6}$	_	$1780^{+80}_{-70}$	$1463^{+12}_{-11}$	$596.6^{+0.7}_{-0.7}$	$983.1^{+0.9}_{-0.9}$	$788^{+2}_{-2}$	$828.2^{+1.6}_{-1.6}$
$t_{\rm p,rel}$ (d)	$-249^{+7}_{-7}$	_	$53^{+8}_{-9}$	$360^{+8}_{-8}$	$230.7^{+0.9}_{-1.0}$	$398^{+3}_{-3}$	$-71.8^{+1.3}_{-1.3}$	$348^{+4}_{-4}$
$\pi$ (mas)	$32.29^{+0.03}_{-0.03}$	_	$18.877^{+0.011}_{-0.011}$	$35.305^{+0.013}_{-0.013}$	$74.92^{+0.04}_{-0.04}$	$29.0560^{+0.018}_{-0.018}$	$21.860^{+0.012}_{-0.013}$	$35.81^{+0.02}_{-0.02}$
$M_{tot}~({\rm M}_{\odot})$	$0.60^{+0.03}_{-0.03}$	_	$1.1_{-0.2}^{+0.3}$	$0.77^{+0.05}_{-0.05}$	$0.285^{+0.005}_{-0.005}$	$0.653^{+0.011}_{-0.011}$	$0.687^{+0.014}_{-0.013}$	$0.632^{+0.016}_{-0.015}$
q	$0.142^{+0.003}_{-0.003}$	_	$0.094^{+0.008}_{-0.009}$	$0.111^{+0.003}_{-0.003}$	$0.349^{+0.003}_{-0.003}$	$0.1182^{+0.0013}_{-0.0013}$	$0.1642^{+0.0018}_{-0.0018}$	$0.1135^{+0.0011}_{-0.0010}$
$M_1~({ m M}_\odot)$	$0.53^{+0.03}_{-0.03}$	_	$1.03^{+0.3}_{-0.19}$	$0.69^{+0.05}_{-0.04}$	$0.211^{+0.004}_{-0.004}$	$0.584^{+0.011}_{-0.010}$	$0.590^{+0.013}_{-0.012}$	$0.568^{+0.014}_{-0.014}$
$M_2  \left( \mathrm{M_{jup}} \right)$	$79^{+3}_{-3}$	_	$102^{+19}_{-12}$	$80^{+4}_{-4}$	$77.3^{+1.4}_{-1.3}$	$72.3_{-0.7}^{+0.7}$	$101.5_{-1.3}^{+1.3}$	$67.5^{+1.2}_{-1.2}$
$\mathrm{Age}^{\mathtt{ATMO}}\ (\mathrm{Myr})$	_	_	_	_	$670^{+40}_{-40}$	$1950^{+170}_{-120}$	_	$670^{+40}_{-30}$
Age <sup>Baraffe</sup> (Myr)	_	_	_	$760^{+260}_{-130}$	$650^{+50}_{-40}$	_	_	$630^{+40}_{-30}$
$T_{ m eff}^{ m ATMO}~({ m K})$	_	_	_	_	$2328_{-7}^{+5}$	$1750^{+8}_{-9}$	_	$2083_{-12}^{+15}$
$T_{\rm eff}^{\rm Baraffe}$ (K)	_	_	_	$2319_{-30}^{+11}$	$2316_{-9}^{+17}$	_	_	$2054_{-12}^{+15}$
$R^{ t ATMO} \left( \mathrm{R_{Jup}} \right)$	_	_	_	_	$0.977^{+0.003}_{-0.004}$	$0.844^{+0.003}_{-0.003}$	_	$0.941^{+0.004}_{-0.005}$
$R^{\mathrm{Baraffe}}$ (R <sub>Jup</sub> )	_	_	_	$0.988^{+0.011}_{-0.006}$	$1.000^{+0.006}_{-0.007}$	_	_	$0.967^{+0.004}_{-0.003}$

**Notes.** The indices 1 denote that the shown parameters describe the host star's orbit around the respective system's COM.

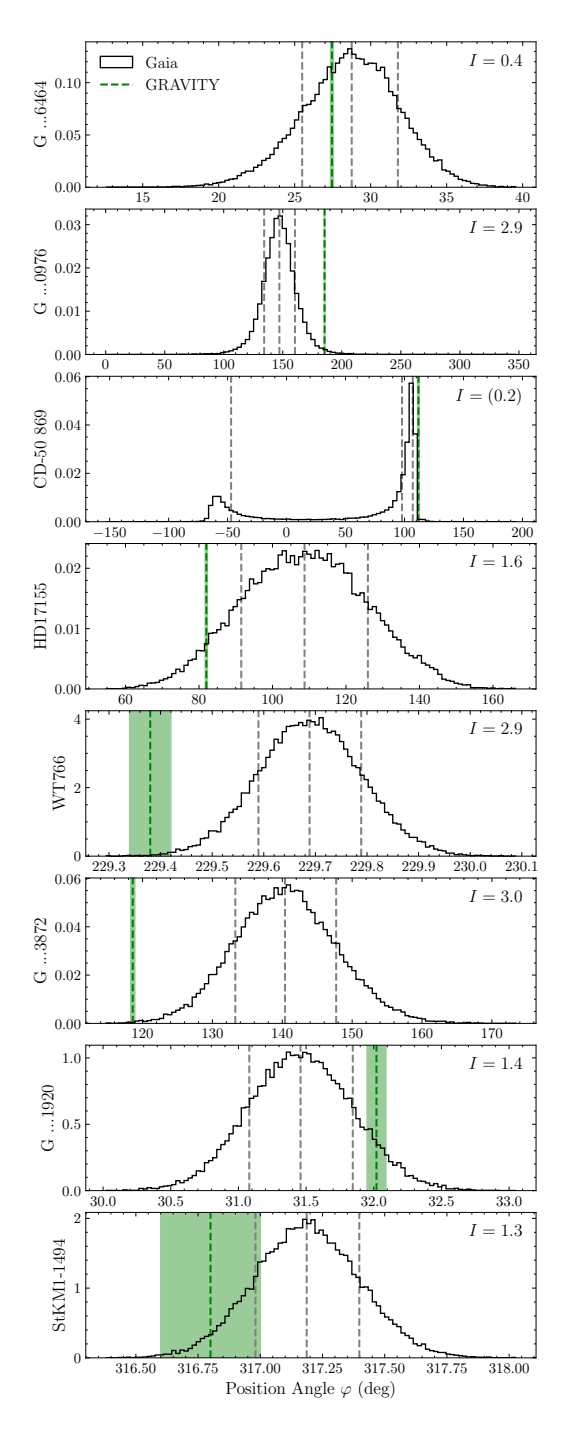
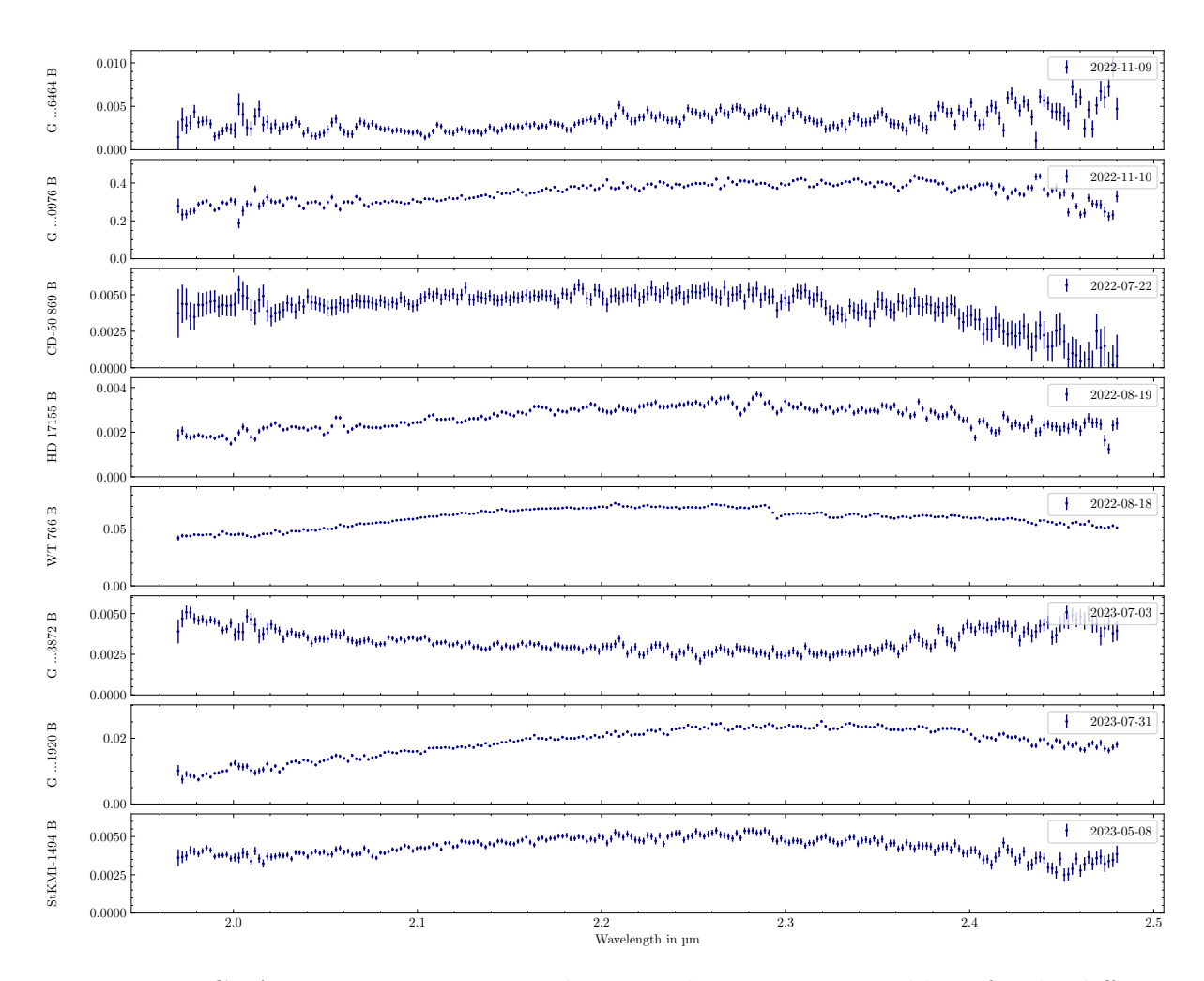


Figure B.2: Position angle distributions of the individual companions as predicted from the Gaia NSS two-body orbit solutions as well as the position angles at which the respective companions were detected using GRAVITY (in green). The inflation factor, I, required to make the  $1\,\sigma$  confidence interval encompass the detection is given in the top-right corner of each panel. Note that the distribution's non-Gaussian shape in the panel for the CD-50 869 system renders the resulting inflation factor unusable.



**Figure B.3:** GRAVITY contrast spectra between the companion and host for the different target systems. For targets that were observed multiple times, the spectrum with the highest signal-to-noise ratio is shown.

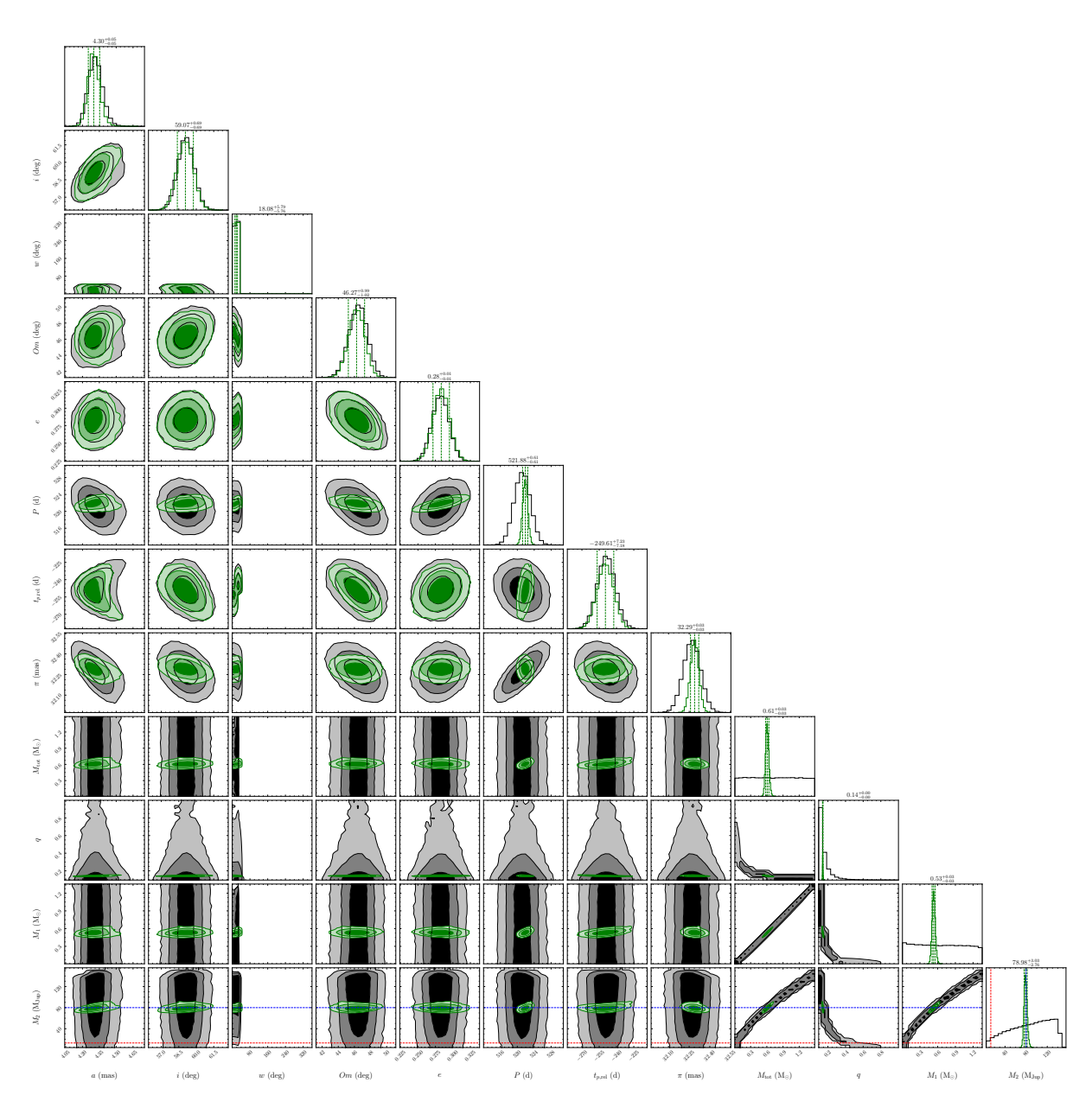
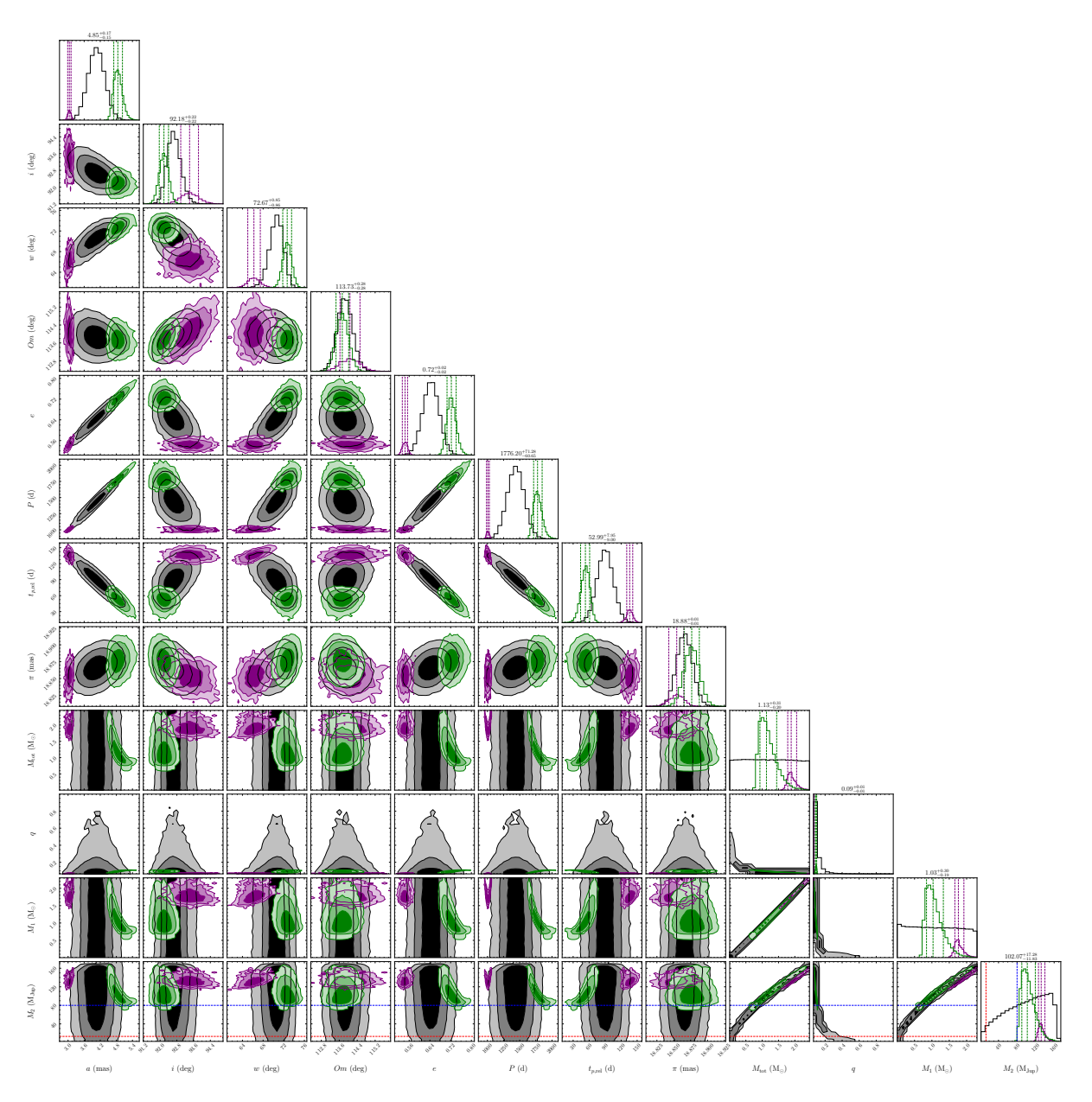


Figure B.4: Corner plot showing the posterior samplings for the G ...6464 system. The Gaia-only and the Gaia-plus-GRAVITY run are presented in black and green, respectively. The indices 1 denote that the shown parameters describe the host star's orbit around the respective system's COM. The dashed blue and red lines in the  $M_2$  row indicate the upper and lower BD mass boundaries, respectively.



**Figure B.5:** Same as Fig. B.4 but for the CD-50 869 system. This bimodal posterior sampling was separated into the preferred (green) and the secondary mode (purple).

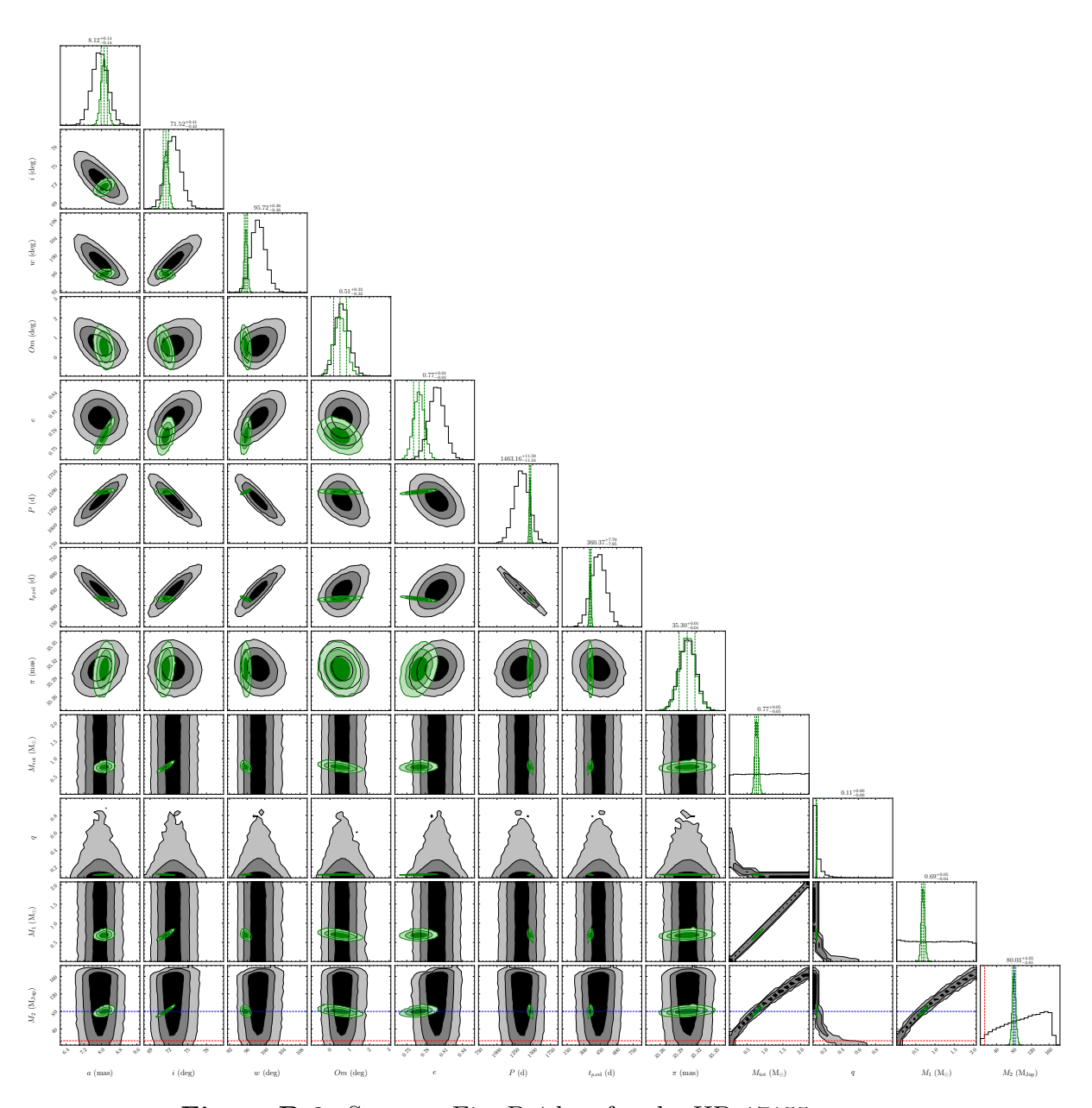


Figure B.6: Same as Fig. B.4 but for the HD 17155 system.

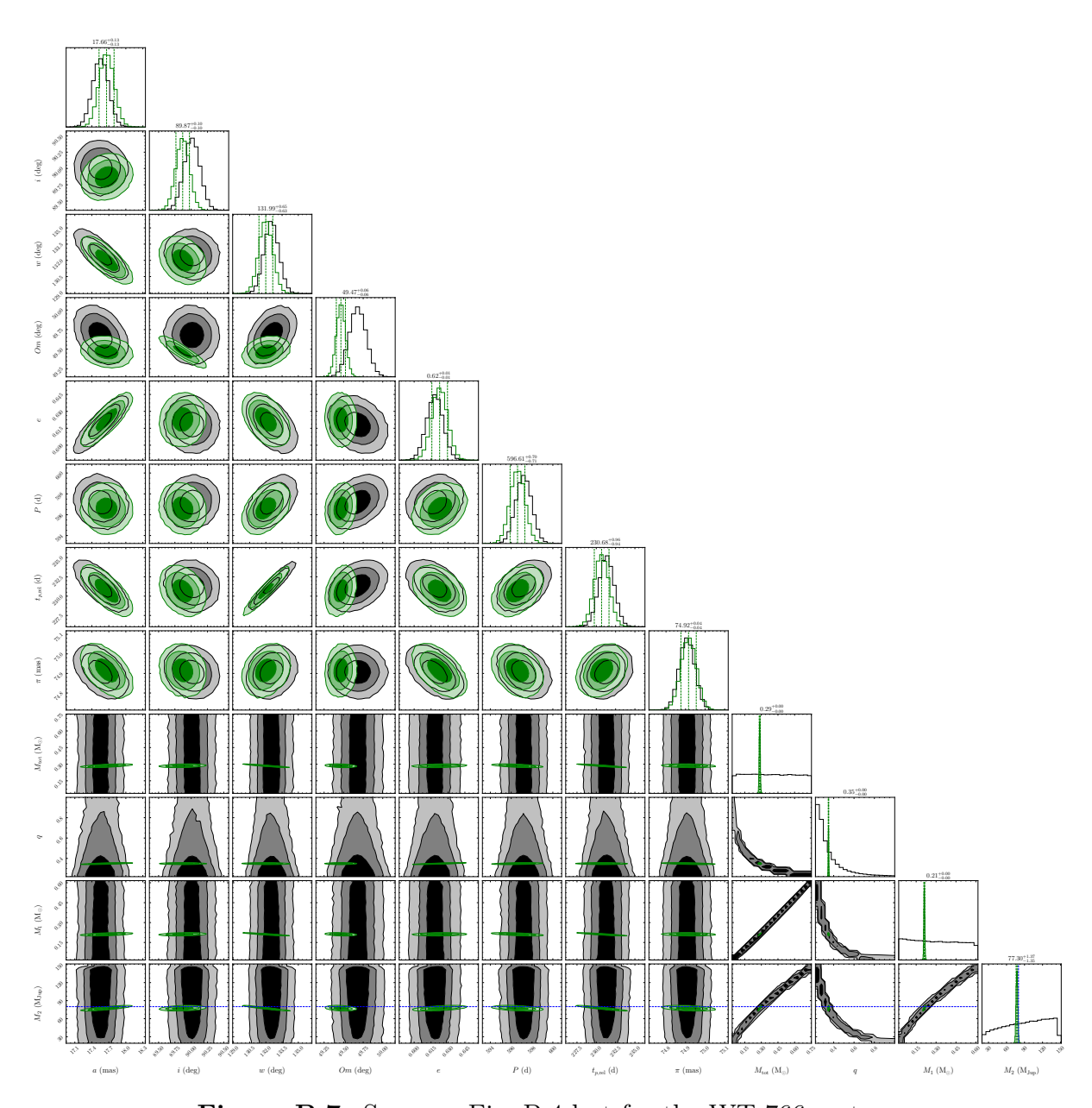


Figure B.7: Same as Fig. B.4 but for the WT 766 system.

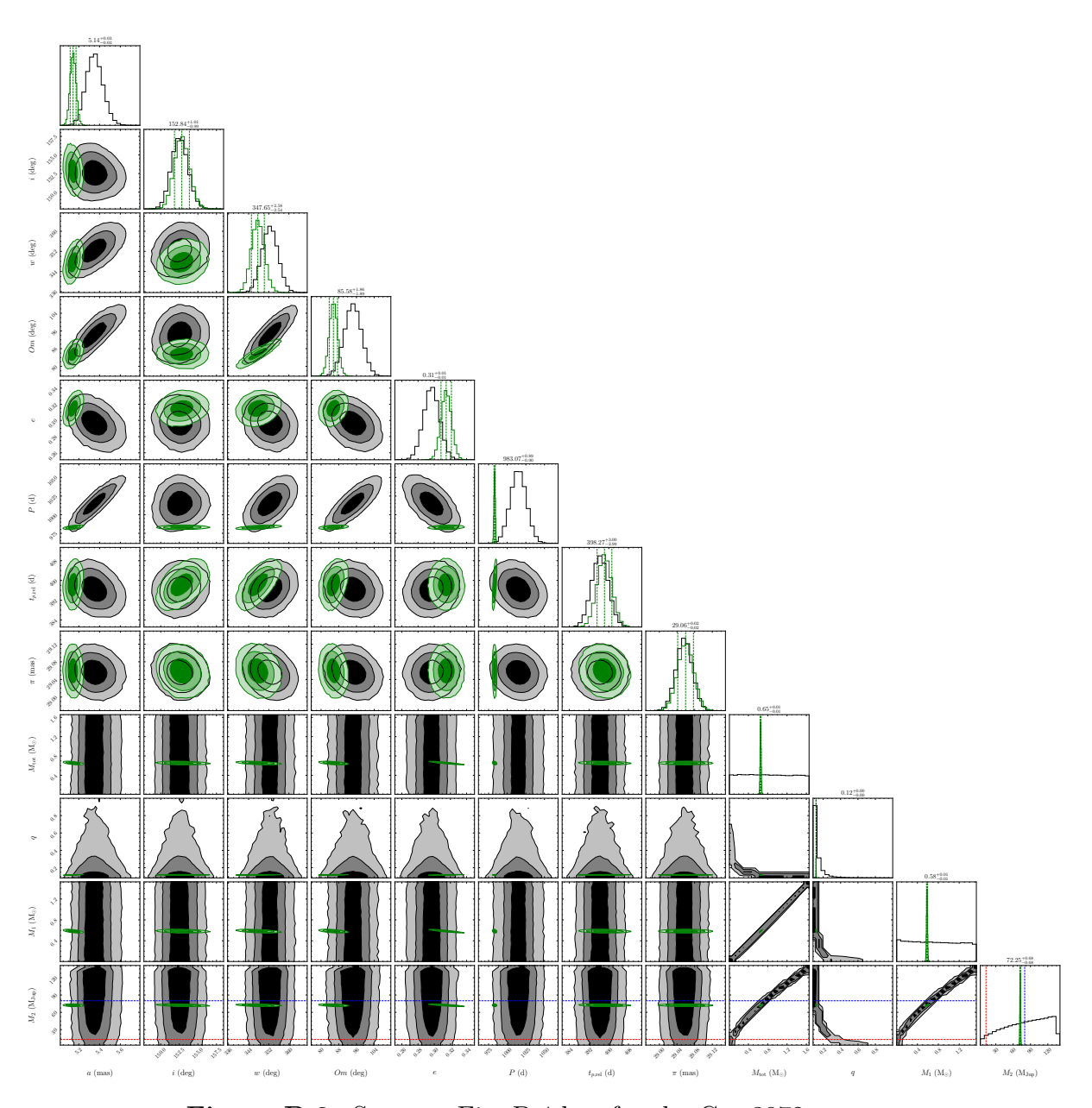


Figure B.8: Same as Fig. B.4 but for the G ...3872 system.

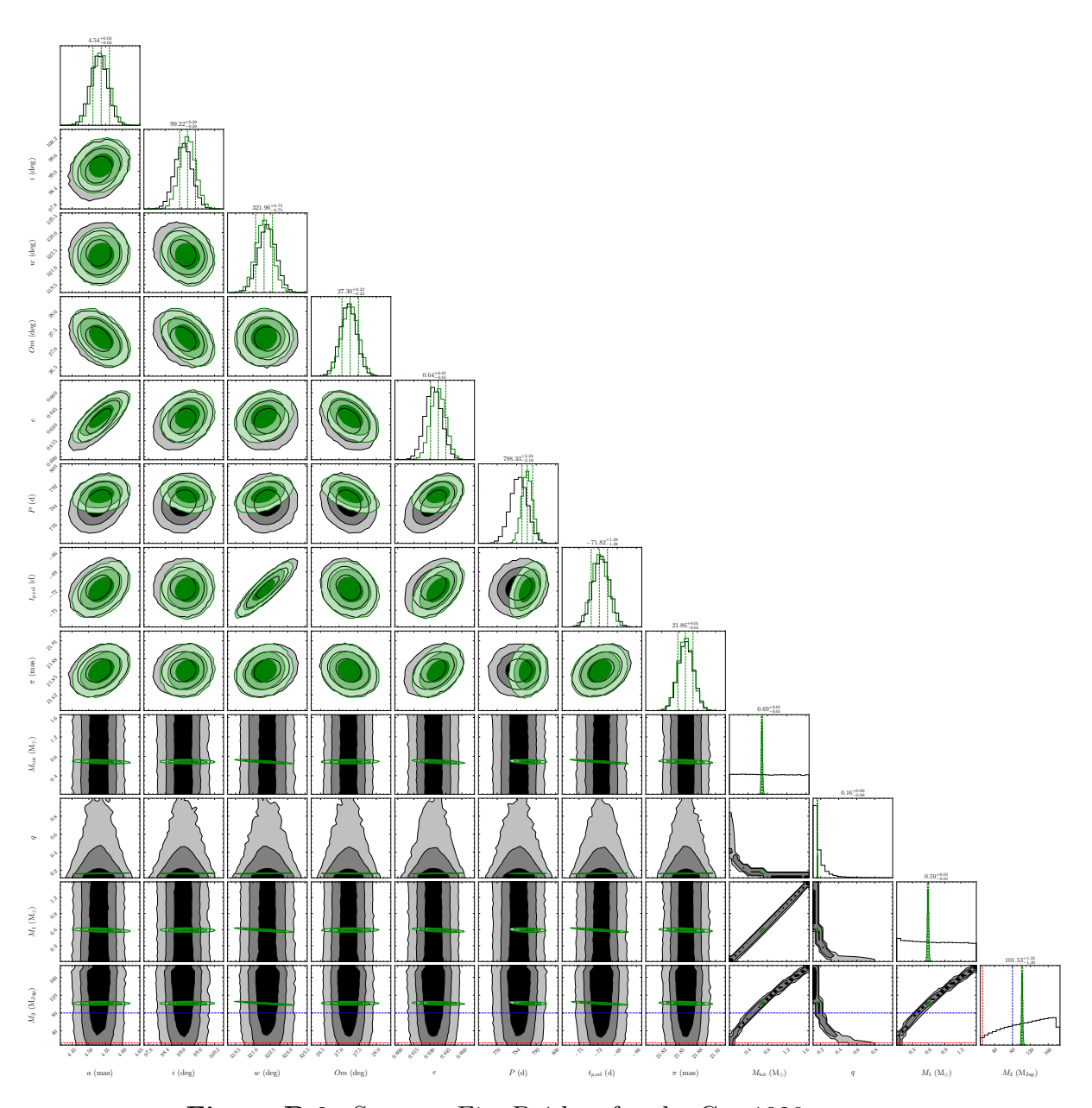


Figure B.9: Same as Fig. B.4 but for the G  $\dots$ 1920 system.

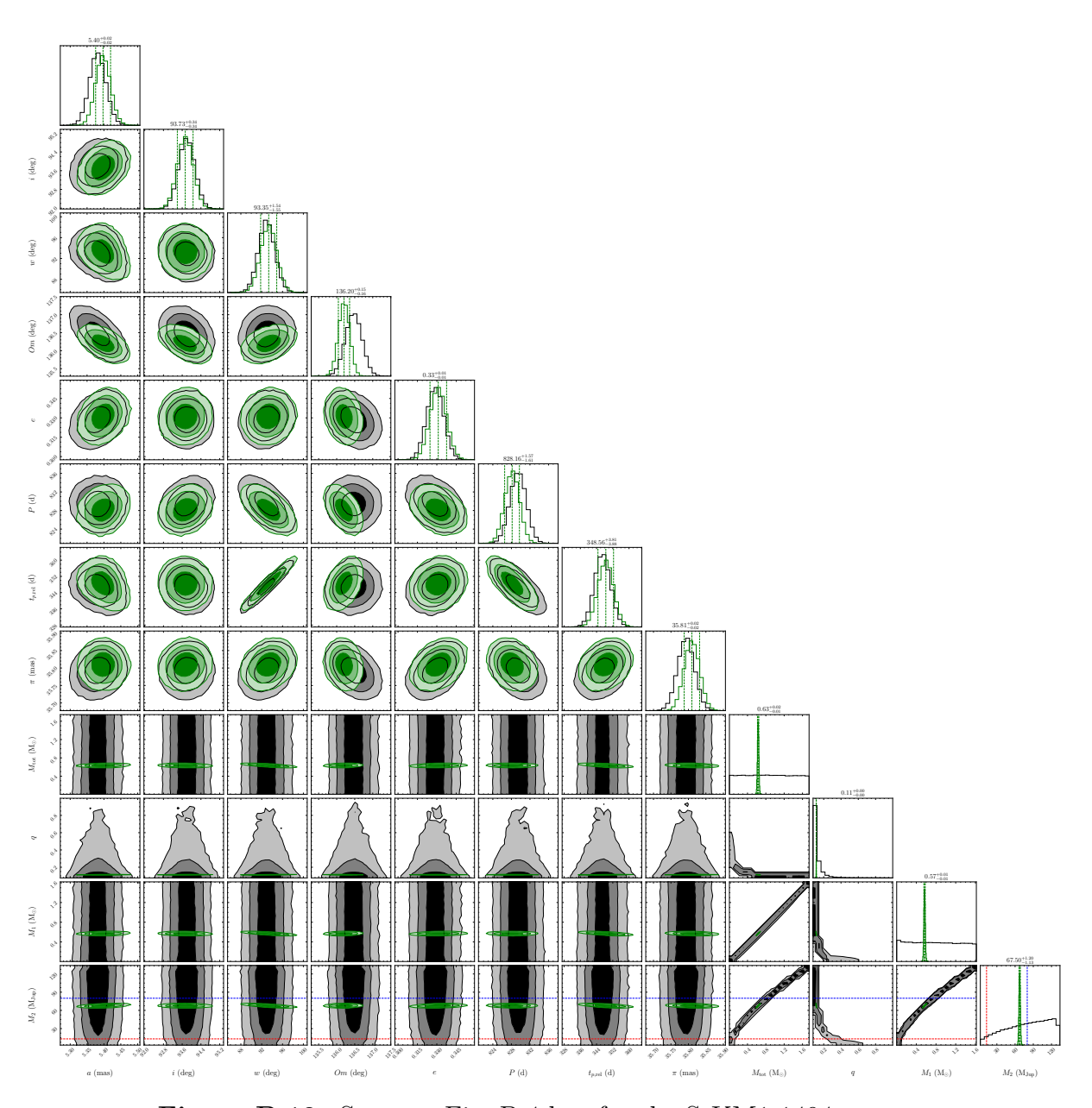


Figure B.10: Same as Fig. B.4 but for the StKM1-1494 system.

# Appendix C

# Appendix to Chapter 4

### C.1 Additional plots

Here, we present additional plots relevant to the PMOIRED fitting procedure described in Sect. 4.3.2.

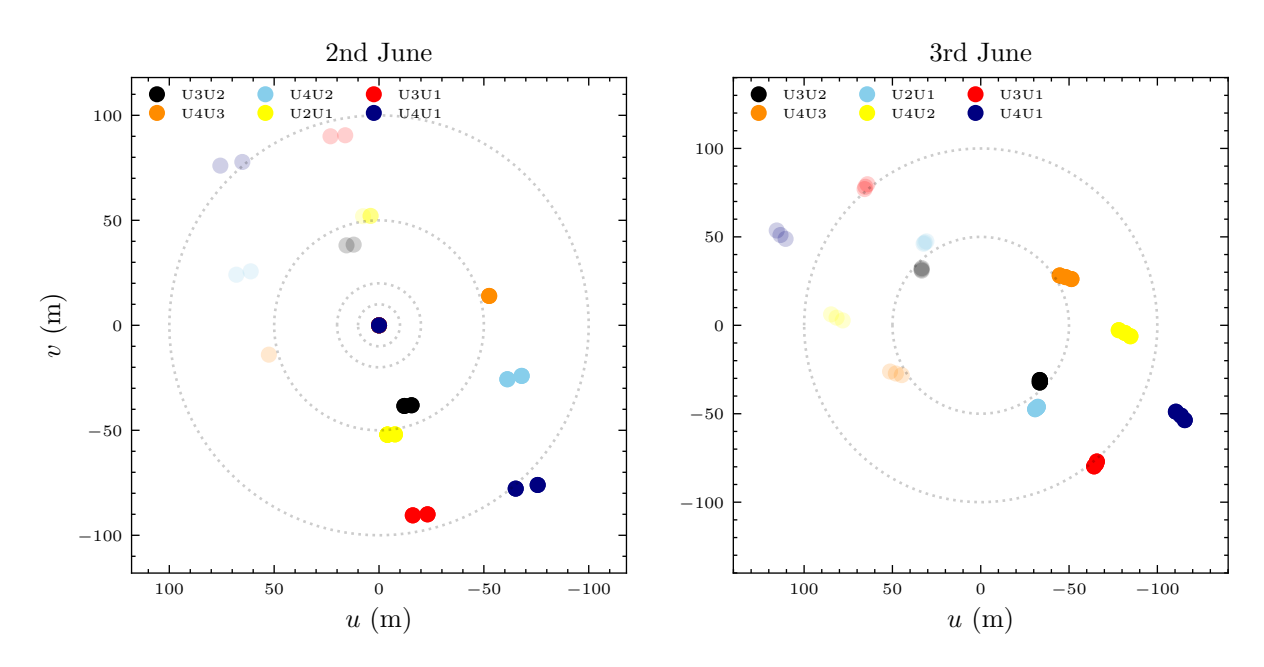


**Figure C.1:** *u-v* plane coverage obtained during the observations of LP 754-5 (b) on the 2nd and 3rd of June 2024. The different colours correspond to the different baselines.

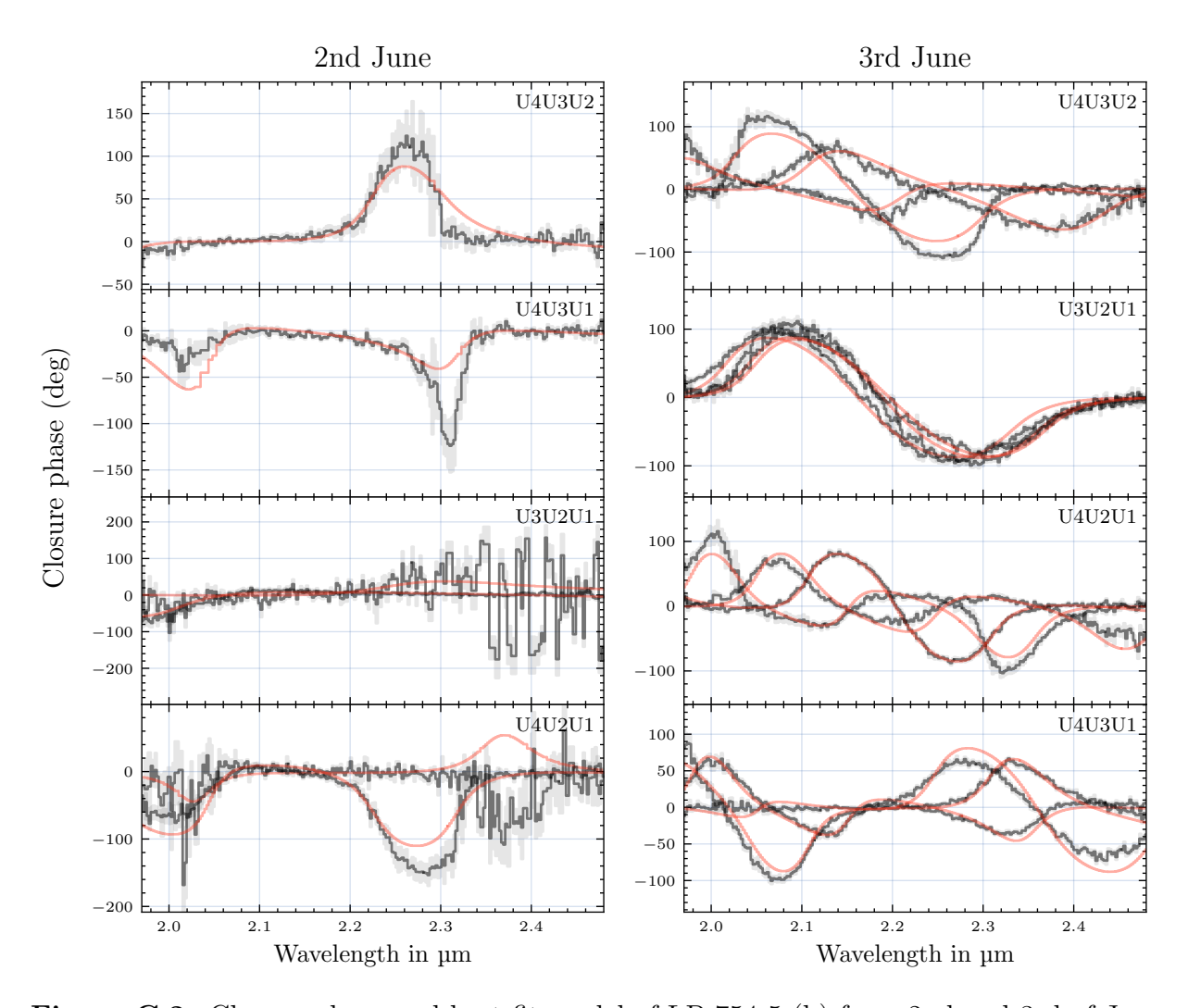


**Figure C.2:** Closure phase and best-fit model of LP 754-5 (b) from 2nd and 3rd of June 2024. The 68% confidence intervals are indicated by the grey margins, the best fit model is shown in orange.

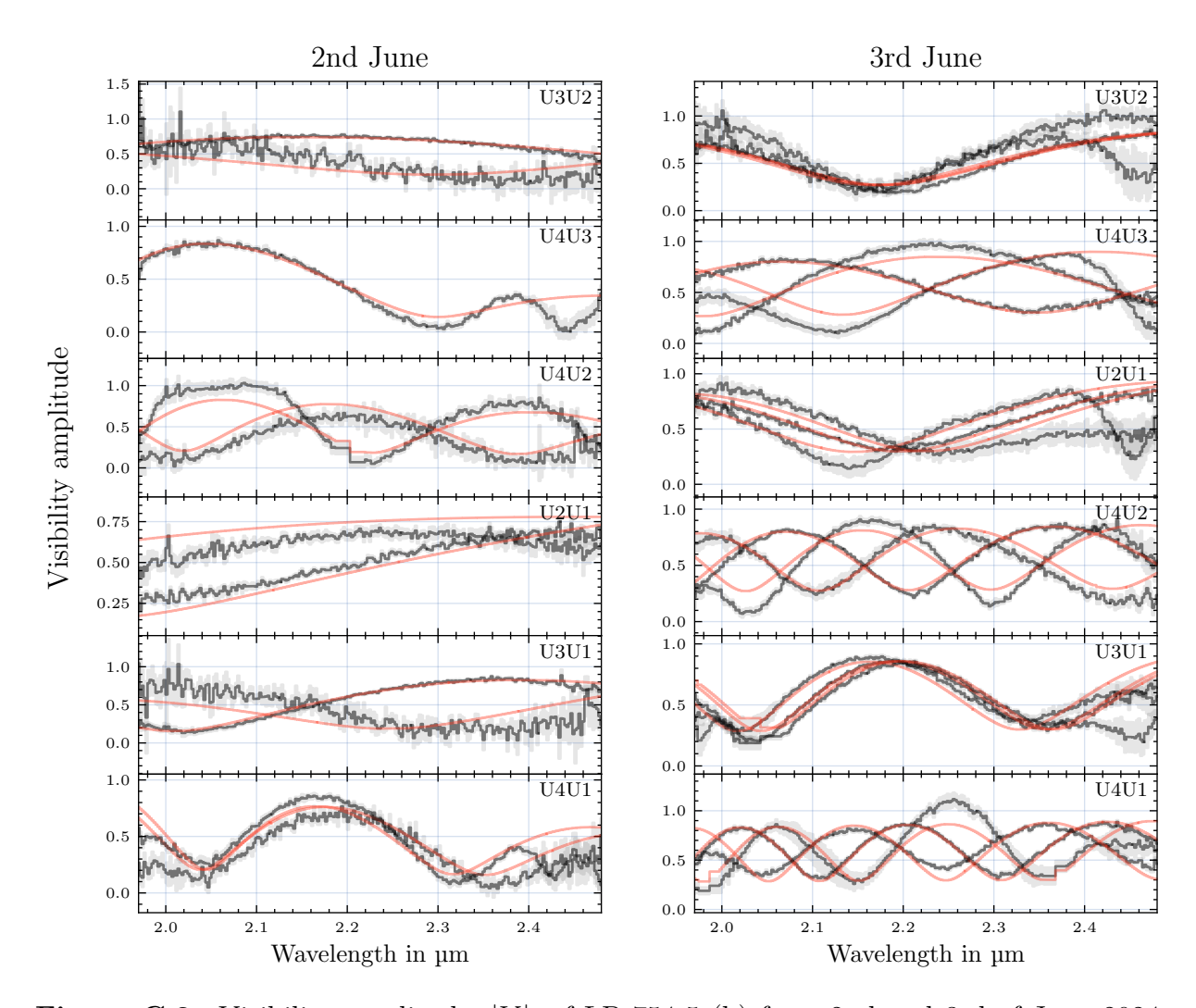


**Figure C.3:** Visibility amplitude, |V|, of LP 754-5 (b) from 2nd and 3rd of June 2024. The 68 % confidence intervals are indicated by the grey margins, the best fit model is shown in orange.

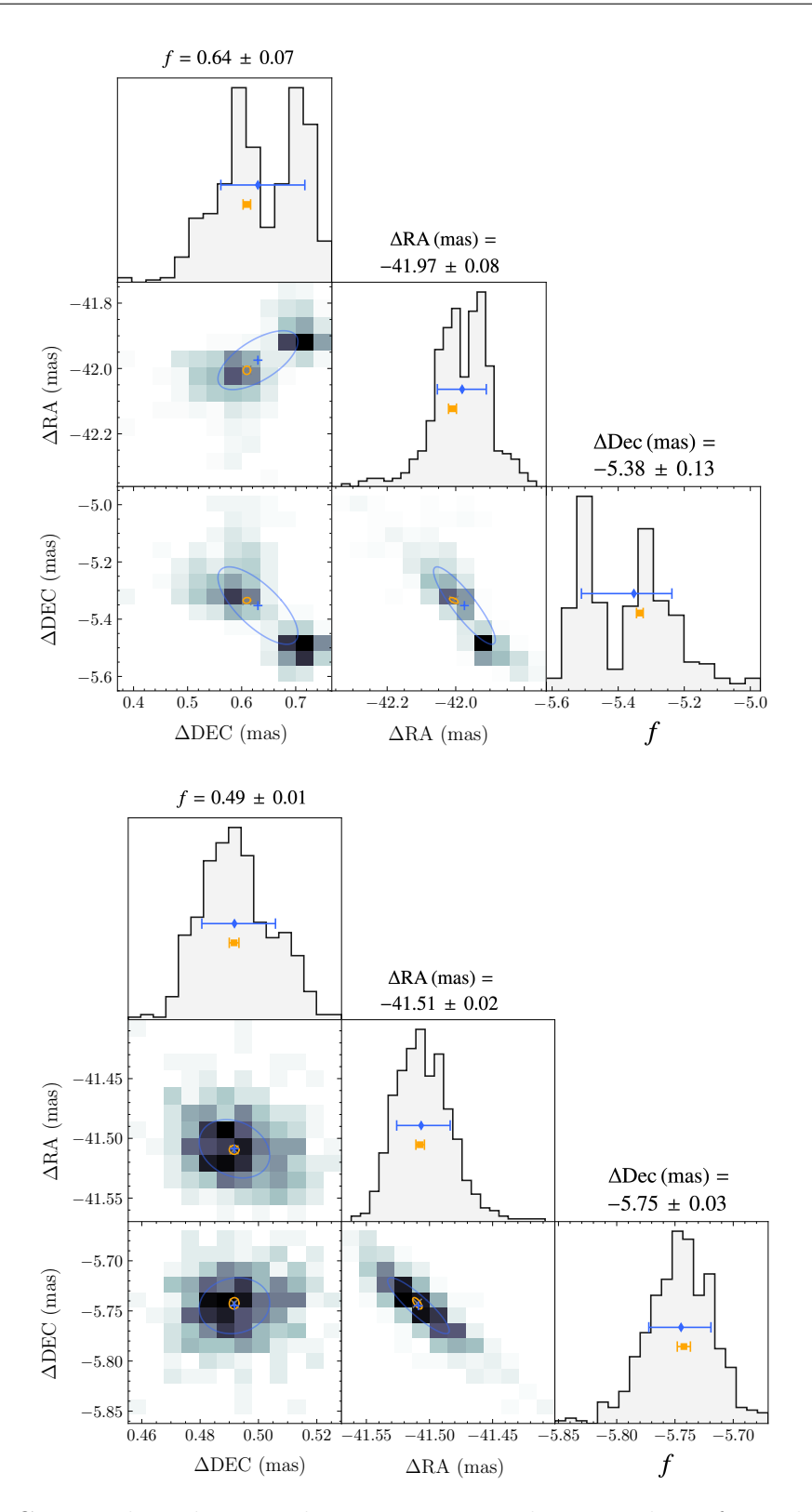


**Figure C.4:** Corner plots showing the posterior samplings resulting from the fits applied to the data obtained during the night of the 2nd in the *top* and 3rd of June in the *bottom*.

## Bibliography

Agol, E. & Fabrycky, D. C. 2018, in Handbook of Exoplanets, ed. H. J. Deeg & J. A. Belmonte, 7

Agol, E., Jansen, T., Lacy, B., Robinson, T. D., & Meadows, V. 2015, ApJ, 812, 5

Airy, G. B. 1835, Transactions of the Cambridge Philosophical Society, 5, 283

Akeson, R. L., Chen, X., Ciardi, D., et al. 2013, PASP, 125, 989

Albrecht, S. H., Dawson, R. I., & Winn, J. N. 2022, PASP, 134, 082001

Allard, F., Guillot, T., Ludwig, H.-G., et al. 2003, in Brown Dwarfs, ed. E. Martín, Vol. 211, 325

Allard, F., Hauschildt, P. H., Alexander, D. R., Tamanai, A., & Schweitzer, A. 2001, ApJ, 556, 357

Allard, F., Homeier, D., & Freytag, B. 2012, Philosophical Transactions of the Royal Society of London Series A, 370, 2765

ALMA Partnership, Brogan, C. L., Pérez, L. M., et al. 2015, ApJ, 808, L3

Alvarez, P., Rodríguez Espinosa, J. M., & Sánchez, F. 1998, New A Rev., 42, 553

Andrews, S. M. 2020, ARA&A, 58, 483

Armitage, P. J. 2011, ARA&A, 49, 195

Arsenault, R., Alonso, J., Bonnet, H., et al. 2003, in Society of Photo-Optical Instrumentation Engineers (SPIE) Conference Series, Vol. 4839, Adaptive Optical System Technologies II, ed. P. L. Wizinowich & D. Bonaccini, 174–185

Babcock, H. W. 1953, PASP, 65, 229

Babusiaux, C., Fabricius, C., Khanna, S., et al. 2023, A&A, 674, A32

Bailer-Jones, C. A. L. 2015, PASP, 127, 994

Balmer, W. O., Franson, K., Chomez, A., et al. 2025, AJ, 169, 30

158 BIBLIOGRAPHY

Balmer, W. O., Pueyo, L., Lacour, S., et al. 2024, AJ, 167, 64

Band, D. L., Ford, L. A., Matteson, J. L., et al. 1997, ApJ, 485, 747

Baraffe, I., Chabrier, G., Barman, T. S., Allard, F., & Hauschildt, P. H. 2003, A&A, 402, 701

Baraffe, I., Homeier, D., Allard, F., & Chabrier, G. 2015, A&A, 577, A42

Barbato, D., Ségransan, D., Udry, S., et al. 2023, A&A, 674, A114

Barnes, J. W. 2007a, PASP, 119, 986

Barnes, J. W. & O'Brien, D. P. 2002, ApJ, 575, 1087

Barnes, S. A. 2003, ApJ, 586, 464

Barnes, S. A. 2007b, ApJ, 669, 1167

Barr, A. C. & Bruck Syal, M. 2017, MNRAS, 466, 4868

Batygin, K. & Adams, F. C. 2025, Nature Astronomy, 9, 835

Beatty, T. G. & Seager, S. 2010, ApJ, 712, 1433

Bell, C. P. M., Mamajek, E. E., & Naylor, T. 2015, MNRAS, 454, 593

Belorizky, D. 1938, L'Astronomie, 52, 359

Benedict, G. F., Henry, T. J., Franz, O. G., et al. 2016, AJ, 152, 141

Benz, W., Broeg, C., Fortier, A., et al. 2021, Experimental Astronomy, 51, 109

Bessel, F. W. 1838, Astronomische Nachrichten, 16, 65

Bessel, F. W. 1844, MNRAS, 6, 136

Beuzit, J. L., Vigan, A., Mouillet, D., et al. 2019, A&A, 631, A155

Binnendijk, L. 1960, Properties of double stars; a survey of parallaxes and orbits.

Binney, J. & Tremaine, S. 2008, Galactic Dynamics: Second Edition

Birkby, J. L. 2018, arXiv e-prints, arXiv:1806.04617

Birnstiel, T., Fang, M., & Johansen, A. 2016, Space Sci. Rev., 205, 41

Bitsch, B., Trifonov, T., & Izidoro, A. 2020, A&A, 643, A66

Blunt, S., Wang, J. J., Angelo, I., et al. 2020, AJ, 159, 89

BIBLIOGRAPHY 159

Bodenheimer, P., D'Angelo, G., Lissauer, J. J., Fortney, J. J., & Saumon, D. 2013, ApJ, 770, 120

Bodenheimer, P. & Pollack, J. B. 1986, Icarus, 67, 391

Bonnefoy, M., Perraut, K., Lagrange, A. M., et al. 2018, A&A, 618, A63

Borucki, W. J., Koch, D., Basri, G., et al. 2010, Science, 327, 977

Boss, A. P. 1997, Science, 276, 1836

Bourdarot, G. & Eisenhauer, F. 2024, arXiv e-prints, arXiv:2410.22063

Bourdarot, G., Eisenhauer, F., Yazıcı, S., et al. 2024, arXiv e-prints, arXiv:2409.08438

Bowler, B. P. 2016, PASP, 128, 102001

Bowler, B. P., Blunt, S. C., & Nielsen, E. L. 2020, AJ, 159, 63

Brandt, G. M., Brandt, T. D., Dupuy, T. J., Li, Y., & Michalik, D. 2021a, AJ, 161, 179

Brandt, G. M., Brandt, T. D., Dupuy, T. J., Michalik, D., & Marleau, G.-D. 2021b, ApJ, 915, L16

Brandt, G. M., Dupuy, T. J., Li, Y., et al. 2021c, AJ, 162, 301

Brandt, T. D. 2021, ApJS, 254, 42

Brown, A. G. A. 2021, ARA&A, 59, 59

Buchner, J. 2021, The Journal of Open Source Software, 6, 3001

Buchner, J., Georgakakis, A., Nandra, K., et al. 2014, A&A, 564, A125

Burgasser, A. J. & Splat Development Team. 2017, in Astronomical Society of India Conference Series, Vol. 14, Astronomical Society of India Conference Series, 7–12

Burke, C. J. 2008, ApJ, 679, 1566

Burrows, A., Hubbard, W. B., Lunine, J. I., & Liebert, J. 2001, Reviews of Modern Physics, 73, 719

Butkevich, A. G. 2018, MNRAS, 476, 5658

Cai, K., Durisen, R. H., Michael, S., et al. 2006, ApJ, 636, L149

Cameron, A. G. W. 1978, Moon and Planets, 18, 5

Canup, R. M. & Ward, W. R. 2006, Nature, 441, 834

160 BIBLIOGRAPHY

Cardelli, J. A., Clayton, G. C., & Mathis, J. S. 1989, ApJ, 345, 245

Carnall, A. C. 2017, arXiv e-prints, arXiv:1705.05165

Carpenter, J. M. 2001, AJ, 121, 2851

Carson, J., Thalmann, C., Janson, M., et al. 2013, ApJ, 763, L32

Casertano, S., Lattanzi, M. G., Sozzetti, A., et al. 2008, A&A, 482, 699

Cegla, H. M. 2019, Geosciences, 9, 114

Chabrier, G., Baraffe, I., Allard, F., & Hauschildt, P. 2000, ApJ, 542, 464

Chabrier, G., Saumon, D., Hubbard, W. B., & Lunine, J. I. 1992, ApJ, 391, 817

Charbonneau, D., Brown, T. M., Latham, D. W., & Mayor, M. 2000, ApJ, 529, L45

Charbonneau, D., Brown, T. M., Noyes, R. W., & Gilliland, R. L. 2002, ApJ, 568, 377

Chauvin, G. 2024, Comptes Rendus Physique, 24, 139

Chauvin, G., Lagrange, A. M., Dumas, C., et al. 2004, A&A, 425, L29

Chauvin, G., Videla, M., Beust, H., et al. 2023, A&A, 675, A114

Chen, J. & Kipping, D. 2017, ApJ, 834, 17

Chomez, A., Delorme, P., Lagrange, A. M., et al. 2025, A&A, 697, A99

Clarke, C. J., Harper-Clark, E., & Lodato, G. 2007, MNRAS, 381, 1543

Colavita, M. M., Wallace, J. K., Hines, B. E., et al. 1999, ApJ, 510, 505

Crossfield, I. J. M. 2015, PASP, 127, 941

Cumming, A., Marcy, G. W., & Butler, R. P. 1999, ApJ, 526, 890

Currie, T., Biller, B., Lagrange, A., et al. 2023a, in Astronomical Society of the Pacific Conference Series, Vol. 534, Protostars and Planets VII, ed. S. Inutsuka, Y. Aikawa, T. Muto, K. Tomida, & M. Tamura, 799

Currie, T., Brandt, G. M., Brandt, T. D., et al. 2023b, Science, 380, 198

Cushing, M. C., Marley, M. S., Saumon, D., et al. 2008, ApJ, 678, 1372

Cutri, R. M., Skrutskie, M. F., van Dyk, S., et al. 2003, VizieR Online Data Catalog: 2MASS All-Sky Catalog of Point Sources (Cutri+ 2003), VizieR On-line Data Catalog: II/246. Originally published in: 2003yCat.2246....0C

Cutri, R. M., Wright, E. L., Conrow, T., et al. 2021, VizieR Online Data Catalog: AllWISE Data Release (Cutri+ 2013), VizieR On-line Data Catalog: II/328. Originally published in: IPAC/Caltech (2013)

- D'Angelo, G., Durisen, R. H., & Lissauer, J. J. 2010, in Exoplanets, ed. S. Seager, 319–346
- Davies, R., Hörmann, V., Rabien, S., et al. 2021, The Messenger, 182, 17
- de la Reza, R., Torres, C. A. O., Quast, G., Castilho, B. V., & Vieira, G. L. 1989, ApJ, 343, L61
- De Rosa, R. J., Nielsen, E. L., Wahhaj, Z., et al. 2023, A&A, 672, A94
- Deeg, H. J. & Alonso, R. 2018, in Handbook of Exoplanets, ed. H. J. Deeg & J. A. Belmonte, 117
- Delorme, J.-R., Jovanovic, N., Echeverri, D., et al. 2021, Journal of Astronomical Telescopes, Instruments, and Systems, 7, 035006
- Delplancke, F. 2008, New A Rev., 52, 199
- Deming, D. & Knutson, H. A. 2020, Nature Astronomy, 4, 453
- Deming, D., Seager, S., Richardson, L. J., & Harrington, J. 2005, Nature, 434, 740
- Deng, H., Mayer, L., & Helled, R. 2021, Nature Astronomy, 5, 440
- Denis, A., Vigan, A., Costes, J., et al. 2025, A&A, 696, A6
- Deshmukh, K., Shenar, T., Mérand, A., et al. 2025, A&A, 695, L20
- Desidera, S., Chauvin, G., Bonavita, M., et al. 2021, A&A, 651, A70
- Dobos, V., Charnoz, S., Pál, A., Roque-Bernard, A., & Szabó, G. M. 2021, PASP, 133, 094401
- Dobos, V., Haris, A., Kamp, I. E. E., & van der Tak, F. F. S. 2022, MNRAS, 513, 5290
- Dodson-Robinson, S. E., Veras, D., Ford, E. B., & Beichman, C. A. 2009, ApJ, 707, 79
- Domingos, R. C., Winter, O. C., & Yokoyama, T. 2006, MNRAS, 373, 1227
- Dupuy, T. J., Brandt, G. M., & Brandt, T. D. 2022, MNRAS, 509, 4411
- Dupuy, T. J., Liu, M. C., & Ireland, M. J. 2009, ApJ, 692, 729
- Durisen, R. H., Boss, A. P., Mayer, L., et al. 2007, in Protostars and Planets V, ed. B. Reipurth, D. Jewitt, & K. Keil, 607
- Eadie, W. T., Drijard, D., & James, F. E. 1971, Statistical methods in experimental physics

Eisenhauer, F., Monnier, J. D., & Pfuhl, O. 2023, ARA&A, 61, 237

El-Badry, K., Lam, C., Holl, B., et al. 2024, The Open Journal of Astrophysics, 7, 100

El-Badry, K., Rix, H.-W., & Heintz, T. M. 2021, MNRAS, 506, 2269

Faherty, J. K., Beletsky, Y., Burgasser, A. J., et al. 2014, ApJ, 790, 90

Fang, J. & Margot, J.-L. 2012, ApJ, 761, 92

Feng, F., Anglada-Escudé, G., Tuomi, M., et al. 2019, MNRAS, 490, 5002

Fernandes, R. B., Mulders, G. D., Pascucci, I., Mordasini, C., & Emsenhuber, A. 2019, ApJ, 874, 81

Feroz, F. & Hobson, M. P. 2008, MNRAS, 384, 449

Feroz, F., Hobson, M. P., & Bridges, M. 2009, MNRAS, 398, 1601

Fischer, D. A., Anglada-Escude, G., Arriagada, P., et al. 2016, PASP, 128, 066001

Fischer, D. A. & Valenti, J. 2005, ApJ, 622, 1102

Follert, R., Dorn, R. J., Oliva, E., et al. 2014, in Society of Photo-Optical Instrumentation Engineers (SPIE) Conference Series, Vol. 9147, Ground-based and Airborne Instrumentation for Astronomy V, ed. S. K. Ramsay, I. S. McLean, & H. Takami, 914719

Fontanive, C., Bedin, L. R., De Furio, M., et al. 2023, MNRAS, 526, 1783

Foreman-Mackey, D., Hogg, D. W., Lang, D., & Goodman, J. 2013, PASP, 125, 306

Forgan, D. & Rice, K. 2013, MNRAS, 432, 3168

Fortier, A., Benvenuto, O. G., & Brunini, A. 2007, A&A, 473, 311

Franson, K., Bowler, B. P., Bonavita, M., et al. 2023a, AJ, 165, 39

Franson, K., Bowler, B. P., Zhou, Y., et al. 2023b, ApJ, 950, L19

Fulton, B. J. & Petigura, E. A. 2018, AJ, 156, 264

Fulton, B. J., Petigura, E. A., Howard, A. W., et al. 2017, AJ, 154, 109

Fulton, B. J., Rosenthal, L. J., Hirsch, L. A., et al. 2021, ApJS, 255, 14

Gagné, J., Mamajek, E. E., Malo, L., et al. 2018, ApJ, 856, 23

Gaia Collaboration, Arenou, F., Babusiaux, C., et al. 2023a, A&A, 674, A34

Gaia Collaboration, Panuzzo, P., Mazeh, T., et al. 2024, A&A, 686, L2

Gaia Collaboration, Prusti, T., de Bruijne, J. H. J., et al. 2016, A&A, 595, A1

Gaia Collaboration, Vallenari, A., Brown, A. G. A., et al. 2023b, A&A, 674, A1

Gammie, C. F. 2001, ApJ, 553, 174

Gaudi, B. S. 2012, ARA&A, 50, 411

Gaudi, B. S., Meyer, M., & Christiansen, J. 2021, in ExoFrontiers; Big Questions in Exoplanetary Science, ed. N. Madhusudhan, 2–1

Gaudi, B. S., Seager, S., Mennesson, B., et al. 2020, arXiv e-prints, arXiv:2001.06683

Glindemann, A. 2011, Principles of Stellar Interferometry

Gondoin, P. 2023, A&A, 678, A39

Granada, M. A. 2008, Journal for the History of Astronomy, 39, 469

Gratton, R., Bonavita, M., Mesa, D., et al. 2024, A&A, 685, A119

GRAVITY Collaboration, Abuter, R., Accardo, M., et al. 2017, A&A, 602, A94

Gravity+ Collaboration, Abuter, R., Alarcon, P., et al. 2022, The Messenger, 189, 17

GRAVITY Collaboration, Abuter, R., Amorim, A., et al. 2018, A&A, 615, L15

GRAVITY Collaboration, Abuter, R., Amorim, A., et al. 2021, A&A, 647, A59

GRAVITY Collaboration, Lacour, S., Nowak, M., et al. 2019, A&A, 623, L11

GRAVITY Collaboration, Nowak, M., Lacour, S., et al. 2020, A&A, 633, A110

Groff, T., Chilcote, J., Brandt, T., et al. 2017, in Society of Photo-Optical Instrumentation Engineers (SPIE) Conference Series, Vol. 10400, Society of Photo-Optical Instrumentation Engineers (SPIE) Conference Series, ed. S. Shaklan, 1040016

Guillot, T. 1999, Planet. Space Sci., 47, 1183

Guillot, T., Chabrier, G., Morel, P., & Gautier, D. 1994, Icarus, 112, 354

Guyon, O. 2005, ApJ, 629, 592

Guyon, O., Pluzhnik, E. A., Kuchner, M. J., Collins, B., & Ridgway, S. T. 2006, ApJS, 167, 81

Haffert, S. Y., Bohn, A. J., de Boer, J., et al. 2019, Nature Astronomy, 3, 749

Haisch, Jr., K. E., Lada, E. A., & Lada, C. J. 2001, ApJ, 553, L153

Halbwachs, J.-L., Pourbaix, D., Arenou, F., et al. 2023, A&A, 674, A9

Hall, C., Dong, R., Teague, R., et al. 2020, ApJ, 904, 148

Hansen, B. M. S. 2019, Science Advances, 5, eaaw8665

Hatzes, A. P. 2016, in Astrophysics and Space Science Library, Vol. 428, Methods of Detecting Exoplanets: 1st Advanced School on Exoplanetary Science, ed. V. Bozza, L. Mancini, & A. Sozzetti, 3

Hawarden, T. G., Leggett, S. K., Letawsky, M. B., Ballantyne, D. R., & Casali, M. M. 2001, MNRAS, 325, 563

Hayashi, C. 1981, Progress of Theoretical Physics Supplement, 70, 35

Hecht, E. & Zajac, A. 1974, Optics (Boston: Addison-Wesley Publishing Company Inc.)

Helled, R., Bodenheimer, P., Podolak, M., et al. 2014, in Protostars and Planets VI, ed. H. Beuther, R. S. Klessen, C. P. Dullemond, & T. Henning, 643–665

Heller, R. & Hippke, M. 2024, Nature Astronomy, 8, 193

Heller, R., Rodenbeck, K., & Bruno, G. 2019, A&A, 624, A95

Helling, C., Dehn, M., Woitke, P., & Hauschildt, P. H. 2008, ApJ, 675, L105

Helling, C. & Woitke, P. 2006, A&A, 455, 325

Henry, G. W., Marcy, G. W., Butler, R. P., & Vogt, S. S. 2000, ApJ, 529, L41

Hinkley, S., Lacour, S., Marleau, G. D., et al. 2023, A&A, 671, L5

Hodgkin, S. T., Harrison, D. L., Breedt, E., et al. 2021, A&A, 652, A76

Hogg, D. W., Myers, A. D., & Bovy, J. 2010, ApJ, 725, 2166

Holl, B., Perryman, M., Lindegren, L., Segransan, D., & Raimbault, M. 2022, A&A, 661, A151

Holman, M. J. & Wiegert, P. A. 1999, AJ, 117, 621

Holt, J. R. 1893, Astronomy and Astro-Physics (formerly The Sidereal Messenger), 12, 646

Horstman, K., Ruffio, J.-B., Batygin, K., et al. 2024, AJ, 168, 175

Howard, A. W., Marcy, G. W., Bryson, S. T., et al. 2012, ApJS, 201, 15

Howe, A. R., Mandell, A. M., & McElwain, M. W. 2023, ApJ, 951, L25

Hoyer, P., Hog, E., Poder, I., & Lindegren, L. 1981, A&A, 101, 228

Hubickyj, O., Bodenheimer, P., & Lissauer, J. J. 2005, Icarus, 179, 415

Huygens, C. 1698, Kosmotheoros: sive, de terris coelestibus, earumque ornatu conjecturae. (Eng. transl.: The Celestial Worlds discover'd) (Den Haag: Adriaan Moetjens)

Ida, S. & Lin, D. N. C. 2004a, ApJ, 604, 388

Ida, S. & Lin, D. N. C. 2004b, ApJ, 616, 567

Ida, S. & Lin, D. N. C. 2005, ApJ, 626, 1045

Ida, S., Tanaka, H., Johansen, A., Kanagawa, K. D., & Tanigawa, T. 2018, ApJ, 864, 77

Jacobson, R. A. 2022, AJ, 164, 199

Jennison, R. C. 1958, MNRAS, 118, 276

Jovanovic, N., Martinache, F., Guyon, O., et al. 2015, PASP, 127, 890

Kaeufl, H.-U., Ballester, P., Biereichel, P., et al. 2004, in Society of Photo-Optical Instrumentation Engineers (SPIE) Conference Series, Vol. 5492, Ground-based Instrumentation for Astronomy, ed. A. F. M. Moorwood & M. Iye, 1218–1227

Kammerer, J., Lacour, S., Stolker, T., et al. 2021, A&A, 652, A57

Kasper, M., Cerpa Urra, N., Pathak, P., et al. 2021, The Messenger, 182, 38

Kastner, J. H., Zuckerman, B., Weintraub, D. A., & Forveille, T. 1997, Science, 277, 67

Kenworthy, M., Lock, S., Kennedy, G., et al. 2023, Nature, 622, 251

Kenworthy, M. A. & Haffert, S. Y. 2025, arXiv e-prints, arXiv:2506.02907

Keppler, M., Benisty, M., Müller, A., et al. 2018, A&A, 617, A44

Kervella, P., Arenou, F., Mignard, F., & Thévenin, F. 2019a, A&A, 623, A72

Kervella, P., Arenou, F., & Thévenin, F. 2022, A&A, 657, A7

Kervella, P., Coudé du Foresto, V., Glindemann, A., & Hofmann, R. 2000, in Society of Photo-Optical Instrumentation Engineers (SPIE) Conference Series, Vol. 4006, Interferometry in Optical Astronomy, ed. P. Léna & A. Quirrenbach, 31–42

Kervella, P., Gallenne, A., Remage Evans, N., et al. 2019b, A&A, 623, A116

Kervella, P., Mignard, F., Mérand, A., & Thévenin, F. 2016, A&A, 594, A107

Kiefer, F., Hébrard, G., Sahlmann, J., et al. 2019, A&A, 631, A125

Kiefer, F., Lagrange, A.-M., Rubini, P., & Philipot, F. 2024, arXiv e-prints, arXiv:2409.16992

Kipping, D., Bryson, S., Burke, C., et al. 2022, Nature Astronomy, 6, 367

Kipping, D. M. 2009, MNRAS, 392, 181

Kipping, D. M. 2010, MNRAS, 409, L119

Kipping, D. M. 2013, MNRAS, 434, L51

Kirkpatrick, J. D. 2005, ARA&A, 43, 195

Kirkpatrick, J. D., Marocco, F., Gelino, C. R., et al. 2024, ApJS, 271, 55

Kirkpatrick, J. D., Reid, I. N., Liebert, J., et al. 1999, ApJ, 519, 802

Klahr, H. & Bodenheimer, P. 2006, ApJ, 639, 432

Kley, W. & Nelson, R. P. 2012, ARA&A, 50, 211

Koch, D. G., Borucki, W. J., Basri, G., et al. 2010, ApJ, 713, L79

Kokubo, E. & Ida, S. 1998, Icarus, 131, 171

Kopparapu, R. K., Hébrard, E., Belikov, R., et al. 2018, ApJ, 856, 122

Kramer, M. 2018, in Handbook of Exoplanets, ed. H. J. Deeg & J. A. Belmonte, 5

Kratter, K. & Lodato, G. 2016, ARA&A, 54, 271

Kratter, K. M., Murray-Clay, R. A., & Youdin, A. N. 2010, ApJ, 710, 1375

Kreidberg, L. 2018, in Handbook of Exoplanets, ed. H. J. Deeg & J. A. Belmonte, 100

Kreidberg, L., Luger, R., & Bedell, M. 2019, ApJ, 877, L15

Kuiper, G. P. 1951, in 50th Anniversary of the Yerkes Observatory and Half a Century of Progress in Astrophysics, ed. J. A. Hynek, 357

Kuzuhara, M., Currie, T., Takarada, T., et al. 2022, ApJ, 934, L18

Labeyrie, A. 1975, ApJ, 196, L71

Lacour, S., Dembet, R., Abuter, R., et al. 2019, A&A, 624, A99

Lacour, S., Eisenhauer, F., Gillessen, S., et al. 2014, A&A, 567, A75

Lacour, S., Wang, J. J., Nowak, M., et al. 2020, in Society of Photo-Optical Instrumentation Engineers (SPIE) Conference Series, Vol. 11446, Optical and Infrared Interferometry and Imaging VII, ed. P. G. Tuthill, A. Mérand, & S. Sallum, 114460O

Lacour, S., Wang, J. J., Rodet, L., et al. 2021, A&A, 654, L2

Lagrange, A. M., Philipot, F., Rubini, P., et al. 2023, A&A, 677, A71

Lagrange, A. M., Wilkinson, C., Mâlin, M., et al. 2025, Nature, 642, 905

Lambrechts, M. & Johansen, A. 2012, A&A, 544, A32

Landman, R., Stolker, T., Snellen, I. A. G., et al. 2024, A&A, 682, A48

Lane, B. F. & Muterspaugh, M. W. 2004, ApJ, 601, 1129

Langlois, M., Gratton, R., Lagrange, A. M., et al. 2021, A&A, 651, A71

Laughlin, G., Bodenheimer, P., & Adams, F. C. 2004, ApJ, 612, L73

Launhardt, R., Queloz, D., Henning, T., et al. 2008, in Society of Photo-Optical Instrumentation Engineers (SPIE) Conference Series, Vol. 7013, Optical and Infrared Interferometry, ed. M. Schöller, W. C. Danchi, & F. Delplancke, 70132I

Lawson, P. R., ed. 2000, Principles of Long Baseline Stellar Interferometry

Le Bouquin, J. B., Berger, J. P., Lazareff, B., et al. 2011, A&A, 535, A67

Leclerc, A., Babusiaux, C., Arenou, F., et al. 2023, A&A, 672, A82

Leinert, C., Graser, U., Przygodda, F., et al. 2003, Ap&SS, 286, 73

Lenzen, R., Hartung, M., Brandner, W., et al. 2003, in Society of Photo-Optical Instrumentation Engineers (SPIE) Conference Series, Vol. 4841, Instrument Design and Performance for Optical/Infrared Ground-based Telescopes, ed. M. Iye & A. F. M. Moorwood, 944–952

Lightkurve Collaboration, Cardoso, J. V. d. M., Hedges, C., et al. 2018, Lightkurve: Kepler and TESS time series analysis in Python, Astrophysics Source Code Library

Lindegren, L. 1980, A&A, 89, 41

Lindegren, L., Hernández, J., Bombrun, A., et al. 2018, A&A, 616, A2

Lindegren, L., Klioner, S. A., Hernández, J., et al. 2021, A&A, 649, A2

Lindegren, L., Lammers, U., Hobbs, D., et al. 2012, A&A, 538, A78

Lippa, M., Gillessen, S., Blind, N., et al. 2016, in Society of Photo-Optical Instrumentation
 Engineers (SPIE) Conference Series, Vol. 9907, Optical and Infrared Interferometry and
 Imaging V, ed. F. Malbet, M. J. Creech-Eakman, & P. G. Tuthill, 990722

Lissauer, J. J., Ragozzine, D., Fabrycky, D. C., et al. 2011, ApJS, 197, 8

Lomb, N. R. 1976, Ap&SS, 39, 447

Long, A. A. 1974, The Classical Review, 24, 46–48

Lopez, B., Lagarde, S., Petrov, R. G., et al. 2022, A&A, 659, A192

Lovis, C. & Fischer, D. 2010, in Exoplanets, ed. S. Seager, 27–53

Luhman, K. L., Tremblin, P., Birkmann, S. M., et al. 2023, ApJ, 949, L36

Ma, B. & Ge, J. 2014, MNRAS, 439, 2781

Macintosh, B., Graham, J., Palmer, D., et al. 2006, in Society of Photo-Optical Instrumentation Engineers (SPIE) Conference Series, Vol. 6272, Advances in Adaptive Optics II, ed. B. L. Ellerbroek & D. Bonaccini Calia, 62720L

Macintosh, B., Graham, J. R., Barman, T., et al. 2015, Science, 350, 64

Macintosh, B., Graham, J. R., Ingraham, P., et al. 2014, Proceedings of the National Academy of Science, 111, 12661

Madore, B. F. & Freedman, W. L. 2005, ApJ, 630, 1054

Maire, A. L., Baudino, J. L., Desidera, S., et al. 2020, A&A, 633, L2

Maire, A.-L., Langlois, M., Delorme, P., et al. 2021, Journal of Astronomical Telescopes, Instruments, and Systems, 7, 035004

Makarov, V. V. & Urban, S. 2000, MNRAS, 317, 289

Mamajek, E. E. 2009, in American Institute of Physics Conference Series, Vol. 1158, Exoplanets and Disks: Their Formation and Diversity, ed. T. Usuda, M. Tamura, & M. Ishii (AIP), 3–10

Marcussen, M. L. & Albrecht, S. H. 2023, AJ, 165, 266

Marleau, G.-D., Coleman, G. A. L., Leleu, A., & Mordasini, C. 2019, A&A, 624, A20

Marleau, G. D. & Cumming, A. 2014, MNRAS, 437, 1378

Marley, M. S., Fortney, J. J., Hubickyj, O., Bodenheimer, P., & Lissauer, J. J. 2007, ApJ, 655, 541

Marley, M. S., Saumon, D., Visscher, C., et al. 2021, ApJ, 920, 85

Marois, C., Lafrenière, D., Doyon, R., Macintosh, B., & Nadeau, D. 2006, ApJ, 641, 556

Marois, C., Macintosh, B., Barman, T., et al. 2008, Science, 322, 1348

Martínez-Rodríguez, H., Caballero, J. A., Cifuentes, C., Piro, A. L., & Barnes, R. 2019, ApJ, 887, 261

Mason, B. D., Wycoff, G. L., Hartkopf, W. I., Douglass, G. G., & Worley, C. E. 2001, AJ, 122, 3466

Matthews, E. C., Carter, A. L., Pathak, P., et al. 2024, Nature, 633, 789

Mayor, M. & Queloz, D. 1995, Nature, 378, 355

McKee, C. F. & Ostriker, E. C. 2007, ARA&A, 45, 565

McLaughlin, D. B. 1924, ApJ, 60, 22

Meech, K. & Raymond, S. N. 2020, in Planetary Astrobiology, ed. V. S. Meadows, G. N. Arney, B. E. Schmidt, & D. J. Des Marais, 325

Mejía, A. C., Durisen, R. H., Pickett, M. K., & Cai, K. 2005, ApJ, 619, 1098

Mérand, A. 2022, in Society of Photo-Optical Instrumentation Engineers (SPIE) Conference Series, Vol. 12183, Optical and Infrared Interferometry and Imaging VIII, ed. A. Mérand, S. Sallum, & J. Sanchez-Bermudez, 121831N

Mesa, D., Gratton, R., Kervella, P., et al. 2023, A&A, 672, A93

Miles, B. E., Biller, B. A., Patapis, P., et al. 2023, ApJ, 946, L6

Milli, J., Mawet, D., Mouillet, D., Kasper, M., & Girard, J. H. 2016, in Astrophysics and Space Science Library, Vol. 439, Astronomy at High Angular Resolution, ed. H. M. J. Boffin, G. Hussain, J.-P. Berger, & L. Schmidtobreick, 17

Mizuno, H. 1980, Progress of Theoretical Physics, 64, 544

Mizuno, H., Nakazawa, K., & Hayashi, C. 1978, Progress of Theoretical Physics, 60, 699

Mollière, P., Molyarova, T., Bitsch, B., et al. 2022, ApJ, 934, 74

Mollière, P. & Mordasini, C. 2012, A&A, 547, A105

Monnier, J. D. 2003, Reports on Progress in Physics, 66, 789

Moraes, R. A. & Vieira Neto, E. 2020, MNRAS, 495, 3763

Mordasini, C. 2013, A&A, 558, A113

Mordasini, C., Alibert, Y., & Benz, W. 2009a, A&A, 501, 1139

Mordasini, C., Alibert, Y., Benz, W., & Naef, D. 2008, in Astronomical Society of the Pacific Conference Series, Vol. 398, Extreme Solar Systems, ed. D. Fischer, F. A. Rasio, S. E. Thorsett, & A. Wolszczan, 235

Mordasini, C., Alibert, Y., Benz, W., & Naef, D. 2009b, A&A, 501, 1161

Mordasini, C., Alibert, Y., Klahr, H., & Henning, T. 2012, A&A, 547, A111

Morley, C. V., Mukherjee, S., Marley, M. S., et al. 2024, ApJ, 975, 59

Mousis, O., Marboeuf, U., Lunine, J. I., et al. 2009, ApJ, 696, 1348

Murphy, S. J., Gray, R. O., Corbally, C. J., et al. 2020, MNRAS, 499, 2701

Murphy, S. J. & Paunzen, E. 2017, MNRAS, 466, 546

Murray, C. D. & Dermott, S. F. 1999, Solar System Dynamics

Muterspaugh, M. W., Lane, B. F., Konacki, M., et al. 2006, A&A, 446, 723

Nagpal, V., Blunt, S., Bowler, B. P., et al. 2023, AJ, 165, 32

Nasedkin, E., Mollière, P., Lacour, S., et al. 2024, A&A, 687, A298

Nelson, A. F. 2000, ApJ, 537, L65

Nielsen, E. L., De Rosa, R. J., Macintosh, B., et al. 2019, AJ, 158, 13

Nowak, M., Lacour, S., Abuter, R., et al. 2024a, A&A, 687, A248

Nowak, M., Lacour, S., Abuter, R., et al. 2024b, A&A, 684, A184

Nowak, M., Lacour, S., Lagrange, A. M., et al. 2020, A&A, 642, L2

Owen, J. E. & Wu, Y. 2013, ApJ, 775, 105

Owen, J. E. & Wu, Y. 2017, ApJ, 847, 29

Padovani, P. & Cirasuolo, M. 2023, Contemporary Physics, 64, 47

Palla, F. & Stahler, S. W. 1993, ApJ, 418, 414

Papaloizou, J. C. & Savonije, G. J. 1991, MNRAS, 248, 353

Paresce, F., Van Boekel, R., Correia, S., et al. 2003, in Society of Photo-Optical Instrumentation Engineers (SPIE) Conference Series, Vol. 4838, Interferometry for Optical Astronomy II, ed. W. A. Traub, 235–242

Parker, L. T., Birkby, J. L., Landman, R., et al. 2024, MNRAS, 531, 2356

Paunzen, E., Andrievsky, S. M., Chernyshova, I. V., et al. 1999, A&A, 351, 981

Paunzen, E., Handler, G., Weiss, W. W., et al. 2002, A&A, 392, 515

Peale, S. J. & Canup, R. M. 2015, in Treatise on Geophysics, ed. G. Schubert, 559–604

Pecaut, M. J. & Mamajek, E. E. 2013, ApJS, 208, 9

Pepe, F., Cristiani, S., Rebolo, R., et al. 2021, A&A, 645, A96

Perri, F. & Cameron, A. G. W. 1974, Icarus, 22, 416

Perryman, M., Hartman, J., Bakos, G. A., & Lindegren, L. 2014, ApJ, 797, 14

Perryman, M. A. C., de Boer, K. S., Gilmore, G., et al. 2001, A&A, 369, 339

Petrov, R. G., Malbet, F., Weigelt, G., et al. 2007, A&A, 464, 1

Phillips, M. W., Tremblin, P., Baraffe, I., et al. 2020, A&A, 637, A38

Pollack, J. B., Hubickyj, O., Bodenheimer, P., et al. 1996, Icarus, 124, 62

Poon, M., Rein, H., & Pham, D. 2024, The Open Journal of Astrophysics, 7, 109

Pourbaix, D., Tokovinin, A. A., Batten, A. H., et al. 2004, A&A, 424, 727

Pourré, N., Winterhalder, T. O., Le Bouquin, J. B., et al. 2024, A&A, 686, A258

Quanz, S. P., Ottiger, M., Fontanet, E., et al. 2022, A&A, 664, A21

Queloz, D., Henry, G. W., Sivan, J. P., et al. 2001, A&A, 379, 279

Quirrenbach, A. 2001, ARA&A, 39, 353

Quirrenbach, A. 2010, in Exoplanets, ed. S. Seager, 157–174

Quirrenbach, A., Coudé du Foresto, V., Daigne, G., et al. 1998, in Society of Photo-Optical Instrumentation Engineers (SPIE) Conference Series, Vol. 3350, Astronomical Interferometry, ed. R. D. Reasenberg, 807–817

Ranalli, P., Hobbs, D., & Lindegren, L. 2018, A&A, 614, A30

Rayleigh, L. 1880, MNRAS, 40, 254

Reggiani, M., Meyer, M. R., Chauvin, G., et al. 2016, A&A, 586, A147

Rein, H., Fujii, Y., & Spiegel, D. S. 2014, Proceedings of the National Academy of Science, 111, 6871

Rice, W. K. M., Armitage, P. J., Bate, M. R., & Bonnell, I. A. 2003, MNRAS, 339, 1025

Ricker, G. R., Winn, J. N., Vanderspek, R., et al. 2015, Journal of Astronomical Telescopes, Instruments, and Systems, 1, 014003

Rickman, E. L., Ceva, W., Matthews, E. C., et al. 2024, A&A, 684, A88

Roddier, F. 1981, Progess in Optics, 19, 281

Roddier, F. 1999, Adaptive optics in astronomy

Rossiter, R. A. 1924, ApJ, 60, 15

Rousset, G., Lacombe, F., Puget, P., et al. 2003, in Society of Photo-Optical Instrumentation Engineers (SPIE) Conference Series, Vol. 4839, Adaptive Optical System Technologies II, ed. P. L. Wizinowich & D. Bonaccini, 140–149

Ruffio, J.-B., Horstman, K., Mawet, D., et al. 2023, AJ, 165, 113

Saar, S. H. & Donahue, R. A. 1997, ApJ, 485, 319

Sahlmann, J. & Gómez, P. 2025, MNRAS, 537, 1130

Sahlmann, J., Henning, T., Queloz, D., et al. 2013a, A&A, 551, A52

Sahlmann, J., Lazorenko, P. F., Mérand, A., et al. 2013b, in Society of Photo-Optical Instrumentation Engineers (SPIE) Conference Series, Vol. 8864, Techniques and Instrumentation for Detection of Exoplanets VI, ed. S. Shaklan, 88641B

Sahlmann, J., Lazorenko, P. F., Ségransan, D., et al. 2013c, A&A, 556, A133

Sahlmann, J., Ségransan, D., Queloz, D., et al. 2011, A&A, 525, A95

Saumon, D. & Guillot, T. 2004, ApJ, 609, 1170

Saumon, D. & Marley, M. S. 2008, ApJ, 689, 1327

Scargle, J. D. 1982, ApJ, 263, 835

Schuyer, M. 1985, ESA Bulletin, ISSN 0376-4265

Shao, M. & Colavita, M. M. 1992, A&A, 262, 353

Snellen, I. A. G., de Kok, R. J., de Mooij, E. J. W., & Albrecht, S. 2010, Nature, 465, 1049

Soderblom, D. R. 2010, ARA&A, 48, 581

Soderblom, D. R., Oey, M. S., Johnson, D. R. H., & Stone, R. P. S. 1990, AJ, 99, 595

Sozzetti, A. 2005, PASP, 117, 1021

Sozzetti, A. & de Bruijne, J. 2018, in Handbook of Exoplanets, ed. H. J. Deeg & J. A. Belmonte, 81

Speedie, J., Dong, R., Hall, C., et al. 2024, Nature, 633, 58

Spiegel, D. S. & Burrows, A. 2012, ApJ, 745, 174

Spiegel, D. S., Burrows, A., & Milsom, J. A. 2011, ApJ, 727, 57

Stefánsson, G., Mahadevan, S., Winn, J. N., et al. 2025, AJ, 169, 107

Stevenson, A. T., Haswell, C. A., Barnes, J. R., & Barstow, J. K. 2023, MNRAS, 526, 5155

Stevenson, A. T., Haswell, C. A., Faria, J. P., et al. 2025, MNRAS, 539, 727

Stevenson, D. J. 1982, Planet. Space Sci., 30, 755

Stolker, T., Quanz, S. P., Todorov, K. O., et al. 2020, A&A, 635, A182

Teachey, A., Kipping, D., Burke, C. J., Angus, R., & Howard, A. W. 2020, AJ, 159, 142

Teachey, A. & Kipping, D. M. 2018, Science Advances, 4, eaav1784

The LUVOIR Team. 2019, arXiv e-prints, arXiv:1912.06219

Thiebaut, E. & Giovannelli, J. F. 2010, IEEE Signal Processing Magazine, 27, 97

Thorngren, D. P., Fortney, J. J., Murray-Clay, R. A., & Lopez, E. D. 2016, ApJ, 831, 64

Tokunaga, A. T., Simons, D. A., & Vacca, W. D. 2002, PASP, 114, 180

Toomre, A. 1964, ApJ, 139, 1217

Toomre, A. 1981, in Structure and Evolution of Normal Galaxies, ed. S. M. Fall & D. Lynden-Bell, 111–136

Torres, C. A. O., da Silva, L., Quast, G. R., de la Reza, R., & Jilinski, E. 2000, AJ, 120, 1410

Torres, C. A. O., Quast, G. R., Melo, C. H. F., & Sterzik, M. F. 2008, in Handbook of Star Forming Regions, Volume II, ed. B. Reipurth, Vol. 5, 757

Traub, W. A. & Oppenheimer, B. R. 2010, in Exoplanets, ed. S. Seager, 111–156

Tyson, R. K. 1998, Principles of adaptive optics

van Cittert, P. H. 1934, Physica, 1, 201

van den Berg, H. A. 2019, Science Progress, 102, 249, epub 2019 Aug 26

Vanderburg, A. & Rodriguez, J. E. 2021, ApJ, 922, L2

Vigan, A., El Morsy, M., Lopez, M., et al. 2024, A&A, 682, A16

Vigan, A., Fontanive, C., Meyer, M., et al. 2021, A&A, 651, A72

Villaume, A., Conroy, C., Johnson, B., et al. 2017, ApJS, 230, 23

174 Bibliography

Virtanen, P., Gommers, R., Oliphant, T. E., et al. 2020, Nature Methods, 17, 261

von der Lühe, O., Quirrenbach, A., & Koehler, B. 1995, in Science with the VLT, ed. J. R. Walsh & I. J. Danziger, 445

Vousden, W. D., Farr, W. M., & Mandel, I. 2016, MNRAS, 455, 1919

Wallace, A. L., Casey, A. R., Brown, A. G. A., & Castro-Ginard, A. 2025, MNRAS, 536, 2485

Wang, J. J., Graham, J. R., Pueyo, L., et al. 2016, AJ, 152, 97

Wang, J. J., Vigan, A., Lacour, S., et al. 2021, AJ, 161, 148

Wheatley, P. J., West, R. G., Goad, M. R., et al. 2018, MNRAS, 475, 4476

Whitebook, S., Brandt, T. D., Brandt, G. M., & Martin, E. C. 2024, ApJ, 974, L30

Winn, J. N., Fabrycky, D., Albrecht, S., & Johnson, J. A. 2010, ApJ, 718, L145

Winterhalder, T. O., Kammerer, J., Lacour, S., et al. 2025, A&A, 700, A4

Winterhalder, T. O., Lacour, S., Mérand, A., et al. 2024, A&A, 688, A44

Woitke, P. & Helling, C. 2003, A&A, 399, 297

Wolszczan, A. & Frail, D. A. 1992, Nature, 355, 145

Xuan, J. W., Mérand, A., Thompson, W., et al. 2024, Nature, 634, 1070

Youdin, A. N. 2011, ApJ, 742, 38

Youdin, A. N. & Goodman, J. 2005, ApJ, 620, 459

Zahnle, K. J. & Catling, D. C. 2017, ApJ, 843, 122

Zari, E., Hashemi, H., Brown, A. G. A., Jardine, K., & de Zeeuw, P. T. 2018, A&A, 620, A172

Zernike, F. 1938, Physica, 5, 785

Zhang, Y., Xuan, J. W., Mawet, D., et al. 2024, AJ, 168, 131

Zhang, Z., Mollière, P., Hawkins, K., et al. 2023, AJ, 166, 198

Zuckerman, B. & Song, I. 2004, ARA&A, 42, 685

Zuckerman, B., Song, I., Bessell, M. S., & Webb, R. A. 2001a, ApJ, 562, L87

Zuckerman, B., Song, I., & Webb, R. A. 2001b, ApJ, 559, 388

Zurlo, A., Goździewski, K., Lazzoni, C., et al. 2022, A&A, 666, A133

Zurlo, A., Vigan, A., Galicher, R., et al. 2016, A&A, 587, A57

## List of Publications

As stated at the beginning of Chapters 2, 3 and 5, the bulk of this thesis is inspired by three works, two of which are published, the third was submitted in July 2025:

- T.O. Winterhalder et al. submitted, Planetometric exomoon detection via optical interferometry (working title), A&A
- T.O. Winterhalder et al. 2025, Orbit and atmosphere of HIP 99770 b through the eyes of VLTI/GRAVITY, A&A, 700, A4
- T.O.Winterhalder et al. 2024, Combining Gaia and GRAVITY: Characterising five new directly detected substellar companions, A&A, 688, A44

Additional publications I contributed to as second author while working on this thesis:

- J. Kammerer, **T.O. Winterhalder** et al. in prep., The ExoGRAVITY project: a K-band spectral library of giant planet and brown dwarf companions (working title)
- N. Pourré, **T. O. Winterhalder** et al. 2024, High contrast at short separation with VLTI/GRAVITY: Bringing Gaia companions to light, A&A, 686, A258

Publications I contributed to as co-author while working on this thesis:

- T. Stolker et al. (incl. **T.O. Winterhalder**) 2025, Direct imaging discovery of a young giant planet orbiting on Solar System scales, A&A, in press
- W. Thompson et al. (incl. **T.O. Winterhalder**) 2025, On the Orbit of the Binary Brown Dwarf Companion GL 229 Ba and Bb, AJ, 169, 193
- W. O. Balmer et al. (incl. **T. O. Winterhalder**) 2024, VLTI/GRAVITY Observations of AF Lep b: Preference for Circular Orbits, Cloudy Atmospheres, and a Moderately Enhanced Metallicity, AJ, 169, 30
- J. Xuan et al. (incl. **T.O. Winterhalder**) 2024, The cool brown dwarf Gliese 229 B is a close binary, Nature, 634, 1070

176 Bibliography

• E. Nasedkin et al. (incl. **T.O. Winterhalder**) 2024, Four-of-a-kind? Comprehensive atmospheric characterisation of the HR 8799 planets with VLTI/GRAVITY, A&A, 687, A298

- M. Nowak et al. (incl. **T.O. Winterhalder**) 2024, Catalogue of dual-field interferometric binary calibrators, A&A, 687, 248
- W. O. Balmer et al. (incl. **T. O. Winterhalder**) 2024, VLTI/GRAVITY Provides Evidence the Young, Substellar Companion HD 136164 Ab Formed Like a "Failed Star", AJ, 167, 64
- S. Blunt et al. (incl. **T.O. Winterhalder**) 2023, First VLTI/GRAVITY Observations of HIP 65426 b: Evidence for a Low or Moderate Orbital Eccentricity, AJ, 166, 257
- W. O. Balmer et al. (incl. **T.O. Winterhalder**) 2023, VLTI/GRAVITY Observations and Characterization of the Brown Dwarf Companion HD 72946 B, AJ, 956, 99

## Acknowledgements

The last three years have flown past. At ESO, nothing marks the bitter passage of time more demonstratively than the clockwork regularity with which we have to bid farewell to many good friends. Now that it is almost time for me to take my leave, I want to give a quick shout-out to a handful of dear friends, acquaintances, role models and archenemies – some people combining all of these roles with effortless ease – who have made these three years such a good laugh:

To my ESO mates, whether they only got to spend a few months here or signed up for the long game. To Adrien, the first friend I made in this place while shopping for leather trousers and long socks. Co-discoverer of Tumult, indie connoisseur and Beer Friday committee member during its heyday. To Andrea, the guy who made me call an ambulance for the first time in my life. To Alice, seemingly a bully, but kind at heart. To Samuel, my gunslinging, FIFA-playing and election-rigging office mate. To Justyn, ever partying and always up for a bit of banter, a real-life example that fellows can be fun! To David, buckaroo and unlikely substitute for the trip up to Berlin. To Ivanna, Alice's bullying partner in crime and suspiciously frequent user of my desk when I was not around. To Matt, the human flag, and Tom, the most improved table football player, the only man to have ever added a figure to an abstract and troublemaking enthusiast. To Felipe, troublemaker himself, gossip girl, radio show co-host and solely responsible for turning E.5.04 into a zone where no work whatsoever gets done. To Josh, always one for heading in a goal from a cross you thought you hit just a bit too high. To Pierrick Pascal, the biggest ESO movie club aficionado. To Simon, the napper, Rik, the brick, Giulia, my academic sister, Julienne from the East and everyone else! To the usual suspects at Science Coffee, most notably Jason and the coffee machine. To the ESO football team: Ronald, Paulo, Serban, Pawel, Jorge and the rest. To Nelma and Adele, always to the rescue when I had once again forgotten how to work the ERP or had submitted a travel request for a trip I have returned from already.

To my Max Planck mates. From Carbonara evenings in the MPA kitchen to Friday nights at the common room, here's to our next-door neighbours! To Cata, the best student rep out there, to Capucine, the gullible, to William, the serial business flight booker, to Fabi, the sports freak, to Matteo G., my yapper brother, to Forelle, bearer of the first nickname, and Diogo, soon-to-be cycling mate. And of course, to my two flatmates, Matteo and Benedetta, who made Landwehrstraße 63 my home in Munich.

The biggest thanks go out to my supervisors Antoine, Sylvestre and Jens! I've learned a lot throughout the past three years and I'm grateful for your patience with my struggles to fully grasp optical interferometry. I vow to catch up on it.

And finally, to those dearest to me: Danke für die Unterstützung, Mama und Papa, Patrick und Christoph. And of course, thank you, Chiara. Ever since that fateful encounter in the stairwell of Einsteinstraße 10, you have been a constant source of joy and comfort. Here's to many more years!

Danke euch allen.